Towards Optimal Control of Fuel Cell Hybrid Electric Vehicles

Towards Optimal Control of Fuel Cell Hybrid Electric Vehicles

Philipp Kemper

Southwestfalia University of Applied Sciences
and
University of Bolton

A dissertation submitted in partial fulfillment of the requirements of the University of Bolton for the degree of

Doctor of Philosophy

July 2019

Abstract

Global warming, the decline of natural resources as well as the strengthening of emission regulations have led to a research focus in new drive technologies. Within the group of alternative propulsion systems, fuel cell hybrid electric vehicle (FHEV) are considered especially promising. Since system efficiency as well as the operation characteristics are determined by the chosen energy management system (EMS) scheme, an optimal approach is a key aspect to guarantee optimal system operation in terms of power and energy efficiency, as well as component lifetime and costs. Existing research efforts mostly focus on the optimisation of the hydrogen consumption, while neglecting component degradation as additional important part of total system and operation cost. Furthermore, almost no published work considers the thermal management of a FHEV. Therefore, the presented work propose a novel model predictive control based energy management approach with a special focus on preventing fuel cell (FC) and battery (BAT) degradation and the vehicle's thermal management. In order to minimise component ageing and degradation, the objective function which is used in the developed method, includes cost which account for both decreasing BAT state of health as well as FC operation conditions which accelerate the degradation of the FC. To be able to test the developed EMS, a model and a hardware based test environment were developed. Since there are no thermal management systems for FHEV presented in literature, a new concept with a hierarchical control scheme was designed. Because the newly developed energy management shall be tested based on real world data, a method to generate test cases representing typical driving scenarios based on real world driving data was developed and implemented. Finally, the hardware system was used to validate the simulation model and vice versa, the model based approach was validated on real hardware.

Contents

List of Figures

List of Tables

ACRONYMS

A-ECMS adaptive ECMS

ASS all solid state battery

BAT battery

BEV battery electric vehicle

CADC Common Artemis Driving Cycles

D duty cycle

DC drive cycle

DoD Depth of Discharge

DoE Department of Energy

DP dynamic programming

DUT device under test

ECMS equivalent consumption minimization strategy

ECSA electrochemically active surface area

EMS energy management system

EV electric vehicle

FC fuel cell

FCM Fuzzy C-means clustering

FHEV fuel cell hybrid electric vehicle

FIBC floating-interleaving boost converter

GDL gas diffusion layer

HES hybrid energy system

HEV hybrid electric vehicle

ICE internal combustion engine

ICV internal combustion engine vehicle

LAB lead acid battery

LCO lithium oxide cobalt

LHV lower heating value

LFP lithium iron phosphate

LIB lithium-ion battery

LMO lithium manganese oxide

LTO lithium titanate

MEA membrane electrode assembly

MPC model predictive control

NASA National Aeronautics and Space Administration

NCA nickel-cobalt-aluminium

NEDC new European drive cycle

NGA National Geospatial-Intelligence Agency

NiMH nickel metal hydride battery

NMC nickel-cobalt-manganese

PC passenger compartment

PCA principle component analysis

PEMFC proton exchange membrane fuel cell

PHEV plug-in hybrid electric vehicle

PI proportional-integral

SC Super Capacitor

SEI solid electrolyte interface

SEPIC single-ended primary inductor converter

SoC state of charge

SoH state of health

SRTM Shuttle Radar Topography Mission

TMS thermal management system

USABC United States Advanced Battery Consortium

List of Publications

Some ideas and figures of this thesis have appeared previously in the following publications of the same author:

[1] P. Rehlaender, P. Kemper, A. Schwung, and U. Witkowski, "Control of a fuel cell vehicle thermal management system," in *2018 IEEE International Energy Conference (ENERGYCON)*. IEEE, 2018, pp. 7–12.

[2] P. Rehlaender, P. Kemper, A. Schwung, and U. Witkowski, "A fuel cell vehicle thermal system model," in *2018 IEEE International Energy Conference (ENERGYCON)*. IEEE, 2018, pp. 1–6.

[3] P. Kemper, P. Rehlaender, U. Witkowski, and A. Schwung, "Competitive evaluation of energy management strategies for hybrid electric vehicle based on real world driving," in *UKSim-AMSS 11th European Modelling Symposium on Computer Modelling and Simulation*. IEEE, 2017, pp. 151–156.

[4] P. Rehlaender, P. Kemper, A. Schwung, and U. Witkowski, "A novel predictive energy management system," in *UKSim-AMSS 11th European Modelling Symposium on Computer Modelling and Simulation*. IEEE, 2017, pp. 145–150.

[5] P. Kemper and U. Witkowski, "Model based design of a renewable energy supply with hybrid energy storage system," in *EMS 2016*. IEEE, 2016, pp. 117–123.

[6] P. Kemper, T. Tetzlaff, U. Witkowski, R. Zandian, M. Mamrot, S. Marchlewitz, J.-P. Nicklas, and P. Winzer, "Small-size robot platform as test and validation tool for the development of mechatronic systems," in *Robot Intelligence Technology and Applications 4*. Cham: Springer International Publishing, 2017, pp. 383–396.

[7] M. Mamrot, S. Marchlewitz, J.-P. Nicklas, P. Winzer, T. Tetzlaff, P. Kemper, and U. Witkowski, "Model-based test and validation support for autonomous mechatronic systems," in *Big data analytics for human-centric systems*. IEEE, 2015, pp. 701–706.

1

INTRODUCTION

In modern societies, one of the basic human needs, is individual mobility and the chance to move within a network to connect with other humans. Since the internal combustion engine (ICE) was invented, the exclusive guarantee for individual mobility is the transformation of chemical energy bounded in fossil fuels to kinetic energy through combustion. A rapid increasing awareness to minimise the human impact on the global environment, caused by the effects of global warming, has led to questioning this concept and forces the transformation towards an emission free mobility. Another central problem is that fossil fuels are not only a limited resource, but its combustion also causes harmful emissions such as carbon monoxide (CO), carbon dioxide (CO2) and oxides of nitrogen (NOx). This conflict is aggravated by the dramatically increasing demand for personal transportation over the past 20 years. The two driving factors are the rapidly growing world population and the economic growth of developing countries such as China, India and Mexico, which continue to expand [28]. Hence, the decline of natural resources as well as the strengthening of emission regulations in combination with a contentiously increasing demand for personal mobility, are also amplifying this transition. Today, consumer requests as well as taxation and emission regulations are globally putting the automotive industry under increasing pressure to produce more efficient and less polluting vehicles. Even if increasing fossil fuel as well as legislation has forced the industry to increase the efficiency and reduce the emission of pollutant gases in the last decade, the ICE technology itself is limited to the Carnot process efficiency and the fact that burning fossil fuels in all cases produce carbon monoxide. Because of the

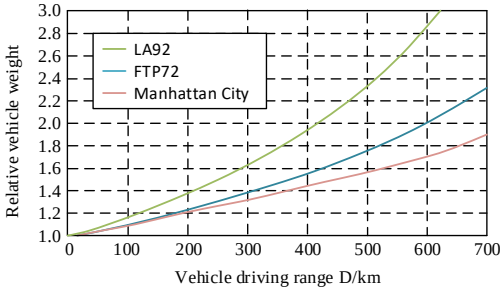

Figure 1.1: Vehicle curb weight sensitivity to the BEV driving range depending on various DCs, considering a compact car [1].

ongoing improvements, further reduction of emission or increasing the efficiency is only realisable under high cost. Thus, the industry is forced to explore new technologies. In general, it can be stated that the general objective is to shift mobility towards an electric based mobility. For the purpose of successfully complete this transition, it is inevitable that electromobility adapts to certain habits and costumes mobility patterns which are dominated at the time and shaped based on internal combustion engine vehicle (ICV).

Within the field of emission free power sources, two technologies are the most suitable and accepted ones at the moment, BAT and FC. BEV are commercially available in different configurations, almost all automotive manufacturers offer either a hybrid electric vehicle (HEV) or BEV and have announced to significantly enlarge their product portfolio in 2019 and 2020. BEV have several advantages, especially regarding high efficiency and zero emission. These benefits made BEV evolve their full potential in urban environments. Nevertheless, BEV are also subject to significant drawbacks. Due to the low gravimetric energy density of BAT, the range is typically limited and the recharge time is relatively high. Thus, with regards to long range driving, BEV suffer from significant drawbacks. Today the Tesla Model S can be considered as reference BEV. The maximum range is under optimal operation condition up to $480\,\mathrm{km}$ and the required charging time is $1\,\mathrm{h}$ under ideal conditions. Figure 1.1 depicts the driving range of a compact BEV related to the relative weight of the vehicle. It can be seen that the relative vehicle weight rises significantly with the driving range, which can be explained by the fact that the energy storage capacity of a BAT is directly related to the number of cells and thus to the weight. When considering Figure 1.1, one can

derive that with increasing driving range not only the vehicle curb weight increases but also the required motor power and thus the needed BAT power capability rises dramatically as well. In the last decade, especially HEV, combining a BAT and a ICE, allowed the automotive industry and its customer a smooth transition from fossil fuel based mobility towards electromobility. A typical HEV on sale now uses a combination of an ICE with a BAT to maximise the benefits of each source and overcome the individual drawback of the ICE and the BAT. In summary, a hybrid powertrain has a number of advantages compared to a conventional powertrain with regards to both efficiency and emissions.

Besides BAT, due to the higher volumetric and mass related energy density, FC are highly capable to be used as on-board energy source. In direct comparison against a BEV, due to the higher specific mass related storage capacity, a FHEV has the capability to enable a significantly higher driving range while still maintaining the full benefits of an electric vehicle (EV). The fact that the conversion, or electric power related, device and the energy storage elements are decoupled is beneficial in terms of system design and vehicle curb weight. The FC can be designed to meet the power demand, while the hydrogen storage meets the energy demand. Since the mass of the FC itself does not contributes to the energy storage capacity, the specific mass is comparable high, for systems with low storage capacities. Yet, with increasing storage capacity this negative effect can be neglected and only the high specific energy of the storage dominates the overall specific energy. Thus, the specific mass of the vehicle does not increase cubic with an increasing driving range. Instead, high energy storage capacities can be realised without significantly increasing the vehicle mass. Another advantage of storing energy separately is that, in contrast to BAT, fuel can be re-filled in comparable manner to fossil fuels.

Nevertheless, FCs also have significant drawbacks. The maximum power dynamic is limited and recuperating breaking energy is not possible without system extension. An efficient solution to overcome this drawback is to combine a FC with a BAT and a SC to form a FHEV. To combine different energy sources offers the chance to overcome the specific limitations of the single sources and makes best use of the individual subsystems. In a FHEV, the FC guarantees a long driving range, whereas the BAT ensures high efficiency by enabling the recuperation of breaking energy, while the SC provides the capability to handle high power dynamics. A detailed description as well as the fundamentals and operation characteristics of FHEV are given in Chapter 2.

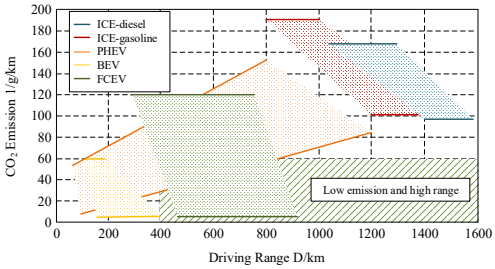

Figure 1.2: Estimation of CO2 emissions and range of medium size vehicles of different technologies in 2010 (upper regions) and 2050 (lower border) [2].

Figure 1.2 depicts an estimation of CO2 emissions related to the driving range of a medium sized vehicle with various technologies in 2010 and a prediction for 2050. While for BEV and FHEV, especially the assumed transition of the electrical energy supply towards a renewable energy causes the significant specific emission reduction, ICE based vehicles advance in emission control and an increase of the efficiency which cause lower CO2 emissions. Mahmoudzadeh Andwari et al. define that a low emission and long range vehicle must have a driving range of more than $400\,\mathrm{km}$ and a CO2 emission which is lower than $60\,\mathrm{g\,km^{-1}}$. In accordance to Figure 1.2, these requirements are solely met by a FHEV. In summary it can be said that FCs are a strong candidate for the transportation market in the long-term, but in the near future a number of technological challenges are to overcome, whereas FHEV have a good chance to surmount these challenges.

In the long term, hydrogen can be considered superior to fossil fuels. An essential benefit of hydrogen is that it can be generated almost anywhere in the world based on renewable energy sources through electrolysis of water. Thus, it is not only unlimitedly available but also can support the implementation of purely renewable energy, even in remote parts of the world. Additionally, it also alleviates various energy security issues caused by the dependency on oil-producing but politically unstable countries. Since it can be produced locally, high energy costs can be eliminated because the transportation of the fossil fuel to the demand centres will be reduced. Finally, and most importantly, the oxidation of hydrogen, used in a FC to generate electrical energy, does not emit any harmful pollutant

emission, just water. This does not only help to prevent the global climate change by minimising the overall emission of the mobility sector, but also reduces local emission peaks. In this respect, eminently high traffic density in urban environments in combination with the high local pollutant emission, are a huge problem. Since no harmful emissions are produced, hydrogen based mobility is also capable to significantly improve the air quality in urban environments. In [3] it is stated that both technologies, BAT and FC based mobility are in the initial stage of their market development and are posed to take advantage of the unavoidable surplus electricity that characterises renewable dominated energy systems. One criterion to favour either BAT or a FC based mobility is the required investment cost to set up a large scale infrastructure required for a complete mobility transition. In [3], a comprehensive comparison with the goal to perform a detailed design analysis of the required infrastructure for supplying BEV and FHEV vehicles in Germany at multiple scales, was outlined. With the intention to consider the total costs, the underlying question of the presented study analyses the investments, costs, efficiencies and emissions for an infrastructure capable of supplying between one hundred thousand to several million vehicles with hydrogen or electricity. For both infrastructures, a complete renewable energy supply was assumed. Thus, for the BAT case, sufficient energy storage capacity as well as a sufficient number and distribution of charging stations was considered. In the case of hydrogen based mobility, decentral electrolysis are used as an energy storage to support the large-scale renewable energy supply. For the transportation of hydrogen, both pipelines as well as the distribution via trucks was assumed. Figure 1.3 depicts the cumulative investment required for BAT and hydrogen infrastructure, related to the number of EVs. For a low number of FHEV the hydrogen generation is assumed to be based on existing source. Only after more than one million EV will be in the market, a complete transition to renewable based generation is realised. Summarising, it can be said that, with regards to low market penetration levels of a few hundred thousand vehicles, the costs of infrastructure roll-out are essentially the same for both technology pathways. While hydrogen was found to be more expensive during the transition period to electricity-based generation via electrolysis, the costs to build a large scale BEV charging infrastructure matches the cost for hydrogen infrastructure at 15 million EV and are significantly higher at more than 40 million EV. Until now, the estimated costs do not consider the costs caused by a secure electrical infrastructure, which solely depends on renewable energies. In comparison, in the hydrogen case, sea-

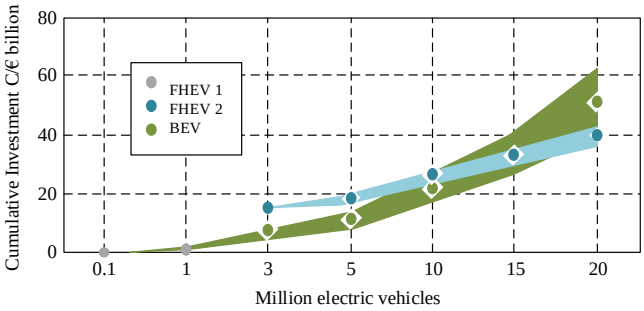

Figure 1.3: Comparison of the cumulative investment of supply infrastructures required for the large scale deployment of BEV and FHEV [3].

sonal storage capacity is set to bridge 60 days at low renewable electricity generation. [3] also estimates the mobility cost per kilometre, in the high market penetration scenario those are at $0.045\,€\,\mathrm{km}^{-1}$ for electric charging and $0.046\,€\,\mathrm{km}^{-1}$ for hydrogen fuelling. In accordance to [3], the total energy demand of a hydrogen infrastructure which is needed to supply 20 million FHEV is equal to $93\,\mathrm{TW\,h}$, which is nearly twice as high as the one required to charge the same number of BEV ($46\,\mathrm{TW\,h}$). Nevertheless, the low efficiency of electrolysis and FC causing that difference, can be compensated by the fact that you can use the surplus energy generated by renewable sources to supply the electrolysis. In the case of a BEV infrastructure, enough storage capacity is needed to be installed to have the same effect. If the use of surplus electricity is compared to an equivalent of renewable and fossil electricity supplied by the grid, the emission of CO2 per kilometre can be estimated. For 20 million EV, the emission of BEV are estimated to be $20.9\,\mathrm{g\,km}^{-1}$ and the one of an FHEV to be $2.7\,\mathrm{g\,km}^{-1}$ [3]. The numbers prove that the hydrogen infrastructure with the inherent seasonal storage option has lower CO2 emissions because of the high use of renewable surplus electricity.

Despite the releases of the Honda FCX-Clarity, Toyota Mirai and the Hyundai ix35 FCEV, there are still a number of challenges which have to be faced when trying to increase the market share of FHEV. Especially the costs and reliability of the FC, as well as the required hydrogen infrastructure which is not available and yet preventing FHEV from being competitive to ICV. Even if there is a more detailed analysis of FHEV in Chapter 2, a brief summary of the most essential challenges shall be discussed at this point. Although hydrogen storage has a high mass related energy density of $33\,\mathrm{kW\,h\,kg}^{-1}$, in contrast to $12\,\mathrm{kW\,h\,kg}^{-1}$ of fossil

fuels, the significantly lower volume related energy density ($3\,\mathrm{kW\,h\,m^{-3}}$) makes it hard to compete with liquid fossil ($9500\,\mathrm{kW\,h\,m^{-3}}$). This typically reduces the effective energy density to just $10\,\%$ of an equivalent tank of fossil fuel. Therefore, one aspect to improve the readiness of FHEV is to improve existing storage technologies. Of course FC are regarded as being expensive compared to conventional ICE. For example the costs of the Toyota Mirai with minimum configuration are $78\,600\,€$, while a comparable HEV, for example the Toyota Prius, starts with basic features at $28\,400\,€$. The high costs for the FHEV can be explained by various reasons „ including the immaturity of the technology and manufacturing processes, the low production volumes, but also because of the expansive materials required [29]. The component with the highest costs is the catalyst with a high quantity of platinum required. Thus, strong efforts are made to reduce the amount of platinum in the catalyst layer. Not only high costs and a limited volumetric energy density, but also durability and degradation issues have to be discussed when challenges for FHEV needed to be assed.

In order to be competitive to conventional technologies, FC power systems must be as durable and reliable as current automotive engines. Key contributors to FC degradation include the reduction of the size of the catalytic surface area, the membrane degradation and the corrosion of the carbon support, especially under conditions of load-cycling, high electrode potentials and high-temperature operation. Membrane durability is affected by both humidity variations which cause mechanical stress and chemical degradation, which can be accelerated by degradation products from the bipolar plates and other components in the FC. The U.S. Department of Energy (DoE) has defined a clear target for 2020, which is a durability of $5000\,\mathrm{h}$. This is equivalent to approximately $240\,000\,\mathrm{km}$ of driving. In this context however, durability is defined as a performance reduction of $10\,\%$ after a specified operation time [4]. Kurz et al. report that a projected durability of $3900\,\mathrm{h}$ (2015) before $10\,\%$ degradation for the automotive FC is realistic. Figure 1.4 depicts the 2015 DoE targets related to the 2020 targets. While a complete readiness of the power density as well as the specific power and the cold-start is indicated by the facts that those have not been strengthened from 2015 to 2020, the peak efficiency is not yet at its full potential. As shown, durability and costs are the primary challenges to FC commercialisation in a light-duty vehicle automotive application.

In summary, FHEV are still in the market introduction stage. They are not yet truly competitive with conventional ICE or BAT technology and

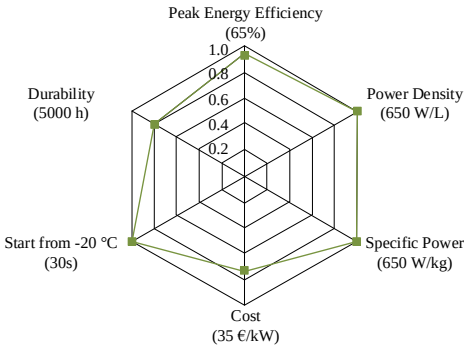

Figure 1.4: FC 2020 targets (black) versus 2015 status (green) for light-duty vehicle applications. Cost status is for a modelled system when manufactured at a volume of 500,000 units/year [4].

are only available for a limited number of suppliers and are obtainable in limited regions. The two key challenges which impede higher market penetration are the high costs and the limited infrastructure deployment. Even though politics and commercial consortiums announced to invest in a higher infrastructure deployment as well as the fact that increasing production rates, economics of scale, and technological improvements will lead to lower cost, FHEV will still be a niche product which aims at the premium segment. Nevertheless, it can be expected that in the next decade due to incremental improvements, the natural cost reduction and higher production volumes several technical and commercial goals will be achieved and FHEV will begin to become more competitive with current ICE and BEV vehicles.

1.1. Background and Motivation

This PhD project is part of the Hy2Energy - Centre for Hydrogen based Mobility located at the South Westphalia University of Applied Sciences (Hy2Energy), which is embedded in the funded research project “Energy4Mobile”. The project is funded by the “Ministerium für Innovation, Wissenschaft und Forschung des Landes Nordrhein-Westfalen”. Major objectives of the funded project are the development and optimisation of a FHEV and a metal hydride based hydrogen tank. Especially the TMS as well as the EMS are in the scope of the optimisation. The minimisation of the hydrogen consumption, maximisation of component’s life and reuse of waste heat of the FC are of special interest.

Besides E-Mobility today there are two other major trends in automotive industry, autonomous driving and connected car. Wahl described autonomous driving as being close to the commercial outline. Several research projects and automotive companies prove the functionality of prototypes [32]. Starting with semi-autonomous driving, like adaptive cruise control on motorways, the progression reaches full-autonomous driving for low speed. In order to realise fully autonomous driving, different standard advanced driver assistance systems can be combined [33]. One solution is to combine the sensors of a lane departure warning system and an adaptive cruise control. However, the cruise control is capable to control the longitudinal dynamics and the lane departure warning system the transverse dynamics. [31] The term "connected car" summarises different communication channels and various functions, in general there are four different options. *Vehicle to Infrastructure* summarises all functions and information a single car can exchange with the infrastructure. The infrastructure collects data from various cars, concentrates it and derives information which are transmitted to passing vehicles. The objective is to minimise traffic jams, avoid accidents and optimise the traffic flow. *Vehicle to vehicle* communication uses direct connections between different cars to exchange traffic related information. By propagating information via a chain of several vehicles, even medium distance information can be exchanged. Again the major objective is to reduce dense traffic and to increase safety. *Vehicle to cloud* communication integrates the vehicle into the internet of things and enables to exchange information with smart homes for example. *Vehicle to pedestrian* realises a connection between a vehicle and a smartphone and enables to automatically exchange information with the aim to avoid accidents and increase safety [34]. Of course non of these three major trends can be considered solely. The connected car as well as autonomous driving offer essential advantages for an efficient electric vehicle, especially for a FHEV. Precise information of the vehicle's sensors can be combined with information gathered from other vehicles or the surrounding infrastructure to form a complete picture of the vehicle's close range as well as a medium and long range environment. This information can be used to support autonomous driving by estimating the vehicle's optimal velocity for a specific road interval or to determine the maximum range of an FHEV. If a predictive control scheme is used to operate the power system of the FHEV, additional benefits arise. The underlying concept of a predictive optimal control scheme is to operate the power system in that way resulting in minimisation of the predefined cost function. In general, the cost function is minimal if

the energy consumption and the component degradation are minimum. Hence it can be stated that all major trends in the automotive industry are combined. Based on this combination a strong benefit for FHEVs arises, if those are controlled by an EMS, capable to utilise those benefits.

To support the evolution of mobility towards an autonomous connected FHEV, an intelligent EMS is required. The control requirements of any HES are not necessarily trivial. In a traditional ICV, the driver controls the engine using the accelerator pedal. The pedal angle in combination with the torque demand of the longitudinal dynamic of the vehicle determines the operating state of the ICE in order to produce the mechanical power required to drive the vehicle. In a HES, respectively a FHEV, having several energy sources means that there are now two additional degrees of freedom. Depending on the specific system topology, the number of inputs is also increasing. However, from a power system control perspective, the number of the disturbance is still one. This single disturbance is the demand of the electric drive system, depending on the acceleration demand of the driver, the traffic and road condition as well as the road inclination. Nevertheless, this demand can be supplied by the FC, the BAT or the SC. Even while there are additional degrees of freedom, system limitation also plays a significant role. The FC can not supply negative power, the BAT is limited to the maximum charge and the maximum discharge current, and the SC energy provision capability is limited by the amount of charge which is stored. Also costs and operation related aspects are essential. While using the FC to supply a load demand, hydrogen is consumed and thus, the fuel cost increases. In contrast when the BAT is used to supply a specific load, it leads to a reduction of the SoC and thus in a later phase of the trip, this energy can not be used any more. With additional BAT usage, the SoC depletion progresses, unless breaking energy is recuperated or the FC is used to recharge the BAT, but the increase of the overall fuel cost in inevitable. In the case of a direct couple SC the energy equilibrium of the SC is even more critical. The charge balance, respectively the SC current, determines the SC voltage directly, since the motor performance depend on the maximum input voltage, the vehicle driveability and performance is directly related to the SC voltage. The overall operating efficiency of the system highly depends on how the load is applied to the different energy sources over time. With the objective to make this decision, almost all FHEV use a EMS as a supervisory controller.

The decisions made by the EMS determine the operating points of various powertrain components, and therefore will have a large effect on

the overall operating efficiency of the vehicle. Thus, EMS is a large field of research and today there is a great quantity of publications presenting new ECMS approaches. Due to the high market penetration, the vast majority of this research efforts focus on ICE based HEV, but much of the presented approach can also be applied to FHEV. Due to the additional power conversion unit, and the more complex operation characteristics of FC and BATs, a number of requirements and impacts that are specific to FC and BATs have to be considered. Also the EMS has no direct influence on the component sizes, an efficient EMS might allow to reduce the required reference power and thus the costs of the powertrain. The two major costs benefits when applying an optimal EMS, are that both hydrogen consumption as well as the degradation of the components, can be reduced which leads to lower operation as well as maintaining costs. Both issues are approached by the central DoE 2020 targets, costs and durability, which were depicted in Figure 1.4.

1.2. Research Objectives and Contribution

The overall objective of this research is to find the best method to optimise the operation of a FHEV which in parallel minimises the hydrogen consumption and the degradation of the BAT and FC. Therefore, the presented research focuses on two related aspects: the electrical EMS and the TMS. The decision to investigate both topics was made because both are interdependent. Even while a stronger focus is put on the optimisation of the EMS, the operation temperatures of the FHEV's components have a significant impact on the durability of the system as well. Hence, the co-generation of waste heat used to heat the PC, can only be utilised when a suitable TMS is applied, which is also a unique benefit regarding overall energy demand and operation cost. The EMS will have a significant impact on the overall system efficiency as well as the component durability, however without the full potential of a FHEV, this cannot be achieved. The development of both approaches will be outlined based on an iterative method. In a first step models of both the electrical and the thermal system will be developed. These models will be validated either based on real hardware or based on datasheets provided by manufacturers. In a next step, a TMS is developed and implemented to control the simulation model. Finally, the performance of the implemented TMS is validated. A similar approach is followed to develop the predictive energy optimal EMS. In contrast, with regards to the electrical control system, prior to the development, the most discussed state of the art EMSs are implemented and their performance will be evaluated.

The specific objectives of this research project are:

- To determine and analyse the specific requirements for an EMS controlling a FHEV and to identify these operation conditions, which most of all induce degradation processes of the FC and of the BAT.
- To analyse existing TMS, derive requirements and to develop and to implement a suitable TMS, which guarantees optimal operation temperatures and enables the reuse of waste heat for heating the passenger compartment.
- To implement and test state of the art EMS approaches. Whereas these tests are executed on a virtual test bench and with regards to representative real world driving data. To evaluate the performance of these standard EMS and to derive options of improvement.
- The development of an energy optimal predictive EMS, which minimises both, the hydrogen consumption and the component degradation based on DP algorithm. The reduction of the DP's computational burden, by applying a novel two stage parallel optimisation approach.

Following these research objectives, this thesis will make specific contributions as follows:

- A comprehensive survey of the technological challenges and opportunities offered by FHEV, including degradation mechanisms, suitable system topologies as well as a conventional system design of FHEV.
- A novel TMS, including a hierarchical control system as well as the design of the cooling system structure and the configuration, which is capable to control the operation temperatures of all components included in a FHEV.
- A detailed performance analysis of the most important state of the art EMS schemes based on representative real world driving data. A method to derive a representative set of test cycles out of a set of unspecified real world driving data using a FCM was developed.
- A novel optimal predictive EMS scheme based on a MPC control approach using DP capable to both minimise the energy demand and components degradation. Due to a two stage parallel optimisation approach, a two input, second order system can be optimised based on DP in a reasonable processing time. As a means to consider the total operation cost including the cost caused by component degradation, each of the applied cost factors have been weighted based on real components and hydrogen cost.

1.3. OUTLINE OF THE THESIS

In this thesis the development of both and predictive energy optimal EMS as well as a TMS for a FHEV is described. The content of each chapter is:

Chapter 2 - Fuel Cell Hybrid Electric Vehicle introduces the fundamental aspects of FHEV as theoretical basis of the outlined work. Starting with a detailed survey of the required components, containing the state of the art as well as operation characteristic of the specific components. In the second part of chapter 2, the specific operation requirements of each energy source is given. A special focus is put on degradation mechanism which causes performance reduction of FC and BAT. The objective is to identify those operation condition inducing high degradation. Additionally, typical system topologies of FHEV powertrains are discussed. Subsequently, after the most suitable powertain topology was identified, the conventional system design is explained. Based on driveability constraints and the characteristics of a full-size vehicle, a power train is designed and the target system defined. Finally, the state of the art of conventional BEV and FHEV is discussed in the last segment of chapter 2.

In **Chapter 3 - FHEV Test Bench** the implementation of a virtual test bench is described. With regards to evaluate the EMS, a test bench required. In Chapter 3 the virtual test bench is introduced. In this work the test bench is used as evaluation platform. This chapter also includes the identification of reference test cycle derived from real world driving data as well as the hardware system used to validate the implemented models are introduced. The first section discusses the used data recording tool, subsequently followed by the description of the method applied to derive reference test cycles from the unspecified real world driving data. In the second section the scaled hardware used to validate the implemented models is introduced. Finally, in the third section, the model based virtual test bench is described. The models which are used to simulate the operation behaviour of all relevant components are explained.

Chapter 4 - Thermal Management System describes the development and test of a TMS of a FHEV. In the first section of Chapter 4, a detailed analysis of the thermal operation condition of the components of the FHEV's powertrain is outlined. Based on this analysis the configuration of a TMS capable to guarantee the optimal operation temperatures is explained in the second section. The simulation model of the thermal system used to validate the developed approach, is discussed in the third section. The fourth and final section describes the developed TMS including a hierarchical control approach.

State of the Art EMS schemes are evaluated in **Chapter 5 - Energy Management System**. In the cause to evaluate the performance of the most relevant state of the art EMS approaches, different EMS were implemented and their performance evaluated. In the first section of Chapter 5, a detailed survey of the requirements of the EMS of a FHEV is given. The implementation of the different EMS schemes are described in the Section 5.2 to 5.5. In the second section the implementation of a PI control scheme is discussed, in the third section a state machine based approach is introduced, in the fourth and fifth each a fuzzy control system and a ECMS approach are discussed. In the end of this chapter, the results of the EMS evaluation are presented and discussed.

Chapter 6 - A Predictive Energy Optimal Energy Management System presents the development, implementation and test of a novel predictive energy optimal EMS based on a MPC controller. In the first two segments the fundamental concepts of MPC control and DP optimisation are discussed. After the underlying concepts are introduced, section three and four present the implemented control oriented inverse system model and the electronic horizon based predictive disturbance model. In Section five a DP based MPC controller minimising the hydrogen consumption and component degradation is described. The implementation of the DP, optimising the two input second order system, prove that a real time application is not realisable. Because the computational burden of a DP increases exponentially with system order and the number of inputs, the processing time is in the range of the required sample interval. Based on the analysis of the combined approach, a two stage parallel DP is developed. This novel approach is described in detail in Section six of Chapter 6. Finally, the performance of the developed and implemented MPC is evaluated as seen in Chapter 5.

2

FUEL CELL HYBRID ELECTRIC VEHICLES

In general the high costs, the reliability of the FC and the sparse infrastructure deployment of refill stations are considered as key limitations preventing a wide market penetration of FC vehicles [35, 36]. While a FC has the highest energy density, the specific power density is comparably low. Additionally FC lack the ability to store recuperated energy. Thus, a hybridisation with a BAT or a SC or both to form a FHEV is necessary. Typically, an energy system of a FHEV contains a FC as the primary energy source and at least one additional energy storage element, for example a BAT or a SC. To determine the best power train topology and to realise its control is one of the key challenges of a FHEV. In order to make the best choice, the individual operation characteristics have to be taken into account. While a BAT system has a higher energy density, a SC is able to supply high power demands. The increased vulnerability against dynamic power changes is a drawback of BATs. In contrast, for SCs the low energy density is a challenge. Figure 2.1 compares the features of BATs and SCs. In order to overcome the specific drawbacks of the various sources, various hybridisation topologies to form a HES have been presented. A detailed review will be given in Section 2.2.3. A FC vehicle powered by a HES which uses multiple sources provides significant advantages [25, 37, 38]. A HES which supports a FC is capable to compensate the slow dynamics of the FC and recover breaking energy. Another advantage are the additional degrees of freedom, which enable a more flexible operation. For example, the FC operation can also

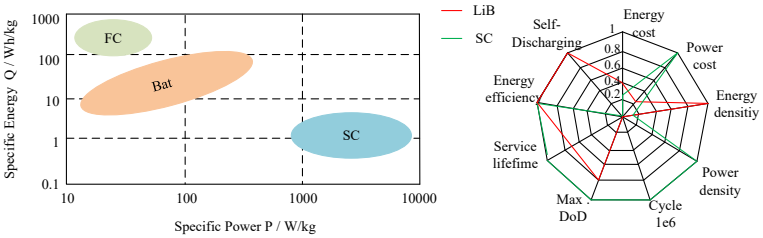

Figure 2.1: Comparison of energy storage technologies [5].

be oriented on the efficiency instead of solely related to the load demand. In total, the possibility to control the system based on different energy sources, the fuel efficiency can significantly be increased. Thus, by making best use of the specific operation characteristics of a FC, a SC and a BAT hybridisation creates remarkable benefits. Due to its fast refill ability and the longer driving range, a FHEV can be considered in multiple ways superior to EVs.

Almost all major car manufacturers have presented prototypes of FC vehicles. The first was the 'Electrovan', presented by GM in 1966. The 'Electrovan' contains a $1800\,\mathrm{kg}$ 'Union Carbride' alkaline FC system with a contentious power provision capability of $32\,\mathrm{kW}$ and a peak power of $160\,\mathrm{kW}$. The FC system was supplied by a liquid hydrogen storage. The vehicle was capable to drive $60\,\mathrm{km\,h^{-1}}$ with a maximum range of $240\,\mathrm{km}$ [39]. GM realised the transition from alkaline to PEM FC in 4^{th} generation of the HydroGen framework. In 1994, Daimler-Benz AG was the first to introduce a PEM FC vehicle, the NECAR 1. The energy system powering a MB-180 van includes a $500\,\mathrm{kW}$ FC from Ballard Power Systems supplied by a $300\,\mathrm{bar}$ compressed gaseous hydrogen storage. In 1996, the NeCar 3 was Mercedes' first FC passenger car [40]. With a focus on everyday capability and over 100 cars deployed in the US and Germany, GM's HydroGen 4 included a $1.8\,\mathrm{kWh}$ nickel metal hydride battery enabling a cold start ability down to -25 °C and was capable to accelerate from 0 to $100\,\mathrm{km\,h^{-1}}$ in $12\,\mathrm{s}$ [41]. In 2002, Toyota launched the world's first leasing of its FHEV in USA and Japan. The vehicle combined range was $250\,\mathrm{km}$. Since then, almost all major automotive OEM like Mazda, Volkswagen, Ford, Honda, and Nissan were producing and testing FHEV prototypes. The last major milestone was achieved by Hyundai and Toyota in 2015 when they introduced their first commercially available FHEV, the Toyota Mirai and the Hyundai ix35 FCEV [40].

Knowledge and know-how about components, system topologies as well as operation requirements are indubitable a fundamental precondition to discuss optimal control and design of a specific system. Hence, this chapter addresses these aspects of FHEV. First, key components are characterised, followed by a discussion of operation requirements and prevention of component ageing. Finally, based on the introduced fundamental prerequisite and system characteristics, a conventional design approach of a FHEV is presented.

2.1. Components of the Energy System

Central components of an EVs HES are a SC, a BAT and a FC, whereas power electronic based converters are utilised in order to interface the different voltage levels of the individual sources and control the operation states of the sources related to the EMS. In the following section the fundamental principles, all relevant types, and the operation characteristics of the named components are going to be be discussed further in this chapter.

2.1.1. Fuel Cells

The FC concept was first published in 1839 by William R. Grove. The first technical application was realised in the 1950s for the American manned space programme. General Motors developed the first FC powered car in 1966, other automotive manufacturers followed in the 1990s. The long time span until application was mainly caused by the requirement for sophisticated materials and the high catalysts cost [42]. The basic operation concept of a FC is comparably simple. A FC is a galvanic cell similar to a BAT, whereas chemical energy is transferred into electrical energy by a redox reaction. The simplest way to look at a FC is to say that gaseous hydrogen fuel is being combusted, whereas instead of liberating heat, electrical energy is produced. The amount of generated electrical energy is directly proportional to the contact area and in inverse ratio to the distance between the electrodes. Therefore the electrode's structure is commonly of porous material and assembled as flat plates. Depending on the basic FC type (acid or alkaline) different electrochemical reactions may process at the anode and at the cathode. Figure 2.2 depicts the basic architecture and the corresponding chemical reactions of an alkaline and of an acid FC.

Today there are several FC types and technologies, Table 2.1 gives a short overview. The molten carbonate FC uses a molten mixture of alkali metal carbonate as electrolyte and require carbon dioxide from the air to run its reaction. Similar to the solid oxide FC, the high operation temper-

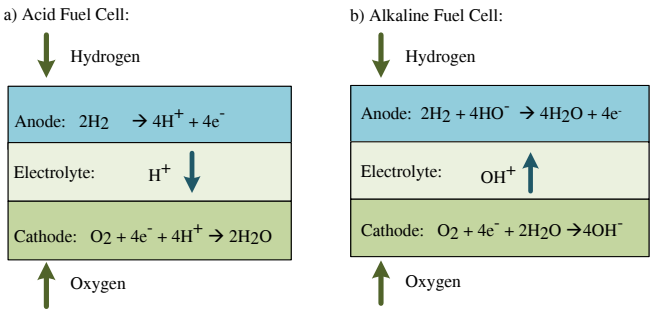

Figure 2.2: Operation concept different FC types. Illustration of the electrode reactions and charge flow for a) acid and b) alkaline FCs

ature (700 °C - 800 °C) of the molten carbonate FC leads to a fast reaction rate without an expensive catalyst. Also it is possible to use methane or coal gas as fuel. Nevertheless, also the limited dynamics as well as the corrosive mixture of lithium, potassium and sodium carbonate as electrolyte are disadvantages of the molten carbonate FC. The solid oxide FC operates at a temperature at approximately 600 °C - 1000 °C. Caused by the high temperature, the reaction rate of the process is high without the need for an expensive catalyst. The operating temperature also enables the direct use of natural gas. Disadvantages are the need for ceramic materials, which are complicated to handle, the limited operation dynamics, and the slow start-up. In phosphoric acid FC porous electrodes, platinum catalyst and high temperatures (220 °C) are used to enhance the chemical reaction. This type of cell was the first one produced in commercial quantities. Due to the early availability, there are various systems worldwide running continuously as a nearly maintenance-free power source. Furthermore, phosphoric acid FC are usually used in large scaled combined heat and power systems. It is also possible to operate the phosphoric acid FC with natural gas. If hydrogen is used as fuel an efficiency of 40 % - 45 % can be reached.

In automotive applications, PEMFC appear to be the most suitable FC technology. Here the low operation temperature is especially benefitial and allows the system to start up faster. Moreover, the solid state of its electrolyte (no leakage and low corrosion) and the high power density make them fit for transport applications. Because of the complex system architecture, only few automotive manufacturers like Toyota, Honda and GM develop and manufacture PEMFCs. As automotive suppliers, more specialised companies like Ballard Power Systems, Hydrogenics,

Table 2.1: Overview FC types and materials

Typ	AFC	PEM	DMFC	MCFC	SOFC
Electrolyte	aqueous KOH solution	proton-exchange-membrane	phosphoric acid	KCO_3 melt in $LiAIO_2$ matrix	ceramic solid ZrO_2
Tempera-ture [°C]	<100	40-120	40-120	600-800	800-1000
Fuel	H2	H2	methanol water	natural gas	natural gas, coal gas
Oxident	O2	air O2	air O2	air O2	air O2
Anode	Ni, Pt, Pt	Pt	PtRu	Ni|NiO	Ni-YSZ
Cathode	Ag, Pd, C	C	Pt	Ni|NiO	Cermet
Bipolar Plate	Ni coated	graphite, coated stainless steel	graphite, coated stainless steel	coated inconel	ceramic

or FuelCell Motors produce FCs. The PEMFC's chemical reaction is comparable to the acid FC one's, shown in Figure 2.2. The mechanical structure of a PEMFC is depicted in Figure 2.3. The membrane electrode assembly (MEA) contains the electrodes, the catalyst layer and a thin solid ionic conductive polymer membrane as separator. The membrane's functionality is comparable to the one of a separator in LIB. It separates the anode and cathode and thus needs to be gas tight against hydrogen, oxygen, and nitrogen. It also requires a high mechanical stability and low electron conductivity while a high proton conductivity is essential. Today membranes are 50 - 200 µm thick and made of Nafion, a polytetrafluorethylene (PTFE) structure with sulphonic acid (SO_3H) channels enabling proton conductivity. The reaction layer, electrochemically active surface area (ECSA), is the most essential part of the MEA. Here the three phase contact is realised and hydrogen oxidation and oxygen reduction supported by a catalyst taking place. Also part of the MEA is the catalyst layer, formed of platinum as catalyst and a carbon catalyst support layer. Next to good catalytic properties, a high electrical conductivity, high gaseous transport, and large ECSA are essential requirements

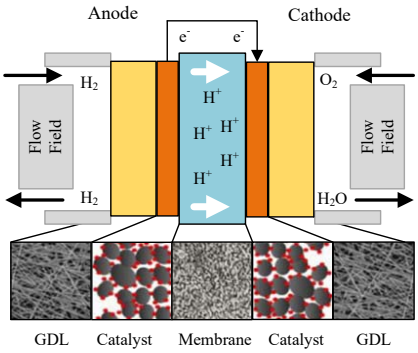

Figure 2.3: Schematic scheme of a PEM FC including the corresponding medium flows and charge transfers.

for the catalytic layer. Since platinum has the most significant impact for FC's costs, the platinum loading was reduced to $0.2\,\mathrm{mg/cm^2}$ at the cathode and $0.4\,\mathrm{mg/cm^2}$ at the anode. The MEA is between two bipolar plates with gas supply and cooling channels. Those plates needed to be chemically stable against the reactants, have high electrical and thermal conductivity and need to be gas tight. Between the bipolar plates and the MEA a thin gas diffusion layer (GDL), which distributes gaseous hydrogen and oxygen over the complete electrode's surface and conducting released electrons, is assembled. To enable a porous structure, the GDL is typically realised with PTFE coated carbon fibre. Bipolar plates realise the laminar gas supply to the GDL.

Due to the low operating temperature as well as the solid and immobile electrolyte, the technical requirements and structure of a PEMFC is comparably simple, see Figure2.3. Additional benefits which result from the low operating temperature is ability to fast start up and the ability to operate under dynamic power changes. PEM FCs are sensitive to impurities in the hydrogen supply, especially sulphur compounds and carbon monoxide. Whereas carbon monoxide reduces the active membrane area, H2 purging supports reactivating the membrane. In contrast sulphur acts as catalyst poisoning and leads to irreversible damage of the membrane. Therefore, the supply with pure hydrogen ($99.8\,\%$) is required. Another important aspect is the humidity dependent ionic conductivity of the polymer membrane. At the cathode water is a reaction product. The generated water diffuses through the membrane to the anode, where ionic transport drags water molecules back to the cathode. thus, water

molecules constantly pass the membrane. In the case of high air humidity, gaseous water passing the membrane condensates and liquid water molecules may interfere with the hydrogen and oxygen flow. Therefore a complex humidity and water management is needed in order to guarantee an optimal membrane humidity and best operation conditions. The PEMFC efficiency is determined by four effects. The maximum efficiency is characterised by the thermodynamic equilibrium, the released energy is equal to the difference of upper heat value of hydrogen, and the change of entropy. The activation losses are determined by the energy required for electron and ion transfer, the ohmic losses are caused by the resistance of the membrane and the electrodes, the concentration losses arise due the limited diffusion rate. Figure 3.12 depicts a typical polarisation curve of a PEMFC. A non-linear model of a PEMFC enabling loss calculation is described in detail in Chapter 3.3.2. When building FC power systems one obstacle is the low cell voltage ($<1\,\mathrm{V}$). To overcome this challenge a number of cells are connected in series. The series connection of several single cells is called a FC stack. The gas transport within a stack is realised by horizontal and vertical channels in the bipolar plates. A stack in combination with auxiliary systems, like a controlled reactant supply, a temperature and humidity control as well as operation supervision is called a FC system. Because a complete power system and not the optimisation and control of a FC at cell level is in the scope of this work, the expression FC is used for a PEMFC system. Though, a FC is still the most costs intensive part of a FHEV's power system, in the past decade FC cost has been reduced from $275\,\$\,\mathrm{kW}^{-1}$ in 2002 to $73\,\$\,\mathrm{kW}^{-1}$ in 2008, and further reduced to $61\,\$\,\mathrm{kW}^{-1}$ in 2009 [24]. On behalf of the United States Department of Energy (DOE), Brian D James et al. and Wilson et al. summarise recent development of FC's costs. Exemplary the cost of a $80\,\mathrm{kW}$ automotive FC was analysed. In accordance to [44], for a production batch of 100,000 units per year the costs are $50\,\$\,\mathrm{kW}^{-1}$, and $45\,\$\,\mathrm{kW}^{-1}$ at 500,000 units per year in 2017. The projected costs at system level expected by 2020 and 2025 are approximately $\$47\,\mathrm{kW}^{-1}$ and $40\,\$\,\mathrm{kW}^{-1}$, respectively when manufactured at a volume of 100,000 units per year. When manufactured at a volume of 500,000 units per year the predicted costs decrease to $43\,\$\,\mathrm{kW}^{-1}$ and $36\,\$\,\mathrm{kW}^{-1}$. The long term DOE target at high volume production, 500,000 units per year, is $30\,\$\,\mathrm{kW}^{-1}$. [43, 44]

2.1.2. Hydrogen Storage

A central component of a vehicle is the main energy storage, in the case of a FHEV this is the hydrogen storage. In accordance to [45], there are

Table 2.2: Metal hydrides and the corresponding operating conditions

	Low temp. hydrides	Medium temp. hydrides	High temp. hydrides
Temperature	40-80 °C	>100 °C	>300 °C
Pressure	10-50 bar	1-5 bar	1 bar
Material	$TiFeH_2$,$CaNi_5H_6$	MgH_2	$MgNiH_4$

three main technologies to store hydrogen:

- Compressed gasous storage
- Cooled liquid storage
- Metal hydrided storage

Compressed gaseous hydrogen is usually stored in a pressure tank made of steel or aluminium. Commercially available are systems up to 700 bar. Klell et al. stated that compressed gas storage is the technology with the longest history and lowest cost. Because of the material dependant pressure, the gravimetric energy density of hydrogen stored in pressure tanks also depends on the chosen material. In order to pressurise a certain gas quantity, a defined amount of energy is necessary. Klell et al. estimate the minimal energy needed to compress hydrogen from 1 bar to 1000 bar at standard temperature is $9409\,\mathrm{kJ\,kg^{-1}}$, this is equal to 8 % of the lower heating value (LHV) of hydrogen. When a compressor efficiency of 50 % is assumed, the storage loss increase to 16 % [45]. If hydrogen is cooled below -253 °C, it changes to a liquid state, which reduces the specific volume by a factor of 800. Klell et al. assess that the required energy for the described cooling process to be 30 % of the LHV. Thus, the required energy to store hydrogen in liquid phase is significantly higher than the amount of energy which is required store it pressurised. Furthermore, the storage device which is capable to store liquid hydrogen needs to fulfil specific requirements. Typically, a two-phase structure, which contains a vacuum between the inner and outer shell, is used to guarantee the required thermal isolation. So not only the energy demand to cooled liquid hydrogen, but also the mechanical design of the storage is more complex. [45]

Hydrogen can also be stored in metal hydrides via chemical compounds, hydrogen, and a metal or an alloy react to form metal hydrides. The metal or alloy can store multiple hundreds of its capacity of hydrogen

in solid state. Thus, metal hydrides have the highest volumetric storage density of all three presented methods. During the storage process, heat is released, vice versa the extraction of hydrogen requires heating. Thus, the storage process can be described as an exothermic reaction, the release of hydrogen as an endothermic reaction. The characteristics of a specific metal hydride are defined by the metal or alloy used. Table 2.2 summarises three standard temperature ranges and the corresponding hydrides.

2.1.3. BATTERIES

Implemented in plug-in hybrid electric vehicle (PHEV)s or BEVs, batteries are an essential integral part of electrifying vehicle propulsion systems. In BEV BAT are used to supply the energy demand of the propulsion system and store surplus energy when recuperating energy while breaking. Within the wide field of different BAT technologies, there are three basic chemistries used in vehicle propulsion systems; lead acid battery (LAB), nickel metal hydride battery (NiMH) and LIB. LAB have been used as starter lighter ignition BAT over the last decades. Each cell provides a voltage of $2\,\mathrm{V}$. The main advantage is their comparable low cost, whereas high degradation, low energy density ($0.04\,\mathrm{kW\,h\,kg^{-1}}$ - $0.09\,\mathrm{kW\,h\,kg^{-1}}$), and low usable Depth of Discharge (DoD) can be considered as key drawbacks. NiMH have a lower cell voltage of about $1.2\,\mathrm{V}$, but their energy density is significantly higher ($0.08\,\mathrm{kW\,h\,kg^{-1}}$ - $0.250\,\mathrm{kW\,h\,kg^{-1}}$). Additionally, because of the comparable small internal resistance NiMH can supply high power. The major disadvantage is the high self-discharge rate and low cycle efficiency. Nowadays, PHEV as well as BEV solely use LIB. Even while the individual cost is the highest, the high efficiency and high power and energy density ($0.26\,\mathrm{kW\,h\,kg^{-1}}$) as well as high Coloumbic efficiency are crucial positive factors. Figure 2.4 presents a Ragone plot of different BAT technologies.

A survey of BAT technologies used in the transportation sector can be found in [2, 46–48]. A more general approach with a focus on stationary application is described in [20]. In summary, the key parameters to compare BAT technologies are the energy and power density, the cycle and calendar life and the specific cost per kWh. The United States Advanced Battery Consortium (USABC) defines specific target values for the energy density to allow long term commercialisation of BEVs and to enable a minimum driving distance of $500\,\mathrm{km}$, to be $235\,\mathrm{W\,h\,kg^{-1}}$ at BAT pack level, corresponding to $350\,\mathrm{W\,h\,kg^{-1}}$ at cell level. The USABC also specifies a maximum costs goal at cell level equal to $150\,\$/\mathrm{kg}$ and $125\,\$/\mathrm{kg}$ at pack level. The BAT's longevity targets demand a minimum a calendar

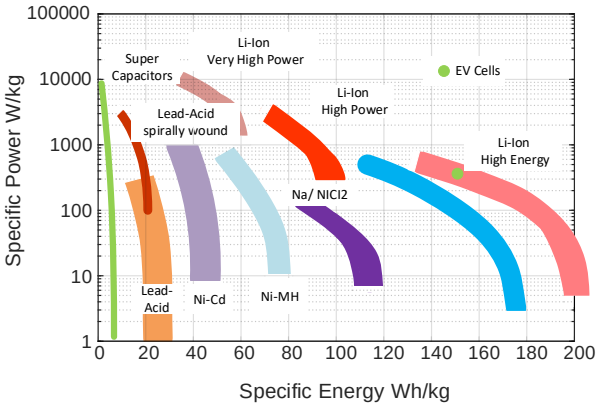

Figure 2.4: Specific energy and power capability of different BAT technologies [2].

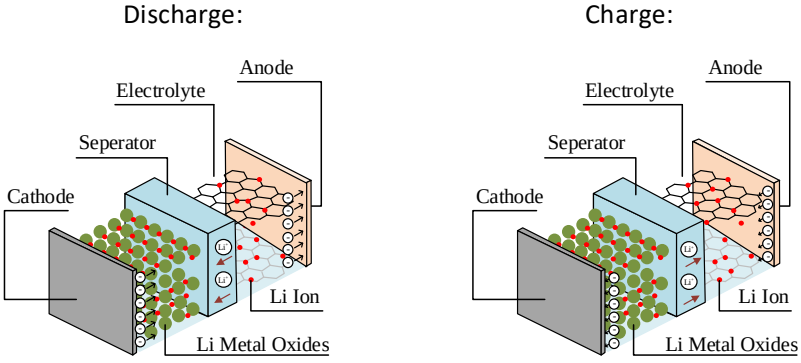

Figure 2.5: Lithium ion discharge and concept and moving charge carrier.

life of ten years and a cycle life of 1,000 cycles. Today, automotive LIB reach an energy density of up to $140\,\mathrm{W\,h\,kg^{-1}}$, see 2.3 [2, 6]. Among the available technologies, lithium based BATs are most promising for the near future. Due to high electrochemical potential and low equivalent mass, LIBs show the highest energy density. Furthermore the wide range of possible power to energy ratio (P:E) allow the BAT to be adapted to various requirements. Therefore, in the following the fundamental concept as well as different LIB cell technologies are going to be discussed.

LIB is a comparably new technology; in 1980 John Goodenough discovered $LiCo_2$ as cathode material. In 1996, Goodenough suggests $LiCo_2$

as cathode material with higher potential. Due to its various positive properties, like low cost, non-toxic, and high specific capacity, it spread rapidly. In LIB, the moving charge carriers are lithium ions, while discharging lithium ionises in the solvent at the anode. The solved lithium ions pass with the solvent, the electrolyte and separator and intercalate at the cathode. During operation, a thin lithium ionic conductive solid electrolyte interface (SEI) layer is generated and separates the anode and electrolyte preventing anode corrosion. Respectively, charging takes place vice versa. A schematic presentation of the charge and discharge process of a LIB is shown in Figure 2.5. Exemplary the reaction equation for $LiFeO_4$ are:

Anode (graphite): $Li_1C_6 \longrightarrow C_6 + Li^+ + e^-$

Cathode (iron phosphate): $Li^+ + e^- + FePO_4 \longrightarrow LiFePO_4$

Today LIB is not limited to a specific cell chemistry, instead various material combinations are applied in commercial cells [49]. Ansean et al. name six well-established LIB technologies to be used in BEV: nickel-cobalt-aluminium (NCA), lithium oxide cobalt (LCO), lithium manganese oxide (LMO), lithium titanate (LTO), or lithium iron phosphate (LFP). Due to its high specific capacity and low volumetric variation, graphite is most commonly used as anode material (market share > 95%), whereas in some cases a small amount of silicon is added to achieve higher energy density. Also lithium titanate based cells are commercially available. As cathode material several combinations are used, most widespread are nickel-cobalt-manganese (NMC) or NCA blended with LMO. Therefore, the selected cathode material has the strongest impact on the cell's electrochemical potential. Key requirements for material selection are high specific and volumetric capacities and high discharge potentials versus Li/Li+, high intrinsic safety, high tap density and fast kinetics. Today nearly all commercial cells contain an electrolyte based on lithium hexaflourophosphate ($LePF_6$) as conducting salt that is dissolved in a mixture of cyclic and linear organic carbonate solvents. Because of the liquid organic electrolyte, a porous membrane as separator is required. Today four different types are used, micro-porous membranes, non-woven mats, ceramic-coated operators, and solid inorganic polymeric electrolytes (separators and electrolyte combined). A state of the art survey about performance and cost of LIB technologies is given by Schmuch et al. and summarise in Tables 2.32.4.

In the last decade, energy capacity of BEV BATs has increased to $100\,\mathrm{kWh}$, which correspondes to a driving range of up to $100\,\mathrm{km}$. The

Table 2.3: Overview of LIB cell chemistries and characteristics of prismatic cells and batteries for BEV [6].

Anode	Cathode	Capacity (A h)	Voltage (V)	Specific Energy (W h kg)	Energy (W h)	Range (km)	OEM Model
C	LMO-NMC	50	3.7	109	16	160	Mitsubishi i-Miev (2008)
LTO	NMC	20	2.3	89	20	130	Honda FIT EV (2003)
C	LMO-NMC	63	3.65	172	24	140	Fiat 500e (2013)
C	LMO-NCA-NMC	60	3.7	122	22	130	BMW i3 (2014)
C	NMC	25	3.7	130	24	190	VW e-Golf (2015)
C	LMO-NCA-NMC	37	3.7	185	36	300	VW e-Golf (2016)
C	LMO-NCA-NMC	94	3.7	189	33	183	BMW i3 (2017)

key reasons for the continuous increase in storage capacity are new materials and optimised cell topologies. Today in automotive applications prismatic, pouch and cylindrical cells are the main cell types. Whereas the highest specific energy and power density is achieved by 18650-type cylindrical cells. Even while different cell chemistries can be established to meet specific requirements, Tables 2.3 - 2.4 show that in the vast majority of commercially available BEV synthetic graphite anodes dominate. With NMC as state of the art cathode material. Nevertheless, regarding the most important parameters for BEV (specific energy, cost, and specific power), each of these technologies has individual advantages as well as disadvantages, without any clear choice for any technology. However,

Table 2.4: Overview of LIB cell chemistries and characteristics of cylindrical and pouch cells and batteries for BEV [6].

Anode	Cathode	Capacity (A h)	Voltage (V)	Specific Energy (W h kg)	Energy (W h)	Range (km)	OEM Model
C	NCA	3.2	3.6	236	60-100	330-500	Tesla S(2012)
Si	NCA	3.4	3.6	236	60-100	330-500	Tesla X (2015)
Si-C	NCA	4.75	3.6	260	75-100	490-630	Tesla 3 (2017)
C	NMC	52	3.65	152	17	145	Smart Fortwo EV (2013)
C	NMC	38	3.70	-	27	145	Kia Soul EV (2014)
C	LMO-NCA	40	3.75	167	30	172	Nissan Leaf (2015)
C	NMC	56	3.65	186	60	383	Chevrolet Bolt (2016)
C	NMC	59	3.70	241	41	400	Renault Zoe (2017)

due to their high power capability, intrinsic safety, low toxicity, high cycle lifetime, as well as availability of materials and low cost, LFP gain attention in BEV application. [20, 48–51] The specific energy per volume and per weight of different cell chemistries is illustrated in Figure 2.6. basic

A comprehensive summary of state of the art BAT technologies and the key characteristic with regards to the application in automotive systems is given in Table 2.6. When looking on the depicted parameter, it appears that not only the specific technology determines the BATs characteristics, also the cell design has a significant impact. Basically, a cell

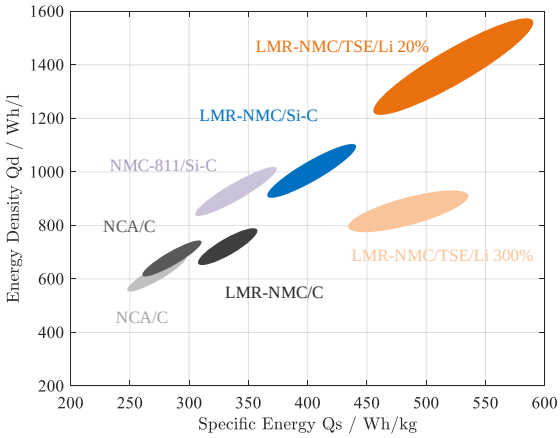

Figure 2.6: Specific energy capability of state of the art LIB. *graphite - C; silicon-carbon - Si-C; silicon-carbon composite - Si-C; $LiNi_1CoMnO_2$ - NMC; $LiNiCoAlO_2$ - NCA; lithium-manganese rich NMC - LMR-NMC; thiophosphate-based solid electrolyte - TSE; lithium metal - Li* [6].

can be designed to have a high energy density or a high specific power. In the case of high power, a cell is designed with high electrolyte conductivity, strong tabs and terminals as well as a thin active mass layer. In contrast, high energy BATs typically have large electrodes, thin tabs and a low rate of conductivity additives in order to maximise active mass ratio.

In summary can be stated that depending on the BAT technology and design, a BAT system has either high specific energy or high specific power. Therefore, the criteria to determine the most suitable BAT system depend most of all on the application. For the application of BEV, a high energy cell is in almost all cases the optimal choice, whereas the benefits of a HES can be utilised most if a cell with high power capability is chosen.

2.1.4. SUPERCAPACITORS

SCs are electrochemical energy storages based on an electric double-layer capacitor. SCs do not have a specific dielectric like standard capacitors, instead the energy storage ability is caused by two effects, faradaically charge storage or electrochemical pseudocapacitance. In contrast to BATs, SCs are capable to supply high power, but lack the ability to store large amount of energy storage capacity. Compared to conventional capacitors, SC are capable to store up to a 100 times more energy per unit

Table 2.5: Main characteristics of LIB technologies [20].

Type	LMO	LFP	LNMC	LTO	Li-S
Energy density (Wh/kg)	160	120	200	70	500
Power density (W/kg)	200	200	200	1000	-
Cycle Life (100% DoD)	>20k	>2.5k	>2k	>10k	100
Cost (US$/kWh)	360	360	360	380	-
Maturity	Commer-cial	Commerc--cial	Commer--cial	Demo -	R&D -

mass. A SC consists of two electrodes, namely the anode and the cathode, which are separated by an ion permeable membrane, and an electrolyte establishing an ionically conductive connection between the anode and the cathode. If an external voltage is applied, an electric double layer of opposite polarity to the electrode's polarity is formed at the electrode/electrolyte. Figure 2.7 depicts the basic structure of a SC. Since both electrodes act as individual capacitors, the total SC's capacitance is determined by their series connection.

If adsorbed electrolyte electrons pervade the double-layer, a reversible faradaic redox reactions occurs at the electrodes surface and cause a pseudocapacitance to originate. Pseudocapacitance is accompanied with an electron transfer between electrolyte and electrode. This faradaic charge transfer originates by a fast sequence of reversible redox processes. Because only charge transfer takes place, the adsorbed ions have no chemical reaction with the atoms of the electrode, no chemical bonds arises. The ability to originate pseudocapacitance is determined by the chemical affinity of the electrode materials to the ions adsorbed on the electrode surface as well as on the structure and dimension of the electrode pores. Materials exhibiting redox behaviour for use as electrodes in pseudocapacitors are transition-metal oxides like RuO_2, IrO_2 or MnO2. These are inserted by doping in the conductive electrode material such as active carbon, as well as conducting polymers such as polyaniline or derivatives of polythiophene covering the electrode material. [52]

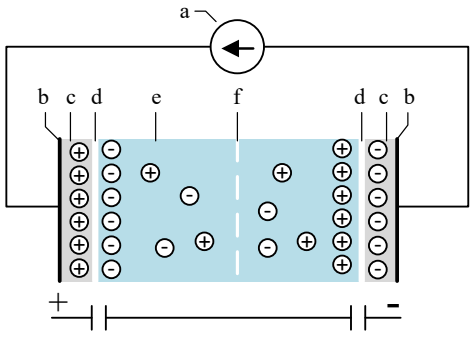

Figure 2.7: SC structure with (a) power source, (b) collector, (c) polarised electrode, (d) Helmholtz double layer, (e) electrolyte having positive and negative ions, (f) separator.

Table 2.6: Key feature of the main SC technologies [21].

	Symmetric	Asymmetric	Hybrid
Main Storage	double layer	double layer + pseudocapacitance	double layer + faradaic
Spec. Energy	$5\,\mathrm{W\,h\,kg^{-1}}$	$30\,\mathrm{W\,h\,kg^{-1}}$	$100\,\mathrm{W\,h\,kg^{-1}}$
Spec. Power	$9\,\mathrm{kW\,kg^{-1}}$	$5\,\mathrm{kW\,kg^{-1}}$	$4\,\mathrm{kW\,kg^{-1}}$
Applicability	Commercial	Material RD	Manufacturing RD
Temperature	-40/80 °C	-25/60 °C	-40/60 °C

2.1.5. Power Conversion

If different energy sources are combined with the aim to make best use of their individual benefits, one has to be able to ensure optimal operation states and to control the power and energy flows. For the targeted system topology, see 2.2.3, an energy flow from the FC to the SC and a bidirectional flow between BAT and SC have to be controlled. Since these sources typically operate under different DC voltage-current-characteristics, a DC-DC converter is required. The specific voltage levels depend on the selected components. For example, Hydrogenics FC modules typically operate at output voltages between minimum $20\,\mathrm{V}$-$180\,\mathrm{V}$ and maximum $40\,\mathrm{V}$-$360\,\mathrm{V}$ [53]. The voltage level of a BAT and the one of a SC both depend on the specific module configuration. The comparison of commercially available vehicles, indicates that most vehicle's BAT voltage levels vary strongly. The Toyota Mirai is equipped with a NiMH BAT, with 34 series cells and a nominal voltage of $244\,\mathrm{V}$. In contrast the

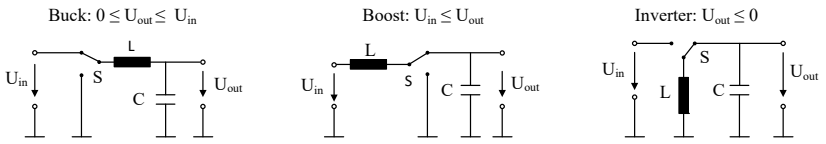

Figure 2.8: Basic concepts of buck, boost and inverter power stages.

Honda Clarity FC's power system contains a BAT with an output voltage of 346 V [54][55].

In general there are two different DC-DC converter concepts, linear voltage converter and switching power converter, whereas switched mode converter can be subdivided into isolated and non-isolated topologies. While linear converters typically are either applied at small power applications or to realise continuous supply levels, switching DC-DC converters are suitable for high power and high voltage conversion ratios at high efficiency. Since neither the design nor the optimisation of DC-DC converters are in the scope of this work, only basic concepts for switching mode converters are discussed. A concise summary of state of the art DC-DC converters applied in FHEV follows subsequently.

Figure 2.8 depicts the three basic concepts of DC voltage conversion, buck, boost and an inverter topology. Each of them contains three components: a switch S, an inductance L, and a smoothing capacitor C. Depending on switching frequency and the relation of on to off time, energy is stored in the inductances. In the first circuit, the buck topology, the switch applies an alternating voltage at the LC output filter, which results in an output voltage between zero and U_{in}. In the boost topology, energy is stored in the inductor during on time and released to the output while the switch is turned off. The input voltage plus the induced voltage from the energy stored in the inductor generates an output voltage larger than U_{in}. In the last plot, the inductance is recharged while the switch is in the right position. When the switch is turned, a continuous inductor current charges the capacitor to the negative output voltage.

In a buck converter, the alternation switch is replaced by a transistor and a diode. When the transistor conducts, the input voltage drives an increasing current through the inductor and the capacitor. In a next step the transistor turns off and the inductor drives a decreasing current through the capacitor and the diode. Depending on the ration of on to off time as well as the inductor value, a continuous or discontinuous inductor current is obtained. To describe the basic concept, steady state operation in

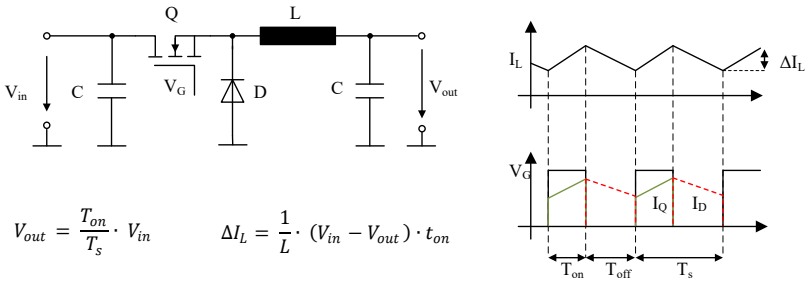

Figure 2.9: Buck power stage in continuous conduction mode.

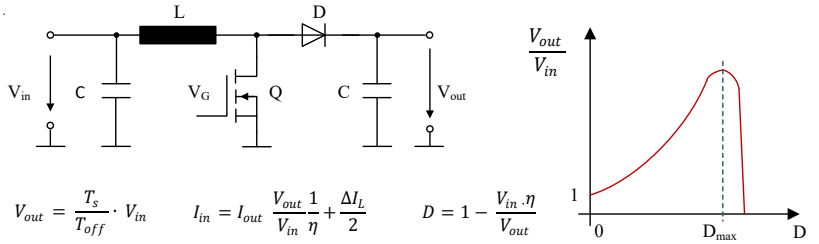

Figure 2.10: Boost power stage in continuous conduction mode.

continuous mode is assumed. Figure 2.9 depicts a MOSFET based buck converter equivalent circuit and the corresponding current waveform, as well as the current and voltage equation. The transistor current is displayed in green, the diode current in red. As sum of transistor and diode current, a triangular inductor current waveform is established. The output voltage is proportional to the duty cycle (D), as the ratio of on time to switching period.

Similar to buck circuits, the alternation switch is exchanged with a transistor and a diode resulting in an equivalents circuit of a boost converter. Figure 2.10 shows a simplified schematic of a boost converter. Assuming a lossless operation and a continuous conducting transistor, the minimum output voltage is equal to the input voltage. Since the transistor of a boost converter short circuits the inductor, the transistor current is directly related to the converter input current and is therefore always larger than the load current. Parasitic resistance in the inductor and the MOSFET as well as the voltage drop across the diode will set an upper limit for the duty cycle D and thus limits the output voltage. As shown in Figure 2.10, all practical boost regulators have a maximum duty cycle, beyond which the regulator will not boost. When operating a continuous switching boost converter, open circuit as well as short circuit operation have to be prevented. In open circuit mode, the switching transistor continuously transfers energy to the output capacitor, causing a continuously rising output voltage. Otherwise, if the output is shorted, a potentially large current will flow from the input supply to the output short. If the output of a boost regulator is pulled down to the input voltage or below, the inductor current will try to increase without limit.

Depending on the duty cycle D, a buck-boost converter is able to generate an output voltage below or above the input voltage. Different topologies are possible, the simplest one uses an inverter topology given in Figure 2.8. A second option is a Cuk converter, it also converts an input voltage into an inverted output voltage, which can be higher or lower than the applied input voltage [56]. A single-ended primary inductor converter (SEPIC)'s boost-buck stage overcomes the limitation of an inverted output voltage. The concept is a boost converter, followed by a buck stage. Swapping the boost and buck stage lead to a Zeta converter with the same functionality as the SEPIC but with a more stable feedback loop. A simple bidirectional buck-boost topology is given in Figure 2.11. In this case either an energy flow from the low voltage side to the high side or from the high side to the low side can be realised.

Power dissipation in DC-DC converters is typically dominated by the inductor conduction losses and the MOSFET switching and conduction losses. The inductor conduction losses are determined by the DC resistance of the inductor and its RMS current. The conduction losses in the MOSFET can be described similarly by the RMS MOSFET current and the on-state resistance of the transistor. The switching losses are characterised by the switch-on energy and the switching frequency. While switching losses dominate for low load currents, conduction losses are

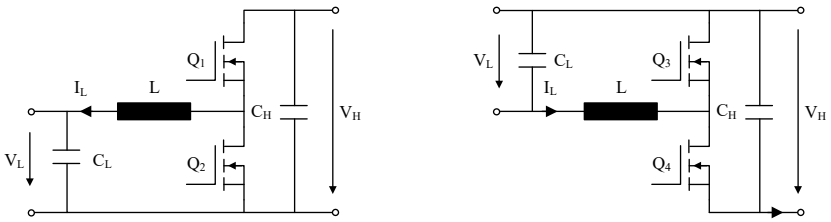

Figure 2.11: Schematic of a bidirectional buck boost converter.

relevant at higher load currents. One option to guarantee high efficiency rates over a broad area of operation are multiphase topologies. A multiphase regulator, or interleaved converter, is a parallel set of power stages. Figure 2.12 illustrates an equivalent circuit of an interleaved buck stage. The single phases are connected in parallel and share both input and output capacitors. During steady state operation individual phases are active at spaced intervals equal to $360°$ divided by the total number of phases throughout the switching. The efficiency characteristic of an interleaved converter is depicted in Figure 2.12. It can be seen that allowing phases to be dropped or added depending on the load current, enables a high efficiency over a large load current spectrum. At low currents fewer phases are used, down to a single phase, to minimise the FET switching losses. As the load current increases, conduction losses begin to dominate over switching loss and more phases are activated to keep the efficiency as high as possible. The optimum set point to turn on a phase occurs at the intersection of two efficiency curves.

A second family of DC-DC converter are isolated topologies. Isolated DC-DC converters realise the energy transfer from input to output via a transformer. In the case of isolated transformer based converters, the desired characteristic can be achieved via the transformer winding ratio. Due to the additional transformer losses, the efficiency of isolated converters are lower than the one of non-isolated converters. The flyback converter stores energy in the transformer core during transistor on time and transfer it to the secondary side during off time. The output voltage can be determined similar to the inverter, but the ratio of primary to secondary windings has to be considered. The forward converter can be described as a switched transformer with a buck converter at the secondary side. The primary and the secondary voltage of a forward converter has the same polarity. The active clamp converter is a variation of the forward

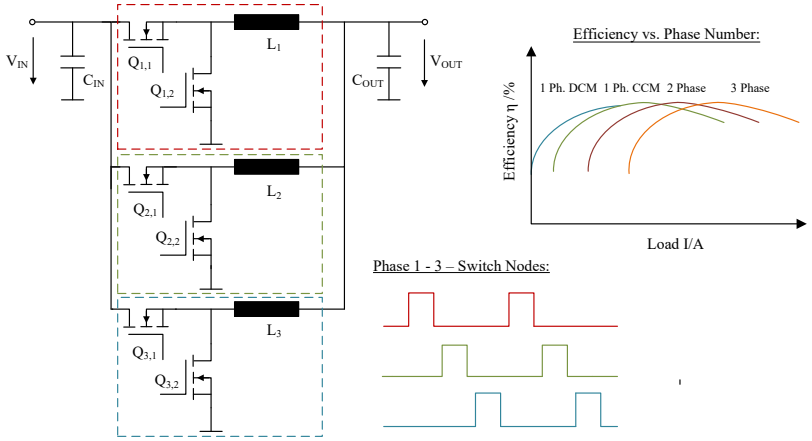

Figure 2.12: Schematic of an interleaved buck converter, efficiency vs. phase number and applied switching pattern.

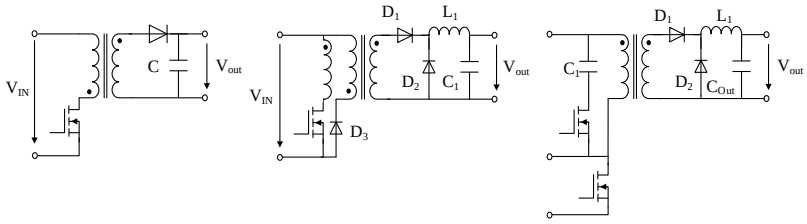

Figure 2.13: Isolated DC-DC converter topologies.

converter, but instead of a third reset winding an active clamp circuit, allowing the demagnetising current flow through a parallel transistor and capacitor, is applied. Bridge converters use a full or a half bridge topology to transform the DC input voltage to an AC voltage, which is applied to the primary winding of a transformer. On the secondary side the transformed voltage is rectified. By applying a full bridge at the primary and the secondary side, a full buck-boost bidirectional DC converter can be realised.

In order to transform the typically comparably low FC voltage to the high intermediate circuit level, the main requirement for the FC's DC-DC converter is a high boost ratio. Since the operation state of the FC shall also be controlled via the DC-DC converter an input current con-

trol is necessary. In order to enhance the FC's life, low FC current variation is essential, see Section 2.2.1. Additionally, FHEV impose physical constraints such as volume and weight under limited cost. [57, 58] Despite the wide input and output range and required high transformation ratios, the main drawback of a bridge converter, respectively isolated converter topologies, is the additional weight of the transformer. Whereas the lacking ability to control the input current as well as the high number of components are reasons against resonant converter topologies [59]. In accordance to [59] a simple boost converter is the best option to realise FC's DC-DC converter. In contrast, Kabalo et al. name the high current ripple and the complex design of the magnetic components as major drawbacks of using conventional boost converter in a FC application and propose a new DC-DC converter family, defined as floating-interleaving boost converter (FIBC) [60]. The proposed FIBC topology combines an interleaved input with a floating output reducing voltage and current stress. With the focus on voltage stress on the semiconductors, Zhang et al. describe a three-level boost DC-DC converter with a wide input voltage range for FC vehicles [61]. The proposed three-level boost converter reduces voltage stress to half of the output voltages and establishes a high voltage gain at medium duty cycle. A technique to estimate the drying and flooding conditions of a FC based on signals injected by the converter is presented by Dotelli et al.. Whereas high frequency current ripple of switched mode converter allow one to estimate the ohmic resistance indicating a dry membrane, ad hoc switching control allows measurement of the low frequency impedance as a measurement for membrane flooding [62]. A review of boost topologies with a focus of FC connection to the grid is given in [63] whereas Kabalo et al. review DC-DC topologies used in FC applied in vehicles.

Also in BAT - SC EV the selection of the bidirectional DC-DC converter topology is of great importance. Since typically both BAT and SC show high efficiency, the DC-DC converter is one of the major factors contributing to the overall system efficiency. As for the FC converter, the BAT converter also faces the same limitation regarding size and cost. An analysis comparing a presented three level buck-boost approach with state of the art non-isolated buck-boost DC-DC converter topologies, two level and interleaved, used in automotive application is given in [64]. The three different topologies were tested under the Urban Dynamometer Driving Schedule, the presented results imply that the three level buck-boost converter shows a higher efficiency, especially at high switching frequencies, and has the smallest size of the magnetic components.

Table 2.7: Comparison of different multi-input converter approaches [22].

	[66]	[67]	[68]	[69]	[22]
Topology	full bridge	half bridge	buck-boost	boost	buck-boost
No. of ports	3	3	3	3-4	3
Extension	Yes	Yes	No	Yes	Yes
Isolation	isolated	isolated	non-isolated	non-isolated	non-isolated
No. of Switches	12	6	7	4	6
Voltage Range	Wide	Wide	Wide	Limited	Wide
Power Flow	Yes	Yes	Limited	Limited	Yes
Control	Phase-Shift	Phase--Shift	Duty-Cycle	Duty-Cycle	Duty-Cycle

Instead of using single converter in order to interface the FC and BAT to the SC DC link, a bidirectional multi input DC-DC converter topology can be used. Here different DC sources are controlled independently. Consequently, a single converter controls the power flow in the HES. In research such as [65] or [66], approaches to realise a multi-input converter, capable to connect different DC sources, are presented. Akar et al. compare three different possible solutions, one is a combination of parallel buck-boost topologies, second is a parallel cascaded buck-boost converter and in a third approach, different DC sources are applied via individual power switches and an inductors to a single buck-boost stage. Zhao et al. discus a three port converter using three full bridge cells applied to a single three winding transformer, able to control the power flow in a multiple voltage system [66]. In contrast, Tao et al. control the voltages applied to a three winding transformer with half-bridge cells and forms a multi-port DC-DC converter. The converter is applied to a SC-FC hybrid system feeding a DC link of a load inverter. Consequently only the SC port is interfaced with a boost half-bridge cell including an additional inductor.[67] A different approach using a buck-boost topology is presented by [68]. Jiang and Fahimi focus on the stationary application of HES, presenting a multi-port power electronic interface with a modular topology. Here four half-bridge cells act as four boost converters enabling the connection of four independent DC sources to a DC-link of a grid

inverter [69]. A bidirectional approach connecting a BAT and a SC to a common DC link based on a non-isolated buck-boost converter topology is presented in [22]. An essential feature of the presented approach is the possibility to interface additional DC sources by a combination of a half-bridge and an inductor. Furthermore, due to the half bridge topology, boost as well as buck mode for each applied source is possible. A matrix comparing the different multi-input approaches is given in [22], Table 2.7 summarises the results.

2.2. System Design and Operation

Operating a FHEV implies two essential aspects. One is to supply sufficient power for the vehicle propulsion system, the second is to ensure optimal operation conditions for the single components. While the power demand is characterised by the requested driveability, optimal operation and operating conditions are characterised by operating a system under specific conditions to ensure ideally high efficiency and low degradation. Almost every technical system suffers operation induced and calendar ageing caused degradation. Since this section focusses on operation and operating condition, only operation stress dependent ageing is considered and calendar ageing is not discussed. In the following, main ageing effects of all electro-chemical components of a FHEV are discussed, assuming that optimal operation and operating conditions are derived. Finally specifications to ensure high drive-ability are summarised.

batde

2.2.1. Fuel Cell Degradation Mechanisms

FCs are affected by different processes that cause ageing and degradation. Independent to the origin, two different degradation effects can be observed: a reduced cell voltage and higher H_2 permutation through the membrane. In automotive applications, both effects are relevant, decreasing cell voltage causes lower maximum power capacity and higher currents, whereas higher H_2 permutation rates lead to higher H_2 concentration in the exhausting gas and lower H_2 efficiency. In summary, both effects cause increasing H2 consumption and higher costs. A typical measure for FC degradation is cell voltage reduction in $\mu V\,h^{-1}$ per cell. In accordance to Herb, FC's end of life is defined at a cell voltage reduction of $10\,\%$. A detailed analysis of different degradation mechanisms is given in [7]. MEA degradation under accelerated humidity cycling is analysed in [70], whereas [71] focuses on degradation under open-circuit conditions. A more general review with a focus on the long-term performance

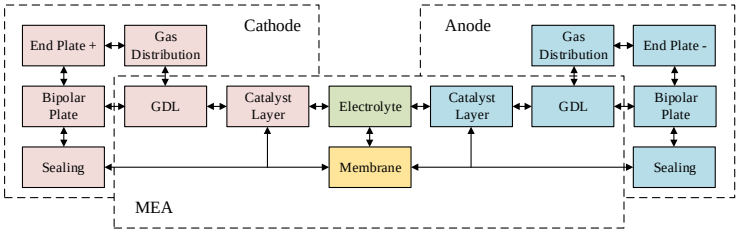

Figure 2.14: Schematic structure of FC components [7].

and durability of a FC is given in [72]. Placca and Kouta analyse FC degradation as a fault tree analysis including a detailed overview about literature related to the individual degradation effects [73]. A lifetime prediction model with a focus on the economic lifetime of FC is presented in [24]. Zhou et al. present degradation prediction based on a multi-physical ageing model using a particle filter [74]. Additional methods related to the prediction of FC degradation can be found in [75–78]. With a focus on the development of EMS for a low speed campus vehicle with an optimised FC lifetime, Fletcher et al. presented a comprehensive review of MEA performance degradation [79]. With the aim to design an EMS preventing component degradation, a central question is, what operation condition causes which degradation effect? In order to answer this question, all relevant effects related to the affected component are going to be discussed in further more detail. Figure 2.14 summarises FC's components affected by degradation processes, the relevant components are the membrane, the catalyst layer, the bipolar plates, the GDL and the seals.

Membrane failure mechanisms can be classified as mechanical (pin-hole and crack formation), as thermal (dryout, solvolysis, and desulfonation), or as chemical (peroxide initiated free radical degradation) degradations [70]. During operation pressure, humidity and temperature variations as well as vibrations causing mechanical stress, temperature variations and humidity cycling have direct impact on the chemical reactions and material properties. The most common failure mode induced by a FC's membrane is gas crossover through pin-hole formation. Provoking formation of pin-holes is typically caused by failures introduced by assembling and materials processing, high temperatures, vibration, pressure changes, and low humidity during operation. Hydrogen crossover leads to hot spots and local heat enhances pin-hole formation. Not only mechanical stress but also chemical degradation, caused by hydrogen peroxide or hydroxyl, can have an effect on the membrane. A reduction of the mem-

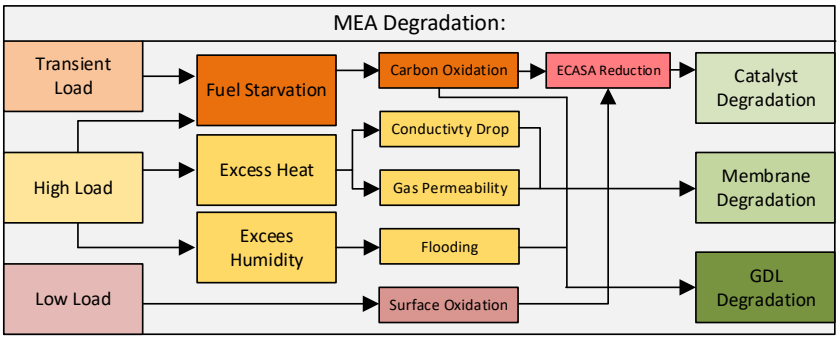

Figure 2.15: Schematic illustration of the MEA degradation mechanisms that depend on FC load.

brane's ionic conductivity can occur because of impurities in the supply air or by mechanical stress which can trigger GDL delamination. Additionally, platinum particles can deliminate at high pressure, humidity or temperature variations. Furthermore, a variation of the pore size impeded water discharge and causes swelling of the membrane. [7, 23, 70, 73, 79]

In accordance to Placca and Kouta, catalyst layer degradation can occur at both sides, anode as well as the cathode. Whereas in each case Nafion degradation, platinum dissolution or carbon degradation are possible causes. The degradation of Nafion as membrane material can also occur under cycling operation condition, [23] reported a degradation of Nafion after a test cycle of $900\,\mathrm{h}$ operation under cycling conditions leading to a cell voltage reduction of -$29\,\mu\mathrm{V\,h^{-1}}$. While platinum dissolution at the anode side is primarily caused by long term operation, at the cathode also global or local operation at high potentials has a significant impact. Clustering of platinum particles can be triggered by high temperatures or humidity as well as load transients and cycling. Long periods at open circuit voltage, cycling as well as non homogeneous current distribution are main causes for local or global high potentials at the cathode. At the cathode side, carbon degradation can be a result of long term operation and insufficient reactant supply due to high transients in FC power. At the anode side cell reversal, caused by either insufficient reactant supply due to high transients, or maldistribution of reactants, are primary reasons for carbon oxidation. Reactant crossover through membrane pin-holes, contaminations or ice can cause failures in the distribution of reactants. [7, 73, 80]

Table 2.8: Dominant degradation mechanisms at specific operation condition that FCs might be exposed to [23].

Condition	Dominant Degradation
Ideal Condition ($T \leq 75\,°\mathrm{C}$, $RH \geq 95\,\%$, $U_{Cell} \leq 0.8\,\mathrm{V}$)	GDL loss of hydrophobicity
Low relative humidity ($\leq 95\,\%$, $U_{Cell} \leq 0.8\,\mathrm{V}$)	Membrane degradation
Relative humidity cycling	degradation membrane mechanical properties
Open Circuit Voltage	Membrane degradation
Potential cycling	Pt clustering and dissolution at cathode
Start/Stop cycles	Carbon corrosion
Fuel Starvation	Carbon corrosion

Table 2.9: Operation induced voltage degradation rates [24].

Operation Condition	Voltage Degradation Rate
Start-Stop	$13.790.8\,\mu\mathrm{V}$ per cycle
Idling	$8.70.8\,\mu\mathrm{V\,h^{-1}}$
Load Change	$0.420.8\,\mu\mathrm{V}$ per cycle
Idling	$8.70.8\,\mu\mathrm{V\,h^{-1}}$
High Power Load	$100.8\,\mu\mathrm{V\,h^{-1}}$

Zhou et al. give two main degradation mechanisms acting on the GDL, one is PTFE decomposition, the second physical deformation due to carbon losses or unbalanced force distribution from either the membrane or the bipolar plates. Resulting effects especially hydrophobicity loss and change of the GDL pore structure lead to an increase in water content of the GDL and thus impending gas transport. Similar to the catalyst layer, high temperature or fuel starvation at high currents or local starvation at start/stop can cause carbon oxidation. [72, 74, 81, 82]

Table 2.8 lists different operation conditions and the corresponding degradation mechanism. Even while high current transients are not mentioned, high temperature, fuel starvation and low relative humidity are results of high current transients. Table 2.9 summarises empiric factors related to the degradation of a FC with regards to operation condition based on measurements outlined by [24]. In summary,it can be stated that

the most important stress factors enhancing FC degradation are the operation temperature, current transients, start/stop events, humidity management, and idle phases. Though when operating a FC system, an optimum between suitable power supply and limited degradation needs to be found [7]. Figure 2.15 summarises the discussed degradation mechanism and the operation states supporting such effects. All the mentioned processes finally lead to degradation of the catalyst, the GDL and the membrane causing either a higher hydrogen permutation or lower cell voltage.

2.2.2. Battery Degradation Mechanisms

BAT ageing is a degenerative process which changes the material properties of a cell. The degradation typically leads to a capacity and power reduction. An increasing internal resistance and decreasing capacity are the main indicators. The BATs calendar age, the operation temperature, the depth of discharge as well as the BAT current and load cycling accelerate cell ageing. Smaller maximum range and performance reduction are consequences for BAT degradation in an EV. Figure 2.16 shows exemplary the effect of cell degradation. Here peak power versus energy removed for a fresh cell and one 20 weeks aged at $55\,^{\circ}\mathrm{C}$ and with $100\,\%$ SoC are depicted. After 20 weeks, both peak power and energy capacity were significantly reduced.

In related literature, a wide range of analysing, testing or modelling BAT degradation mechanisms are presented. Smith et al. give a short overview of the state of the art BAT degradation models with a special focus on a control perspective. A detailed summary of ageing mechanisms effecting LIB regarding specific cell chemistries is given by [84]. Käbitz present a comprehensive summary of ageing and degradation of LIB cells and linked it to results of electrochemical impedance spectroscopy. Jaguemont et al. verify accelerated LIB ageing at subzero temperature by performing accelerated load cycle and calendar ageing tests at $20\,^{\circ}\mathrm{C}$ and $25\,^{\circ}\mathrm{C}$. In [87] a power law model to describe the calendar ageing of LFP cells, depending on the cell temperature and the SoC, is given. Brand et al. analyse the influence of current ripples on LIB's lifetime. Various approaches to model LIB degradation are presented. Basically, these can either be classified in theoretical models or empirical approaches. Theoretical models typically focus on specific electro-chemical effects, and therefore provide detailed explanation of degradation mechanisms and how these are affected by different operation conditions [89–91]. Empirical models are often developed based on degradation tests or experiments and tailored for a specific application. Nevertheless, those models

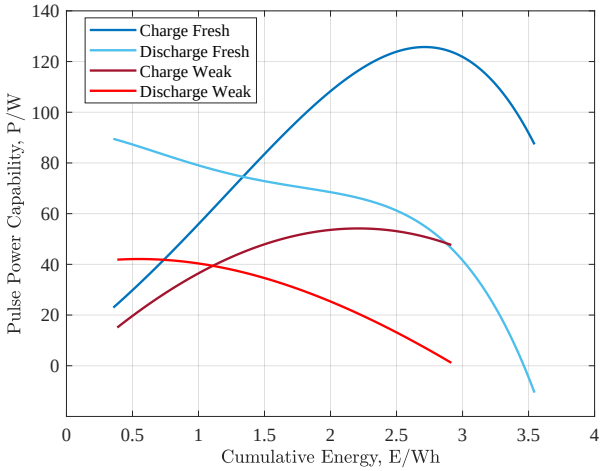

Figure 2.16: Power capability vs. energy taken from for a fresh 100 W cell and the same cell aged 20 weeks at 55 °C, 100 % SOC [8].

are more convenient to be used in control and operation [92–94]. A semi-empirical LIB degradation model, adaptable to different cell chemistries, to assess cell life loss based on operation profiles is presented by [95]. The presented approach offers the benefit that neither time intensive ageing experiments need to be carried out nor only specific mechanisms are modelled, instead only calendar and cycle life test data typically provided by most cell manufacturers are required.

Similar to the FC, all relevant components of a BAT (electrodes, electrolyte, SEI-layer, current collector and separator) can also be affected by degradation mechanisms and ageing. In the following, these effects are be discussed in the order of the component the specific mechanism has an impact on. It is quite difficult to formulate general mechanisms independent from cell chemistry and design. Considering the scope of this work being a specific system which consits of LFP cells, mechanisms affecting this specific cell chemistry are going to be analysed in detail.

The negative electrode can be affected by different degradation mechanisms. Mechanical stress, like temperature cycling or acceleration, as well as expansion of lithium ions with the solvent can cause the graphite to be peeled off or lead to morphological changes in the graphite structure. The graphite's active surface can be reduced by expansion of the SEI layer. High temperatures can reduce the conductive binder and increase the internal ohmic resistance. High humidity or other impurities can im-

pede direct conductive contact between lithium ions and the anode electrode enhancing irreversible intercalation. At the anode, the significantly higher potential enhance the oxidation process. This especially happens at open circuit condition. The resulting oxide layers between the electrolyte and electrode reduce the active surface area. Also the anode's morphological structure can change, causing reduced lithium intercalation and finally reduced BAT capacity. Since $LiFePO_4$ transition to $FEPO_4$ while discharging is accompanied with volumetric changes, it results in additional mechanical stress. An increase of internal resistance can also occur if contact between the electrolyte and anode is interfered. Additionally, mechanical stress can decrease the anode porosity and hence reduce the active surface. Similar to the cathode, the anode's binder can also corrode due to high temperature. Binding of lithium in the SEI layer cause degeneration of the electrolyte's conductive salt. Impurities, especially high humidity, also have a negative impact on the electrolyte. Though the SEI is an essential part of the LIB, high temperatures can increase SEI layer growth. An increased thickness of the SEI layer decreases BATs capacity and increase the internal ohmic resistance. Dendrite formation can also damage the BAT. The formation of copper dendrites is accelerated by deep discharge, whereas lithium dendrites are caused by charging at low temperatures or overcharging. The separator is mostly affected by oxidation. As a result typically the ionic conductivity is reduced, which leads to an increased internal resistance. In summary, it can be stated that BAT degradation cause lower power capacity, lower energy storage capability and an increased ohmic resistance, as well as higher self-discharge, self-heating, and lower efficiency. BAT's temperature, depth of discharge, total transferred charge, temperature and load cycling as well as maximum and minimum SoC have most influence.

Summarising, the ageing and degradation of a BAT are dominated by complex electrochemical processes, with a wide number of triggers and impacts acting on all components of a LIB. In order to relate all possible influences to the affected elements and the resulting degradation effect, Herb present an ageing effect matrix. In Figure 2.17 a graphical representation of that matrix is depicted. The degradation consequences are displayed in the centre, whereas the triggering impacts are on the left and on the right. The width of the connecting arrows are proportional to the degree of influence of the corresponding mechanism. For example the operation temperature has a strong impact on nearly all degradation consequences, but the strongest is on power and efficiency decrease. Based on Figure 2.17 it becomes apparent that the most relevant degradation pro-

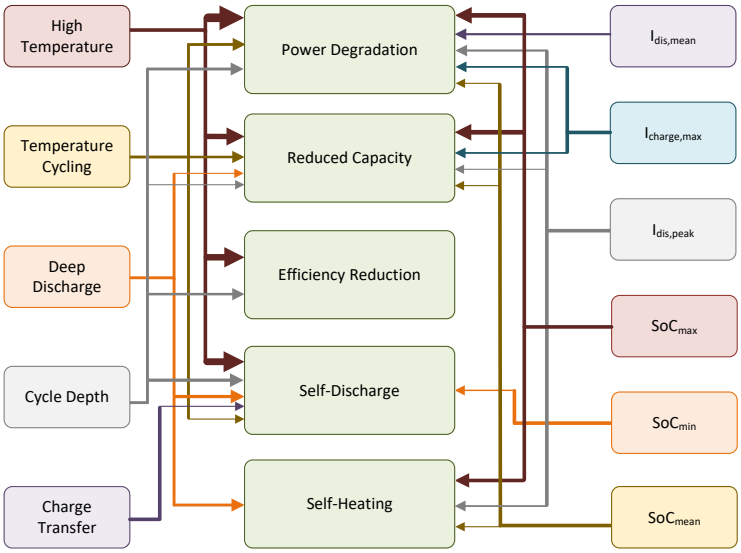

Figure 2.17: Schematic illustration of BAT degradation causes and effects.

cesses, which lead to a reduction of power capability and energy capacity, are affected by high temperature and temperature cycling, as well as high discharge rates, high and low SoC, and the current level. Therefore, while operating a BAT the control of operation condition is essential. The temperature needs to be regulated within a narrow band. It also needs to be ensured that the BAT's SoC and current are in the range of the operation borders.

2.2.3. System Architecture Fuel Cell Hybrid Electric Vehicle

One of the most fundamental choices when designing a FHEV is the selected topology. Since the topology has a strong impact on the vehicle usability and fuel efficiency, a careful decision is essential. It is well known that all suitable sources have unique operation characteristics and efficiencies. Thus, each combination is expected to show specific operation characteristic and overall efficiency [96–98]. By making best use of the specific sources an increased efficiency is expected, but by including power converter stages, a reduced efficiency is also possible. In FHEV different topologies are possible, several of these are discussed in

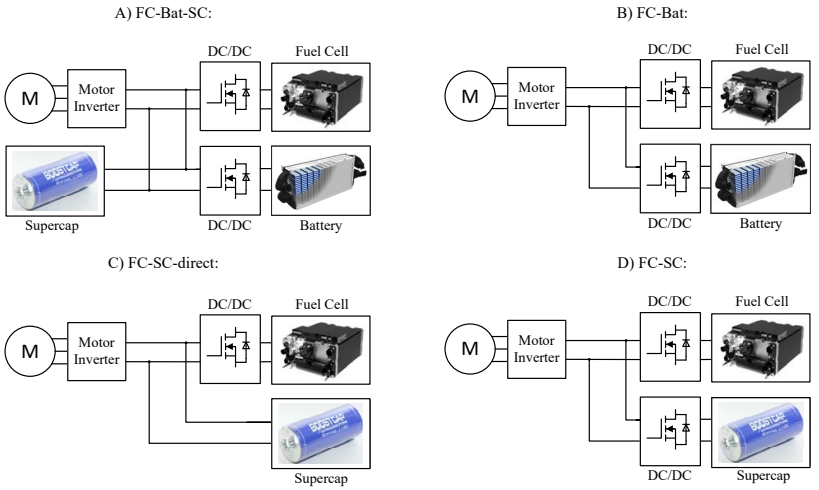

Figure 2.18: System structure of different FHEV power train topologies.

research, like [5], [99], and [100]. Xun et al. argue a direct coupling of an SC and FC reduces cost and size and also increases the overall efficiency. Nevertheless, in this topology neither FC's nor SC's operation points can be controlled, resulting in high FC degradation. Dawei et al. analyse a directly coupled FC system including converter coupled SC and two converter coupled FCs systems, supported either by a direct interfaced BAT or SC. A key drawback of a direct coupled FC is that the FC's operation state can not be controlled. Because the FC voltage varies significantly with current, a wide input voltage motor inverter is required [100].

Bauman and Kazerani compare three different topologies, a converter interfaced FC with a direct coupled BAT, one with a direct coupled SC and a topology with a converter coupled FC and BAT including a direct applied SC. The results indicate that FC-BAT and FC-BAT-SC are close competitors, both with high fuel economy, whereas the system including a SC has a slightly higher fuel economy [96]. Thounthong et al. also focus on topologies with converter coupled FC and compare a direct BAT coupling and a converter interfaced SC. Because of the high power capability of the SCs, Thounthong et al. assess the SC topology in more detail but nevertheless emphasise that as soon as a BAT is considered the overall system efficiency is significantly improved, this is especially true for start up or regenerative breaking events [97].

Since this work discusses solutions to realise an optimal control, tar-

Table 2.10: Comparison of different HES approaches in accordance to [25].

Topology	$F_{FC,avg}$ (NL/WS)	Equivalent Fuel of HES	W_{total} (kg)	Fuel Consumption
FC-UC	0.051	0.5 NL	26.4	632.5 NL
FC-UC direct	0.604	0 NL	25.4	754 NL
FC-Bat	0.055	1.6 NL	28.2	693.6 NL
FC-Bat-UC	0.028	4.8 NL	31.6	407.8 NL

geting minimal hydrogen consumption and to minimise the degradation of BAT and FC, only topologies capable to control the operation states of FC and BAT are considered. Therefore the number of suitable systems is limited to the ones with DC-DC converter interfacing the BAT and the FC. Figure 2.18 depicts these options. A comprehensive evaluation of the specific systems, shown in Figure 2.18, is given by Vural et al.. In order to guarantee comparable results all topologies where operated with a fuzzy based EMS and tested on an experimental test platform. The comparison of a direct coupled SC and a coupling via a DC-DC converters proves that when controlling an SC via a converter, the system is able to maintain the DC link voltage. In contrast, in the case of a direct coupled SC, the variation of SC voltage is equal to a variation of the DC link voltage. Vural et al. prove that a standard EMS is capable to maintain the DC link voltage of a direct coupled SC within specified boundaries. Since the usable energy of a SC depends on the SC's voltage deviation, the SC utilisation factor is low, thus requiring a lager SC capacitance. From table 2.10 it is derived that the FC-BAT-SC system provides the highest energy efficiency and lowest hydrogen consumption rate. The high efficiency results from the fact that with two additional sources, the power burden of the FC gets lower and the operation area tends towards high conversion ratios. With some limitations this is also true for the single SC or the single BAT systems. The slight difference in efficiency is because the SC has a higher energy conversion efficiency than the BAT. The highest hydrogen consumption can be recognised for the direct coupled SC system. In this case the utilisation area of the SC is low, hence the power load of the FC is high. Additionally the maximum power peaks as well as the power deviations are high, both cause lower conversion efficiencies and higher degradation. Even while the high efficiency and low con-

sumption rate indicates that the FC-BAT-SC system is the best option, the named advantages as well as the additional degrees of freedom increase the total system cost and system weight. Therefore, Vural et al. state that the optimal solution depends on the specific constraints and requirements whereas the corresponding cost function weights the opposing objectives. Equation 2.1 summarises the proposed cost function which describes the total operation cost. It can be seen that the costs are determined by linear factors which describe the hydrogen consumption (C_{H2}, w_{cons}), component cost (C_{cost}, w_{cost}) and cost related to the weight of the power system (C_{weight}, w_{weight}).

$$J = min(C_{H2} \cdot w_{cons} + C_{cost} \cdot w_{cost} + C_{weight} \cdot w_{weight}) \qquad (2.1)$$

2.2.4. Conventional System Design

The HES design process starts with the selection of the system topology. In the previous Section 2.2.3 a detailed analysis of possible options was outlined. It was shown that as long as no other criteria and constraints than minimum fuel consumption and minimum energy storage degradation are assumed, the ideal FHEV's power train consists of a FC, a BAT as well as a SC, see Figure 2.18 A. This configuration optimises the fuel consumption and enhances the lifetime of the BAT and of the FC [5, 25, 96]. When considering the system control the proposed system leads to additional benefits. Since the SC is directly coupled, the high frequency power demand of the electric drive is smoothed by the SC and the controller can react with a larger time constant to control the DC link voltage, respectively the SC voltage. Because of the aforementioned reasons, in this thesis a FC-BAT-SC HES is assumed to be the optimal system. Thus, the EMS approaches under test are going to be developed for and tested on this system topology. In the following the terms HES or FHEV will correspond to a power system with this system topology.

The next task is to determine the specific components and required power sizes and the required energy storage capacities. Therefore, basic requirements of passenger cars are going to be derived. Based on that, the system parameters will be determined. Guzzella and Sciarretta name four key requirements for passenger cars operating in individual transport sector:

- autonomous energy supply, do not depend on fixed supply-grid
- refuelling time negligible compared to possible driving time
- transport capacity of up to six persons
- acceleration of approximately 0 to 100 in 10 to 15 seconds and can drive uphill a 5 % at legal top speed

Since FHEV system typically show refuelling times below ten minutes and do not depend an a fixed energy supply the first two requirements can be considered as fulfilled. More significant are the remaining three conditions which can be summarised as drivability of a vehicle. In this thesis, an enhanced form of the drivability concept is used. Here additionally the ability to fulfil everyday requirements is also given focus. Thus, an energy storage capacity to ensure driving range larger than $300\,\mathrm{km}$ with an average driving speed of $130\,\mathrm{km\,h^{-1}}$ is required. Additionally the HES shall not suffer significant performance reduction under standardised environmental temperatures, corresponding to a range from $-7\,^{\circ}\mathrm{C}$ to $23\,^{\circ}\mathrm{C}$. The aforementioned requirements are based on the target market, Central Europe. The two crucial factors ensuring high drivability are the power and the energy storage capacity of the vehicle's HES. The US National Highway Administration [NHTSA] separates passenger cars by the curb weight of the vehicle with standard equipment including the maximum capacity of fuel, oil, coolant, and air conditioning, if so equipped, into six classes. In contrast, Guzzella and Sciarretta summarise these classes in four typical car body styles, light-weight, compact, full-size and SUV. Since neither heavy vehicle nor light ones are in the scope of this work, in the following Guzella's car classification scheme is going to be used. Table 2.11 lists characteristic parameter for each class.

In order to assess the required power and energy capacity, the top speed and acceleration performance as well as the capability to drive uphill criterion are evaluated for each of the four vehicle classes. In order to estimate the required energy, a $300\,\mathrm{km}$ standard motorway trip with a constant average driving velocity of $130\,\mathrm{km\,h^{-1}}$ and perfect recuperation

Table 2.11: Drivability requirements and characteristics for different vehicle categories.

	SUV	full-size	compact	light
$A_f \cdot c_d$	$1.2\,m^2$	$0.7\,m^2$	$0.6\,m^2$	$0.4\,m^2$
c_r	0.017	0.013	0.012	0.008
m_V	$2000\,kg$	$1500\,kg$	$1000\,kg$	$750\,kg$
$P_{acc,10}$	$154\,kW$	$116\,kW$	$77\,kW$	$58\,kW$
$P_{acc,15}$	$103\,kW$	$77\,kW$	$51\,kW$	$35\,kW$
P_{uphill}	$35\,kW$	$27\,kW$	$18\,kW$	$13\,kW$
E_{MW}	$105\,kWh$	$61\,kWh$	$49\,kWh$	$31\,kWh$
E_{Batt}	$3\,kWh$	$2\,kWh$	$1.3\,kWh$	$0.9\,kWh$
F_{SC}	$13\,F$	$10\,F$	$6\,F$	$4\,F$

is assumed. In the case of perfect recuperation, the energy spent to accelerate the vehicle is completely recuperated during braking. With the assumption that only aerodynamic and roll resistance have an impact, the mean power demand and thus the required energy can be estimated.

Typically in FHEV the main power demand is supplied by the FC, the BAT as well as SC are used to support FC's operation, e.g. by flattening short-time high power demands, in order to prevent degradation and enhance H2 efficiency. Therefore the estimated power demand for driving uphill at $130\,km\,h^{-1}$ (see Table 2.11) can be considered as the required FC's maximum power, P_{FC}. Since FC are sensitive to low temperature, the BAT must be capable to supply the vehicle during cold start and heat up the FC's thermal system to an operating temperature of $40\,°C$. Therefore in a conventional system design, it is assumed for BAT energy capacity to supply sufficient power and energy to accelerate the vehicle to velocity of $70\,km\,h^{-1}$ and drive for 15 minutes at this speed. In the focussed power system concept, see Section 2.2.3, the SC is used to stabilise the DC link voltage. Therefore a minimum SC capacitance can be determined based on a maximum allowable DC link voltage drop caused by the maximum power demand, $P_{acc,15}$. In this work a maximum DC link voltage drop of $5\,\%$ which last for maximum $2\,s$ is assumed.

2.3. Heating and Cooling

Section 2.2.1 and 2.2.1 describe the harmful impact of non-optimal operation temperature on FCs and BATs. Thus, TMS of FC and BAT is an essential part of designing a HES. In order to give a brief overview of

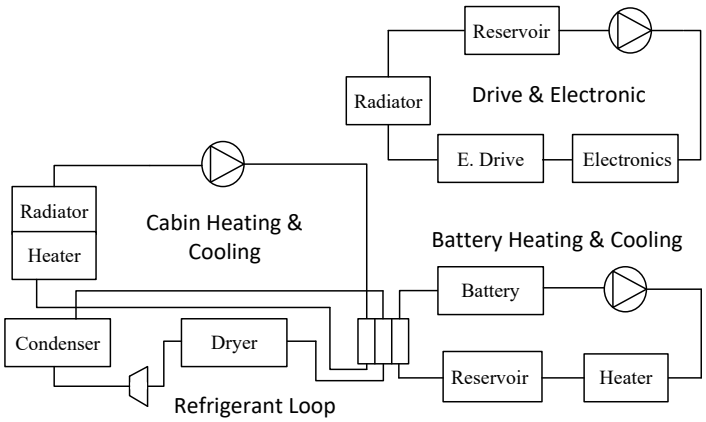

Figure 2.19: Structure of a BEV cooling loops presented by Tesla Motors, Inc. Patent No. US11786108 [9].

existing solutions, this section describes TMSs of commercially available vehicles. For the reason to understand the system configuration as well as the system models presented in Chapter 4, this is a vital aspect. So far the thermal requirements of a FC and BAT were discussed, besides these a TMS of a FHEV includes also the cooling of power electronics as well as the control of the vehicle interior temperature. To sum up, a TMS has to control the temperatures of all HES components, the BAT and FC as well as the temperatures of the DC-DC converter and the passenger compartment and keep those within operating limits.

For their BEV, Tesla presented a TMS consisting of four different cooling loops [9] (depicted in Figure 2.19). The first loop includes all high temperature components and a dedicated radiator. Depending on the operation constraints, it can also be connected to the second cooling circuit, responsible for cabin heating and cooling. This circuit also contains a radiator and is connected to a three-way heat exchanger with the third loop, the refrigerant loop, responsible to cool the BAT as well as the PC. The third port is connected to the BAT heating and cooling loop. These four cooling loops ensure optimal temperature conditions while using as least power as possible. The connection of the electric power train cooling circuit to the cabin cooling circuit ensures that waste heat can be reused. The connection of the refrigerant loop to the BAT cooling loop ensures optimal BAT's temperature and the least degradation.

While TMSs for conventional vehicles usually consist of three cool-

ing loops [101], those applied to HEV typically also contain several loops [102, 103]. Zhou present a TMS for a HEV based on two cooling loops with two different radiators – one for the internal combustion engine and one for the inverter and the electric drive. The passenger compartment is connected to the electrical cooling circuit via a liquid-liquid heat exchanger. Both radiators can be bypassed. Additionally, an air conditioning system can be connected to the circuit in order to cool the passenger compartment. Dage and Smith present a comparable system, it consists of a main cooling circuit to dissipate the waste heat of the engine and a second circuit to ensure optimal temperatures of the BAT, the motor and the power converter. To use waste heat for heating the cabin, the cabin heater can be connected to the engine cooling circuit [103]. For FHEV only few TMS have been presented. [104] presented a TMS which connects all components of a FHEV by one cooling loop. Nolan presented a comparable system, consisting also of a single cooling loop [105]. Nevertheless, both do not include the thermal management of the BAT or the passenger compartment. Nasri and Dickinson present a TMS controlling the temperatures of a HES, including a BAT and a high temperature FC. Again the passenger compartment is not part of the TMS, but here BAT, FC and power electronic components are connected via two separated cooling loops. With the rise of all-electric vehicles, cooling circuits became more and more complex. While Tesla cools their BAT through cooling channels moving snakelike through 18650 BAT cells, General Motors and Porsche use flat BAT cells sandwiched by flat cooling plates inserted between the cells, a coolant flows through small pipes [107–109]. Audi and LG, on the other hand, use direct expansion for cooling their batteries [107, 110]. A detailed investigation about the energy savings due to an improved BAT TMS was done in [111]. The presented BAT cooling systems are especially complex because they also need to dissipate the power loss during charging. Usually charging currents are far greater than discharging currents during driving. The BAT of a FHEV, on the other hand, is not charged by external charging stations but by the FC. There is no need to dissipate a comparable power loss density. The FHEV's BAT is configured to power the vehicle during cold start-up as long as the FC is not at operating temperature. FC typically contain a dedicated TMS, which is controlled internally via a control system. A review of the cooling systems of FC is given in [112]. More information on the modelling and control of these components is given in [105].

2.4. SUMMARY

This chapter gave a concise overview of the development, design, operation and all essential components of a FHEV. In the first section all relevant components were introduced. In the following second section, the system design and the operation of a FHEV was discussed. Since the operation temperature has a significant impact on both FC and BAT, state of the art of TMS capable to control the components temperature in a FHEV were focussed on in the third section. In summary it can be stated that the combination of different energy sources in order to make best use of their individual benefits is a promising solution. Due to its high specific energy density, the FC enables long driving ranges. The use of a BAT allows to recuperate energy while breaking and can be used to supply short and low load demand. Since the SC is robust to high current transients, it can be used to decouple the more sensitive BAT and FC to increase their life cycle. Today different DC-DC converter topologies and concepts are available, the most promising to be used in a FHEV are multi-input interleaved or bridge converters, a comparing summery of state of the art converter was given in Table 2.7. In conclusion, from a EMS point of view the most important degradation influences on a FC are carbon corrosion of the catalyst and dehydration of the membrane. With the objective to limit degradation effects, the EMS has to ensure that the FC is operated at a constant operation point, at medium cell potential, and in that way that low output power is avoided. In the wide group of operation conditions inducing a BAT to degrade, overcharging, deep-discharge, excessive cycling and high BAT currents are controlled by the EMS and thus have to be considered when developing a predictive control scheme. Also high or low operation temperatures have a negative impact and thus are considered when discussing the development of a TMS for a FHEV. Based on review of possible system topologies the most promising one was selected. In order to configure an exemplary target system, the presented predictive EMS approach shall be applied to, the conventional design of a FHEV energy system was discussed. Based on the introduced drivability requirements an exemplary design was set-up. For a full-size car, a $110\,\mathrm{kW}$ FC is required, the BAT have to be capable to store $2\,\mathrm{kWh}$ energy and SC capacity of $13\,\mathrm{F}$ is optimal, the motor reference power was assumed to be $100\,\mathrm{kW}$, the DC link voltage $250\,\mathrm{V}$. Thus, in the following a HES based on a FC and a BAT coupled via two DC-DC converters and directly connected SC and the aforementioned reference ratings is defined as the system under test.

3

FHEV TEST BENCH

A central aspect when developing new systems or concepts is the test and evaluation of its performance. This is also true for EMS controlling a FHEV vehicle. To be capable to test and to evaluate both, state of the art EMS schemes as well as the developed predictive energy optimal EMS concept, a test system, which is able to emulate the behaviour of a HEV is required. Since a HES, which is capable to power a real vehicle, would cause high cost and also require significant efforts to realise a safe operation, in this work a virtual test bench based on a simulation model was used. Therefore, to form the virtual test bench, models for all components are derived. Whereas the validation of the models was done based on real downscaled hardware components, the models emulating the full-size components are parametrised based on manufacturers datasheets. The evaluation of the performance requires also specific test cases. Because the operation characteristics of both EMS and HES depends on the drive scenario, in this work real world driving data is used as test cases. Based on recorded trips, a set of reference test cycles is derived and applied as test DCs. In the first section of this chapter, the data recording as well as the method to derive the representative test cycles are presented. In the second Section, the hardware used to validate the implemented models is introduced, subsequently followed by the last section discussing the implementation of the virtual test bench.

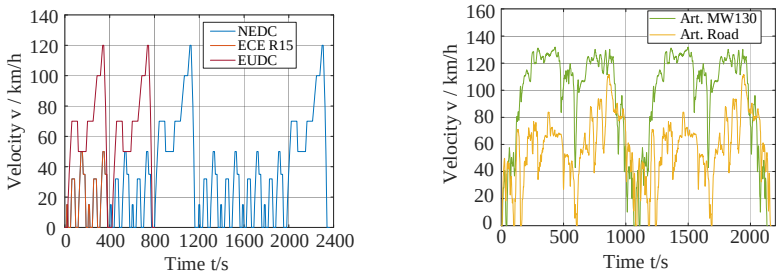

(a) (b)

Figure 3.1: Standard DC used in automotive industry (a) and 'Main Road' and 'Motorway130' Artemis cycles (b) [10].

3.1. Drive Cycle based Test Case Generation

A DC is represented by a velocity versus time profile and can either be generated based on real world measurements or synthesised to met specific criteria. DCs are used in automotive industry to assess and compare the performance of vehicles, examples are emission levels of car engines or fuel consumption tests [52, 113–115], traffic control [116] or evaluating the requirements for a reliable charging infrastructure [115]. Furthermore, DCs are used as a tool to compare different powertrain concepts and topologies [117, 118]. One of the critical metrics in the evaluation and analysis of FHEV is the DC. The acceleration as well as the maximum velocity has strong impact on the characteristic of the load demand supplied by the FHEV's energy system. Depending on the applied drive scenario, the efficiency and performance of topologies under test may show different results. Thus, to understand what type of DCs is used to evaluate the power train is essential. In order to evaluate the device under test (DUT) in all relevant drive scenarios, different DCs have to be applied. Several studies regarding the impact of DCs on assessing the performance and efficiency of BEV and FHEV have been presented [10, 114, 119–121]. Nevertheless, it is widely accepted that a single DC is not capable to represent all possible use cases and driving scenarios. [10, 122].

Figure 3.1 depicts different standard legislative DCs used in European automotive test procedures. These DCs were designed based on protracted periods at a constant cruise speed, spaced by constant acceleration and deceleration steps. A comprehensive review of international test pro-

cedures and DCs can be found in [10] and [52]. One of the most used standard cycle is the new European drive cycle (NEDC), which is applied to determine exhaust gas emission and fuel consumption of commercial automotive vehicle. With the objective to develop a set of reference real-world driving cycle the European ARTEMIS project developed the Common Artemis Driving Cycles (CADC). Based on statistical analysis of a large dataset. To build the dataset 58 cars were monitored for 1400 days and in total 8200 trips travelling $73\,000\,\mathrm{km}$. Based on this data a set of three representative DC, corresponding to three basic drive scenarios urban, rural road and motorway, was derived [116, 121, 122]. Comparing the synthetic NEDC, Figure 3.1 (a), and the real world based CADC, Figure 3.1 (b), it becomes apparent that, due to the low levels of acceleration and slow maximum velocity, the synthetic NEDC is not representative for real world driving. Furthermore the number of acceleration events is also significantly lower than for the CADC. If one evaluates a powertrain or fuel consumption solely based on the NEDC, the evaluation is resulting in the risk to test the design under a wrong use case. An even greater problem arises if the NEDC is used to optimise the design, in this case there is a chance that this design will be suboptimal under real driving conditions [118, 123]. Thus, in this work only real world based DCs are used as test cases. To avoid the problem to optimise the design for a specific test cycle, a set of different representative cycles will be used as evaluation references. Therefore, real world driving data was recorded and a method to derive representative DC based on that data developed. In the following two sections, 3.1.1 and 3.1.2, the data recording and the method to derive the reference cycle is going to be discussed.

3.1.1. Data Recording

With the objective to derive a set of representative DCs, real world driving data needs to be recorded. Therefore, a data recording tool was developed and driving trips of different drivers in various driving scenarios recorded. In order to increase the number of participating drivers, the used tool needed to be easy to use and be capable to be set up prior to the trip. The data provision needed to be as easy as possible. Since the DCs are used to estimate a vehicle's power demand, not only the velocity and acceleration is required, but also the altitude profile of the trip has to be recorded, see Section 3.3.1. In summary a cheap data recording tool that can be used easily and is capable to record a vehicle's velocity and the road altitude was required. In a first approach, two different concepts are compared:

- Smartphone internal GPS sensor

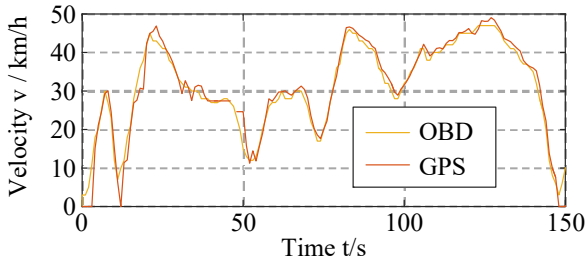

Figure 3.2: Comparison of two different datasets, one recorded based on OBD data and the other with a GPS sensor.

- Vehicle On-Board-Diagnoses bus

To record data from smartphone's GPS sensors, an Android application, that includes automated data upload to a central server was programmed. As a second option, the velocity information from the automotive on-board-diagnoses (OBD) bus is used. ISO 15031 as well as corresponding SAE J2012/J1979 describes the OBD bus system as a vehicle diagnosis system capable to record all exhausting gas relevant information and motor related data as well as the vehicle velocity [124]. In order to record the OBD data a commercially available Bluetooth® OBD interface and related smartphone application is used. Since the application records also the smartphone GPS sensor, a direct comparison of OBD and smartphone's GPS data is possible. Figure 3.2 depicts an exemplary segment of a recorded trip, this segment proof that GPS and OBD data are nearly identical and therefore it can be assumed that both methods are suitable as a recording tool. Thus, to guarantee a maximum number of participating drivers the smartphone application is used as main recording tool.

GPS uses time of flight measurements between orbital satellites and the target on the terrestrial surface in order to determine the distance between the target and the satellites, by triangular fusing of measurements from different satellites, the surface position can be determined. In case of three dimensional positioning, at least four satellites are required. Time dependent positioning of available satellites, shading in valleys, between buildings or in a vehicle by the vehicle's roof have an impact on the accuracy. In consumer application the position can be estimated with a horizontal error of $9\,\mathrm{m}$ and a vertical $15\,\mathrm{m}$ (at worst sides: horizontal $17\,\mathrm{m}$, vertical $37\,\mathrm{m}$) [125]. Based on the Doppler shift in the carrier-phase ranging signal GPS provides good velocity values with an accuracy of $5\,\mathrm{cm\,s^{-1}}$, a detailed analysis of vehicle measurements using

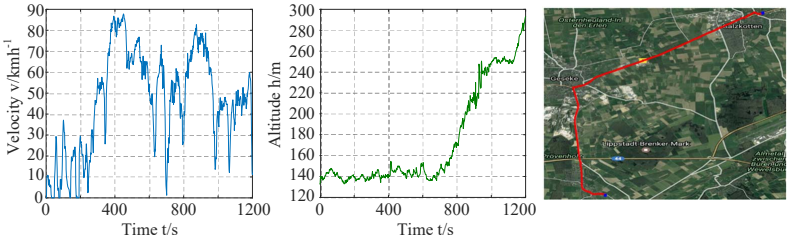

Figure 3.3: Example of a recorded trip. Recorded velocity, altitude, and the geographic location of the recorded DC.

GPS velocity is given in [126].

Figure 3.3 depicts a recorded trip, including the velocity and altitude profile as well as the recorded longitude and latitude coordinates. In order to extract reference velocity profiles, the raw data are post processed. Since the Android GPS recording application is not executed in a real time environment the sample period is not constant. To overcome this problem the recorded data is linear interpolated to generate a constant sample period of $1\,\mathrm{s}$. In a next step, the GPS accuracy and disturbances induced noise is filtered. To avoid high phase lag, which high order filter would induce, a fast Fourier transform related approach is used. Therefore, a complete trip is transformed to frequency domain. In the frequency domain, spectral components higher than a specific cut off frequency are deleted. Finally the filtered spectrum is transformed back to time domain using the inverse discrete Fourier transform. The specific cut off frequency is chosen to be the maximum acceleration of the DC. In accordance to Section 2.2.4, a maximum acceleration of $1.85\,\mathrm{m\,s^{-2}}$, which corresponds to an acceleration from 0 to $100\,\mathrm{km\,h^{-1}}$ in $15\,\mathrm{s}$, has to be considered.

A more complex problem arises when analysing the altitude data, sampled from the GPS sensor. In Figure 3.3, an exemplary interval of a recorded altitude profile is depicted. Even while the mean altitude is reasonable, the deviation between single samples is significantly large. Renfro et al. describe the vertical accuracy of a consumer GPS receiver to be in the range of $15\,\mathrm{m}$ to $37\,\mathrm{m}$ [125]. Since the road inclination shall be determined based on the recorded altitude profile, even small errors cause high road gradients. A significant higher accuracy could be achieved if a barometric altitude sensor is used. Since neither a standard smartphone typically include such a sensor, nor stand-alone barometric sensor can be

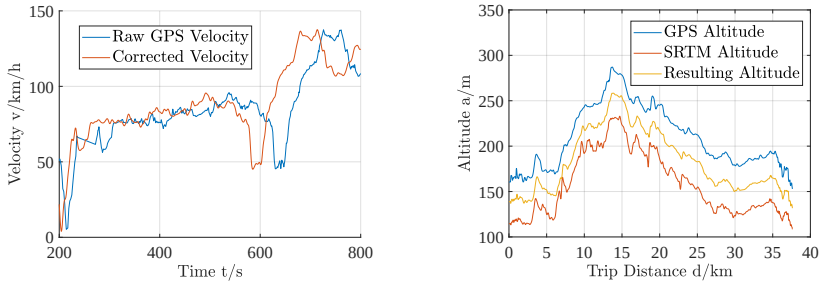

(a) (b)

Figure 3.4: (a) Comparison of recorded and filtered velocity data. (b) Illustration of the recorded GPS altitude data, the SRTM mapped on and the resulting altitude data.

distributed to a large number of potential test drivers, another approach was followed.

In order to increase the accuracy of the recorded GPS altitude data, it was fused with a geographic altitude map, the Shuttle Radar Topography Mission (SRTM) data set [127]. The SRTM data sets result from a collaborative effort by the National Aeronautics and Space Administration (NASA) and the National Geospatial-Intelligence Agency (NGA) to generate a near-global digital elevation model of the earth using radar interferometry. The data-set is provided as one degree by one degree cells, including altitude data in an 1 arc-second resolution, corresponding to roughly $30\,\mathrm{m}$ in horizontal extend. Prior to fusion, both data sets were smoothed by a IIR low pass filter. The cutoff frequency was determined based on the assumption that the recorded roads have a maximum slope of $10°$. Figure 3.4 shows an example of the filtered SRTM data and the recorded GPS altitude of corresponding datasets. Because a road inclination shall be determined the approximately $50\,\mathrm{m}$ offset between GPS and SRTM data is not relevant. The resulting altitude profile, yellow characteristic in Figure 3.4, is the filtered mean value of both data sets. Since the proposed method generates satisfying results, the described data post processing is applied in the following. In total, over 250 different driving trips from 20 different drivers were recorded and processed, these datasets form the basis to generate the representative test cycles. Figure 3.5 depicts a histogram of the trip distances and average velocity of the recorded DCs. The histogram emphasises that a clear majority of the recorded trip were either primary motorway trips or recorded on rural road. Never-

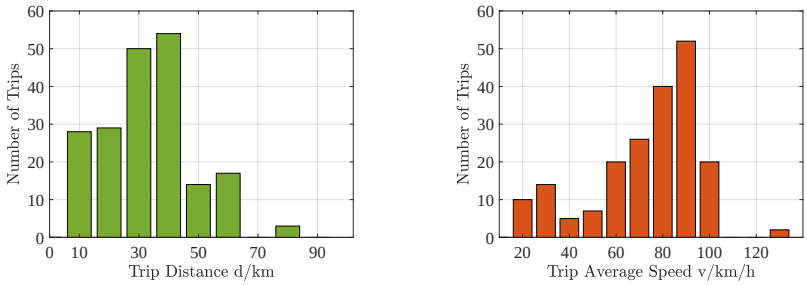

(a) (b)

Figure 3.5: (a) Histogram of the trip distances. (b) Histogram of the average driving speed.

theless, also short trips with low average speed were recorded, indicating that also a significant number of urban trips are included in the dataset.

3.1.2. Test Cycle Extraction

Drive scenarios can be described as urban, rural, motorway or stop and go. Whereas the first three depend on the road, stop and go is mainly caused by congested traffic and can occur on every road type [118]. Rural trips typically are determined by frequent stops and low velocity. In contrast, motorway trips typically show long driving distance as well as a high average and maximum velocity. Characteristics of real world driving are influenced by various properties such as road type, traffic condition, weather, topography or driver preferences, which all show partial interdependencies. Since the stated features are only a small selection of possible influences, the task to generate representative DCs, which characterise specific driving scenarios is a complex one.

Different approaches to create DCs are summarised by André and grouped into two categories. One category is defined by DC generation based on recorded data, for example the CADC, the other one includes DCs which were build by fusing sequences of steady speed and acceleration events (see the NEDC Figure 3.1). Applied methods typically concentrate on creating reference cycles, which has certain statistical characteristics similar to the original drive scenarios (average velocity, idle time or percentage of city, motorway or rural driving). In literature, three typical methods are presented. One option is to generate cycles based on segments of real world data or use the recorded DCs directly [128, 129]. Another common approach creates DCs by assembling different micro

Table 3.1: FCM features and generated cluster centres. Feature: V_{Max} - maximum velocity, V_{Avg} - average velocity, T_{Stop} - stop time, a_{Avg} - average acceleration , D - distance.

Cycle	V_{Max} $[\mathrm{km\,h^{-1}}]$	V_{Avg} $[\mathrm{km\,h^{-1}}]$	T_{Stop} $[\%]$	a_{Avg} $[\mathrm{m\,s^{-2}}]$	D $[\mathrm{km}]$
MW	147	87	1.6	0.39	52
RU	115	63	2.7	0.50	30
UR	62	28	13.5	0.56	8
ArtMW150	150	100	8.5	0.42	30
ArtRoad	115	59	2.7	0.50	17
ArtUrban	57.7	25	27	0.73	4.9

trips, corresponding to velocity profiles between two consecutive stops, to form a representative cycle. These micro trips can either be selected randomly [130] or by an iterative process with the target to meet specific speed acceleration frequency distributions [131].

Alternative approaches utilises Markov chain and transition probability matrices [115, 123, 132]. Lee et al. use synthetic DCs to evaluate the consumption and charging opportunities of BEV. The used DCs were synthesised through a stochastic process using Markov Chain and transition probabilistic matrices. Whereas the matrices were determined based on data recorded in the Midwest Region of the Unites States. Long distance trips showed comparable long cruising segments and lower frequently stops, in contrast short distance trips are characterised by high frequent start/stops and barely no constant velocity cruising segments [115]. A synthesis procedure based on a two dimensional Markov chain, which also includes a recorded road slope profile is presented in [133]. Nyberg presented a method to transform given standard cycle into an equivalent driving cycle or into a cycle with a given equivalence measure. In order to be able to make fair comparison, the aim of the presented method is to create cycles with prescribed traction requirements based on recorded real world data [134]. A detailed description including related literature of the single steps (pre-processing, synthesis, validation) to create representative DCs is given in [133].

In this work, real world driving data shall be used to evaluate the presented EMS approaches. Therefore, different trips were recorded. Within the recorded data set, 100 of the measured cycles can be characterised as mainly rural driving and 75 can be classified in each case as urban or motorway. Each trip covers a wide variety of driving situations. The complete dataset covers different driving styles and various trip length, from $430\,\mathrm{m}$ to $502\,\mathrm{km}$. Although the dataset is not sufficiently large, it includes a wide range of realistic driving conditions and trip lengths. Therefore a selection of representative cycles extracted from this dataset can be considered as suitable test cases, covering all relevant driving situations and trip characteristics for the region the data was recorded in. In order to identify DCs representing real world drive scenarios, a two step FCM approach was used. In a first step the unspecified data is clustered with regards to the road type: urban, rural or motorway. In a second step each road type cluster is subdivided in to two cluster representing dense and free flow traffic condition of the specific road type. Finally, based on the specific degree of membership to a cluster, the most representative DCs in each cluster are identified. To apply the described approach, suitable feature sets, describing the recorded data, needed to be defined. In literature, various feature sets describing specific DCs can be found.

Lee and Filipi. state that DCs can be categorised either with respect to the trip distance or the mean velocity. The trip distance correlates with the road type. Thus, if a general differentiation between urban road or for example motorways shall be executed, the trip distance is a suitable criterion. The mean velocity can be used to analyse single trip characteristics, like driving style or to isolate particular segments. Lee et al. categorise real world cycles regarding the trip length, a short trip is less then nine miles, medium trips are between nine and 20 miles and long distance trips range over 20 miles. André present a list of six features, which were used to create the CADC. In contrast, Shahidinejad et al. give a comprehensive list of 25 parameters used to characterise DC. While both feature sets include time proportional features, for example time percentage of acceleration, Shahidinejad et al. also include features related to the velocity and the acceleration characteristics. De Hann and Keller present a set of 19 parameter describing the kinematic characteristic of a driving pattern.

In order to describe the recorded dataset, a feature set based on [114] and [130], was derived. Table 3.1, summarises the selected features. Because the amplitude of the different features varies, in a first step the extracted features were normalised and then FCM clustering applied. The

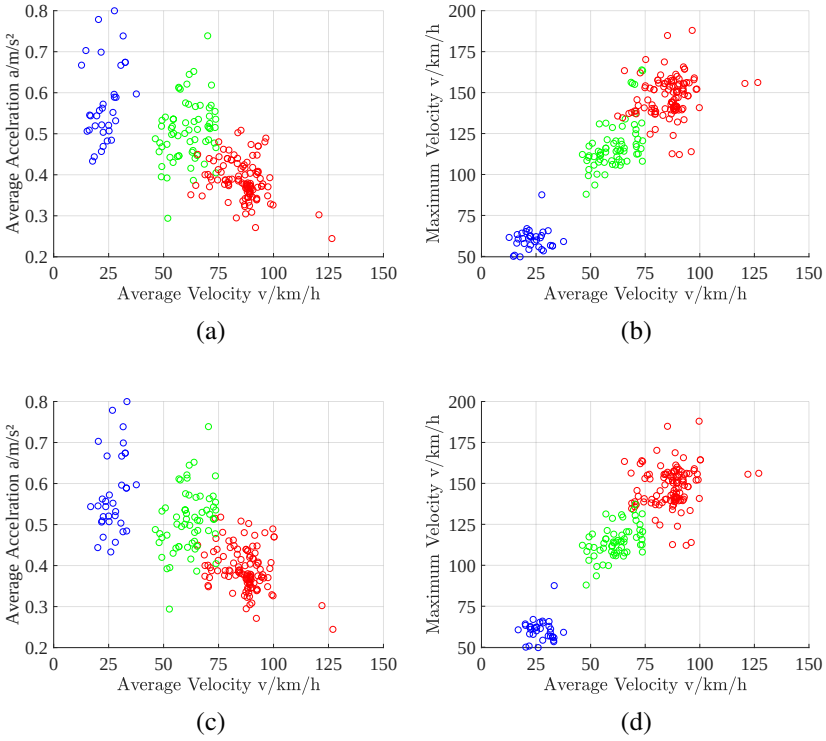

Figure 3.6: (a) Variability of the trips of clusters based on de Hann features. (b) Variability of the driving conditions of clusters based on de Hann features. (c) Variability of the trips of clusters based on reduced feature set. (d) Variability of the driving conditions of clusters based on the reduced feature set.

result of the applied FCM are three clusters of trips, related to the specific road type. Figure 3.6 (a) and (b) depict the average acceleration related to the average velocity and maximum velocity related to the average velocity of the different cluster. The different colours indicate the specific cluster, blue urban, green rural and red motorway. While the urban cluster is clearly separated, rural road and motorway can not clearly be distinguished. A key problem is the diving style preferences of some participating driver, which tend to drive at high average and maximum velocity. In order to improve the performance of the FCM clustering, the feature set was reduced, thus velocity related features are emphasised higher.

Table 3.2: FCM features and generated cluster centres. Features: $D_{V_{Avg}}$ - difference in average velocity driving and complete trip, $D_{V_{Max}}$ - difference in maximum velocity driving and complete trip, E_{Acc} - acceleration events, $T_{Driving}$ - time driving, T_{Stop} - time stop, a_{avg} - average acceleration.

Feature	$D_{V_{Avg}}$ $[\mathrm{km\,h^{-1}}]$	$D_{V_{Max}}$ $[\mathrm{km\,h^{-1}}]$	E_{Acc}	$T_{Driving}$ $[\%]$	T_{Stop} $[\%]$	a_{avg} $[\mathrm{m\,s^{-2}}]$
MW dense	1.6	55	3	97.4	0.8	1.1
MW free	6.5	68	4.6	90.2	4.8	1.4
RU dense	1.9	50	7.55	96	1.24	1.58
RU free	6.2	53	8.6	88	6.6	1.65
UR dense	3	33	24	83	6	1.94
UR free	7.11	30	24.5	68.5	22.3	1.80

Figures 3.6 (c) and (d) depict the results of the clustering executed based on the reduced feature sets. It can be seen that the boundary between rural and motorway driving is sharpened. The reduced cluster contains the maximum velocity, the average velocity while driving, the proportional stop time, the average positive acceleration and the trip distance. Table 3.1 summarises the reduced feature set and the resulting cluster centres and compares the centres with the corresponding feature of the CADC.

To divide each cluster into two subclusters, which represent congested and free flow traffic condition for each specific road type, the next step is to derive a new set of characteristic features. Because in particular frequent stop and go events as well as higher acceleration characterise congested traffic, especially features related to acceleration and deceleration as well as to stops were chosen. Table 3.2 summarises the feature set and the generated cluster centre. In order to find the most representative trips for each category, the five recorded trips with the highest degree of membership of its specific cluster were identified and chosen to form the test set.

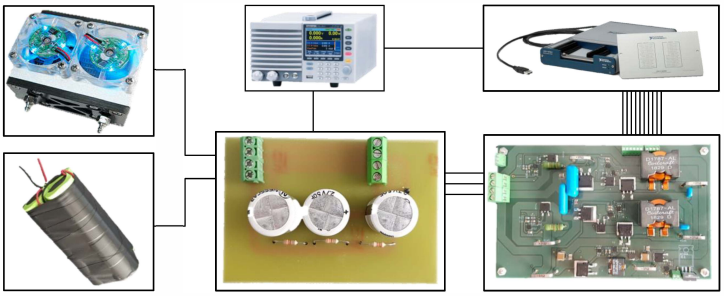

Figure 3.7: Schematic representation of the hardware system (BAT, FC, SC DC-DC converter and load emulation) used to validate the implemented models.

In summary can be said that, a methodology to extract a set of reference cycles representing three different road types with free-flow and congested traffic based on unspecified real world driving data was presented. Based on the method and the recorded driving data, a set of 30 reference DCs, which represent characteristic test cycles to simulate a vehicle driving on urban and rural roads as well as on motorways in free flow and congested traffic condition. This set of DC is used in this work to evaluate the EMS under test.

3.2. Hardware Test System

An essential part of the development of an EMS is test and evaluation. In this work the evaluation of the different EMS is realised based on a virtual test bench. The design and implementation of this virtual test bench is going to be discussed in the next section of this chapter. Nevertheless, the implemented models have to be validated with real components, thus a hardware system is required. In order to validate the models, a discrete hardware test system was configured and installed. The system was set-up based on target system topology, discussed in Chapter 2.2.4. Because the usage of components with reference power and energy storage capacity, capable to power a real vehicle, would result in high cost and safety issues, the validation was realised based on scaled components with lower reference power.

Figure 3.7 illustrates a schematic representation of the implemented hardware based test system. The system contains a $35\,\mathrm{W}$ FC, a $12\,\mathrm{W\,h}$ BAT, a SC and a $100\,\mathrm{W}$ multi channel DC-DC converter which con-

trols the operation states of the different energy sources. Additionally, a programmable DC load is used to emulate the power demand of the drivetrain, for data acquisition and control purposes, a multifunctional digital-analogue data acquisition module is used. A key problem with the comparison of components with different reference power is that scaling effects arise when hardware of one size is emulated by hardware of a another size [135]. For example, doubling the number of series cells in a FC does not double the electrical current but only the stack voltage. If in contrast the number of parallel strings is doubled, the stack current is also twice the one of a single string. In both cases, the reference power of the complete system is doubled, but the characteristics of both system are different. The same effect occurs for BATs, the number of parallel cells define the maximum system current, the number of cells in series the charge and discharge voltage. If thermal characteristics like conductive or convective heat transfer shall be analysed, the specific geometry and structure of the system also has a significant impact.

One solution to scale hardware of a HEV powertrain with the goal to be used in a hardware-in-the-loop simulation is presented by [135]. In the presented work, Petersheim and Brennan use dimensionless variables, as defined by the Pi Theorem, to scale HEV components for the purpose of taking all relevant scaling effects into account. The central objective of the discussed method is to develop an understanding of how to compare dissimilarly sized components using scaling factors that are physically based, e.g. tied to experimentally measurable variations in key parameters rather than numerical methods. Because in this work the hardware components are used to validate models and not to design or test control schemes, the mentioned scaling effects are not relevant. As long as the models are adapted to the used hardware, the validation can be executed.

The implemented FC model was validated based on a H-30 FC, manufactured by Horizon Fuel Cell Technologies. The H-30 is a semi-integrated $30\,\mathrm{W}$ FC system. The hydrogen supply is realised based on metal hydride storage tanks (HydroStik-Pro), also manufactured by Horizon Fuel Cell Technologies. Each metal hydride cylinder is capable to store 10NL hydrogen, the storage weight is $90\,\mathrm{g}$, the charge pressure is $10\,\mathrm{bar}$. The self-humidified H-30 PEM FC contains 14 cells and an integrated air cooling, the rated performance is $8.4\,\mathrm{V}$ and $3.6\,\mathrm{A}$. Figure 3.8 (a) shows the FC voltage related to the FC current, Figure 3.8 (b) the output power related to the FC current. It can be seen that a maximum output power of $35\,\mathrm{W}$ can be supplied. The applied BAT system contains three in series connected Emmerich ICR-18650NH-SP cells. Each cell includes an in-

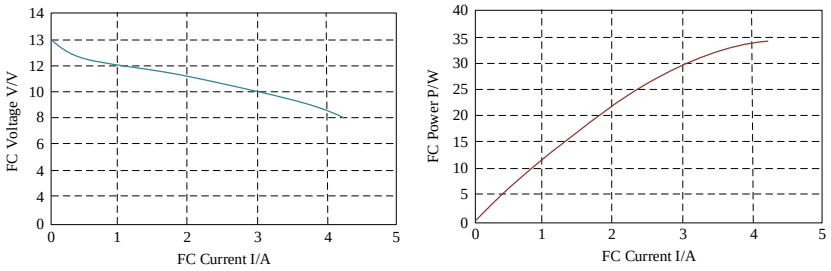

(a) (b)

Figure 3.8: (a) Voltage characteristic related to the FC current HD-30 FC. (b) Power characteristic related to the FC current HD-30 FC.

Table 3.3: Emmerich ICR-18650NH-SP BAT cell parameters and BAT system feature: V_{Nom} - nominal cell voltage, Q_{Typ} - typical charge, Z_{Int} - internal impedance, $I_{ch,max}$ - maximum charge current, $I_{dis,max}$ - maximum discharge current, $V_{Ch,max}$ - maximum charge voltage, $V_{Dis,cut-off}$ - discharge cut-off voltage.

Parameter	BAT cell	BAT system
V_{Nom} [V]	3.7	11.1
Q_{Typ} [A h]	2.2	2.2
Z_{Int} [mΩ]	<150	<450
$I_{ch,max}$ [A]	2.2	2.2
$I_{dis,max}$ [A]	2.2	2.2
$V_{Ch,max}$ [V]	4.2	12.6
$V_{Dis,cut-off}$ [V]	3.7	11.1

tegrated cell management and under- and over-voltage and current protection. Table 3.3 summarises the relevant parameters of the specific BAT cell and of the combined system. The series connection results in a higher cell voltage, which enables an easier DC-DC converter design. In total the higher system voltage leads to an increase of the energy storage capacity, in summary $24.4\,\mathrm{W\,h}$ was reached. The SC module was realised based on three Nesscap ESHSR-0050C0-002R7 SC cells. Each capacitor has a reference capacity of $50\,\mathrm{F}$ and a rated voltage of $2.7\,\mathrm{V}$. The maximum continuous current is $6.1\,\mathrm{A}$, the maximum peak current $37.5\,\mathrm{A}$ and the average DC equivalent series resistance $10\,\mathrm{m\Omega}$. In order to realise a module voltage of $7.2\,\mathrm{V}$, three capacitors are connected in series, resulting

in a rated voltage of $8.1\,\mathrm{V}$ and an average DC equivalent series resistance of $30\,\mathrm{m\Omega}$. The Gw Instek Pel3021 was used to apply a controlled load. The maximum power demand which can be applied is $175\,\mathrm{W}$, the maximum voltage range starts from $1.5\,\mathrm{V}$ to $150\,\mathrm{V}$. The charging of the BAT was realised with a Rhode&Schwarz HMC 8041 power supply. The control of both devices was implemented with the National Instruments LabVIEW$^{\mathrm{TM}}$ software tool. In order to realise a controlled power flow between the three components, a multi-stage DC-DC converter was developed and implemented on a printed circuit board. The converter contains three independent stages with each $50\,\mathrm{W}$ reference power, two buck stages to enable a power flow from FC and BAT to the SC and one boost stage to control a power flow from the SC to the BAT. Since the FC and BAT current have to be controlled, the two buck stages contain an input current controller, whereas the boost stage an output current control. The current reference can be applied via an analogue interface, connected to National Instruments LabVIEW$^{\mathrm{TM}}$ software environment via a National Instruments USB-6343 multifunction I/O device.

3.3. Vehicle Model

An indispensable component of the development process described in this work are the mathematical models, only those permit a systematic implementation and test of EMS. The approach to use a virtual test bench enables the test of state of the art approaches and the developed EMS under varying drive scenarios without using a large scaled hardware system. Guzzella and Sciarretta present a complete analysis related to modelling of vehicle propulsion systems. Two different approaches are discussed, the dynamic and the quasistatic modelling approach. The dynamic approach uses an exact mathematical description of the physical system, typically expressed with differential and algebraic equations. While these equations include all transient and static characteristics of a powertrain, not all of these dynamic processes are relevant for the evaluation and test of EMS. Most characteristics that have an significant impact on the management of the power flows in a HES a very slow. The fast and highly dynamic effects are typically significant for the design of the individual sub-controllers of the components. A drawback using exact dynamic models is the high computational burden and the typically high number of required parameters describing the system behaviour. In contrast to quasistatic simulations, it is assumed that the system inputs (velocity, acceleration and road inclination) are constant for a fixed time step. Based on the constant inputs, the force required to act on the wheels, to fol-

low the applied cycle, is determined. Based on this force, the propulsion system model estimates the power demand and the energy storage state of charges. Isidori, Johnson name the evaluation of the performance, the fuel consumption or the comfort, the drivability and the pollutant emission as central task of quasistatic models of vehicle propulsion system models.[139, 140]. Vehicle models can be classified also in either forward or backward oriented models. Forward models try to follow a specific input value, in the case of a vehicle model this reference is the velocity. Based on the difference of reference and actual value, a controller determines a control variable, the state variables are then defined by the control variable. In backward oriented models it is assumed that the trajectory of input values, acceleration, velocity and road inclination, are exactly followed and the state variable result directly from the input variable trajectories.

Typically, only single components of a HES or a FHEVs are modelled, with the objective to either design a controller or analyse the operation. Models of a complete system are implemented in most cases either with the aim to optimise the system design [141–143] or the EMS [144–151]. With the focus to evaluate EMS strategies for a more electric aircraft Njoya Motapon et al. describe a forward oriented simulation model of a HES, built of a FC, a BAT and a direct coupled SC. Froberg and Nielsen present an approach to combine the time-efficient advantage of the quasistatic simulation and to include also important dynamics without significantly losing simulation performance. The presented approach is implemented based on an inverse dynamic simulation. Hu et al. use a convex model of a FC - BAT vehicle to determine the optimal dimensioning of the components.

Because the developed model shall be used to evaluate and test different EMS, a forward oriented approach was selected. After implementing the models for all required components, see sections 3.3.1 to 3.3.5, a complete system model was developed and implemented using MATLAB® Simscape® toolbox. Figure 3.9 depicts a schematic representation of the basic model architecture. The driver, which is modelled by a PI controller, generates a reference torque related to the difference of reference velocity and the current velocity. This torque is applied to the model of the electric drive, which determines an input current related to the applied torque. The SC model estimates the SC voltage based on the current equilibrium, resulting from the difference of the electric drive current and the output currents of the FC's and BAT's DC-DC converter. The BAT model determines the SoC of the BAT, the FC model the consumed hydrogen,

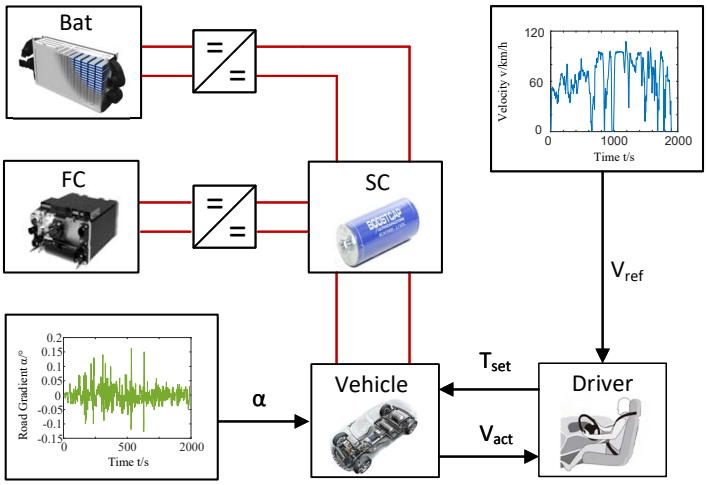

Figure 3.9: Schematic of the implemented forward oriented physical system model. The depicted model components are: BAT model, FC model, SC model, model of a driver an velocity reference and a model of the vehicle dynamics and the road inclination profile.

related to BAT and FC current. The vehicle velocity is determined related to the result of the vehicle's longitudinal dynamics model using the road gradient as well as the torque applied by the electric drive. In the next sections, a detailed description of the single models is outlined. All component models were implemented under the precondition that every required parameter can be determined based on the manufacturer's data sheet or application nodes. Each model was validated based on hardware components described in the previous Section 3.2. All models were implemented, simulated and tested based on the MATLAB® Simulink® technical computing and simulation environment.

3.3.1. VEHICLE

The vehicle subsystem contains different models, one for the vehicle's longitudinal dynamics, models of the tires, the elective drive and one representing the driver. In the following subsection the implementation of the different components is going to be discussed. The causal representation of the integrated models of the vehicle and the driver are depicted in Figure 3.10. The model inputs are the road gradient and the vehicle velocity reference. The driver can be considered as velocity controller determining a toque related to the deviation of the actual vehicle velocity and the ref-

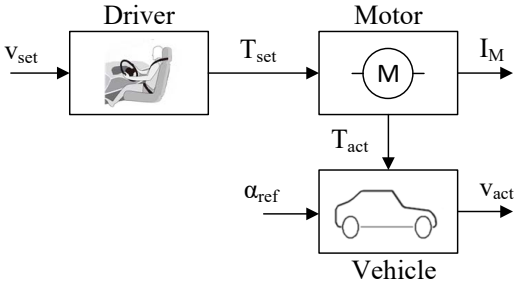

Figure 3.10: Schematic illustration of model structure of the vehicle dynamics, electric drive, and the vehicle driver model.

erence velocity. The electric drive realises the torque reference, the motor model determines the corresponding motor current related to the demanded torque. The generated torque is applied to the vehicle longitudinal dynamics model which determines the vehicle velocity based on the road inclination and the applied torque.

The electric drive is represented by a simplified model of a brushless motor and including also the motor inverter with an integrated closed-loop torque controller. The motor model follows a predefined torque speed envelope between the operation limits. The electrical losses are determined based on a simplified model which considers a series resistance between DC source and motor drive and also fixed losses, independent from torque and speed, as well as speed and torque dependent electrical losses. The motor parameters were determined based on the electric drive of the Toyota Mirai. A linear torque velocity characteristic over the complete operation range ($T_{max} = 330\,\mathrm{N\,m}$, $N_{max} = 360\,\mathrm{rad\,s^{-1}}$) was assumed [154]. The electrical losses were assumed based on [155].

The driver was modelled with a standard PI controller, the controller parameters were determined so that a maximum acceleration from 0 to $100\,\mathrm{km\,h^{-1}}$ in $15\,\mathrm{s}$ is achieved. A controller output saturation ensure that the calculated torque is below the maximum motor torque. In order to simulate the vehicle longitudinal dynamics, a model of the drive train was implemented. The rotation and torque of the rotor is applied to a gear box model considering the friction and inertia of a gear. The transferred rotation is the input to two tire models representing the two wheels of the vehicle's drive axle. The tires were modelled based on the Magic Formula, an empirical equation used to model the gear uses four fitting coefficients, which were presented by [156]. The normal force acting on

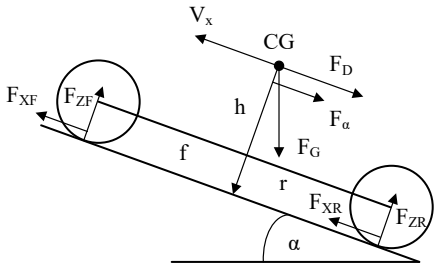

Figure 3.11: Schematic illustration of the vehicle longitudinal dynamics and forces which acts on a vehicle on the road.

the tires and drive axle is determined using the net sum of all forces and torque acting on the vehicle. Figure 3.11 illustrates a schematic representation of theses forces. The longitudinal forces, F_{XF} and F_{XR} drive the vehicle forward, the mass of the vehicle acting through its centre of gravity (CG) pulls the vehicle to the ground. Depending on the road angle α, this results in a forward or backward oriented forces F_α. Additionally the aerodynamic drag, F_D, antagonises the moving force and slows the acceleration down.

The normal forces acting on the front and rear axle result from the force equilibrium, Equation 3.1 and 3.2 give a mathematical representation of these normal forces. A vehicle is described by size and geometry related parameters, an overview of typical vehicle parameter, representing SUV full-size compact and light car, can be found in Table 2.11 in Section 2.2.4 or in [136]. The distance to front and rear axle, f and d, is assumed to be equal, the number of wheels, n, is four.

$$F_{\mathrm{ZR}} = \frac{h(F_{\mathrm{D}} + mg \cdot \sin(\alpha) + mV_{\mathrm{x}} + f \cdot mg\cos(\alpha)}{n(f+r)} \tag{3.1}$$

$$F_{\mathrm{ZF}} = \frac{-h(F_{\mathrm{D}} + mg \cdot \sin(\alpha) + mV_{\mathrm{x}} + r \cdot mg\cos(\alpha)}{n(f+r)} \tag{3.2}$$

3.3.2. PEM FC

Several approaches to model FC are possible, a simplified approach can be implemented based on two parameters, the hydrogen consumption rate and the efficiency. Since both parameters depend on the operation states and are effected by various conditions, this simple model does not emulate

the FC behaviour sufficiently. A more detailed approach also takes the operation state related characteristic of a FC into account. The cell voltage is determined by four effects, current voltage characteristic, the temperature and the concentration of the reactants. The current dependent cell voltage is characterised by the equilibrium potential resulting from the reversible cell voltage reduced by three loss mechanism. The activation losses depend on the catalyst and are the result of the energy demand required to initiate the electrochemical reaction. The limiting reaction is the one at the cathode, which is significantly slower than the one at the anode. The semi-empiric Tafel equation, see Equation 3.3, describes the relation of the activation losses and the FC current [157]. The parameter A can be expressed via an electrode reaction depending charge-transfer coefficient, the gas constant and the Faraday constant. The exchange current, I_0, expresses the equilibrium of reaction and reverse reaction. The exchange current is equal to that current, for which the activation voltage becomes zero.

$$U_{\mathrm{act}} = A \cdot \ln\left(\frac{I_{\mathrm{FC}}}{I_0}\right) \tag{3.3}$$

Ohmic losses occur due to the ohmic resistances of the electrodes, the one of the membrane and the catalyst layer resistance. Assuming that that membrane, catalyst and electrode conducting can be described by Ohm's law, the ohmic losses can be expressed by a single resistance, see Equation 3.4. The resistance of the membrane, and so the overall ohmic resistance depends on the humidity of the membrane. Modelling this effect would result in the demand of a complex dynamic reactant model, since not the optimization of a FC system but its integration in a HES is in the scope of this work, an optimal humid membrane is assumed.

$$U_{\mathrm{Ohm}} = R_{\mathrm{FC}} \cdot I_{\mathrm{FC}} \tag{3.4}$$

The concentration losses are caused by an inhomogeneous change in the reactant concentration at the surface of the electrodes. Also insufficient reactants supply can induce concentration losses. As the reactant consumption is high for high currents, these losses have the strongest impact at high FC current densities. Based on [157] an empiric approach is best to use. The empiric Equation 3.5 can be fit to measurements, by varying the Parameters m and n.

$$U_{\mathrm{Con}} = m \cdot e^{(n \cdot I_{\mathrm{FC}})} \tag{3.5}$$

The Nernst equation describes the open circuit voltage of a FC cell. The cell voltage at standard conditions can be determined by Faraday's

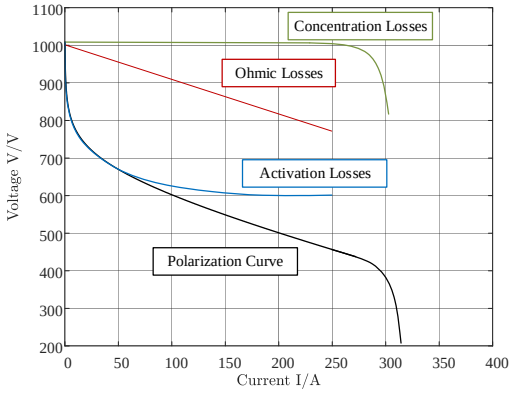

Figure 3.12: Polarisation curves of a PEMFC if different operation losses are assumed.

law, the change in Gibb's free energy of formation, the number of exchanged electrons and the Faraday constant. Additionally, the change in activity of the reactants also has to be considered. According to [157], the activity of the reactants can be assumed to be the ratio of the partial pressures of the species related to the environmental pressure. Equation 3.6 calculates the reversible cell voltage.

$$U_{\text{Cell}} = -\frac{\Delta g_{\text{f},0}}{2F} + \frac{RT}{2F} \cdot \ln\left(\frac{p_{\text{H}_2} \cdot p_{\text{O}_2}^{\frac{1}{2}}}{p_{\text{H}_2\text{O}}}\right) \tag{3.6}$$

FC systems typically contain at minimum one stack of single cells, as mentioned in Section 2.1.1. The stack voltage is the product of the stacked cells and the equilibrium potential of a single cell. Multiplying the cell voltage U_{Cell} with the number of cells N determines the stack voltage. In order to increase the maximum FC current, multiple stacks can be arranged in parallel. The system current is defined by the product of the number of parallel stacks and the maximum current of one stack. Figure 3.12 exemplary shows the polarisation curve of a $100\,\text{kW}$ FC system. The concentration losses are depicted in green, the ohmic in red and the activation losses in blue.

The hydrogen consumption of a FC system is proportional to the FC current. The cell current is determined by the product of the quantity of flow rate of electrons, the electron charge and the Avrogadro constant. Based on the definition of the molar flow rate of hydrogen and the hydrogen mass flow rate, the rate of consumed hydrogen related to N cells,

the cell current and the hydrogen molar mass M_H results in Equation 3.7. The factor λ_H represents the operation dependent excess supply factor, required to guarantee a uniform feeding for hydrogen. [52]

$$\dot{m_{H2}} = \lambda_{\mathrm{H}} \frac{N \cdot I_{\mathrm{FC}} \cdot \mathrm{M_H}}{n_e \mathrm{F}} \tag{3.7}$$

Njoya et al. summarise presented FC models in three classes, electrical, chemical or experimental models. The presented chemical models typically include thermodynamic and complex chemical effects like detailed mass or heat transfer as well as species diffusion [136, 158]. The high number of required parameters as well as the problem that these parameters typically can not easy be determined is the key drawback using chemical models on system simulation level. In contrast neither experimental nor electrical models include FCs thermodynamics or mass transportation. Experimental models result from experiments and often are implemented look-up tables [159, 160]. Operating condition dependent behaviour of the cell voltage is often neglected. Since these effects are included in electrical models [161], theey are more suitable to be used in system simulations. In nearly all presented models extensive tests, like polarisation curves, current interrupt, frequency response tests and impedance spectroscopy are required to determine the model parameter.

With the aim to implement a model which can be completely configured based on the polarisation curve of a FC, Njoya et al. present a generic approach to model a FC combining the benefits of a electrical and a chemical model. Since polarisation curves are typically provided by the manufacturer, extensive tests are not required. Due to its capability to simulate all relevant effects of a FC and because all parameters can be determined based on manufacturer data, this modelling approach was used in the virtual test bench discussed in this work. Figure 3.13 depicts a schematic representation of the implemented model. The operation parameters, fuel and air pressure, operation temperature as well as the composition of fuel and air define the Tafel slope A, the exchange current i_0 and the reversible cell voltage U_0. The electrical behaviour can expressed with the depicted equivalent circuit, representing the Nernst equation 3.6. Block A determines the utilisation of hydrogen ($U_{f,H2}$) and oxygen ($U_{f,O2}$), using the utilisation factors, block B is used to calculate the reactant's partial pressure, Equations 3.8 and 3.9 , as well as U_0 and i_0.

$$P_{\mathrm{H2}} = (1 - U_{\mathrm{f,H2}}) \cdot x \cdot P_{\mathrm{Fuel}} \tag{3.8}$$

$$P_{\mathrm{O2}} = (1 - U_{\mathrm{f,O2}}) \cdot y \cdot P_{\mathrm{Air}} \tag{3.9}$$

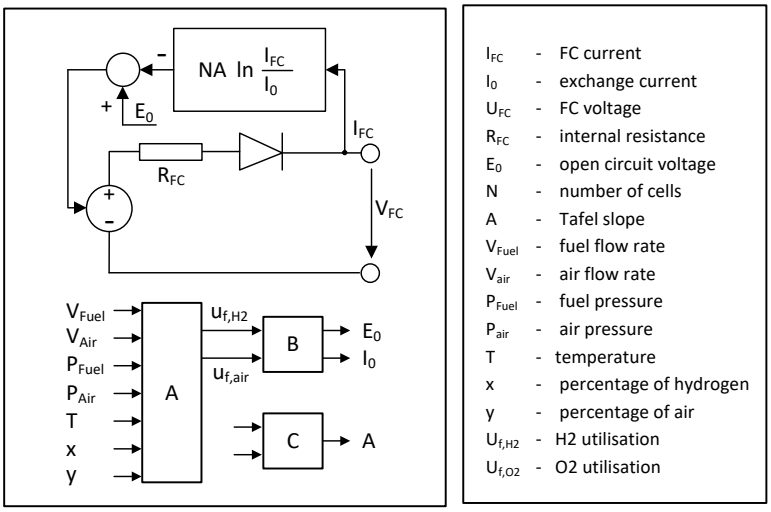

Figure 3.13: Schematic structure of the implemented FC model and the corresponding parameters used to model the FC [11].

$$U_{\mathrm{N}} = 1.229 + (T - 298) \cdot -\frac{44.43}{zF} + \frac{RT}{zF} \ln\left(P_{\mathrm{H2}} P_{\mathrm{O2}}^{\frac{1}{2}}\right) \tag{3.10}$$

Equation 3.10 is used to determine the Nernst voltage, the resulting reversible cell voltage can be calculated with the voltage constant $\mathrm{K_C}$, see Equation 3.11. The exchange current and the Tafel slope can be determined using the partial pressure of the reactants, see Equations 3.12 and 3.13.

$$U_0 = K_c \cdot U_N \tag{3.11}$$

$$i_0 = \frac{zFK(P_{\mathrm{H2}} + P_{\mathrm{O2}})}{Rh} \cdot e^{-\frac{\Delta G}{RT}} \tag{3.12}$$

$$A = \frac{RT}{z\alpha F} \tag{3.13}$$

The generated heat is calculated through the voltage difference of the open-circuit voltage and the FC voltage multiplied with the stack current and the number of cells. By using this simple formula, all losses are considered. Equation 3.14 summarises the generated waste heat.

$$\dot{Q}_{\mathrm{gen,FC}} = (V_{\mathrm{OC}} - V_{\mathrm{FC}}) \cdot I_{\mathrm{FC}} \cdot N \tag{3.14}$$

While some model parameters are explicitly given in specifications provided by the FC manufacturer, most model parameters can be extracted from the polarisation curve. The implemented model is characterised

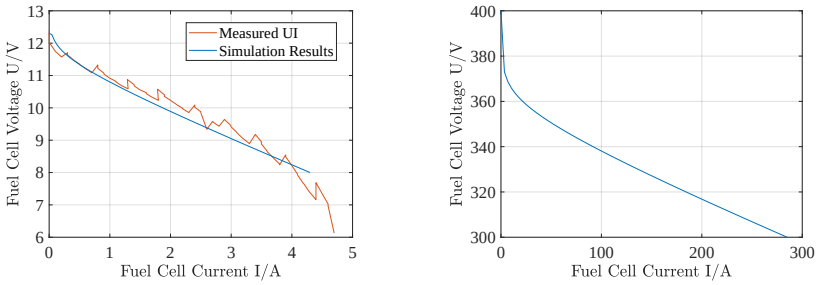

(a) (b)

Figure 3.14: (a) Measured and simulated polarisation curves of a 30 W FC.(b) Simulated polarisation curve of a 100 kWFC model [12].

by eight parameters. To determine these, the current and voltage at nominal and maximal operation and the voltages at zero and 1 A are required. Additionally, the number of series cells, the nominal stack efficiency and operating temperature, as well as the nominal air flow rate, the absolute supply pressure and the composition of fuel and air are needed. A detailed description how to determine the model parameters can be found in [11]. The implemented model was validated based on the 30 W FC introduced in the previous Section 3.2. Figure 3.14 (a) depicts the polarisation curve of the real FC, the voltage steps periodically appearing over the complete operation range are caused by the purging mechanism of the used FC. Since no complex humidity management is used to operate the FC system, periodic purging blows out the excess water. Consequently after each purge the FC voltage abruptly increases, followed by a smooth voltage degradation until the next purge is executed. Based on the characteristics of the 30 W FC, model parameters were determined and the model configured. The simulation results depicted in Figure 3.14 (a) compare the simulated polarisation curve with the measured one. Since optimal humidification is assumed, the simulated polarisation curve does not show the purging caused voltage variations of the real FC. In summary it can be stated, when neglecting the voltage variation due to purging, the comparison of the simulation results and the recorded polarisation curve shows the accurate performance of the implemented models.

Figure 3.14 b) shows the polarisation curve of the 100 kW FC system used in the virtual test bench. In accordance to the system design discussed in Chapter 2.2.4, a FC with a nominal power of 100 kW is sufficient to power a full-size vehicle and guarantee an acceleration from 0

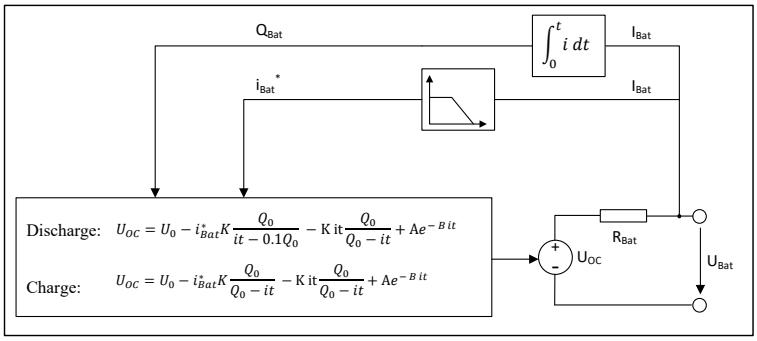

Figure 3.15: Schematic illustration of the implemented BAT model [13].

to $100\,\mathrm{km\,h^{-1}}$ in $15\,\mathrm{s}$. The system characteristics to extract the required model parameters as well as the validation of the derived model can be found in [12].

3.3.3. BATTERY

The BAT model is used to determine the BAT voltage and SoC depending on the applied BAT current. Basically, there are three different approaches to model a BAT. Detailed electrochemical models typically are represented by a system of coupled time-varying partial differential equations [162, 163]. Such models are best suited for optimisation of the physical and materials design aspects of for example the internal electrodes or the electrolyte. The drawback of these detailed models are the high computational burden simulating electrochemical models. The difficult determination of the required parameter is also a challenge, these are typically not provided by manufacturers and often require extensive experiments and investigations [162, 164]. Another option to model a BAT is to use an empirical model [165]. While this approach is capable to predict the capacity and the SoC by using empirical or stochastic equations, they are often not accurate [164]. Additionally, to determine the required parameters, requires different experiments. The third option to simulate the BAT characteristics is to use an electrical model, represented by an equivalent circuit.

In accordance to Cao et al., electrical models are most suitable to be implemented in comprehensive system-level dynamic models. Electrical models are often related to Thevenin equivalents, those typically assume the open circuit voltage to be constant and use a combination of

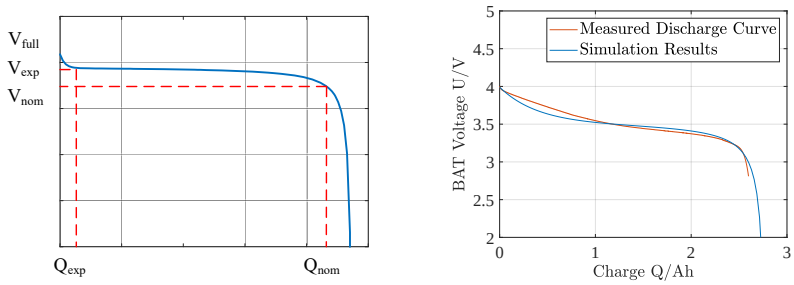

(a) (b)

Figure 3.16: (a) Typical discharge curve and characteristic points of a BAT (b) Simulated and measured discharge curve.

resistors and capacitances to track the BAT response to transient loads [164, 167]. Impedance-based electrical models employ electrochemical impedance spectroscopy to obtain an AC equivalent impedance model in the frequency domain, and then use equivalent network to fit the impedance spectra [168]. Another option to realise an electrical BAT model is a runtime based approach. Those approaches use an equivalent circuit network to simulate BAT runtime and DC voltage response for a constant discharge current in SPICE based simulators [164]. A detailed analysis of electrical BAT models and corresponding model parameter extraction is presented by [164].

Shepherd describe the electrochemical behaviour of a BAT with an equation related to the terminal and the open circuit voltage, the internal resistance, the discharge current and the SoC [169]. Tremblay et al. present a BAT model, based on the Shepherd model, with only the SoC as single state variable [170]. Not only that the approaches are integrable into system level simulation, but also the fact that the presented model can be completely parametrised from a manufacturer's discharge curve are major benefit. Thus, the BAT modelling method presented in [170] and [13] is used to implement the BAT model and integrate it into the virtual test bench. Figure 3.15 illustrates a schematic representation of the implemented model. The depicted discharge and charge equations are similar to the one of the Shepherd model. The BAT voltage depends on the BAT current and the actual BAT charge, the nominal capacity, a polarisation constant K, the exponential zone amplitude A and the exponential zone time constant inverse B as well as the internal resistance R_{Bat}.

The possibility to extract all required parameters from the manufac-

turers data sheet is an elemental feature of the selected BAT modelling approach. The required values are the voltage and charge at the end of the exponential and at the end of the nominal zone as well as the fully charged voltage. These required points are marked in the depicted discharge curve, see Figure 3.16 (a). Additionally, the maximum capacity and the internal resistance are required to parametrise the implemented model. The BAT was validated based on one cell of the BAT used in the hardware test bench, see the previous section 3.2. Figure 3.16 summarises the results of a simulated discharge curve and a measured one. In order to record the discharge characteristic curve, the fully charged BAT cell was continuously discharged with a regulated current of $1\,\mathrm{A}$. One reason for the deviation in the exponential zone might by the included management and security related electronics. Nevertheless, the maximum deviation is $2\,\%$ and thus the implemented BAT model can be considered as validated.

3.3.4. SUPERCAPACITOR

The SC model is used to determine the SC voltage related to the SC current. A complex equivalent circuit SC model was presented by [171]. The SC is modelled with three resistor-capacitor branches, one of them with a voltage-dependent capacitance. The required parameter result from a single pulse current controlled fast charge. Nevertheless, in order to achieve valid measurements a precisely timed and controlled current source, to control exactly the provided charge, is required [172]. [173] use also a three branch equivalent circuit to model a SC, but unlike to Bonert and Zubieta, Weddell et al. do not assume that branches act identical. This assumption allows to simulate a wider range of time periods. Since both presented approaches require extensive measurements and targeted at the exact modelling of a SC's behaviour, for the purpose of optimising the operation of power electronic devices, in this work a different approach was followed.

Figure 3.17 depicts a schematic representation of the implemented model. The implemented model is oriented at the Stern model. The SC charge Q_T depends on the SC current, the self-discharge rate is considered as a constant current, determined by the SC capacity, the internal resistance (R_{SC} and a time depending factor. The open circuit voltage (V_{OC}) is determined by the SC charge and modelled via a Stern equation, see 3.17. The parameters which describe the open circuit voltage are the SC's geometry and structure describing features, the number of parallel and series capacitors (N_p, N_s), the interfacial area between the electrodes and the electrolyte (A_i) as well as the number of the electrode's layer, the mo-

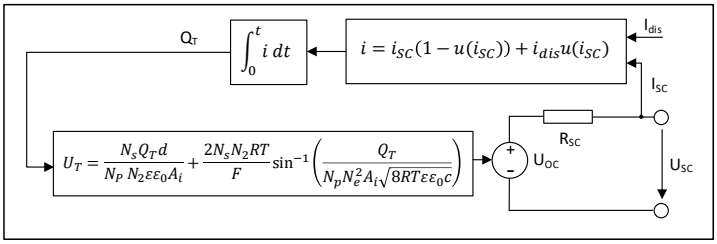

Figure 3.17: Schematic structure of the implemented SC model.

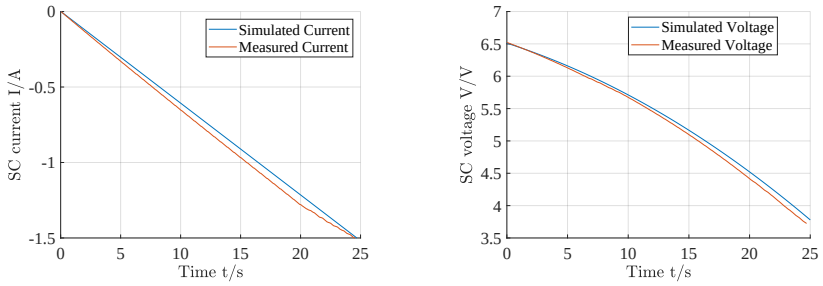

(a) (b)

Figure 3.18: (a) Measured and simulated SC current characteristics. (b) Illustration of the measured and simulated SC voltage.

lecular radius and the material related permittivity (N_e, d, ϵ) [174, 175]. The required parameters were assumed based on the Maxwell DuraBlue $48\,\mathrm{V}$ modules. In order to realise the DC link voltage of $250\,\mathrm{V}$, six series modules were assumed. The material and electrode structure related parameters were taken from a set of empirically determined parameter set provided by Mathworks®.

The implemented SC model was also validated against the hardware module described in section 3.2. In order to validate the designed model, it was parametrised to emulate the small hardware SC. Therefore, a current ramp was applied to the charged $16\,\mathrm{F}$ SC module. Similar to the experiment, a current ramp was applied to the virtual SC. Figure 3.18 depicts the simulated and measured current and voltage. It can be seen that the simulation results correspond to the measured results. The small deviation of approximately $100\,\mathrm{mV}$ between simulated and measured voltage occur because of the not exactly matched current ramp generated by the

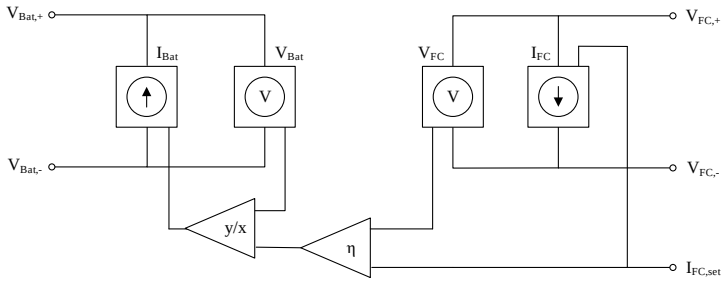

Figure 3.19: Illustration of the schematic structure of the implemented DC-DC converter model.

used source-measurement unit (Agilent B2911A). In summary can be stated that the simulation results of the developed model sufficiently meet the hardware results.

3.3.5. DC-DC CONVERTER

The DC-DC converter transforms the BAT and FC voltage to the level of the SC. They are also used to control the FC and BAT current. In the presented simulation test bench, the BAT DC-DC converter realises a boost (discharge) or buck (charge) characteristic, whereas the FC DC-DC converter has a buck characteristic. Different approaches to model the operation characteristic of DC-DC converter are presented. Basically, those can be grouped in either switching models or average-value approaches. The switching models are mainly used for design purposes, to optimise the DC-DC converter topology, the modulation scheme or the converter control or used to analyse the losses. Due to the typically high switching frequencies, the switching models needed to be executed with low sampling times, resulting in a large simulation time. In contrast, due to their comparable fast execution time, average models are suitable to be used in system level simulation. [176] presented a method to obtain non-linear, switched, state-space models of power converters, suitable for simulation and control designs. A mean value equivalent model for a unidirectional DC-DC converter that connects a FC with a DC bus is presented in [177]. Valdivia et al. propose a black-box modelling method of DC-DC converters with input current control, oriented to FC power conditioning. While the model does not represent the internal structure and detailed operation characteristics of the converter, is is less complex and the parameter identification process can be executed based on exper-

iment. Because the implemented model is used to form a test bench with the target to analyse and test system level performance of EMS strategies, an average value DC-DC converter model approach was chosen. Since the minimum time resolution of the input is 1 s, a quasi-static behaviour can be assumed and the transient characteristics of the DC-DC converter can be neglected. Therefore, both converters are modelled with two controllable current sources, respectively voltage sources [152]. Figure 3.19 shows a schematic representation of the FC DC-DC converter model. The FC current is the model input. The output power is calculated by assuming a constant efficiency and measuring the current depending FC voltage. Finally, the output current can be determined with the measured DC link voltage.

3.4. SUMMARY

In this chapter a complete virtual test bench capable to evaluate the performance of EMS strategies was presented. Because today standard test cycles are not capable to emulate all possible driving scenarios and conditions, test cases based on real world data were derived. The required data was recorded with a smartphone application and 20 different drivers participated. In order to derive a set of representative DC, a FCM oriented method to identify a set of specific DC from unspecified data was developed. The first section of this chapter describes the data recording as well as the method to derive the representative DC from the unspecified data. In order to validate the component models implemented to form the virtual test bench a set of scaled hardware components was configured. The second section describes this hardware set-up. The central third section of this chapter discussed the implemented models. To avoid excessive tests to configure the models, the selected models can be parametrised based on the manufacturers data-sheet and specifications. In total, models to simulate the operation behavior of the electric drive, the longitudinal vehicle dynamics, the driver, a FC, a BAT and SC as well as simplified model of the DC-DC converter are presented. Based on these component models a complete system model was implemented. The inputs of the simulation are a DC and a trajectory of driving distance related road inclination profile, as outputs all operation variables of the components. The interface to the EMS contains the state variable, SoC and SC voltage, the control inputs are FC and BAT current, respectively the FC and BAT power.

4

THERMAL MANAGEMENT SYSTEM

Chapter 2.2 describes the negative impact and enhanced degradation of BAT and FC when operated under non optimal temperature. Even while power electronic components are not so sensitive against non optimal condition, the fact that waste heat is generated in small areas, locally high temperature can cause significant damages. Thus, an effective cooling system is required. A central drawback of a FC is its comparable low efficiency resulting in a high amount of generated waste heat. When using the waste heat to support the thermal control of the passenger compartment, this alleged drawback can help overcome a key problem of electric vehicles. Since the waste heat of the combustion engine is not available, heating the passenger compartment at low environmental temperatures is a key problem for BEV. Typically, electric high volt heaters are used to generate the required heat. Of course this increase the overall energy demand. Exemplary, the driving range related energy consumption of the Nissan Leaf at $0\,^{\circ}\mathrm{C}$ is $30\,\%$ higher than for an environmental temperature of $15\,^{\circ}\mathrm{C}$ [179]. Hence, a thermal management which is capable to ensure optimal operation temperatures and also supports the reuse of waste heat to heat the passenger compartment can significantly improve the performance of a FHEV and in parallel minimise component degradation. In order to make best use of the FC waste heat and to control the component temperatures to be in the specified operation ranges a TMS is required. Since an optimal control also includes optimal operation conditions in the following the development of a novel TMS is going to be described. The

TMS has been constructed of four different cooling loops; one for the FC and the metal hydride storage, another one is used to cool the power electronics and the motor, a third controls the BAT temperature, and a fourth loop is used for the chiller-cooling loop to cool down the BAT and the passenger compartment. To be able to test the developed approach, a detailed model, including models of all relevant drive train elements such as DC-DC converters, motors and the BAT, has been developed. It consists of 27 states of which nine states represent the temperatures of the FC, the BAT, the power electronics etc. The developed model is capable to simulate the behaviour of the fluid flow as well as the thermal characteristics of the components. To control the operation, respectively to regulate the temperature of the FC, the BAT, the passenger compartment and the power electronics, a hierarchical state machine based control has additionally been developed and implemented. The implemented control scheme consists of three individual state machines, one for the FC, one for the interior and another for the BAT. The specific operation state is chosen with regards to the current temperature as well as the ambient temperature. The TMS proves to accurately regulate all relevant temperatures to their desired values. Synergies of the components such as the reuse of the waste heat of the FC to heat the interior and to use the chiller to cool the BAT as well as the passenger compartment have been successfully applied. The implemented TMS limits the degradation mechanisms while in parallel ensures optimal operation conditions.

This chapter is organised in three sections subsequently followed by a short summary. The first section discusses optimal operation conditions of all relevant components and derives the requirements for the TMS. In the second section the configuration of the TMS is described. The third section explains the implementation of the simulation model. Finally the description of the implemented control strategy is given in Section 4.

4.1. Optimal Operation Conditions

A fundamental aspect in order to increase the lifetime of the BAT and the FC and to limit degradation mechanisms is to operate both components at optimal operating temperature, see Section 2.2.1. The BAT degradation mechanisms are influenced by the cell's temperature, the depth of discharge as well as the BAT current [180–182]. The operating temperature of BAT exponentially degrades the capacity over the time. Herb described the exponential degradation by Arrhenius law [7]:

$$\gamma = \gamma_0 \cdot e^{-\frac{E_a}{RT}} \tag{4.1}$$

Equation 4.1 describes the degradation coefficient γ, E_0 is the activation energy required to start a reaction, γ_0 is the speed of the reaction, R is the universal gas constant and *T* the temperature. Arrhenius law implies that a maximal low BAT temperature maximises its lifetime, but of course a low temperature also slows down the electrochemical reaction and so minimises the performance of the BAT. BU5 state that an operating temperature of $30\,^{\circ}\mathrm{C}$ would cause a lifetime reduction of $20\,\%$, whereas for temperatures below $17\,^{\circ}\mathrm{C}$, the BATs capacity is reduced to nearly $50\,\%$. Since BAT capacity is reduced for temperatures below $20\,^{\circ}\mathrm{C}$, the systems presented in [184, 185] also include an active heater. Due to the hybrid topology, the investigated system will require an active heater. In the presented MPC, Lopez-Sanz et al. linearly penalise temperatures below $20\,^{\circ}\mathrm{C}$. Another factor which impacts the operation of the TMS, is the fact that BAT cells which are connected in series, should be operated at approximately the same temperature. A temperature difference across a BAT pack leads to an increase of the internal resistance of the warmer cells which causes an uneven discharge and uneven SoC [186]. The optimal BAT temperature was defined to be $26\,^{\circ}\mathrm{C}$, while temperatures above this value are more crucial than values below. To ensure an approximately equal degradation, the maximum allowable temperature variation of the cooling fluid was defined to be $5\,^{\circ}\mathrm{C}$.

The FC should be operated at a membrane temperature between $50\,^{\circ}\mathrm{C}$ and $60\,^{\circ}\mathrm{C}$ [187]. Herb state that a higher temperature would result in an exponential degradation which is caused by the release of fluorine. A temperature below the minimum operating temperature causes a reduction of the available power [7, 188]. At temperatures below $23\,^{\circ}\mathrm{C}$, the operation is almost impossible. In order to maximise the FC lifetime, the operation temperature should be kept at the minimum temperature. Thus, the optimal FC temperature was defined to be $55\,^{\circ}\mathrm{C}$. Similar to the BAT, the maximum temperature deviation of the cooling fluid was defined to be $5\,^{\circ}\mathrm{C}$ [189]. Since it is assumed that the hydrogen storage is realised as a metal hydride tank, it also has to be considered. When hydrogen is desorbed by a metal hydride, the storage acts as a heat sink. Vice versa, if hydrogen is absorbed, it behaves like a heat source. The absorption and desorption rate of the storage depends on the temperature. At lower temperatures, the output pressure of the hydrogen is below the necessary access pressure of the FC and thus must be increased by a compressor. The typical operation temperature of a metal hydride storage is $30\,^{\circ}\mathrm{C}$ [190].

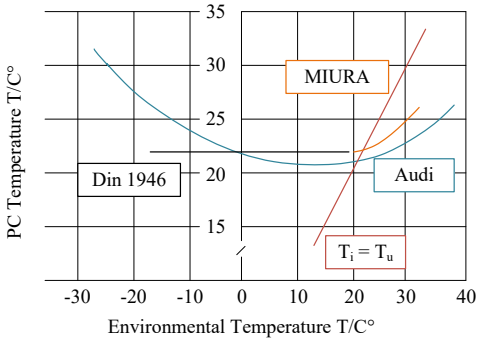

Figure 4.1: Desired vehicle's PC temperature related to the environmental temperature [14].

The DC-DC converters, the motor inverter and the motor itself are robust against high temperatures. Nevertheless, the temperatures must be kept within the ranges specified by the manufacturer. The maximum coolant temperature of the DC-DC converter is $65\,°C$, while the optimal temperature is $55\,°C$ [191]. The maximum operation temperature of the power electronics is determined to be $90\,°C$. The operation temperature of an electric motor is in the range from -40 °C to 85 °C [192].

The temperature of the vehicle's interior is defined by the driver request. Großmann investigate the comfort temperature with regards to the ambient temperature. Figure 4.1 depicts the approximated desired interior temperature, it can be seen that it changes with the ambient temperature. If an operation temperature in the range from $-20\,°C$ to $40\,°C$ is assumed, the desired interior temperature changes from $28\,°C$ to $21\,°C$, while direct radiation may lower it to $15\,°C$. In this work a value of $21\,°C$ is assumed. This is close to the operation temperature of the BAT. To realise this interior temperature, the temperature of the airflow into the passenger compartment has to be significantly lower. In accordance to [193] the air stream temperature is in the range of $5\,°C$ to $10\,°C$.

4.2. System Configuration

The configuration of the TMS depends on the characteristics of the system components. The behaviors of the FC, the BAT, the converter and the motor can be described as a heat source. The characteristic of the vehicle's interior depends on the driver and the environmental temperature and can be described as a heat source or a heat sink. During the refuelling process,

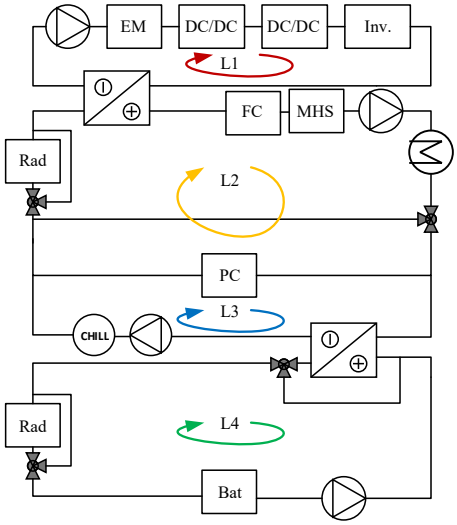

Figure 4.2: Suggested TMS approach based on four different cooling loops to meet the temperature demands of the different components (red: 80 °C; yellow: 55 °C; blue: 30 °C; green: 5 °C to 50 °C).

the metal hydride storage behaves like a heat source, while in the case that hydrogen is supplied, it behaves like a heat sink. While driving, the heat of the heat sources can be dissipated by radiators. Since the passenger compartment as well as the BAT cooling require a lower temperature than the environment temperature, a chiller applied. The review of the state of the art of vehicle heating and cooling, see Section 2.3, proves the necessity to develop a new TMS approach, until now only approaches which are not capable to guarantee optimal operation conditions for all components of the targeted FHEV are presented.

The different temperature ranges in the FHEV make the thermal conditioning more complex and the TMS to consist of several cooling loops. The different operation temperatures vary significantly, the power electronics can reach 80 °C, the coolant entering the FC may vary between 45 °C and 55 °C, the BAT operate at 30 °C and a range between 5 °C and 50 °C is required to cool the passenger compartment. The presented approach is developed based on the Tesla patent presented in 2.3 [9], but in contrast to the Tesla concept, the developed TMS consists of four different cooling loops plus the refrigerant loop of the chiller. The excess heat is dissipated via two radiators and the chiller, two bypasses are required for the cooling circuits and two for the radiators. Figure 4.2 depicts

the developed TMS approach, the different loops are displayed in different colours. The high temperature loop is depicted in red, the FC loop in yellow, the passenger compartment loop in blue and the low temperature BAT loop in green. The high-temperature cooling circuit with the two DC/DC-converters, the inverter and the motor are connected to the FC loop through a counter-flow heat exchanger. The counterflow heat exchanger can cool the flow of the hot fluid below the outflow temperature of the cold fluid. This is especially beneficial during the start-up of the vehicle, when the FC need to be heated up to the operation temperature as quickly as possible. Since counterflow heat exchanger allows to transform almost the total waste heat which is generated by the power electronics to the FC cooling loop, a quick warm-up is ensured. The heat exchanger is placed in front of the FC to ensure that the coolant liquid's temperature is controlled when entering the FC. During operation, the FC generated waste heat is largely dissipated by the metal hydride storage. If the vehicle interior needs to be heated, another large proportion of the heat is dissipated via the vehicle interior. The amount of heat which is not dissipated through the metal hydride or the passenger compartment, is dissipated by a radiator. The three-way directional valve controls the flow rate of the heated coolant and thus the temperature of the airflow that enters the PC. If the vehicle interior has to be cooled, the FC coolant is directed through the bypass and the passenger compartment is connected to the chiller. The chiller reduces the temperature of the coolant with regards to the driver's demand. It is considered that the airflow through the interior heat exchanger can be controlled through air flaps which acts as an air bypass valve. The BAT is connected to the chiller loop by a heat exchanger. In order to optimise the chiller energy demand, the largest amount of BAT waste heat shall be cooled by the BAT radiator. If the radiator is not sufficient, a bypass controls the extent of heat dissipated by the heat exchanger to the chiller circuit. This set-up ensures minimal loss while the reference temperature can be maintained. In summary can be stated that the presented system can operate in three different fundamental states:

- Warm up: Both radiators, the passenger compartment and the BAT heat exchanger are bypassed. The FC is switched off, the power electronics heat exchanger is in counter-flow mode. BAT is resistively heated.

- Cold weather operation: The hot coolant (FC circuit) flows through the passenger compartment's heat exchanger. Power electronics

heat exchanger flows in counter-flow mode. The BAT is cooled solely by the radiator. The chiller is switched off.

- Warm weather operation: The passenger compartment is bypassed. The chiller is active and reduces the temperature of the vehicle interior coolant to the reference temperature. Depending on the ambient temperature, the power electronics heat exchanger may be bypassed. The BAT is cooled down through the heat exchanger. The BAT radiator is bypassed.

The detailed model is described in the next Section 4.3. The component parameters have been taken from literature or assumed if no specific literature was available. The presented system structure guarantees optimal operating conditions for all components of the TMS with the minimum number of components. The power electronics loop is operated at a low flow rate and a high temperature. During the system warm-up, this cooling loop is used to heat the FC to its operating temperature. The FC cooling loop operates at a lower temperature than the power electronics but under a higher flow rate. The waste heat of the FC is used to warm-up the metal hydride storage and at a low environmental temperature, to heat the vehicle interior. If the air conditioning is enabled, a chiller-cooling loop is connected to the interior heat exchanger to dissipate heat from the interior. The BAT is either cooled through its own radiator or through the chiller. The heat exchange components have been determined in order to meet the system requirements. A detailed description of the technical configuration and determination of the required component specification as well as a reference design can be found in Appendix A. Because the implementation of the proposed TMS in real hardware would have induced excessive manufacturing efforts and costs, the system was solely implemented as a simulation model.

4.3. Physical Model

In this section the implemented model is going to be described. The TMS model was implemented using the MATLAB® Simulink® simulation environment. In the following section, all required models are subsequently described. The description starts with the models used to emulate the fundamentals of a liquid mixer and the required fluid mechanics, followed by models for the pump and for the electrical components (FC, BAT, H2 storage and power electronics). Afterwards the model for the vehicle interior is described, subsequently followed by the description of the models of the heat exchange components and the active heater.

4.3.1. FLUID DYNAMICS

The model of the fluid dynamic determine the modelling of the pipes, pumps, valves and other fluid resistive elements such as heat exchangers, FC etc.. Due to the complexity of flows, the fluid flow is often modelled using a lookup table [184]. Tao use a resistance network to describe the fluid flow in every branch of a complex cooling system.

$$P_{pipe} = P_{loss} + \frac{dE_{Kin}}{dt} \tag{4.2}$$

The fluid flow has been modelled based on the first principle using correlations for a rigid pipes. Equation 4.2 represents the power equilibrium. The power losses in a pipe P_{pipe} can be calculated through the pressure loss due to friction δp, the mass flow $\dot{m}$ and the fluid density ρ as Equation 4.3. The kinetic energy, E_{kin}, is calculated based on the pipe's length L, the pipe's cross section A and the momentum flux correction factor β which depends on the nature of the flow, see Equation 4.4. The power exerted on the pipe can be expressed as the product of mass flow rate and pressure drop across the pipe section, see Equation 4.5

$$P_{loss} = \Delta p \cdot \frac{\dot{m}}{\rho} \tag{4.3}$$

$$E_{kin} = \frac{1}{2}\beta\frac{L}{A\rho}\dot{m}^2 \tag{4.4}$$

$$P_{pipe} = \Delta p \cdot \frac{\dot{m}}{\rho} \tag{4.5}$$

State Equation 4.6 describes the fluid mechanics in a rigid pipe section. It can be derived from Equations 4.2 to 4.5. The term $\frac{L}{A\rho}$ is summarised as the kinetic energy factor $\psi(\beta)$. For N consecutive pipe sections the overall kinetic energy factor can be determined by Equation 4.14, the combined pressure drop (p_{comp}) results from sum of the pressure drops p_i.

$$\frac{\dot{m}}{dt} = \frac{A}{L\beta}(\Delta p - \delta p) \tag{4.6}$$

$$\delta\Psi_{comp} = \left(\sum_{i=1}^{N}\frac{1}{\Psi_i}\right)^{-1} \tag{4.7}$$

$$\delta p_{comp} = \sum_{i=1}^{N}\delta p_i \tag{4.8}$$

The pressure loss due to friction is calculated based on the friction factor 4.9. The friction factor f can be determined based on the nature of the flow (laminar, turbulent or transitional).

$$\delta p = f \frac{L}{D} \rho \frac{\bar{v}^2}{2} \tag{4.9}$$

For laminar flows the friction factor depends on the Reynolds number (Re), the shape factor ξ, the relative roughness of the pipe *r* and the pipe's diameter *D*. A general method to determine the shape factor has been presented in [195, 196]. Various correlations to estimate the friction factor for turbulent flows have been presented in [197]. In this work, the Haaland friction formulation is used [198]. In summary can be stated that the friction factor depends on the type of flow and can be determined based on Equation 4.10.

$$f = \begin{cases} \frac{\xi}{Re} & Re_L \geq Re \\ f_L(Re_L) + \frac{f_T(Re_T) - f_L(Re_L)}{Re_T - Re_L} \left(Re - Re_L\right) & Re_L \leq Re \leq Re_T \\ \left(-1.8 \log_{10} \left(\left(\frac{r}{3.7 \cdot D}\right)^{1.11} + \frac{6.9}{Re} \right) \right)^{-2} & Re_T \leq Re \end{cases} \tag{4.10}$$

Valves act like variable orifices, whereas three-way directional valves can be expressed as two variable orifices. The norm ISO 5167 gives a clear definition about how the pressure drop across an orifice can be calculated [199]. Similar to the pressure drop in a pipe for fully developed laminar flow, the pressure drop is proportional to the squared flow rate. The orifice model used for simulation is similar to the model described in [199]. While the model decribed in the norm uses a fully developed turbulent flow, the model composed by MathWorks® is based on a mathematical expression, see Equation 4.11, capable to describe both laminar and turbulent flow types [200]. C_d is the discharge coefficient which is a measure of the mass flow rate through a orifice relative to the theoretical value that it would have in an ideal orifice.

$$\Delta p = \frac{\dot{m} \cdot \sqrt{\dot{m}^2 + \dot{m}_{cr}}}{2 \rho C_d^2 S_R^2} \cdot \left(1 - \left(\frac{S_R}{S}\right)^2\right) \phi_{PR} \tag{4.11}$$

To calculate the mass flow rates in the bypasses and the components, the pressure drop across both parallel flow components, as well as the orifices, must be equal. The flow rates of two parallel branches are considered as sub-controlled. Furthermore, the valve position is dependent on the length and surface area of the bypass. Hence, it is not necessary to simulate the

valves independently, but provide a set point for the required flow rates. The valves are considered to be sufficiently big and the bypass to be ideal. The flow rates in both parallel components depend on the flow factor g and the total mass flow rate $\dot{m}$, see Equations 4.12 and 4.13. The maximum of the pressure drop across two adjacent components (no ideal bypass) is assumed to be the resulting pressure drop, the inertia factor for both is the sum of the individual ones.

$$\dot{m}_1 = g \cdot \dot{m} \tag{4.12}$$

$$\dot{m}_2 = (1 - g) \cdot \dot{m} \tag{4.13}$$

Fluid mixer can be modelled based on the energy equilibrium assuming a zero heat capacity [201]. The resulting temperature $\mathrm{T_{out}}$, see Equation 4.15, results from the ratio of both volumetric flow rates ($\dot{\mathrm{V}}_{\mathrm{in},1}$, $\dot{\mathrm{V}}_{\mathrm{in},2}$), the fluid heat capacity $c_{p,c}$ and the inflow temperatures ($T_{in,1}$, $T_{in,2}$).

$$\dot{m}_{out} \cdot c_{p,c} \cdot T_{out} = \dot{m}_{in,1} \cdot c_{p,c} \cdot T_{in,1} + \dot{m}_{in,1} \cdot c_{p,c} \cdot T_{in,1} \tag{4.14}$$

$$T_{out} = \frac{\dot{V}_{in,1} T_{in,1} + \dot{V}_{in,2} T_{in,2}}{\dot{V}_{in,1} + \dot{V}_{in,2}} \tag{4.15}$$

In order to control the mass flow rates fixed displacement pumps are considered. To emulate the behaviour of a fixed displacement pump, the required factors are the mass flow rate and the pressure rise. In accordance to [202], for a fixed displacement pump these parameters can be calculated through the angular velocity ω, the pump's torque τ and the displacement parameter $\mathrm{D_M}$. Manufacturer's datasheets typically provide the displacement factor. Two factors reduce the efficiency of a pump, the leakage flow and the torque efficiency. In accordance to [203], the leakage coefficient can be described by the Hagen-Poiseuille law and depends on the viscosity of the fluid which is highly non-linear in relation to the temperature of the fluid. The torque efficiency depends on three factors, viscous resistance, sliding friction resistance and shaft sealing resistance. More detailed information about the calculation of the torque efficiency is given in [203]. Instead of modelling both effects, a fix efficiency of $95\,\%$ is assumed for the implemented model.

$$Q = D_M \cdot \omega \tag{4.16}$$

$$\Delta p = \frac{\tau}{D_M} \tag{4.17}$$

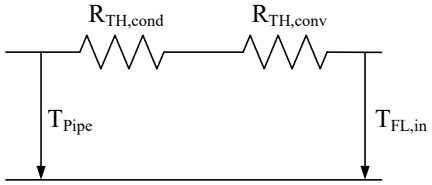

Figure 4.3: Schematic illustration of the thermal equivalent circuit model of the FC.

4.3.2. DRIVETRAIN COMPONENTS

The relevant drive-train components are the BAT, the FC, the DC-DC converters, and the inverter. The presented models will be discussed in terms of electrical correspondences and depicted as thermal equivalent circuits. Since all automotive components are usually encased with aluminium that has a low emissivity, a radiative heat transfer is not relevant and thus neglected. A direct connection to the ambiance is also not existent. Therefore, only heat dissipation via the coolant is considered. All components have a coolant pipe interface which is used to dissipate the heat. Figure 4.3 depicts a schematic of a thermal equivalent circuit of such an interface. Here heat can be dissipated via conductive and convective heat transfer.

Due to the complexity of the components, it is not possible to determine the values of the conductive resistances and the thermal capacitance from the first principle, but an empiric estimation based on experiment is possible. The convective resistance is modelled using the correlation of Gnielinski [204–206]. The relation is used to determine a mathematical expression to calculate the convective heat transfer coefficient, see Equation 4.18. The convective heat transfer coefficient from the pipe to the coolant depends on the flow characteristics of the fluid.

$$h_c = \begin{cases} 3.66 \cdot \frac{\alpha}{D_h} & Re_L \geq Re \\ h_c\left(Re_L\right) + \frac{h_c(Re_T) - h_c(Re_L) \cdot (Re - Re_L)}{Re_T - Re_L} & Re_L \leq Re \leq Re_T \\ \frac{\alpha_c}{D_h} \frac{\left(\frac{f}{8}\right) Re_{D_h} Pr}{1 + 12.7\left(\frac{f}{8}\right)^{\frac{1}{2}} \cdot \left(Pr^{\frac{2}{3}} - 1\right)} & Re_T \leq Re \end{cases} \tag{4.18}$$

Because of the great thermal conductance of the pipe's wall, the wall temperature is considered constant. The differential equation, see Equation 4.20 describing the fluid temperature T can be derived from the differen-

tial heat transfer Equation 4.19. The differential equation can be solved by inserting an e-function. After solving the equation, it is possible to calculate the average temperature difference which is equal to the difference of inflow and pipe temperature. Using again the differential heat transfer equation, results in Equation 4.21 that defines the convective heat transfer resistance, see Equation 4.22.

So far only a constant inlet temperature of the fluid flow is considered. A changing inlet temperature would result in an abrupt change of the heat transfer. Hence, it is necessary to consider a changing effective temperature of the fluid. The given equations were derived based on the inlet temperature purely. Due to the volume of the pipe and the resulting heat capacitance of the coolant volume in the pipe, the heat transfer cannot change abruptly. Thus, the energy equilibrium representing the difference of energy inlet Ψ_{in} and outflow Ψ_{out}, see Equation 4.23 and 4.24, can be used to find a differential equation describing the effective fluid inlet temperature $\bar{T}_{in}$, see Equation 4.25.

$$\dot{Q}_{Diss} = (T - T_W) \cdot h_c \cdot P \cdot dl \tag{4.19}$$

$$\frac{dT}{dl} = -(T - T_W) \cdot \frac{h_c P}{\dot{m} c_p} \tag{4.20}$$

$$\dot{Q}_{Diss} = \frac{\Delta T}{\frac{1}{\dot{m}c_p\left(1-e^{-\frac{h_{cool}A}{\dot{m}c_p}}\right)} + R_{th,cond}} \tag{4.21}$$

$$R_{TH,conv} = \frac{1}{\dot{m}c_p \cdot \left(1 - e^{-\frac{h_{cool}A}{\dot{m}c_p}}\right)} \tag{4.22}$$

$$\Psi_{in} = T_{in} c_{p,c} \dot{m} \tag{4.23}$$

$$\Psi_{out} = \Psi_{in} + \dot{Q}\left(\bar{T}_{in}\right) \tag{4.24}$$

$$V \rho_c c_{p,c} \frac{\bar{T}_{in}}{dt} = \dot{m} c_p \left(T_{in} - \bar{T}_{in}\right) \tag{4.25}$$

The warm up of the liquid flowing through a component is modelled using the pressure loss due to friction ρ_p. The temperature can therefore be calculated with the energy balance, see Equation 4.26. In the following, equivalent circuit oriented models for all heat generating electrical components are going to be presented. Whereas each conductive resistances can be determined based on experiments and the convective

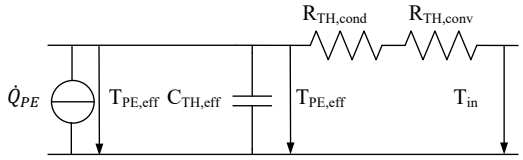

Figure 4.4: Schematic illustration of the thermal equivalent circuit model of the power electronic components.

resistance derived based on Equation 4.22.

$$\dot{m}c_pT_{in} + \delta p\frac{\dot{m}}{\rho} = \dot{m}c_pT_{out} \tag{4.26}$$

The power electronics model consists of a heat capacity and three heat resistances which accounts for the conductive and the convective heat transfer. Similarly to [207, 208], a direct thermal resistance is used to account for the direct temperature rise, which results from the power loss. The heat capacities of the semiconductors are neglected. A thermal capacitance is used to model the mean temperature of the complete component, a conductive and convective thermal resistance is used to model the dissipated heat. A schematic equivalent circuit of the implemented model is depicted in Figure 4.4.

As presented in Section 2.3, BAT state of the art cooling circuits ensure a continuous coolant stream through the complete BAT, thus all cells are in contact to the coolant. By neglecting radiation, the heat flow solely depends on the conduction and convection. Thus, the heat flow is determined by the temperature difference. Therefore, cells, encountered by a warmer fluid, will have the same characteristics as the cells encountered by a colder fluid but with a temperature offset. It is considered that cells are grouped together and so the temperature characteristics of a single cell is neglected. The temperature increase of the fluid is sufficient to describe the temperature increase of the cells. While BATs cannot be seen as a lumped body, because the thermal conductance inside the cells is too low, they can be modelled by describing the thermal behaviour by a thermal capacitance and a thermal resistance accounting for the conductive heat transfer [209]. Forgez et al. present a simplified model which consists of one thermal capacity and two thermal resistances. The model adopted is closely related to the model proposed by [209]. It consists of one thermal capacitance to account for the thermal capacity of the BAT. Furthermore, one thermal resistance is used to model the thermal resistance of the BAT

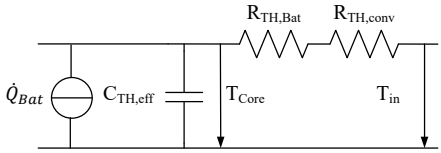

Figure 4.5: Schematic illustration of the thermal equivalent circuit model of the BAT.

and one thermal resistance accounts for the convective heat transfer. The state variable is the BAT's core temperature. The model is depicted in Figure 4.5.

The thermal conductance of the surface of the BAT is considered infinite. Hence, it can be modelled through a sole thermal capacitance. Since the temperature of the core of the BAT cannot be measured, an observer will be required to estimate the core temperature through the temperature of the fluid T_{in} and the temperature of the wall T_W. The heat generated by the BAT cells can be estimated through the electric model. A uniformly generation through the complete cell is assumed. The thermal resistance is calculated as a hollow cylinder, where the internal radius r_i is one half of the external radius r_e, see Equation 4.27. The heat capacitance is calculated through the volume of the BAT and described by Equation 4.28. Finally the differential equation which determines the BAT's core temperature is given by Equation 4.29. The waste heat of the BAT is determined by the BAT electrical model, see Section 3.3.3.

$$R_{TH,Bat} = \frac{1}{\alpha 2\pi h} \ln\left(\frac{r_e}{r_i}\right) \tag{4.27}$$

$$C_{th,eff} = \pi r_e^2 h \rho c_p \tag{4.28}$$

$$C_{th,eff}\frac{dT_{Core}}{dt} = \dot{Q}_{Bat} - \frac{T_{Core} - T_W}{R_{th,Bat}} \tag{4.29}$$

Nolan and Kolodziej model an automotive FC including the FC's intercooler, humidifier, and hydrogen heat exchanger. The thermal domain of the stack was modelled using a continuously stirred tank reactor approach. Besides the thermal model of the stack, Nolan and Kolodziej also account for the anode heat exchanger. The advantage of this approach is that the warm-up of the system can easily be modelled linearly. The disadvantage is that only the information about the temperature of the coolant is available. A change in the inflow temperature would only be

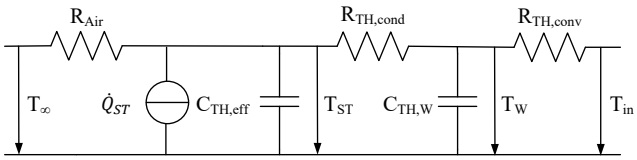

Figure 4.6: Schematic illustration of the thermal equivalent circuit model of the FC.

considered through a delay in the change of the outflow temperature. The FC is modelled using the balanced heat flow equation. It is assumed that no heat is transferred by conduction or convection to the ambient air and that all heat is dissipated through the exhaust air or the TMS [201]. The heat balance is therefore modelled as Equation 4.30. The generated heat is estimated by the electrical FC model see Section 3.3.2.

$$\dot{Q}_{store} = \dot{Q}_{gen} - \dot{Q}_{diss} - \dot{Q}_{exh} \tag{4.30}$$

The dissipated heat through the exhaust air and the exhaust water can be calculated using equation 4.31. Σ is a parametrisation constant used to account for the difference of the FC and air temperature. A conceptual model of the air heat transfer was disregarded due to the insignificant amount of the heat dissipated through the exhaust air [210]. The volumetric flow rate of the air $\dot{V}_{air}$ is controlled by the FC. Look up tables were used to account for the air density and the heat capacity. The stored temperature can be calculated from the effective stack volume V_{eff}, the density ρ_{stack} and its heat capacity $c_{p,stack}$, see Equation 4.32. The dissipated heat is calculated through thermal resistances, which represent the forced convection and the thermal conduction. Since the exact temperature of the FC cannot be measured, the temperature must be reconstructed through the temperature of the pipe connecting the FC to the TMS. Equation 4.33 was used to estimate the dissipated heat.

$$\dot{Q}_{exh} = \dot{V}_{air} c_{p,a} \rho_a \left(T_{FC} - T_\infty\right) \Sigma \tag{4.31}$$

$$\dot{Q}_{store} = \frac{d \rho_{st} V_{eff,st} c_{p,st} T_{st}}{dt} \tag{4.32}$$

$$\dot{Q}_{diss} = \frac{T_{FC} - T_W}{R_{TH,cond}} \tag{4.33}$$

Figure 4.6 depicts the equivalent circuit representation of the implemented thermal FC model. The describing differential equation is given

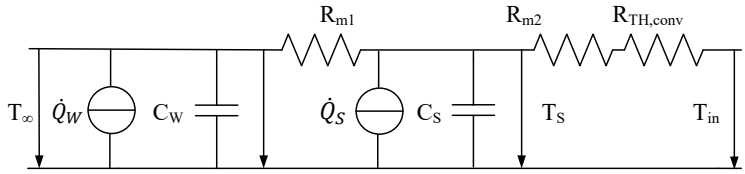

Figure 4.7: Schematic illustration of the thermal equivalent circuit model of the electric drive.

as Equation 4.34. The pipe wall temperature is again estimated similar to the pipe liquid interface described at the beginning of this section.

$$\frac{dT_{ST}}{dt} = \frac{1}{\rho_{st} c_{p,st} V_{eff,st}} \cdot \left(\dot{Q}_{gen,FC} - \dot{Q}_{diss} - \dot{Q}_{exh} \right) \tag{4.34}$$

In literature, detailed models that describe the temperature distribution within a metal hydride hydrogen storage [211] are presented. Ravey et al. describe a lumped parameter model that consists of a thermal resistance only and designs the heat flow through the cylindrical hydride storage. Ravey et al. neglect the heat capacitances of the storage, the dynamic effects as well as thermal resistances to the fluid. Furthermore, Ravey et al. determine the difference in temperature for a given mass flow through experimental analyses. In this work, the hydrogen storage is modelled using a heat capacitance in the centre and a heat resistance. The heat is dissipated and generated in the centre. The necessary heat is evacuated or supplied due to the temperature of the coolant by overcoming the thermal resistance of the metal hydride. To simplify the model, the metal hydride is modelled as a tank embedded in a fluid container. The metal hydride storage is modelled similarly to the BAT with a conductive and a convective thermal resistance. The metal hydride storage is also of cylindrical shape. The thermal capacitance, the resistance as well as state equation are given in the following Equations 4.35 to 4.37.

$$\dot{C}_{MH} = \pi r_e^2 h \rho c_p \tag{4.35}$$

$$\dot{R}_{th,MH} = \frac{1}{\alpha 2\pi h} \ln\left(\frac{r_e}{r_i}\right) \tag{4.36}$$

$$C_{MH} \frac{dT_{MH}}{dt} = -Q_{MH} + \frac{T_{MH} - T_W}{R_{th,MH}} \tag{4.37}$$

Thermal simulations of electric motors have been performed with the Software AMESim in [213]. A detailed thermal model, which consists

only of a thermal resistances is presented by [214]. This model is capable of calculating the temperatures within the motor for the stationary case but not able to contribute for the transient behaviour. In this work, a modified motor model including the convective heat transfer to the fluid was implemented. The equivalent circuit of this model is shown in Figure 4.7. The power loss of the copper winding is defined through $\dot{Q}_{\mathrm{CL}}$, the losses of the stator through $\dot{Q}_{\mathrm{S}}$. $\mathrm{R_{m1}}$ models the thermal resistance between the stator and the winding, $\mathrm{R_{m2}}$ the thermal resistance between the stator and the case and finally $\mathrm{R_{th,conv}}$ the thermal resistance of the case to the coolant. The resulting state equations describing the equivalent circuit are summarised in Equation 4.38 and 4.39.

$$\frac{dT_W}{dt} = -\frac{T_W}{R_{m1}C_{CW}} + \frac{T_S}{R_{m1}C_{m1}} + \frac{\dot{Q}_{CL}}{C_{CW}} \tag{4.38}$$

$$\frac{dT_R}{dt} = \frac{T_W}{R_{m1}C_{m2}} - \frac{T_S}{R_{m1}C_{m1}} + \frac{T_S}{(R_{m2}+R_{conv})\,C_{m2}} + \frac{\dot{Q}_S}{C_S} + \frac{T_{in}}{(R_{m2}+R_{conv})\,C_{m2}} \tag{4.39}$$

4.3.3. Heat Exchange Components

The heat exchanging components are the radiators, the counter flow heat exchanger, the chiller and the active heater. The counter flow heat exchangers have been modelled by using the Number of Transfer Units method [215]. The used approach introduces the definition of heat exchanger effectiveness (ϵ), which is a dimensionless number with ranging between 0 to 1. The hot side of the heat exchanger is referred to as the indices 1, the cold side as the indices 2. The outlet temperature is referenced through a single apostrophe. The normalised temperature difference is given by ϵ_1 and ϵ_2. To consider dynamic changes of the inflow temperature, a state equation (A.7) is derived to determine the inlet temperature, the normalised temperature differences result in Equation 4.41 and 4.42. V_i is the volume, $\rho_{c,i}$ the density of the streaming fluid, $c_{p,c,i}$ the heat capacity and $\dot{m}_l$ the mass flow rate.

$$V_i\rho_{c,i}c_{p,c,i}\frac{\bar{T}_i}{dt} = \dot{m}_l c_p\left(T_i - \bar{T}_i\right) \tag{4.40}$$

$$\epsilon_1 = \frac{\bar{T}_1 - \acute{T}_1}{\bar{T}_1 - \acute{T}_2} \tag{4.41}$$

$$\epsilon_1 = \frac{\bar{T}_1 - \acute{T}_1}{\bar{T}_2 - \bar{T}_2} \tag{4.42}$$

The thermal transmittance is calculated through an inverse summation of the heat transfer coefficient h_c, where the transfer coefficient is calculated for the hot and the cold side through the Gnielinski equation. The conduction is considered through the thermal conductance (α) and the thickness (ρ) of the material. The overall heat transfer coefficient is given by the inverse sum of the inverse single coefficients.

$$h_f = \frac{\alpha}{\delta} \tag{4.43}$$

The overall thermal transmittance is given by the effective heat transfer coefficient and the exchange surface area.

$$kA = \frac{\alpha}{\delta} \tag{4.44}$$

The thermal capacity flow rates $\dot{W}_i$ are the product of the mass flow rate m_i and the heat coefficient. The ratio of the flow rates is equal to the ratio of heat capacities. The dimensionless thermal transfer coefficients N_1 and N_2 can be calculated with Equation 4.45.

$$N_i = \frac{kA}{\dot{W}_i} \tag{4.45}$$

Finally equation 4.46 describes the characteristics of a counter flow heat exchanger.

$$\epsilon_i = \begin{cases} \frac{1-e^{(C_i-1)N_i}}{1-c_i e^{(C_i-1)N_i}} & C_i \neq 1 \\ \frac{N}{1+N} & C_i = 1 \end{cases} \tag{4.46}$$

Due to the complex behaviour, radiators are often modelled using lookup-tables [184]. Shao et al. describe a radiator model based on empirical measurements. Park and Thompson use a comprehensive method to describe the radiator with three thermal resistances which are used to model the thermal behaviour of the coolant, the fins and the tubes. The developed radiator model is closely related to the model developed by [217], while some modifications have been introduced to account for the transient behaviour as well as the correct heat transition from the coolant to the tubes. Figure 4.8 depicts the equivalent circuit diagram . The capacitor describes changes in the inflow temperature, which do not affect the heat transfer directly, see Section 4.3.2. The heat transfer depends on three thermal resistances, the convective thermal resistance $R_{conv,ct}$ from the average fluid temperature $\bar{T}_{in}$, to the tubes, the conductive thermal resistance of the tubes $R_{cond,t}$ and the convective thermal resistance from

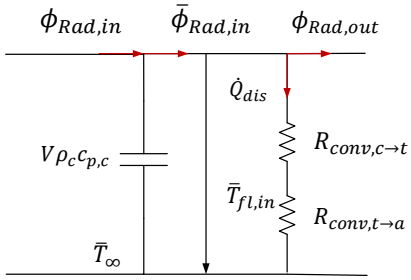

Figure 4.8: Thermal equivalent circuit model of a radiator

the tubes to the air $R_{conv,ta}$. Comparable to the thermal resistance of the fluid the thermal capacitance of the fins or tubes is negligible [217]. The energy flux used to calculate the heat dissipation depends on the average temperature of the fluid $\bar{T}_{in}$. The heat equilibrium is described through the energy flux which enters the radiator $\bar{\Phi}_{in}$, the dissipated energy $\dot{Q}_{dis}$ and the energy flux which exits the radiator Φ_{out}. The dissipated heat can be determined with the mentioned thermal resistances, see Equation 4.47.

$$\dot{Q}_{dis} = \frac{\bar{T}_{in}}{R_conv, ct + R_{cond,t} + R_conv, ta} \tag{4.47}$$

The convective thermal resistance of the fluid to the tubes is described in the previous section the same manner. Due to the comparably low thickness of the tubes, which are assumed to be made from aluminium (α = 237 $\mathrm{W\,K^{-1}}$), the conductive thermal resistance is calculated as a plate resistance.

$$R_{cond,t} = \frac{\delta_t}{A\alpha} \tag{4.48}$$

In Equation 4.49, the heat transfer area is calculated through the perimeter of the tubes multiplied with the tube's length ($A = L \cdot P$). The convective thermal resistance from the tubes to the air is calculated through the air convection coefficient h_a, the overall surface area of the fins and the tubes A_0 and the overall surface efficiency of the fins η_0 [218].

$$R_{conv,ta} = \frac{1}{eta_0 A_0 h_a} \tag{4.49}$$

The convection heat transfer coefficient representing the air contact can be expressed by an empirical approach depending on the radiator geometry and the fin louver characteristic which can be found in [218], see

Equation 4.50. The required Colburn-Chilton factor j is described by the Colburn Chilton j-factor analogy [219, 220].

$$h_a = \frac{c_{p,a}\rho_a \bar{v}_a}{Pr^{\frac{2}{3}}} \tag{4.50}$$

The refrigerant chiller is usually neglected in presented TMS models [184, 194]. While Tao neglect the development of a model completely, Lopez-Sanz et al. considere the chiller through the electrical power consumption by the coefficient of performance (COP). Both studies of [184] and [194] analysed the performance of a TMS. The chiller was controlled by running in an ON/OFF-matter while running at full performance if the temperature is underneath a certain threshold and working in idle if the temperature is above a certain threshold. Nevertheless, at this point it shall be mentioned that lumped parameter models of refrigerant loops are available in literature: Wang and Chua develope a lumped parameter model for a water adsorption chiller. It models the cooling capabilities of the chiller effectively and enables detailed information about the chiller. Lei and Zaheeruddin conduct a detailed analysis of a water-chiller refrigeration system in [222]. Dynamic models of all components were developed and the output and transient response of the system were analysed. Lei revealed a two-time-scale property of the system due to the fast response of the mass flow rate and the pressure as well as a slow response to the thermal characteristics. A detailed simulation of the chiller is not necessary. A refrigerant loop was built up using MATLAB® Simulink®. The performance of the chiller is modelled using a heat dissipation capability and a lag element for considering the delay of the chiller. The active heater was modelled using a simple energy conservation formula whereby the energy flux into the active heater and out of the heater is defined by the product of mass flow rate, heat coefficient and temperature.

$$\Psi_{out} = \Psi_{in} + P_{heater} \tag{4.51}$$

The outlet temperature is calculated through equation 4.52

$$T_{out} = \frac{\dot{m}c_p T_{in} + P_{heater}}{dotmc_p} \tag{4.52}$$

4.3.4. VEHICLE INTERIOR

The vehicle interior is modelled using a lumped capacitance for the temperature of the air. Heat enters the vehicle through the ventilation and through radiation from the sun. Heat exits through the air flaps in the back

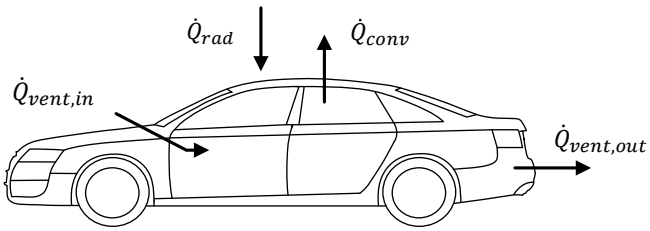

Figure 4.9: Heat flows for the vehicle interior

of the vehicle and through convection at the vehicle's roof. A schematic illustration of the heat flows is given in Figure 4.9. Due to the greenhouse effect, the radiation exiting the vehicle can be neglected. The air entering the vehicle through the ventilation, streams through a heat exchanger, which controls the air temperature to meet the demands of the driver. The air inside the vehicle is considered ideally mixed. The heat flow that streams out of the vehicle can be expressed as follows, the air is considered incompressible ($\dot{m}_{\text{out}} = \dot{m}_{\text{in}}$) . Due to the low pressure loss in the back of the vehicle, the assumption is valid [193]. Equation 4.53 gives the differential equation describing the vehicle interior air temperature.

$$V_{veh}\rho_{air}c_{p,air}\frac{dT_{int}}{dt} = \dot{Q}_{vent,in} + \dot{Q}_{rad} - \dot{Q}_{conv} - \dot{Q}_{vent,out} \tag{4.53}$$

The temperature of the air entering the interior heat exchanger depends on the circulation mode M_{Circ}. If the mode is circulation, the inlet temperature is equal to the temperature of the internal air T_{int}, if exterior mode is active the inflow temperature is ambient temperature T_{amb}. The heat flow exiting through the ventilation ($\dot{Q}_{vent,in}$) is proportional to the temperature of the vehicle, see Equation 4.55.

$$\dot{Q}_{vent,out} = \dot{m}_{out}C_{p,a}T_{int} \tag{4.54}$$

The heat flow entering the vehicle through the ventilation ($Q_{vent,in}$) depends on the heat exchange of the counter-flow heat exchanger and the position of the air flaps $p_{a,fl}$, which control the air flux entering the heat exchanger. By considering the fluid mixer described in 4.3.1, the heat flow entering the vehicle is described as follows:

$$\begin{aligned}\dot{Q}_{vent,in} = p_{a,fl}\dot{m}_{in}C_{p,a}T_{int} + \dot{Q}_{HX}\left(T_{HX,in}\dot{m}p\right) \\ + \dot{m}_{in}\left(1-p\right)C_{p,a}T_{HX,in}\end{aligned} \tag{4.55}$$

The convective heat transfer to the ambient air ($\dot{Q}_{conv}$) is modelled by three thermal resistances. One for the heat transfer from the interior to the chassis, one for the heat transfer through the chassis and one modelling the transfer to the ambient air. [223] states that the chassis can be considered as an even plate. The thermal resistance of the chassis itself can generally be neglected [224], a general correlation is given by [225]. It is clearly visible that the change of the convective heat transfer coefficient related to the vehicle speed is relatively small. The strongest impact has the mass flow through the vehicle, by considering SI-units and an interior volume of $2.5\,\mathrm{m}^3$, Equation 4.56 describes the presented correlation.

$$kA = \left(0.063\nu^{0.7} + 9.36\sqrt{\frac{1}{\rho}}\sqrt{\dot{m}} + 0.606\right) A \tag{4.56}$$

The radiative heat transfer ($\dot{Q}_{rad}$) depends on the day of the year, the time of the day as well as the orientation of the vehicle. The DIN 1946 states that the validation for vehicles shall be done at a vertical radiation of $1000\,\mathrm{W\,m^{-2}}$ [226]. To calculate the intensity, the elevation of the sun is needed which is calculated through the declination δ, as well as the geographic latitude ϕ and the position of the sun ω [193]. The declination and sum position can be determined in accordance to [193]. The power of the sun has been determined by the world organization of meteorology in 1982 to be $1367\,\mathrm{W\,m^2}$ [227]. In the modelling process, the orientation of the vehicle is neglected due to the number of windows and the orientation of the windows. The heat enters the vehicle through the windows. Therefore, the radiation is considered to enter vertically and the radiative heat is calculated through the orientation of the windows. Exemplary, geometric data and the window orientation for a Mercedes C-Class can be found in [193]. Equation 4.57 summarises the heat entering the vehicle by radiation.

$$\dot{Q}_{rad} = 1367 \cdot A_{hor} \cdot \sin(\gamma) \tag{4.57}$$

4.4. Management and Control

Due to the novelty of the TMS described, it is apparent that no control approach was so far described for this particular system design. Lopez-Sanz et al. present a non-linear MPC method to control the cooling loop of a PHEV. Lopez-Sanz et al. use lookup tables to model most of the components. The component's temperature was modelled using an ideally mixed fluid tank, therefore, it did not account for conductive thermal resistances or the dependency of the convective thermal resistance, which depends

on the fluid flow rate. In the presented approach, a direct multiple shooting method to solve the optimisation algorithm was used. The real time implementation of the control is described in [228]. A MPC implementation for the cabin heat in hybrid vehicles is described in [229]. Esen et al. use the exhaust heat of the engine to heat up the vehicle interior by considering the required state of charge of the battery defined by the EMS. Masoudi and Azad describe a non-linear MPC method applied to a PHEV. The investigated TMS consists of an air-cooled BAT, which uses the passenger compartment temperature. The non-linear controller calculates the optimal air velocity needed to cool down the cells. In another study Masoudi et al. apply DP to control a BAT TMS in an EV. Han et al. develop a model reference adaptive controller for an automotive FC to address uncertainties in the system. The resulting controller has a greater robustness compared to conventional feedback controllers. [232] showed that the controller has improved the performance with respect to speed and deviation compared to a nominal feedback controllers.

The dissipated heat of the components is proportional to the component's and the fluids temperature difference and also depends on the mass flow rate. The heat dissipated by the radiator depends on the mass flow rate, but also on the velocity of the air flowing into the radiator. The heat transfer in the heat exchangers can be described by an exponential function of the mass flow rates and the temperatures of the fluids. Due to the non-linearities in the model equations, a non-linear control approach is required. Since the non-linearity stretches over the whole operation range, a high number of linear controller and also an interpolation between them would be required. The knowledge about the system allows to define operation states, which are regulated with individual controllers. Thus, a state machine, which includes subordinated controllers to control the actuators of the system, is defined. The pumps are controlled through subcontrollers as well as the chiller. Since no real hardware was available, the discussed control approach was implemented and tested based on the introduced physical model of the TMS. Thus specific operation points, flow rates and state dependent set points are assumed based on the model and not on specific components and can be considered as a phenomenological discussion. An implementation on a real TMS would need exact parameter setting.

4.4.1. Operation States

From the operation of the vehicle and the exterior temperature point of view, different states of the control can be identified. For the BAT, a

temperature difference of about $5\,\mathrm{K}$ between the optimal BAT temperature and the ambient temperature is necessary to dissipate the losses. At nominal operation, a temperature difference of about $6\,\mathrm{K}$ is required to dissipate the nominal waste heat. If this temperature difference is not possible, the chiller is required to reduce the temperature of the coolant to nominal conditions. If the temperature difference is less than $3\,\mathrm{K}$, the radiator shall not be connected to the coolant. Therefore, the following states for the BAT controller can be identified:

- Turn-off: If the BAT temperature is idle and the BAT is turned off, the cooling circuit is turned off.
- Cell warm-up: If the temperature of the coolant and the one of the BAT is less than $20\,^{\circ}\mathrm{C}$. The BAT and the coolant warm-up to nominal operating temperature. The radiator is disconnected from the cooling circuit, a minimum fluid flow rate ensures that the coolant warms up and the BAT's temperature is kept stable. This is required because the interior temperature of the BAT cells cannot be measured.
- Radiator cooling: The exterior temperature is equal or below $20\,^{\circ}\mathrm{C}$. The BAT is cooled solely by the radiator. The radiator valve acts like a thermostat and is controlled through the temperature of the coolant.
- Chiller cooling: The BAT is cooled mainly by the chiller. If the exterior temperature is greater than $23\,^{\circ}\mathrm{C}$, the radiator is completely disconnected from the cooling circuit. If the temperature is between $20\,^{\circ}\mathrm{C}$, and $23\,^{\circ}\mathrm{C}$, the chiller is switched on and controls the temperature of the cooling loop. Nevertheless, also some amount of the waste heat also is dissipated by the radiator.

The FC state machine is determined by three basic states: warm-up, standard operation and turn-off

- FC warm-up: In the warm-up phase, the FC is not in operation. Warm-up can happen through utilising the waste heat from the power electronics or by active heating
- FC cooling: In the standard operation, the FC dissipates heat through the radiator and partly through the interior heat exchanger.
- Turn off: If the FC is idle or at operation temperature, the cooling loop is turned off.

The interior control is defined by three states: Interior cooling (interior is cooled down through the chiller), Ambient Air (interior is cooled through the ambient air by ventilation) and Interior Heating (passenger compartment is warmed up through the FC's waste heat).

- Interior cooling: Interior heat is extracted through the chiller. The FCs coolant is fully bypassed. The pump of the chiller is active and pumps the fluid through the interior heat exchanger. Since the BAT is also cooled through this chiller, the pump of the chiller-cooling loop has to be powered at all times. The volumetric flow rate of the air is determined by the driver, the temperature of the air is therefore controlled through the amount of air flowing through the heat exchanger by the air flaps.

- Ambient air: No interior heat extracted through the chiller. The ambient air is bypassed from the heat exchanger. Depending on the circulation mode, heat is removed through ventilation

- If the desired interior temperature is higher than the actual temperature, the interior-heat exchanger is connected through the FC cooling circuit. The cooling unit of the FC aims to hold the temperature above $50\,^{\circ}\mathrm{C}$. The valve is controlled through the temperature and the mass flow rate of the FC cooling circuit.

4.4.2. Underlying Controller

In the previous section, the operation states of the vehicle interior, the FC, and the BAT are described. For each of these operation states, individual controllers have to be defined. The BAT control consists of two states. The control mechanisms for these states individually are described. While some of the control modes are trivial, Radiator-cooling and Chiller-cooling involve more complex continuous controllers. If the BAT is idle and its temperature is equal or below the optimal value for more than $30\,\mathrm{s}$, the TMS enters the Turn-Off mode. The BAT pump as well as the radiator fan turn off. Depending on the configuration of the bypass valve, these valves enter the idle mode. If the cell temperature is below the operation point, the cells as well as the fluid in the cooling circuit need to be warmed up. The pump operates with reduced speed, the radiator fan is turned off, and the liquid is fully bypassed from the radiator and the heat exchanger.

The control concept for radiator-cooling consists of a controller for the radiator fan and the coolant pump as well as a controller for the valve

position. As mentioned in Section 4.4, the coolant is fully bypassed from the heat exchanger to the interior; the chiller and the chiller pump are turned off. The BAT temperature is controlled through coolants temperature and flow rate. Since the BAT cells consist of a conductive thermal resistance, the inflow temperature of the fluid should be dynamically adjusted to avoid unnecessary warm-up or cool-down of the cells. Therefore the radiator-cooling concept consists of a PI-controller, which controls the temperature of the cells. This determined set point is passed to a Fuzzy-Mamdami-controller. The Fuzzy controller consists of three membership functions for each of the three different inputs (environmental temperature, vehicle velocity and the dissipated power set point). For the dissipated power and the vehicle velocity, Gaussian membership functions are used and for the environmental temperature, a trapezoidal membership function is used. The reason is that the behaviour of the valve, which is the main actuator to be controlled with regards to the temperature, is almost linear. With membership functions defined for the valve, the set point for the radiator fan and the mass flow are controlled by a set of fuzzy rules. A PI controller is used to control the mass flow rate of the pump and another PI controller would be used to control the speed of the fan. Figure 4.10 a) depicts exemplary the result of heat up process under a random BAT power loss profile. In the test scenario a representative power profile to emulate the power loss of the BAT is applied to the BAT model. The described control approach operates the BAT cooling loop to generate the depicted temperature profile. Over the complete cycle, all three operation modes occur. The depicted BAT temperature curve shows the transition from the state turn-off, over warm-up to the state radiator cooling.

The state chiller-cooling is controlled through a combination of two different controllers. A PI-controller with an anti-windup method of back stepping (back stepping value of 1) is used to control the mass flow rate through the BAT. A P-controller is used to control the valve position of the heat exchanger. The control performance of this state is depicted in Figure 4.10 b). The depicted results show that the temperature varies in the range of $0.2\,\mathrm{K}$ only. The chiller cools down the BAT from the environmental temperature of $30\,^{\circ}\mathrm{C}$ to the target temperature sufficiently fast within $30\,\mathrm{s}$. Even though the chiller cooling loop has a great temperature difference, the coolant temperature gain is limited to $3\,\mathrm{K}$.

The FC cooling state is controlled through a P-controller and an intrusion of the disturbance. Through this, the mass flow rate of the FC and the temperature of the cooling loop are controlled. A negative offset for the desired coolant temperature is therefore passed to the underlying

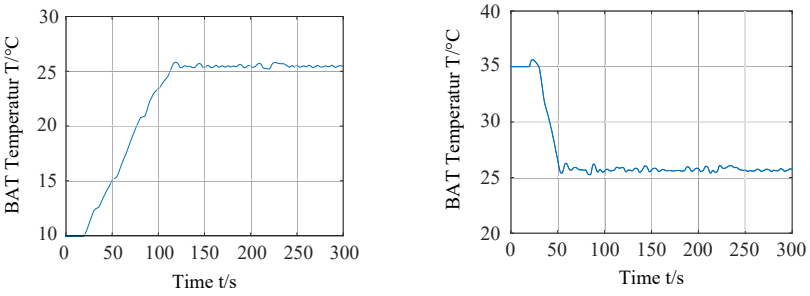

(a) (b)

Figure 4.10: (a) BAT warm up and radiator cooling (b) Chiller based cooling BAT temperature

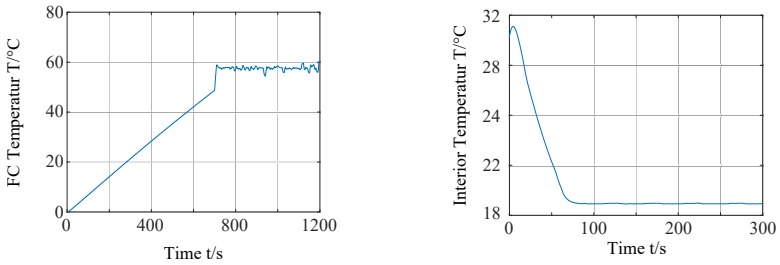

(a) (b)

Figure 4.11: (a) BAT and FC warm up and cooling (b) Interior cooling performance based on interior temperature

controller. Figure 4.11 a) visualises the control performance of this state controller. It is evident that the temperature gain of the FC is limited to 2 K. The figure visualises the states active warm-up as well as FC cooling. The most significant actuator of the interior temperature control is the air flap that controls the amount of air passed through the interior heat exchanger. For the control structure of the interior heating, an underlying controller regulates the liquid, which passes through the heat exchanger to meet the reference mass flow. The pump controls the flow rate to be the same value. The interior is cooled down with a PI-controller to regulate the position of the interior bypass valve. Figure 4.11 b) depicts the control performance of this state. The simulation started with an interior temperature of 30 °C. Due to the radiation from the sun and the the compressor

lag, the interior temperature at first rises to a value of about $31\,^{\circ}\mathrm{C}$. After that, the air temperature is constantly reduced to the desired temperature of $18\,^{\circ}\mathrm{C}$. The interior air valve position varies due to the fluctuations of the coolant temperature.

4.5. SUMMARY

Because the performance as well as the degradation of the components depend on the operation temperature, the TMS of a FHEV is essential. This chapter discusses the requirements, the design and the control of TMS for a FHEV. Based on the operation conditions of the important components, the features of the TMS are derived. With this results, a system topology which consists of four separate cooling loops is presented. After the topology is specified, the required system parameters are determined and a simulation model developed. This model contains a mathematical description of the fluid and the heat flow in all components. Based on this fundamental mathematical expression, equivalent circuit oriented models of all drivetrain and heat exchange components as well as the vehicle's PC are discussed. Finally, the development of a control scheme that is capable to regulate the fluid temperatures in all components, is described. This control approach is implemented with a hierarchical structure. The superior control is realised with a different state machines for each cooling, which defines different operation states related to the environmental temperature and the component's operation state. The underlying control is implemented based on classic PI controllers and a Fuzzy-Mandami set. The central task of the underlying controller is to control the different actuators to follow the reference determined by the superior state machine. In summary can be stated that the developed TMS is capable to ensure optimal operation temperatures for all relevant components. The approach was implemented and evaluated based on the presented simulation model.

5

ENERGY MANAGEMENT STRATEGIES

The general benefits of a FHEV was discussed in chapter 2, in this chapter standard control schemes are going to be evaluated. The use of three energy storages increases the number of degrees of freedom, but leads to a more complex control problem. The EMS has to optimise the drive train's global efficiency under maximum component's lifetime. Obviously, the control parameters change with regards to the power demand, the SoC of the BAT and the SC's voltage. Thus, the EMS defines the FHEV operational characteristics. While SCs are very robust against various operation conditions, FCs and BATs requirements are more complex. FCs are vulnerable to high dynamic load variations as well as operations near ideal [7, 233], see 2.2.1. BATs degradation depends on the number of cycles in relation to the DoD as well as under high currents [7, 83, 95]. An EMS has to minimise the overall operation costs of the trip, thus it should not only minimise the fuel consumption but also the degradation effects.

The task to design a hybrid power system is characterised by two fundamental challenges. The first is to determine the required power capabilities of the individual sources; the second is to implement an efficient EMS. A review of hybridisation topologies has shown that a combination of a FC, a BAT, and a SC improves the lifetime of the components and optimises the fuel consumption, see Chapter 2.2.3. A reasonable decision for a specific EMS strategy can only be made based on a fundamental understanding of all suitable approaches. With the underlying objective to discuss these options, this chapter focuses on the concepts as well as the

design and implementation of state of the art EMS approaches. To analyse the performance of these approaches, the most discussed one were implemented and evaluated against the derived test cases which are discussed in Chapter 3.

Due to the similarities of the control of FHEV and HEV, several control strategies applied to HEV can also be applied to FHEV. The presented strategies can be divided into heuristic strategies and optimisation oriented ones [136, 234]. Heuristic EMS built upon intuitive rules and correlations which typically involve various vehicle parameter. Rules define an instant power split decision between different power sources. Rules are typically defined based on heuristics, intuition, human expertise, as well as mathematical models [235]. [235] classifies rule-based strategies into deterministic and Fuzzy rule-based methods. Classic heuristic EMS approaches are PI control [236], finite state machines [237], Fuzzy Mandami control [177], or frequency based wavelet transform [146, 238]. Mutual drawback of all heuristic approaches is the required knowledge of the system and of all possible operation states in order to achieve high performance. Additionally, heuristic EMS are not capable to adapt to different operation characteristics or driving situations.

Another dominant group are optimisation-based EMS approaches which can be split into global optimisation strategies and online controller. Non-causal global optimisation approaches require knowledge about the whole process which is usually not the case and thus these are typically used offline as benchmark. In most cases, global optimisation is achieved through DP or linear programming [235]. DP is characterised by a recursive solution of the optimisation problem which is processed backward in time. The fundamental concept is to split the problem into several sub-optimisation problems which are recursively solved. DP is often considered to require too much processing power in order to be implemented in real time but Back show that a real-time implementation is possible. Other real-time optimal control strategies are decoupling control and robust control.

Causal or real-time optimal control based EMS extensively focus on ECMS [239]. ECMS is derived from the Pontryagin's Minimum Principle and correlates the use of electrical energy stored in the ESE to the fuel consumption in order to support the instant power split decisions [234]. The basic concept of ECMS is to shift the uncertainty about future driving condition to an uncertainty on the optimal value of the equivalence factor μ [136]. In order to guarantee a sufficiently high SoC for the next driving trip, most approaches use a charge sustaining mode, thus the SoCs

are equal at trip start and at the end [239]. In its core idea, ECMS is a reactive EMS that cannot take future predictions into account [240]. Nevertheless, various modifications have been presented such as [241], which shows that an optimal modification of the equivalent factor significantly improves the fuel economy in hilly terrain. Zhang et al. use a chained neural network as well as vehicle-to-vehicle and vehicle-to-infrastructure communication to predict future velocities. With the predicted velocity the equivalent factor can be adapted. The presented results prove that the discusses approach significantly improves the fuel economy as well as the charge sustainability [242]. [234] proposes an adaptive ECMS (A-ECMS) strategy that use a neural network to predict the energy demand of the vehicle and generates a SoC reference strategy. Guzzella and Sciarretta state that adaptive ECMS can be grouped into three different A-ECMS strategies: adaptation based on driving cycle prediction, adaptation based on driving pattern recognition and adaptation based on exclusive SoC feedback [136].

Another optimal EMS is the MPC approach. MPC is a modern control method capable to realise a predictive control of multi-variable processes. It is especially promising due to its ability to control constrained multi-input-multi-output (MIMO) processes as well as linear and nonlinear plants [240]. Selected solutions have been presented in order to achieve MPC on hybrid vehicles. MPC uses numerical methods to solve the optimal control problem over a finite moving horizon. Usually, stability is ensured by the definition of terminal region constraints [243]. MPC solutions for hybrid vehicles have been presented in [240, 243, 244]. A detailed analysis of state of the art of MPC approaches implemented in HEV and FHEV can be found in the next Chapter 6.1.

A comprehensive evaluation of the most common EMS approaches in the context of a More Electric Aircraft is given in [152]. Within this group especially four widely used schemes can be named: the classic PI controller approach [236, 245, 246], a state machine [237, 247, 248], a fuzzy controller [98, 177, 249], and finally the optimisation oriented ECMS approach [150, 241, 250]. In the following chapter, a detailed evaluation of these EMS schemes is outlined. In the beginning a summary of the requirements and tasks of an EMS is given, followed by a discussion of the characteristics and implementation of the four standard control schemes. Subsequently followed by a comparative evaluation of these schemes based on the virtual test bench and the representative test cycles introduced in Chapter 3.

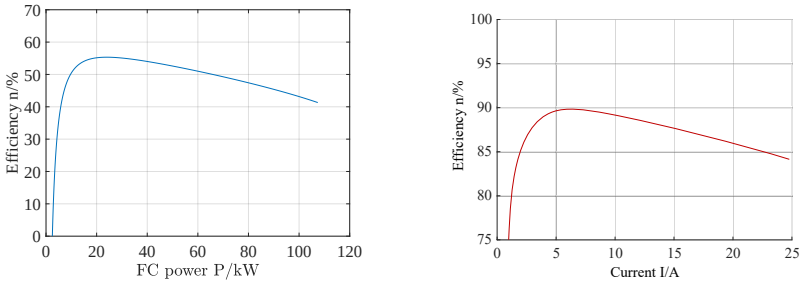

(a) (b)

Figure 5.1: (a) Efficiency characteristic of a 50 kW FC. (b) Typical efficiency characteristic of a 10 W buck converter [15].

5.1. REQUIREMENTS

A central task of an EMS is to provide sufficient power to accelerate the vehicle to reach the demanded velocity. In the proposed system the key role of the EMS is to manage the power distribution between the three energy storage devices (FC, BAT, SC). As discussed in Chapter 2, the BAT and the SC allow to recover regenerative braking energy. The SC is also beneficial to balance the load in order to limit the power dynamics of the FC and the BAT. The additionally degrees of freedom allow operating the different sources in their optimal operation point with high efficiency and minimum degradation. Additional, synergy effects can be used to downsize the FC and the BAT and hence to reduce the total system costs.

The minimisation of the hydrogen consumption is not only important in order to reduce the operational costs, but also to realise longer driving ranges. Figure 5.1 a) depicts the efficiency characteristic of the modelled 50 kW FC. In order to consider an auxiliary power demand, to supply pumps, the compressor, the fans and a humidifier, 5 % of the nominal power is assumed to be required for the auxiliary components. From the depicted characteristics an optimal operation range between 10 kW and 60 kW can be identified. Below the minimum power, the auxiliary demand consumes a significant proportion of the power compared to the useful output. After a maximum efficiency peak of 55 %, the ohmic losses dominates and the efficiency decreases nearly linear with power. At high loads, the limitations in mass transport of the chemical species dominate and the concentration losses become the limiting factor. In this operation range the voltage begins to drop rapidly.

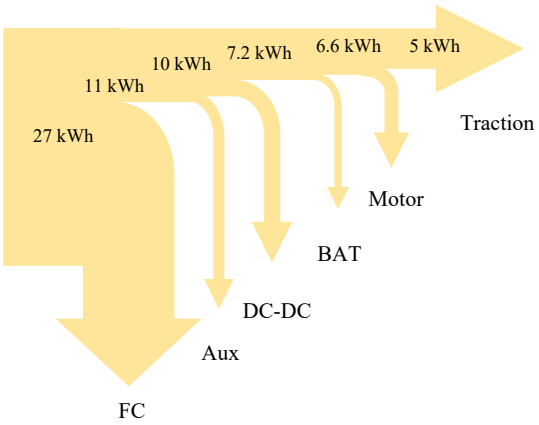

Figure 5.2: Sankey diagram showing losses and useful energy of an experimental FHEV powered by a 1.2 kW FC and a 32 A h BAT [16].

Not only the FC efficiency determines the overall efficiency, but also the characteristics of the other components, especially the one of the DC-DC converter, has a significant impact. The efficiency characteristic of a DC-DC converter is comparable to the one of a FC. An example is depicted in Figure 5.1 b). While at low loads the switching losses prevail, the conduction losses dominate at medium and high load. Thus the DC-DC converter efficiency enhances the characteristics of the FC and confirm the requirement to carefully determine the operation point of the FC. Since the performance of the BAT depends on it's SoC and the motor power demand on the SC voltage, these two state variables have a significant effect on the system performance. For example, if the SoC is to high or the recovering of braking energy would cause the SC voltage to rise above operation limits, the energy will be lost and thus the efficiency reduced. Thus, controlling the SC voltage and the BAT's SoC in order to guarantee complete recuperation of braking energy is important [96]. Figure 5.2 visualises the losses at each stage of an experimental Microcap powered by a FC and a BAT presented by [16]. Even while the overall performance can be enhanced, the diagram clarifies the significance of the individual losses and thus the importance to consider the triggering effects in the EMS.

Besides the focus on the optimal efficiency, minimising degradation of the components is also a central aspect. Since the DC-DC converter and the SC are robust, the operation of the FC and the BAT are in the scope of this objective. A detailed analysis of the effects accelerate or in-

duce the degradation of a FC and a BAT can be found in the sections 2.2.1 and 2.2.2. Negative operation conditions which supports the degradation of FCs are high current transients, frequent start/stops as well as low and high power demands. The analyses of the BAT degradation effects imply that high discharge currents, high and low SoCs as well as the depth of discharge accelerate ageing of a BAT cells. Thus in order to prevent components from enhanced degradation, the EMS has to ensure that these operation conditions are avoided.

In summary can be stated that the EMS shall optimise the hydrogen consumption and operate the individual sources under highest efficiency and minimal degradation in the presence of various constraints due to driveability requirements and component characteristics. The SoC and the SC voltage also needed to be controlled in order to guarantee high recuperation rate. Since different sources may have competitive objectives, the EMS can not only follow the individual objectives but has be capable to reach a global optimum. Exemplary for these competitive objectives is the question whether it is more efficient to operate the FC at highest efficiency despite if this causes the BAT to be cycled more than necessary, even if this includes the consequences of higher losses and higher degradation? Another problem arises win the case a vehicle is driving uphill and the BAT SoC decreases. Is it then necessary to increase the FC output power to be capable to charge the BAT or is waiting for an increased recuperation after the peak is crossed and the vehicles drives downhill the better option? The central task of the EMS is to answer these kinds of questions and to make decisions in order to operate the FHEV in the best possible way.

5.2. PI Control

A classic control approach is a PI controller. A PI controller manipulates an actuator reference based on a proportional integral element and the error between the reference and the controlled variable. Thounthong et al. use a PI controller in a FC SC hybrid system to control the SC's voltage to form a constant DC link. It's basic principle is to use the fastest energy source of the system to supply the energy required to maintain the DC link voltage [246]. Thus in the proposed system, the FC and the BAT are the actuator used to maintain the SC's voltage.

The design of the controller requires detailed analysis of the BAT's and the SC's system dynamics. The approach presented in [246] shows a significant drawback, the constrained charge and discharge current of the BAT is not considered. This causes two problems. The first problem

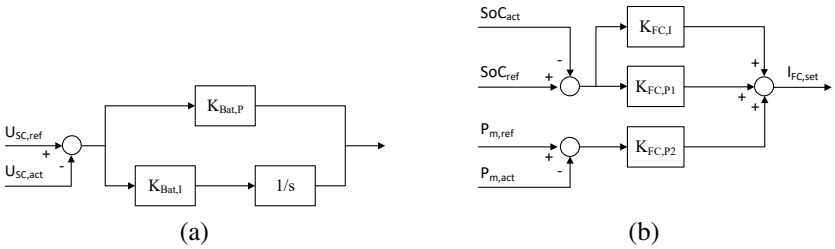

Figure 5.3: (a) Schematic concept of the implemented BAT controller. (b) Schematic concept of the implemented FC controller.

is the wind up of the controller's integrator which can induce an uncontrollable controller behaviour. The second is characterised by the fact that the power capability of the BAT is significantly lower than the maximum demand of the electric drive, in various cases the SC voltage can not be controlled to be in the operation limits because the power capacity of the BAT is exceeded. In order to overcome this problem and to evaluate a comparable PI approach a new PI controller based EMS was developed.

The classic PI control approach is a hierarchical scheme, the BAT regulates the SC voltage and the FC controls the BAT's SoC. A PI controller determines the BAT's current reference related to the SC voltage error, a second controller regulates the FC output current related to the deviation of the SoC. Since the power capacity of a FHEV's supportive BAT is limited, the usage of the BAT to solely control the SC voltage is not sufficient. Thus, a third controller which ensures that the FC current follows the load demand but also guarantees that the SC voltage is within the operational limit is required. In contrast, the SoC is indirectly be controlled. When the SoC is low, the output of the second FC controller rises. The surplus of the sum of the FC controller that follows the load and the rising output of the second controller cause the SC voltage to increase. In order to control the SC voltage the BAT controller generates a negative BAT current which results in an increasing SoC. Vice versa, if the SoC is above the set point, the output of the controller is negative and the FC output current is reduced. In summary, if the the FC current is manipulated, the SC voltage varies and the BAT adapts. The implemented PI controller approach is depicted in Figure 5.3.

The plant controlled by the BAT controller is formed by the SC, the electric drive, and the vehicle dynamics which can be considered as disturbance, see Figure 3.9 in Chapter 3.3. The BAT is the controlled actu-

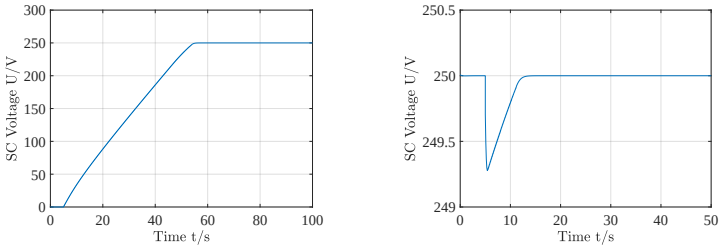

(a) (b)

Figure 5.4: (a) Simulated SC voltage response to a 250 V input step. (b) A voltage response to a simulated disturbance step of 70 A.

ator. Since the capacitive behaviour of the SC and the BAT dominate, both can clearly be classified as integrators. Due to this integrator characteristic, a robust system can be realised either if only a proportional controller or if a PI controller is used. In the case of a P controller the maximum phase results from the plant's phase, which is equivalent to 90°. Thus, the minimum phase reserve is 90° and the system is always stable. A second option is to implement a controller that follows a PI characteristic. In this case the integral part has to be determined carefully in order to ensure a near zero controller phase at the system's gain crossover frequency. If the controller is implemented in that way, the PI controlled system also has a phase reserve near to 90° and thus is stable. [251, 252] To guarantee zero steady state error a PI controller was chosen. Since the BAT's state of health (SoH) depends on the current dynamics the P and I parameter of the PI controller were determined so that a generated BAT's current step for a reference motor current step (70 A) do not exceed 30 % of the BAT's maximum current. The simulated voltage response of a input (a) and a disturbance step (b) are depicted in Figure 5.4. As input the reference SC voltage equal to 250 V and for the disturbance step a motor current of 70 A was applied.

The parameter of the PI controller regulating the BAT's SoC can be determined similar to the one of the SC voltage controller. Figure 5.5 depicts the frequency response of the plant formed by the BAT. Since the FC shall react slower than the BAT, a slower FC controller is required. Thus, the gain crossover frequency of the correct system was defined to be $0.01\,\mathrm{rad\,s^{-1}}$. In order to realise the selected crossover frequency, the controller needs to amplify the plant by factor of 60 dB. The required integral parameter can be determined with the requirement of a near zero

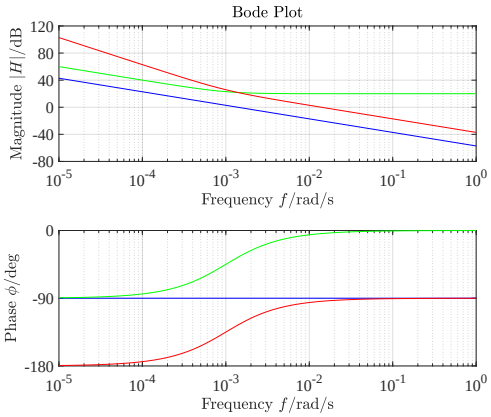

Figure 5.5: Frequency response of the plant (blue), the PI controller (red) and the corrected system (green)

controller phase at the targeted gain crossover frequency. The frequency response of the designed controller and the response of the resulting corrected system are depicted in Figure 5.5. It can be seen that the targeted gain crossover frequency of $0.01\,\mathrm{rad\,s^{-1}}$ was achieved. Due to the near zero controller phase at the gain crossover frequency, the corrected system shows a sufficient phase margin of $90°$ and thus the system is stable. Due to inherent current limits, both actuators, the FC as well as the BAT, can saturate. In order to prevent integrator wind-up, for both controller back calculation scaled by the corresponding proportion factor was implemented. The third controller guarantees a stable SC voltage even when the BAT controller saturates. In this case, the steady state error criterion is not significant, therefore a single P controller is sufficient. A factor of 0.2 shows good results. The trade off between optimal V_{SC} trajectory and minimum FC current dynamics determines the optimal proportional factor. In summary can be stated that the PI feedback control based EMS is capable to manage the three sources and operate the system state variables to be in the operation limits and close to the reference values. However, because the SoC and the SC voltage are controlled to constant set-points rather than based on variables such as the kinetic energy or the vehicles velocity, it is anticipated that the overall system efficiency especially with regards to regenerative breaking is reduced. Since the FC follows the load and the BAT follows the SC voltage deviation, it's operation point is not actively managed. Moreover, there is neither prove nor guarantee that the system efficiency is near optimal.

5.3. State Machine

The development of a state machine based EMS requires extensive system knowledge. All possible states as well as the component's characteristic need to be considered. Nevertheless, the definition of different states allows to adapt the EMS to different operation scenarios and DCs. Based on adaptable rules more complex operation strategies are possible. Garcia et al. describe a state machine based EMS to control FC-BAT HES based on eight different states with the goal to determine the reference power for FC and BAT and the power to be dissipated in a braking resistor. An overall objective is to limit continuous changes in the FC reference power. The FC power is either at minimum or maximum power or follows the load, the state transitions depend on the BAT' SoC [237]. Jin et al. use an EMS based on five different operation modes to control the power flow in a hybrid FC power system. Here the FC power reference depends on the BAT voltage, whereas the BAT supplies the load unless the BAT voltage is below the minimum voltage. Schiffer et al. present a state machine defined by four different states to control the power flow in FC-SC powered vehicle. Depending on the inertial states different operation modes can be realised. For example when the vehicle is in standstill mode, Schiffer et al. state that the BAT could be charged at constant power, at FC' maximum power or maximum efficiency or at maximum power within the acceptable efficiency range. A central finding of the presented work is that the optimal EMS uses the SC during braking and acceleration as much as possible. In contrast to charge the SC is best during constant speed or standstill at the highest current within the acceptable efficiency range of the FC [253]. Xiong et al. present a mode based EMS to control a series-parallel hybrid electric transit bus. Here the different modes are defined with regards to the component operation modes, which depend on the SoC and the driver's torque request. Since neither a state machine based approach to control a FHEV with FC, BAT and SC is presented nor existent EMS approaches can be adapted a new approach was developed.

The implemented state machine was developed with regards to the requirements summarised in section 5.1. The BAT is controlled by the same PI controller presented in the previous section 5.2. In this case the SoC is indirectly controlled by the FC output power. Since the BAT maximum power is not sufficient to guarantee a stable SC voltage the state machine not only determines the FC reference power with regards to the SoC of the BAT, but also considers the SC voltage. The FC reference power is varied between predefined values or follows the load demand. A detailed

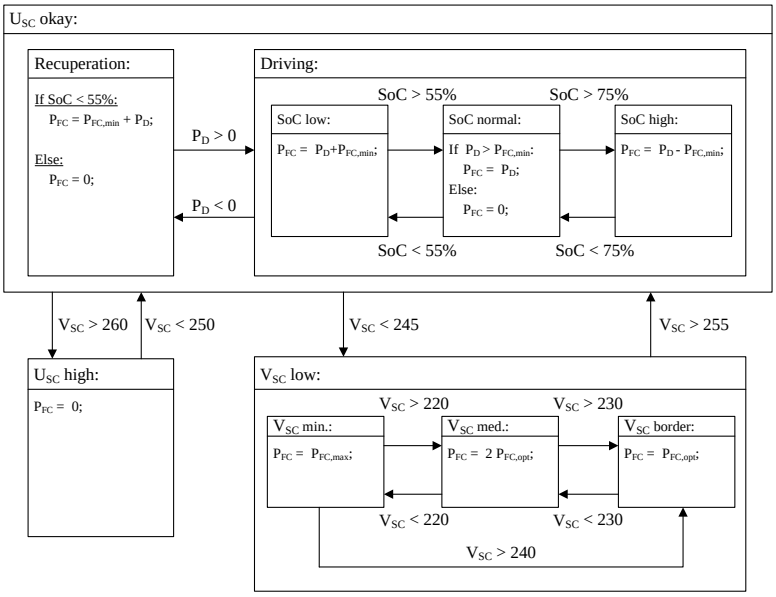

Figure 5.6: Schematic representation of the implemented state machine.

schematic representation is depicted in Figure 5.6. The control of the SC voltage has the highest priority, thus the three basic states are the defined: V_{SC} okay, $_{SC}$ low and V_{SC} high. While in the state V_{SC} high the FC is turned off, the state V_{SC} low is subdivided in three sub-states with regards to the voltage of the SC:

- V_{SC} min.: The SC voltage has reached a critical value ($U_{SC} \leq 220\,V$), the FC reference power is set to the FC's maximum output power $P_{FC,max}$.
- V_{SC} med.: The SC voltage is not critical low, but in order to guarantee a fast recovery of the voltage the FC reference power is set to twice of the optimal output power $P_{FC,opt}$.
- V_{SC} border: The SC voltage is slight below the normal operation voltage range, thus the FC reference power can be set to the optimal value $P_{FC,opt}$. This state can be entered from the states V_{SC} okay and V_{SC} medium. A third transition from V_{SC} minimum was implemented in order to prevent fast SC charging in the case of an abrupt load drop.

As long as the SC voltage is in the predefined operation range ($245\,\mathrm{V} \leq \mathrm{V_{SC}} \leq 255\,\mathrm{V}$), normal operation is active and two states distinguish between vehicle driving or recuperating. These two states are again divided in sub-states which make distinctions with regards to the BAT's SoC. In case of recuperation, the FC reference is either set to zero or to the difference of recuperated power and maximum power. The second case enables maximum BAT charging if the SoC falls below $55\,\%$. The sub-state driving is subdivided in three different states:

- SoC low: If the SoC falls below $55\,\%$, the state SoC low is entered. In order to guarantee a maximum charging, the FC power reference is set to the sum of load and maximum BAT power.
- SoC normal: When the BAT's SoC is between $55\,\%$ and $75\,\%$ the state SoC normal is active. Since neither charging nor discharging is required the FC reference follows the load demand.
- SoC high: If the SoC rises above $75\,\%$ SoC high is activated. To enable enhanced BAT discharging the FC reference follows the load demand reduced by the maximum BAT discharge power, corresponding to $\mathrm{P_{FC,min}}$.

Because the FC reference is generated by a continuous controller the generated current trajectory is not steady but determined by frequent steps between the load, the maximum or the optimal FC power. Therefore, in some cases the FC operates at constant power with changing constant power levels and in others it adapts to the load demand. Even while an optimal constant FC power level can not be established, operation at low power and high power can be avoided. Thus degradation caused by low and high FC power condition is prevented. Since the BAT control is equal to the discussed PI control, see section 5.2, no specific benefits for the BAT can be named for the state machine based EMS.

5.4. Fuzzy Control

The task to control a HES taking care of the different constraints can be implemented based on fuzzy rules that supports a classic controller. This approach leads to a fuzzy system which is more likely a decision system based on fuzzy rules than a fuzzy controller [255]. An online EMS based on a fuzzy interference system optimised by means of a genetic algorithm is presented by Caux et al.. A fuzzy controller which indcludes a set of five different rules as well as the BAT current and it's SoC is used by

Lee et al. to determine a reference current for a FC applied in a BAT-FC FHEV. Zandi et al. present an EMS approach that uses flatness control and fuzzy logic control to control the power flow in a FHEV based on a FC, a BAT and a SC. Zandi et al. use the fuzzy logic controller to determine an optimal power split between SC and BAT based on the load as well as the SC and BAT voltage. The FC output is determined by the flatness control technique. [98] Instead of the use of a fuzzy logic controller to directly determine the FC and BAT power reference, Chen et al. use a fuzzy logic controller to determine the parameter of an adaptive controller which regulates the power flow in a FC BAT HES [177]. In contrast, [258] and [259] determine the BAT and the FC power reference directly based on a fuzzy logic controller. [259] used the SC voltage and the BAT SoC and the power demand as inputs to control the power split in a FC hybrid bus. Hemi et al. implement a less complex approach, based on the power demand and BAT's SoC a fuzzy logic controller determines the power reference of a FC [258].

Since an EMS solely based on a fuzzy logic controller shall be evaluated against other standard EMS approaches a new approach was implemented. Similar to Gao et al. the input of the controller are the power demand (P_D), the SoC and the SC voltage. The membership functions to transfer the SC voltage and the SoC were derived based on the operation borders. For both inputs, three different regions have been defined: low, okay and high. These regions were implemented with three sharp trapezoidal membership functions per input variable.

Because the SC voltage has a significant impact on the performance of the electric drive and on the currents and thus on the operation point of the FC and the BAT, a small region defines an optimal V_{SC}. Therefore, an optimal SC voltage is between $245\,\mathrm{V}$ and $255\,\mathrm{V}$. From zero to $240\,\mathrm{V}$ with a sharp linear border to $245\,\mathrm{V}$ V_{SC} is low, vice versa high voltage region spans from $255\,\mathrm{V}$ to the maximum voltage. The influence of the SoC is not as strong as the one of the SC voltage. Nevertheless, the depth of discharge as well as the number of cycles have a significant impact on the BAT SoH. Thus, the membership functions are developed based on the trade off between low depth of discharge and low number of cycles. Here a broad range of a sufficient SoC between $55\,\%$ and $65\,\%$ was configured.

The detailed membership functions are depicted in Figure 5.7 a) and b). The load demand was transferred based on ten triangular membership functions and one trapezoidal membership function that indicates the negative demand. The ten membership functions which corresponds to a positive power demand, are equally distributed across the complete range

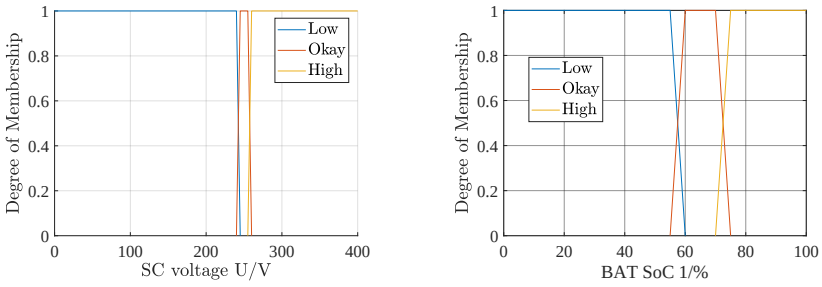

(a) (b)

Figure 5.7: (a) Input fuzzification membership functions of the SC voltage. (b) Input fuzzification membership functions of the BAT SoC.

of the electric drive. Thus, the centres of the specific functions are located equally distributed at 10 kW, 20 kW, etc. up to the maximum power demand of 110 kW.

The output values determined by the fuzzy interference system are the FC and the BAT reference currents. Figure 5.8 a) depicts the membership functions of the FC reference current. Figure 5.8 b) illustrates the one of the BAT reference current. To guarantee a homogeneous operation of the FC and the BAT, triangular membership functions are distributed over the complete current range. Since the power range of the FC is significantly larger than the one of the BAT, eleven membership functions cover the FC current range and seven the BAT's. A sharp triangular membership function realises the turn-off of the FC. Since the BAT can be positive or negative, a comparable sharp function was not required, instead a symmetric triangular function with zero current as centre was used.

A Fuzzy controller derives the outputs based on fuzzified inputs and a set of rules. The rules combine the inputs in order to determine the outputs by emulating the knowledge of an expert which operates the system. Thus, to derive a set of rules to control a FHEV power system is a challenging task and requires excessive knowledge about the system. The first step of the design is to define the extremal operation conditions and to derive sufficient rules to transfer the system to normal operation region. In case of the examined HES the V_{SC} has the highest priority, which must be in the area of safe operation. Thus when V_{SC} is low, P_{FC} is set to the maximum. Vice versa, if V_{SC} is high, P_{FC} is set to zero. Similar rules used to control the SoC were defined. In the case the SoC is low, I_{BAT} is set to the maximum charge current. Accordingly, when the SoC is high max-

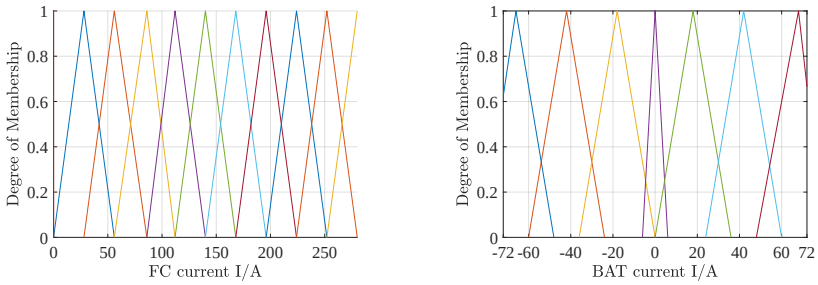

(a) (b)

Figure 5.8: (a) SC voltage membership functions. (b) SoC membership functions.

imum, discharge is enabled. In normal operation mode, the load demand determines the operation of the FC and of the BAT. If the demand (P_D) is negative and V_{SC} is normal, the BAT current is set to medium charging. Because the nominal FC power is significantly higher than the one of the BAT, a positive load demand and the resulting FC output current is granulated in more detail. Thus, the fine resolved load demand can be used to determine the FC output current. Minimum SC voltage variation can be ensured by the concept that a low load demand corresponds to a low FC output current, and a high demand to a high current. Is the load demand low and the SoC not low, the BAT is used to supply the load and the FC is turned off. This mode prevents an inefficient and high degradation inducing operation of the FC.

5.5. Adaptive Equivalent Consumption Minimisation Strategy

ECMS is an online optimal control approach, thus the EMS optimises the operation of the HES online. In order to do that, a non-linear constraint minimisation problem defined by a specific cost function has to be instantaneously solved. The cost function is defined by the sum of the actual fuel (hydrogen) cost and an equivalent fuel consumption related to the energy flow from the BAT. The approach to include the BAT usage by a fuel equivalent is derived from the assumption that the variation of the SoC will be compensated by the FC in the future. A charge sustaining strategy is premised. While non-causal EMS schemes like DP or Pontryagin's minimum principle satisfy global optimality, causal ones,

like ECMS, are not capable to reach a global optimal solution. Nevertheless, ECMS in particular is often considered as a practical solution because when the equivalence factor is online adapted, its near optimality has been shown by simulation or by analogy with Pontryagin's minimum principle [241, 260, 261].

Thus, a central aspect of an online near optimal control approach is the uncertainty about future disturbance behaviour. In an ECMS approach this uncertainty about future driving conditions is transferred to an uncertainty on the optimal value of the equivalence factor. The benefit is that only one parameter has to be predicted. In general there are three different approaches to estimate the trajectory of the equivalence factor online, Guzzella and Sciarretta classify these with regards to the information used: past driving conditions, past and present driving conditions and past, present and future driving conditions. If only past driving conditions are considered, the equivalence factor is determined in advance based on representative driving patterns [262, 263]. When the present driving condition is also taken into account, the equivalence factor can be evaluated online either based on the current driving situation or based on SoC [264, 265]. Guzzella and Sciarretta state that as soon as constraints on the SoC are considered non-predictive strategies perform poorly [136]. This is essentially true for a BAT with a small capacity compared to the amount of recuperated energy. Different approaches have been presented, a standard technique is to consider the GPS altitude profile of the road that the vehicle intends to follow [266]. De Jager et al. include the actual vehicle's kinetic energy in order to guarantee that the BAT can always recuperate energy.

Han et al. name two standard types of predictive ECMS approaches, these are either feed-forward or feedback mechanism. In feed-forward adapted approaches the equivalence factor is directly derived from GPS or geographic information system data. In feedback adaptation schemes, the SoC is controlled to follow a reference trajectory derived either from location data [268] or determined a priori [260]. To help maximise the recuperated breaking energy, Manzie et al. also consider the potential energy that results from driving in hilly terrain when the SoC reference trajectory is synthesised. Since the calculation of the reference trajectory is limited by the disturbance propagation delay, also the SoC reference tracked to determine an optimal equivalence factor is limited. To overcome this limitation, Han et al. present a causal predictive strategy to adapt the equivalence factor based on a non-causal strategy extracted from DP results.

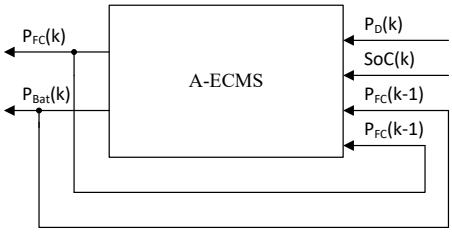

Figure 5.9: Schematic illustration of the implemented ECMS EMS controller with input and outputs.

In this work standard ECMS approaches shall be compared with other non-causal EMS schemes, therefore an adaptive ECMS based on the work of Torreglosa et al. is implemented and evaluated on the virtual test bench. In this approach the adaptation of the equivalence factor was done based on a linear trajectory based on the SoC in the border of low and high SoC (SoC_L, SoC_H), see Equation 5.1.

$$k = 1 - 1.2 \cdot \frac{SoC - 0.5 \cdot (SoC_H - SoC_L)}{SoC_H + SoC_L} \tag{5.1}$$

Figure 5.9 depicts a schematic representation of the implemented ECMS approach. Similar to the fuzzy control schemes, the ECMS algorithm estimates the power reference of the FC and the BAT based on the load demand (P_D) and the SoC. Since the SC is directly coupled, the SC power results from the equilibrium of load demand, the FC and the BAT output power. The power references are determined with the minimal overall operation cost. These are defined by the hydrogen costs and the cost equivalent that represents the BAT discharge. Figure 5.10 depicts the hydrogen cost related to the FC output power. The blue graph displays the simulation results of the FC model discussed in Chapter 3.3. In order to derive a mathematical expression which describes the amount of consumed hydrogen in relation to the FC output power, the simulated hydrogen consumption was interpolated with a quadratic polynomial. Hence, a quadratic representation of the hydrogen consumption can be formulated.

In literature different cost functions are introduced, a comprehensive summary is given by Föllinger and Roppenecker. In summary, there are two basic evaluation criteria, the trajectory of the system states or the trajectory of the inputs. The evaluation of the state variable can be interpreted as the costs that are related to the system behaviour, the assessment

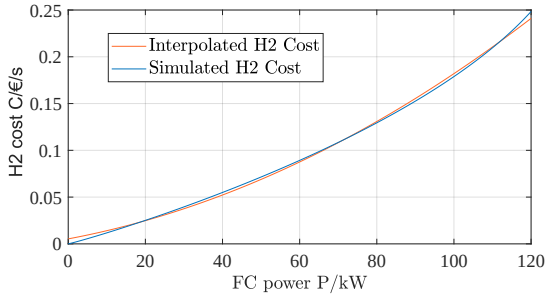

Figure 5.10: Simulated hydrogen cost related to the FC output power and derived interpolated cost function.

of the inputs as the costs which are related to the energy consumption required to operate the system. Since the hydrogen consumption shall be minimised, a cost function only related to the input trajectory can be used. An equation that describes a hydrogen consumption related cost function is given in Equation 5.2. The hydrogen consumption related to the FC operation is expressed with the quadratic interpolation shown in Figure 5.10. The energy converted by the BAT is related to an FC energy equivalent. Therefore it is assumed that the energy transferred from BAT is recharged via the FC and thus suffers from the losses induced by both DC-DC converter (η_{FC}, η_{BAT}). The hydrogen equivalent is then scaled with the equivalence factor k determined with Equation 5.1. The SoC dependent factor k adapts the EMS to different driving conditions.

$$\begin{aligned} C = a \cdot P_{FC}^2 + b \cdot P_{FC} + c + \\ \left((P_{Bat} \cdot \eta_{Bat} \cdot \eta_{FC})^2 + b \cdot (P_{Bat} \cdot \eta_{Bat} \cdot \eta_{FC}) + c \right) \cdot \mu \end{aligned} \tag{5.2}$$

Not only the cost function's minimum defines the power references but also constraints and boundaries of the output trajectory must be adhered. As discussed in the requirement section 5.1 of this chapter, the SoC has to be controlled to be below the maximum charge and above the maximum discharge. The SC voltage must not exceed or undercut the maximum and minimum DC link voltage. The BAT power must not exceed the maximum charge and discharge power. Similar the FC power reference must not be below the minimum FC power ($P_{FC,min}$) or exceed the maximum output power of the FC ($P_{FC,max}$). The optimisation problem is summarised in Equation 5.3. It includes equality as well as boundary constraints that define the system operation limits. The complete ECMS algorithm was implemented based on the interior-point al-

gorithm provided by the optimisation toolbox included in the MATLAB® technical computing environment.

The vector of the output variables is given as x = [P_{FC}, P_{BAT}, k]^T, the cost function $f(x)$ is equal to Equation 5.2. The vectors that define the standard upper (ub) and lower (lb) boundary condition are defined as ub = [P_FC, max, $P_{BAT,max}$,1]$^{\mathrm{T}}$ and lb = [$P_{FC,min}$, $P_{BAT,min}$,0]^T.

$$\min_x f(x) \begin{cases} Aeq \cdot x & = b \\ lb & \leq x \leq ub \end{cases} \tag{5.3}$$

So far, the FC and BAT power maximum and minimum borders were considered, but since also the power transients of the FC shall be limited the FC power boundary is adapted with regards to the power reference of the previous time step. Therefore, the vector of the inputs was extended by the outputs of the previous time step. Figure 5.10 depicts a schematic representation of this output feedback. The input vector is than given as u = [P_D, SoC, V_{SC}, P_{FC}(k-1), P_{BAT}(k-1)]. Prior to the execution of the optimisation algorithm the time step dependent specific boundaries were determined. With the power reference from the last time step the maximum power reference results in the sum of the previous reference and the maximum power transient. Vice versa, the minimum results from the difference of the last reference minus the maximum power change. The maximum power deviation is set to be at maximum $20\,\%$ of the maximum FC output power. In order to guarantee the SoC limits, the constraints on the BAT power were dynamically adjusted. If the SoC reaches its maximum value, the maximum charge power is set to be zero. Similar if the SoC falls below it's minimum, the maximum discharge is set to zero. The control of the SC voltage is realised by the power equilibrium, if the power from the FC and the BAT is equal to the load demand the SC voltage gradient is zero. If the efficiency reduction due to the DC-DC converter is considered, this equilibrium results in Equation 5.4. Since the objective is that the SC voltage is constant, Equation 5.4 is set as a second equality constraint. If V_{SC} falls below the minimum, this constraint is changed. The power reference of both the BAT and the FC are set to be the current maximums. Inversely, if the voltage exceeds it's maximum, the FC is turned off and the BAT power reference constrained to be the maximum charge power. By varying the constraints with regards to the the SoC and the SC voltage, the standard optimisation program was extended and input constraints were considered as well.

$$P_D = \eta_{FC} \cdot P_{FC} + \eta_{BAT} \cdot P_{BAT} \tag{5.4}$$

5.6. SUMMARY AND RESULTS

In order to evaluate the performance of the presented state of the art EMS approaches, all four discussed control schemes were simulated on the virtual test bench, which was introduced in Chapter 3.3. Since the EMS methods shall be evaluated against typical driving scenarios, the DC set presented in section 3.1 was used as test scenario set. Based on these cycles the schemes were tested under typical driving conditions, motorway, rural and urban driving, each with free flow and dense traffic. Thus, four different approaches under six different test sets, each including ten DCs, were simulated, so in total 240 simulation were outlined. In order to guarantee comparable test conditions, each scheme was implemented in MATLAB® Simulink® and each simulation was started under identical initial conditions (SoC = 75 %, V_{SC} = 250 V).

Based on the requirements discussed in section 5.1 six criteria which describe the performance of an EMS were derived. The utilisation of the BAT can be expressed by the maximum, the mean and the minimum SoC as well as the mean BAT energy exchange. The energy exchange is the integral of the BAT charge and discharge power and a measure for the number of charge and discharge cycle. If the approach under test is capable to ensure the BAT operation limits can be estimated with the SoC minimum and maximum. Both indices are also a measure for the operation induced BAT degradation. A second measure whether the system operates within the limits are the minimum and the maximum SC voltage. The FC operation characteristic is evaluated by it's mean power. Since high and low power operation induce accelerated FC degradation, also the time intervals (FC_{min}, FC_{max}) which is the time the FC is operated at low or high load are evaluated. The FC operation is normal if the output power is above 10 % and below 90 % of the maximum power. The fuel efficiency of the EMS scheme under test is characterised by the system efficiency (η_{system}) and the hydrogen consumption per 100 km. The overall efficiency can be determined with the energy consumed by the drive train divided by the amount of supplied energy. Since not the conversion efficiency of the motor and the mechanical parts are in the scope of this work, the energy output is the demanded energy of the electric drive. The load demand can be derived from the simulation results as the product of motor current and SC voltage. The energy transferred from the BAT can be estimated with the start and the final SoC and the BAT's nominal charge. The energy supplied by the FC can be calculated with the amount of consumed hydrogen and the heating value of hydrogen. The results of each DC set were comprised by the criteria's mean value. The results of

Table 5.1: Simulation results fuzzy control based EMS.

Criteria	MF	MD	RF	RD	UF	UD
η_{system} [%]	49.7	51.8	49.0	50.4	50.3	53.0
SoC_{max} [%]	78.0	78.2	75.5	76.3	75.1	75.2
SoC_{mean} [%]	75.7	75.4	74.5	75.0	74.3	73.9
SoC_{min} [%]	73.1	72.9	73.2	73.8	73.7	72.7
$\text{U}_{\text{SC, max}}$ [V]	278.8	283.4	273.8	274.4	261.5	261.7
$\text{U}_{\text{SC, min}}$ [V]	237.2	237.3	244.3	246.4	250	249
$\text{P}_{\text{FC,mean}}$ [kW]	19	18	14	13	13	8
$\text{E}_{\text{Bat,mean}}$ [kWh]	0.82	0.82	2.00	0.70	0.25	2.25
n_{H2} [$\text{kg}\,100\,\text{km}^{-1}$]	1.27	1.10	1.20	1.32	2.63	2.24
FC_{max} [s]	33	10	26	16	4	2
FC_{min} [s]	20	25	108	17	4	10

the simulations are summarised in the tables 5.2 to 5.4. The different test cases are indexed with a combination of two capital letters, the first identifies the road type, M marks motorway, R is rural driving, and U urban driving. The second letter classifies the traffic condition: D dense traffic or F free flow.

The tables 5.1 to 5.4 summarise the simulation results, the characteristic parameter are averaged over a complete DC set. In general can be stated that due to the typically high acceleration and high maximum velocity, motorway driving scenarios show the largest SC voltage deviation. No EMS scheme is capable to ensure a constant SC voltage at $250\,\text{V}$. While this is of cause not an absolute requirement, the SC voltage deviation is an indication of how fast the tested approach can follow a transient load demand. The smallest deviation occur for the ECMS and the Fuzzy type EMS, the highest deviation of $95\,\text{V}$ can be found for a system controlled by a state machine approach.

Figure 5.11 depicts the mean values of the minimum and the maximum SoC for each test scenario and for all EMS schemes under test. While for nearly all EMS approaches the SoC is operated in a narrow band, the ECMS makes best use of the BAT and operates it in a wide SoC range from $55\,\%$ to $85\,\%$. Even while the BAT degradation is directly connected to the depth of discharge, the limit that causes a significantly accelerated cell damaging is not reached. The BAT energy exchange criteria listed in the aforementioned tables 5.1 - 5.4, also point out the high BAT utilisation rate of the ECMS approach. Over all driving scenarios in

Table 5.2: Simulation results state machine based EMS.

Criteria	MF	MD	RF	RD	UF	UD
η_{system} [%]	49.0	51.1	49.0	49.5	49.4	51.2
SoC_{max} [%]	75.5	75.6	75.5	75.5	75.2	75.2
SoC_{mean} [%]	74.1	73.5	74.5	74.6	74.4	74.2
SoC_{min} [%]	71.8	70.6	73.2	73.3	73.4	73
$\text{U}_{\text{SC, max}}$ [V]	300	263	285	260	258	260
$\text{U}_{\text{SC, min}}$ [V]	224	165	161	185	215	240
$\text{P}_{\text{FC,mean}}$ [kW]	19.2	18.7	14.0	13.3	13.3	8.5
$\text{E}_{\text{Bat,mean}}$ [kWh]	3.00	2.95	2.03	2.48	0.79	1.83
n_{H2} [$\text{kg}\,100\,\text{km}^{-1}$]	1.28	1.10	1.20	1.33	2.67	2.32
FC_{max} [s]	48	17	26	24	8	7
FC_{min} [s]	100	125	108	158	28	65

Table 5.3: Simulation results PI controller based EMS.

Criteria	MF	MD	RF	RD	UF	UD
η_{system} [%]	51.5	52.9	52.4	52.6	52.8	54.5
SoC_{max} [%]	75.8	75.9	75.7	75.8	75.2	75.2
SoC_{mean} [%]	75.0	73.5	74.5	74.6	74.4	74.2
SoC_{min} [%]	73.6	73.9	74.0	74.0	74.4	74.5
$\text{U}_{\text{SC, max}}$ [V]	261.2	256.9	255		251.3	251
$\text{U}_{\text{SC, min}}$ [V]	206.7	222	216	220	232	237.7
$\text{P}_{\text{FC,mean}}$ [kW]	19.3	18.8	14.0	13.3	13.5	8.6
$\text{E}_{\text{Bat,mean}}$ [kWh]	1.95	1.56	1.25	1.53	0.43	0.82
n_{H2} [$\text{kg}\,100\,\text{km}^{-1}$]	1.23	1.05	1.13	1.26	2.53	2.20
FC_{max} [s]	5	1	2	0	0	0
FC_{min} [s]	568	466	433	563	273	796

total $2.9\,\text{kWh}$ were exchanged between the BAT and the SC. While the state machine approach also shows sufficient results, only the maximum discharge depth indicates that the full potential of the BAT was not used. The PI EMS and the Fuzzy approach do not make efficient use of the BAT.

The increased FC degradation rate caused by the operation characteristic is evaluated related to the time of operation under high and low loads. The boundary that indicates high load condition was determined to be $100\,\text{kW}$, low load operation under $10\,\text{kW}$. Consequently, due to the

Table 5.4: Simulation results ECMS based EMS.

Criteria	MF	MD	RF	RD	UF	UD
η_{system} [%]	52.8	54.7	53.1	53.2	52.5	51.0
SoC_{max} [%]	76.3	76.0	76.1	76.0	77.9	83.7
SoC_{mean} [%]	63.0	62.1	71.0	71.3	75.7	79.6
SoC_{min} [%]	54.7	54.6	66.7	67.4	73.2	74.0
$U_{SC,\,max}$ [V]	271.4	276.4	269.1	269.5	250.1	250.3
$U_{SC,\,min}$ [V]	233.5	241.6	239.2	240.4	240.1	239.8
$P_{FC,mean}$ [kW]	18.1	17.5	13.3	13.0	13.4	10.0
$E_{Bat,mean}$ [kWh]	3.82	3.49	2.50	3.24	1.08	3.11
n_{H2} [kg 100 km^{-1}]	1.16	0.98	1.08	1.23	2.54	2.52
FC_{max} [s]	20	4	11	6	1	1
FC_{min} [s]	1329	1075	1093	1427	524	1538

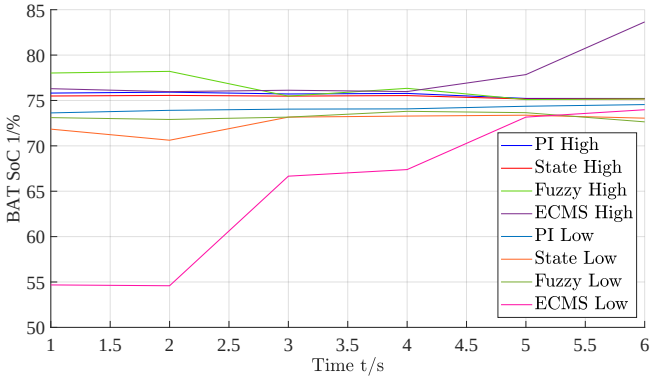

Figure 5.11: Mean values of the minimum and the maximum SoC for each test scenario and for all EMS schemes under test.

high maximum velocity longer high load condition are characteristic for motorway trips. Thus the largest share of high load durations occur in motorway scenarios. Since neither high road slope nor high headwind velocity were considered, high load condition do not occur quite often. Nevertheless, the distribution of high load over the tested EMS approaches can be evaluated. The state machine approach has the highest share of high load conditions, followed by the Fuzzy controller approach and the ECMS. For the PI approach high loads are negligible short. In contrast the occurrence of low conditions is highest for the ECMS control and second

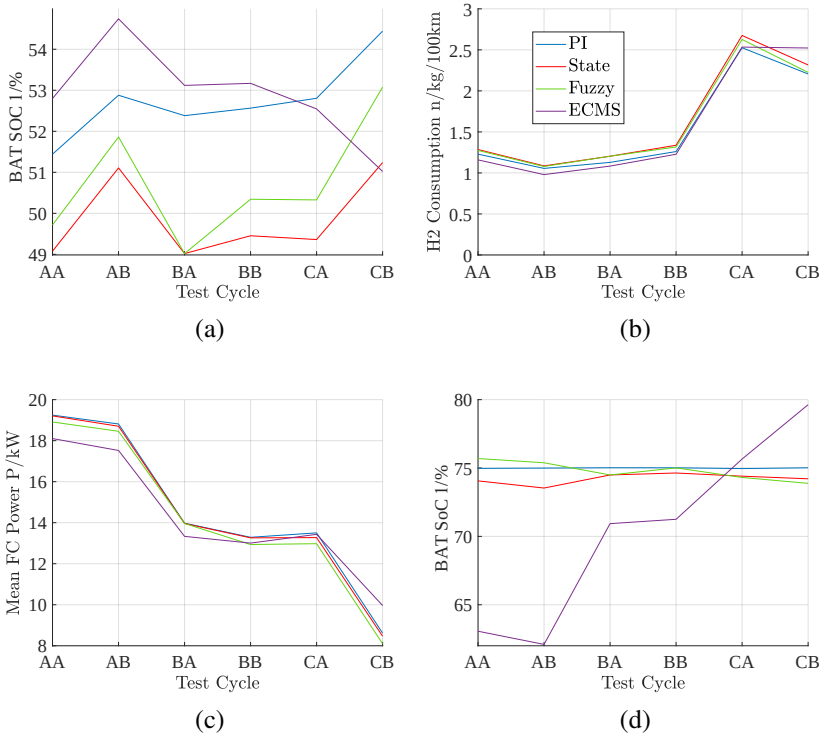

Figure 5.12: (a) Simulation results system efficiency. (b) Simulation results hydrogen consumption. (c) Simulation results mean FC power. (d) Simulation results mean BAT SoC.

for the PI approaches. In summary can be stated that in PI and ECMS approaches low conditions accelerate FC degradation, whereas high load operation is a problem for state machine and fuzzy approaches.

The efficiency is depicted in Figure 5.12 (a), it can be analysed that for five out of six test scenarios the ECMS approach shows the highest efficiency. The second is the PI controlled system, followed by the Fuzzy and the state machine approach. The deviation between the ECMS and the state machine approach is approximately $3\,\%$. In urban scenarios the efficiency of the ECMS approach decreases by nearly $2\,\%$ and falls below the one of the Fuzzy and the one of the PI controlled system. The hydrogen consumption, depicted in figured 5.12 (b), confirms these results. . Figures 5.12 (c) and (d) display the mean FC power and the mean BAT SoC related to the different test scenarios. The high efficiency of

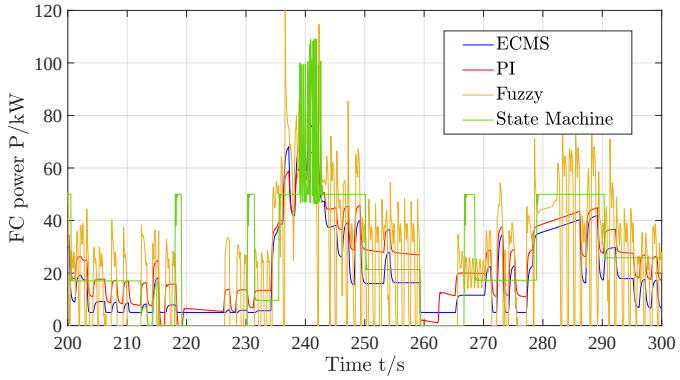

Figure 5.13: FC power for different EMS schemes and an exemplary interval of the Artemis 130MW DC.

the ECMS approach can be reasoned with the lower FC and higher BAT utilisation. The lower mean SoC indicates that in general more BAT energy is used, the lower mean FC power confirms this conclusion. Since the BAT efficiency is significantly higher, the overall system efficiency is also higher. Consequently, the increased hydrogen consumption of the ECMS approach for urban driving results from the higher mean FC power and reduced BAT utilisation. So far the FC power transients are not taken into account, since high dynamic power changes significantly enhance FC degradation effects, the FC power dynamics are also analysed. In order to compare all discussed strategies based on a single cycle, the Artemis MW150 DC, which was discussed in Chapter 3.1, is used as test case. Figure 5.13 depicts an exemplary sample interval of the FC power trajectory. The results clearly indicate that the Fuzzy control approach causes high frequent power changes as well as frequently on and off switching. Even while the results of the state machine approach show phases of constant power, under specific states the FC power follows the load which causes high transient power changes. The smoothest trajectory results from the ECMS and the PI approaches. Hence, the outlined comparison of the different EMS approaches shows that the ECMS and the PI control scheme are the most promising EMS schemes. Both the high efficiency and the low hydrogen consumption indicate that from the presented selection both schemes are highly recommendable. Nevertheless, central aspects, especially the minimisation of the components degradation can not be realised with these standard EMS schemes.

6

Optimal Control Strategy

In Chapters 2 and 5 the importance of an EMS was discussed. The major reason why an EMS is essential is the fact that it is directly responsible to manage the BAT's SoC and the SC voltage. Only an efficient and intelligent EMS allows the vehicle and the driver to take full advantage of the hybrid powertrain. The actions taken by the strategy will have a significant effect on the performance of the vehicle. In particular, the hydrogen consumption, the component degradation and the drive-ability are highly dependent on the operating conditions that are determined by the EMS. Today there are a number of different concepts to develop an efficient EMS. In the previous Chapter 5, a detailed analysis and evaluation of the standard state of the art EMS schemes was outlined. Even while some approaches, especially the ECMS and the PI control schemes, in this test perform with satisfying results, a clear potential for optimisation can be identified. The mean efficiencies of the tested approaches, which are all in the range of the FC efficiency, pointing out that the utilisation of the BAT and SC is low. Further drawbacks of conventional control schemes are the operation induced reduction of the BAT SoH as well as the FC degradation costs which are both not considered. Additionally, neither limiting BAT or FC current transients is possible nor short-term future driving and road conditions are included. In summary can be stated that these limitations clearly prove the demand for a predictive EMS scheme, which is capable to guarantee a high efficiency, minimal hydrogen cost and reduces the degradation of the FC and of the BAT.

The fundamental concept of a predictive EMS is characterised by the combined prediction of the system states and the disturbance. This combination enables the EMS to estimate an input trajectory, which when applied to the system, controls the system states, under the real disturbance, to predefined references, with minimal costs. Due to its ability to determine inputs, to consider state constraints, because of the feedback oriented structure as well as the ability to guarantee global optimalital solutions, in this thesis DP embedded in a MPC scheme is used to develop a predictive EMS controller.

In related literature, different predictive EMS approaches applicable in FHEV or PHEV are presented. Nevertheless, the vast majority of the discussed EMS concepts use a MPC controller as a predictive fuel optimal control scheme. Back present a MPC approach to implement an energy optimal control of a PHEV. Wahl develope an advanced driver assistance systems, which is capable to execute both an energy optimal EMS as well as a velocity control of a PHEV. The developed control system was implemented and tested on a real vehicle. Puig et al. present an economic MPC approach. The economic MPC allows to directly minimise the operational costs, instead of tracking the reference related error. Puig et al. use a cost function including three operational goals: economic, safety and a smooth input trajectory. The implemented MPC is tested on a simulation model using the NEDC cycle, whereas different economic weights were simulated under a prediction horizon of $10\,\mathrm{s}$ [272]. To control a FC-SC HES based on a MPC controller is discussed in [273]. Since the applied test system includes only a SC and a FC, it can be described by a linear equation with a quadratic cost function. Thus, the solution of the MPC can be determined by solving a quadratic program [273]. Hu et al. present a MPC based control of a BAT - FC hybrid vehicle which not only minimises the hydrogen cost but which also accounts for the degradation of the FC and of the BAT. In the discussed approach, the cost caused by the BAT degradation, are evaluated based on the reduction of the BATs SoH, whereas the FC voltage decreasing rate is used to determine the cost related to FC degradation [274]. Amin et al. develop a MPC control for a BAT-FC-SC HES of a vehicle. The combination of EMS and cruise control also is in the focus of research. Uebel et al. introduce a two level MPC to realise an EMS including velocity control of a HEV. Th applied online optimal control uses the combination of two stages, one is solved by a discrete state-space DP approach and the other use Pontryagin's Maximum Principle. [275, 276].

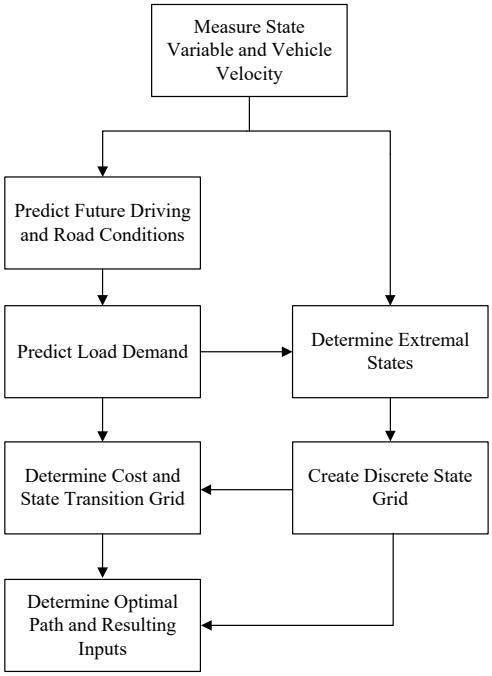

Figure 6.1: Flowchart of the procedure implemented to form the predictive EMS scheme. The depicted scheme has to be executed and solved in each control cycle.

The concept of a MPC is to optimise the future system behaviour based on the prediction of the disturbance. Thus, a constrained optimisation problem defined by the controlled system and a specific cost function has to be continuously solved. In this work, this is realised based on a DP approach. Figure 6.1 depicts a flow chart which describes the implemented predictive EMS. To solve the optimisation problem at each sample interval, the depicted steps have to be successively followed. The first step is to measure the current vehicle velocity, the system states and the inputs. With the recorded velocity and the vehicle position, based on an electronic horizon, the future driving and road conditions are predicted. In a third step the future load demand of the electric drive can be estimated based on the predicted velocity and road inclination trajectories. In combination with the current system states the future extremal states, minimum and maximum, can be determined. These extremal trajectories constraint the discrete state grid and thus allow to determine the costs and

state transition for a minimum number of nodes. Based on a forward recursion and an inverse control oriented system model, all state grid nodes and state transitions costs are evaluated. In the last step the optimal path, which is the one with minimum costs, is determined in a backward oriented search. Finally this path defines the optimal state and corresponding input trajectories.

A major drawback of the DP algorithm, is the high computational burden and thus the challenge to solve the given task in sufficient time. A discrete DP implementation arises additional challenges. In order to overcome the high computational burden, a novel two stage approach was derived. The essential benefit of the system which enables the chance to split the DP in two parallel stages, is the fact that the BAT's SoC only depend on one input. Thus, a parallel optimisation of the SoC and of the SC voltage in two independent DP algorithm is possible. Because in this parallel approach, each DP handles only a first order system, the required processing time is significantly reduced.

In the following chapter all fundamental requirements for the implementation of the two stage predictive EMS scheme are discussed. In the beginning, first the MPC concept, followed by the fundamentals of DP are introduced. Subsequently followed by an introduction of the the inverse system and the disturbance model, which are outlined in Sections 6.3 and 6.4. Afterwards the development and implementation of a single stage MPC approach is discussed. Finally, based on the single stage approach, a two stage MPC scheme is derived. In the final Section 6.6, the implementation of the two stage MPC is discussed and the simulation results of the FHEV controlled by the novel MPC scheme presented.

6.1. Model Predictive Control

The task to minimise the energy consumption of a FHEV can mathematically be described as a constrained optimisation problem. The result of this optimisation is the optimal input trajectory. This trajectory is equal to the specific set of continuous inputs that control the system in that way that the optimisation criterionon is fulfilled. If thinking of a non-feedback control system, this trajectory can directly be applied to the plant. Nevertheless, the operation in non-feedback configuration results in different problems. One is that the trajectory is only optimal within the prediction limits. Non-causal disturbances or uncertainties and inaccuracy arising from the modelling process also induce deviation in the real system response. A solution to overcome these problems is to implement a feedback control scheme. A MPC is a suitable solution to realise such a

optimal feedback control system. The fundamental MPC concept arises from the prediction of the disturbances, which is used to determine the future system response. If a cost function is defined, it can be used to determine those results within the predicted system state space, which minimises this cost function. Thus, a MPC is capable to determine an optimal input trajectory, with regards to the current system state and the future disturbance trajectory.

Today, MPC is a commonly used control approach. Because of its typically larger time constants, MPC was originally implemented in petrochemical or process engineering applications [277, 278]. When applied to control a constrained linear time invariant system, the MPC concept can be considered as sufficiently developed today. In contrast, the control of non-linear plants is more challenging. Back describe the fundamental difference in linear and non-linear MPC to be the fact that in non-linear MPC the optimisation problem is no longer convex [17, 279]. Thus, the appearance of local minima can cause significantly higher requirements on the applied mathematical algorithms. Back name sequential quadratic programming as a standard algorithm to solve non-convex optimisation problems. A consecutive summary of the development of nonlinear MPC and the different approaches can be found in [280].

Figure 6.2 depicts a schematic representation of the state response and inputs of a one dimensional dynamic system, controlled by a MPC algorithm. Based on the model of the dynamic system, the future system behaviour is predicted. The algorithm starts at time step k and is subdivided with the sampling interval $t \in \mathbb{R}$ and executed for a predefined prediction horizon, which reaches to the final time step k+p. With the predicted system response and a cost function an optimal input trajectory, which is applied within the interval of k and the control horizon t+q, is derived [281]. Whereas the sample interval as well as the control (q) and prediction (p) horizon depend on the dynamic characteristics of the controlled system.

If the system model is sufficiently accurate and no disturbances occur, the determined input trajectory would optimally transfer the system to the desired set point. Since disturbances act on every real system and modelling always implies specific assumptions, the implementation of an optimal forward control is not possible. Nevertheless, if a forward control is applied, the deviation between the real system states and the predicted one would increase over time. To overcome this challenge, the optimisation problem can be periodically executed. If executed in this manner, only the first input of the control strategy is applied to the system between two

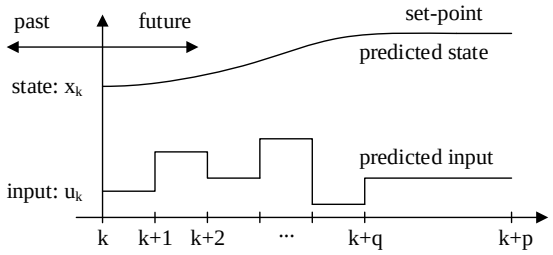

Figure 6.2: MPC concept, schematic representation of a first order system [17]. If the input tractory u is applied over the time steps k to k+p and no disturbance is considered, the system state x_{k} follows the depicted characteristic.

consecutive executions. The next calculation cycle starts with sampling the system state and the disturbances. In this second step, the optimisation is repeated. Again the process starts from the sampled state, yielding a new control and new predicted state path. The prediction horizon keeps being shifted forward and a receding horizon concept followed. Hence, when the actual disturbance and system states in combination with a periodic execution of the optimisation with a shifted prediction interval is applied, a stable feedback control structure is realised. This concept is called receding horizon.

Equation 6.1 summarises the continuous non-linear time variant dynamic system, which is defined by the plant controlled by an MPC scheme. The disturbance is characterised by Equation 6.2. The vector $\underline{u}$ is the input of the system, the parameter vector θ describes the dependency of the disturbance on external influences like the environment.

$$\dot{\underline{x}} = \underline{f}\left(\underline{x}(t), \underline{u}(t), \underline{z}(t)\right), \quad \underline{x}(t_0) = \underline{x}^A \tag{6.1}$$

$$\dot{\underline{z}} = \underline{g}\left(\underline{z}(t), \underline{\theta}(t), t\right), \quad \underline{z}(t_0) = \underline{z}^A \tag{6.2}$$

The optimisation problem can be described with Equation 6.3:

$$J^*(\underline{x}_k, \underline{z}_k, T) = \min_{u_k} \left[J\left(\{x_k\}, \{u_k\}, \{z_k\}, p, T\right)\right] \tag{6.3}$$

The task is to determine this input trajectory, which minimises the cost function J, see Equation 6.4, in the prediction horizon p. The optimal values of a parameter are indexed with *, the braces mark the trajectory of the specific parameter, as a set of discrete values at k = 1, 2, ..., k+p. The

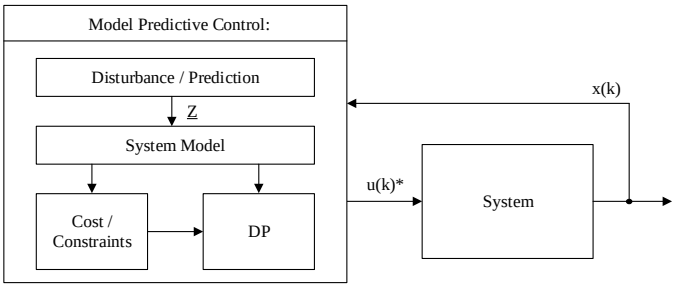

Figure 6.3: Illustration of the MPC control structure. In each iteration the input trajectory $u(k)$ is generated based on the measure states $x(k)$.

cost function typically is a discrete function that contains a term evaluating the costs of the final value and a sum which represents the transition cost. The introduction of the control horizon (k+q < k+p) guarantees a sufficient small calculation time while also the full system dynamics until the end of the prediction horizon are considered. The concept is depicted in Figure 6.2, in the interval k+q until k+p the input trajectory is set to $\underline{u}_{\mathrm{k}}$ = $\underline{u}_{\mathrm{k}+q}$. [17]

$$J = \zeta\left(\underline{x}_{k+p}\right) + T \cdot \sum_{k=1}^{k+p-1} \xi\left(\underline{x}_k, \underline{u}_k, \underline{z}_k\right) \tag{6.4}$$

The implemented approach can be summarised as follows, based on a disturbance model, see Equation 6.2, the discrete disturbance trajectory $\underline{z}_{\mathrm{k}}$ is predicted. With this disturbance and an optimal input trajectory $\mathrm{u}_{\mathrm{k}}^{*}$ and the system model, see Equation 6.1, the optimal future system behaviour $\mathrm{x}_{\mathrm{k}}^{*}$ is determined. This process is repeated for each sample, whereas the current state and disturbance are sampled every time. The optimal input trajectory $\mathrm{u}_{\mathrm{k}}^{*}$ is the result of each optimisation process. Figure 6.3 depicts a schematic representation of the the MPC's control loop structure. The MPC module contains the prediction model, a system model, a module which includes the cost function and the constraints and a solver. If a MPC algorithm is implemented in a real system, the timing of the control approach might be a problem. Freuer state that the periodic cycle time Δ has to be equal or higher than the time required to solve the optimisation problem $\Delta \mathrm{T}_{\mathrm{calc}}$. If this criterion is not fulfilled, Freuer and Bertsekas suggest to compensate the calculation delay by shifting the determined input trajectory time base by one time step ΔT. In that case, the maximum time to solve the optimisation problem is expanded to $2 \cdot \Delta T > \Delta T_{calc}$.

6.2. DYNAMIC PROGRAMMING

The result of the optimisation problem which is described in the previous section, see Equation 6.3, is an optimal time dependent input trajectory u_k^*. Thus the introduced problem can mathematically be described as a dynamic program. Dynamic programs optimise a time dependent function which is characterised by a specific cost functional. In contrast static programming problems are characterised by a finite number of optimisation variables, which corresponds to minimising an algebraic cost function. [283] Freuer name three different types of algorithm which can be used to solve a dynamic program: indirect approaches, direct methods and DP.

In an indirect approach, the optimal criterion derived based on the canonic Hamiltonian equation [271]. The result is a system of differential equations which are typical numerically solved. An optimal control approach, that also includes input constraints is Pontryagin's Minimum Principle [271]. In direct DP methods the dynamic program is transferred to a static program and solve based on a standard static optimisation method. Thus, the input trajectory is transferred to a discrete representation, that is distributed over several intervals. In general can be said that not a time dependent function but a vector of parameter has to be determined. Finally linear quadratic programming can be applied to solve the non-linear static optimisation which results from the transformation. One drawback which arises from quadratic programming is that the evaluated optimisation criterion depend on the cost function's quadratic term and not necessarily guarantee a global optimum [18, 271]. Since the presented predictive EMS approach uses DP, this section focuses on DP as tool to solve a dynamic program. The fundamental concept of DP based optimisation is to subdivide a complex optimisation problem into a set of simpler problems [284, 285]. If the solutions of these simpler problems are combined, the solution of the original complex optimisation problem can be determined. As long as the number of sub problems is sufficiently large, the solution of the DP algorithm is guaranteed to be the global optimal solution [136]. The key drawback is that the computational burden, which results from solving a conventional DP approach, increases exponentially with the number of state variables [271]. Nevertheless, a beneficial property is that in contrast to the system order, DP's computational burden increases only linear with the lengths of the prediction horizon. Wahl summarise that a deterministic multi-stage decision problems is a precondition to apply DP. The characterising features of these problems are:

- The underlying physical system can be analysed in different discrete steps, otherwise discretisation is required.
- The system and its operation states are always describable by a set of state variables.
- At each stage different decisions are possible and each decision results in a transformation of the state variables.
- Decisions have no impact on previous stages.
- The objective of the decision process is either to minimise or to maximise a function depending on the state variables.

A dynamic systems fulfils the named preconditions and thus can be considered as a deterministic multi-stage decision problem. The basis of each decision is the quality measure or function cost. An action that manipulates the state variables is the result of each decision. In terms of control, a decision can be considered as equal to the application of a specific input $\underline{u}$. The trajectory that contains all actions is the operation policy of the dynamic system. The policy that minimises the total operation cost in the final stage N is, within the set of all possible policies, the optimal one [284]. Bellman define the Principle of Optimality based on the property of an optimal policy:

> *"An optimal policy has the property that whatever the initial state and initial decision are, the remaining decisions must constitute an optimal policy with regard to the state resulting from the first decision."* - Richard Bellman

Figure 6.4 graphically illustrates Bellman's Principle of Optimality. The optimal policy $S_{*,0K}$ describes to go from stage 0 to stage K of a N stage optimisation problem. If one considers any given point x_K, the optimal policy, that minimises the cost function J_{X_N} to go from K to N, is identical with the initial complete optimal policy. If a remaining policy S_1 induces less costs as the policy S_*, the sum of the remaining policy S_1 and the partial optimal policy $S_{0,K}$ would be lower than the costs of the complete optimal policy $S = S_* + S_{0,K}$. This would violate the initial assumption that the optimal policy S minimises the cost function J_{X_N}. Thus any remaining policy $(S_1 - S_4)$ must not cause lower cost as the optimal partial policy S_*. [271, 284, 285] The mathematical expression of this principle is the Bellman equation, given as Equation 6.5. The cost

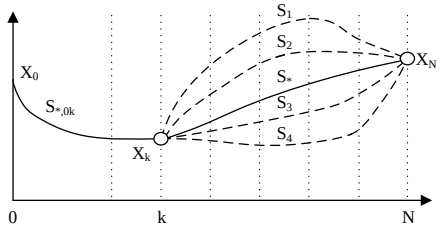

Figure 6.4: Graphical representation of Bellmans Principle of Optimality. If the trajectory S_* is the optimal one, non of the other S_1 to S_4 can connect x_k with X_N under lower cost than S_*, otherwise S_* would not be the optimal one.

to reach the state $x_{\mathrm{k}+1}$ are determined from the cost I_{k} that results the from previous transitions to the state x_{k} and the cost-to-go $J_{\mathrm{k}+1}$ [271].

$$J_{x_{\mathrm{k}}} = \min_{u_{\mathrm{k}}} \left[I_{\mathrm{k}} \left(x_{\mathrm{k}}, u_{\mathrm{k}} \right) + J_{\mathrm{k}+1} \left(x_{\mathrm{k}+1} \right) \right] \tag{6.5}$$

The discrete DP approach is characterised by the discretisation of the state space. The combination with the stage oriented representation results in a discrete grid which is determined by the state space and the number of states. Each point in this grid corresponds to a specific system state at a specific time step. In this case difference equations connect the discrete nodes of the state space. A central problem of the discrete DP are the continuous state transitions of the dynamic system that result in continuous states at the stage k+1. Since these continuous states not necessarily match the discrete state nodes, an adaptation of the determined continuous states to the discrete state nodes is required. Often used methods are either nearest neighbour or interpolation. In contrast to the state variables, the adaptation of the determined continuous inputs is more complex. Since an optimal input policy typically contains steps, a standard interpolation method is not applicable [17]. One solution is to divide the complete DP in a forward and in a backward oriented part. The first step of the forward part is to compute the cost-to-go for all valid state grid nodes based on Bellman's recursive algorithm Equation 6.5. In a second step starting with the current node x_{k}, every valid input policy is evaluated with Equation 6.6. The input trajectory with the minimum costs is the optimal input policy. Proceeding backward in time, the optimal state ($[x^*_{\mathrm{k}}, x^*_{\mathrm{k}+1}, \ldots, x^*_{\mathrm{k}N}$) policy can be determined.

$$u^*_{\mathrm{k}} = \arg \min_{u_{\mathrm{k}}} \left[I_{\mathrm{k}} \left(x_{\mathrm{k}}, u_{\mathrm{k}} \right) + J_{k+1} \left(g_{\mathrm{k}} \left(x_{\mathrm{k}}, u_{\mathrm{k}} \right) \right) \right] \tag{6.6}$$

The backward oriented calculation of the state grid determines most of all the computational burden. The recursive Equation 6.5 has to be evaluated for all stages of the control horizon for each node of the state grid. The difference equations as well as the cost function have to be determined for all discrete state x_k in combination with every discrete input value u_k. The interpolation of the optimal cost and the comparison of these cost against the previously determined costs also have to be executed. The number of grid points per stage are defined by the minimum and maximum values as well as the discretisation interval. The discretisation interval and number of a grid points is defined by a trade-off of accuracy and calculation effort.

$$N_x^\mathrm{k} = \prod_{i=1}^{\eta} \left[\frac{x_\mathrm{i,max} - x_\mathrm{i,min}}{\Delta x_\mathrm{ik}} \right] \tag{6.7}$$

$$N_u^\mathrm{k} = \prod_{i=1}^{\eta} \left[\frac{u_\mathrm{i,max}(x_\mathrm{k}) - x_\mathrm{i,min}(x_\mathrm{k})}{\Delta u_\mathrm{ik}} \right] \tag{6.8}$$

Equation 6.7 defines the number of state nodes at stage k to be $\mathrm{N_x^{*k}}$. Similarly the number of input nodes $\mathrm{N_u^{*k}}$ at stage k can be determined, see Equation 6.8. Based on both numbers and the time required for one evaluation (τ_k), the total computational burden of the backward oriented calculus can be determines based on Equation 6.9.

$$\tau_{back} = \tau_\mathrm{k} \cdot \sum_{k=n+1}^{N} N_x^\mathrm{k} \cdot N_u^\mathrm{k} \tag{6.9}$$

The execution of the forward calculation starts at the first stage k = 1 and proceeds with a successively evaluation of Equation 6.6. The required calculation time can be determined similar to the one of the backward calculus, $\tau_\mathrm{for} = \tau_\mathrm{k} \cdot \mathrm{N_u^k}$. The complete calculation time including the forward and the backward calculation, is the sum of τ_back and τ_for. If it is assumed that the boundaries of the inputs and states are time invariant, the total required calculation time can be summarised as Equation 6.10. It can be stated that the system order and the number of input variables have the strongest impact on the computational burden. Bellman describes this as "The Course of Dimensionality" [31, 271, 284**?**].

$$\Omega_\mathrm{DP} = N^x \cdot N^u \cdot N^q \tag{6.10}$$

Freuer describe a forward oriented DP algorithm that overcomes the interpolation problem by inverting the dynamic system. Consequently,

this approach can only be applied to systems which can be explicitly described and inverted. Based on the inverted differential equations, the inputs can be determined related to related state transitions. Thus, continuous inputs can be considered and the complexity of the problem significantly reduced. The optimisation problem can then be described by the task to find the optimal state transitions between two consecutive stages. Thus, the optimal control problem is transferred to a shortest-path problem[18, 282].

In this work a forward oriented predictive DP approach is used to solve the constrained optimisation problem which arises from the proposed MPC based EMS. The described approach is based on the work of Freuer and discussed in [18]. The discrete optimisation problem can be formulated as follows. A time discrete interval of length $\Delta t_k = t_{k+1} - t_k$, that corresponds to the time interval between two consecutive stages is assumed. Within this interval constant inputs are assumed. The discrete system description is given as Equation 6.11

$$x_{k+1} = F_x\left(\Delta t_k, x_\mathrm{k}, u_\mathrm{k}\right) \tag{6.11}$$

The transfer function F_x describes the transition from x_k to $x_{\mathrm{k+1}}$ caused by the input u_k, typically given as differential equation. For the presented approach it is assumed that an inverse function F_u of F_x exists. The inverse function 6.12 can be used to determine the input u_k responsible for the transition from x_k to $x_{\mathrm{k+1}}$ in the interval Δt_k.

$$u_k = F_u\left(\Delta t_\mathrm{k}, x_\mathrm{k}, x_{\mathrm{k+1}}\right) \tag{6.12}$$

As described in Equation 6.7 and 6.8, it is assumed that the time discrete input constraints depends only on the time discrete state x_k and not also on the following state x_{k+1}. The discrete optimisation problem can be summarised in equations 6.13 - 6.17, the original continuous interval $t \in [0, T_{opt}]$ is subdivided in n_k discrete intervals.

$$\min_{x_\mathrm{k}, k=0,1,\ldots,K} J_K = I_K + i_{f,K} \tag{6.13}$$

$$u_\mathrm{k} = F_u\left(\Delta t_\mathrm{k}, x_\mathrm{k}, x_{\mathrm{k+1}}\right) \tag{6.14}$$

$$I_{n_\mathrm{k}} = \sum\nolimits_{k=0}^{K-1} i_{f,K}\left(x_\mathrm{k}, x_{\mathrm{k+1}}\right) \tag{6.15}$$

$$x_\mathrm{k} \in \left[x_{\mathrm{min,k}}, x_{\mathrm{max,k}}\right] \tag{6.16}$$

$$u_\mathrm{k} \in \left[u_{\mathrm{min,k}}(x_\mathrm{k}), u_{\mathrm{max,k}}(x_\mathrm{k})\right] \tag{6.17}$$

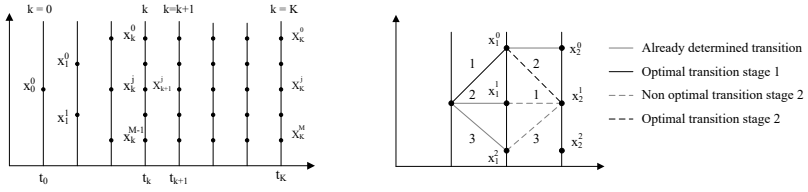

(a) (b)

Figure 6.5: (a) Schematic representation of a one dimensional discrete state grid [18]. (b) Subproblem optimal path to x_2^1.

The solution of the optimisation problem 6.13 - 6.17 are the optimal discrete state trajectory 6.18 and the corresponding optimal input trajectory 6.19:

$$\underline{x}^* = [x_0^*, x_1^*, ..., x_n^*] \tag{6.18}$$

$$\underline{u}^* = [u_0^*, u_1^*, ..., u_n^*] \tag{6.19}$$

With the objective to solve the optimisation problem, the system states are transferred to a discrete grid with discrete state nodes at every stage. The result is a discrete state space and the optimisation problem can be described as a shortest path problem within this discrete space space. A one dimensional representation of a discrete state space is depicted in Figure 6.5 a). The stage is represented by the subscribed index k with the maximum control horizon k $\in [0, K]$, the discrete state node at each state is represented by the superscribed index j $\in [0, M]$. Whereas the maximum number of nodes M can vary over all stages.

Figure 6.5 b) schematically depicts a DP sub-problem that arises when a forward oriented recursive algorithm is applied. In this example, the search for the optimal path, respectively the optimal state transition, to go from stage k = 1 to the node x_2^1 at stage k = 2 is depicted. The optimal transition is characterised by minimum costs. To determine those, the solutions of the previous stages can be recursively used to minimise the computational burden. Doing so, the complexity of the optimisation problem can be reduced. Equation 6.20 exemplary describes the cost to go to x_2^1. These costs are defined by the minimum of the partial solutions of the previous stages and the state transition costs ϕ.

$$\min_{j_1 \in [j_{min,1}, j_{max,1}]} J_2^2 = J_1^{*j_1} + \phi\left(x_1^{j_1}, x_2^2\right) \tag{6.20}$$

In the depicted example, the optimal costs J_2^1 to go to x_2^1 are determined by the minimum in stage k = 1 and the related transition costs. The implemented algorithm starts with the initialisation of the cost at node x_2^1 with J_2^1=∞. In a next step, the node index at the previous stage j_1 is varied within the limits of $j_{1,min}$ = 0 and $j_{1,max}$ = 2 and the corresponding transition cost of that specific predecessor determined. After all suitable predecessors costs are evaluated, the minimum of the estimated solutions is selected. In this example the optimal predecessor is node x_1^0. Based on Equation 6.12 the related optimal input u_1^{*0} can be estimated. Consequently, the optimal costs at x_2^1 are determined based on Equation 6.20 and result from J_1^0 = 1 plus the transition cost to J_2^{*1} = J_1^{*0} + ϕ(x_1^0,x_2^1) = 3. In order to execute the backward oriented calculation the optimal predecessor and the related input for the current node and the predecessor are stored in two matrices. The cost to go J_2^{*1} are also stored in a cost matrix. If no valid predecessors or transition exists the initial matrix values (∞) are stored. Equation 6.21 formulated the cost function in a general form.

$$J_{k+1}^{j+1} = J_k^{*j} + \phi\left(x_k^{j_k}, x_{k+1}^{j_{k+1}}\right) + \begin{cases} 0 & ,k+1 < N \\ \phi_N^{j_k} & ,k+1 = N \end{cases} \tag{6.21}$$

The discrete subproblem solved for all nodes in the state grid can be summarised with the Equations 6.22 - 6.25.

$$\min_{j \in [j_{k,min}, j_{k,max}]} \quad J_{k+1}^{j+1} \tag{6.22}$$

$$u_k^{j_k} = F_u\left(\Delta t_k, x_k^{j_k}, x_{k+1}^{j_{k+1}}\right) \tag{6.23}$$

$$J_k^{*j_k} \neq \infty \tag{6.24}$$

$$u_k^{j_k} \in \left[u_{min,k}(x_k^{k_k}), u_{max,k}(k_k^{j_k})\right] \tag{6.25}$$

The estimation of the optimal state and input trajectories starts at the last stage and proceeds backward in time over all stages. The first step is to determine the optimal state node at the end of the control horizon $x_K^{j_K}$. The optimal node index at the final stage is the determined by the minimisation problem described in Equation 6.26. The determined costs are the solution of the problem defined by the equations 6.13 - 6.17. The node index *j is the optimal state node at the end of the control horizon. Finally, the optimal trajectories of the state and input trajectories are determine based on the matrices that include the optimal states, costs and inputs derived in the forward calculation. The process starts with the optimal final node *j at stage K.

$$\min_{j_\mathrm{k}=0,1,\ldots,M(K)} J_K = J_K^{*\mathrm{j}} \tag{6.26}$$

If the extremal inputs $\mathrm{u}_\mathrm{k}^+ = u_{\mathrm{k,max}}$ and $\mathrm{u}_\mathrm{k}^- = u_{\mathrm{k,min}}$ are determined, borders of the reachable state space (u_k^-, u_k^+) can be defined. Thus, these borders were reached if the minimum or maximum input trajectory is applied. Starting with the current state the minimum and maximum state trajectory result from Equation 6.27 and 6.28. Figure 6.6 clarifies the reachable state space concept.

$$x_{\mathrm{k+1}}^- = F_x\left(\Delta t_\mathrm{k}, x_\mathrm{k}^-, u_\mathrm{k}^-\right) \tag{6.27}$$
$$x_{\mathrm{k+1}}^+ = F_x\left(\Delta t_\mathrm{k}, x_\mathrm{k}^+, u_\mathrm{k}^+\right) \tag{6.28}$$

Vice versa, a reverse application is also possible and discussed by Back. If a predefined target quantity exists, there is a limited state space with valid state transition capable to reach the target quantity. Thus a target-aimed state space can be defined within the state boundaries that is characterised by the ability to reach the target quantity. This target-aimed state quantity can be determined based on the boundaries of the target quantity and a backward calculation for which extremal inputs are assumed. The combination of the target-aimed and the reachable state space forms the reduced state space. This reduced state space is defined by the initial state, the target quantity and the extremal inputs. When a constant discritisation interval is assumed, the essential benefit if only the reduced state space is considered is the significantly reduced number of discrete state nodes that needed to be evaluated. Thus based on the determination of the reduced state space, the computational burden of the DP approach can significantly be reduced. [17]

6.3. Control oriented Process Model

In the previous section, a forward oriented DP approach which is presented by Freuer was discussed. A key feature of this approach is to solve the dynamic optimisation problem in a forward oriented calculation process. This is possible for systems which can be described with an inverse system equation. Thus, a central part of the DP used to implement the MPC based predictive optimal EMS, is the derivation of a set of inverse system equations suitable to determine the FC and the BAT current based on differences in the SC voltage and the BAT SoC. For the implementation of the virtual test bench a complete system model was discussed,

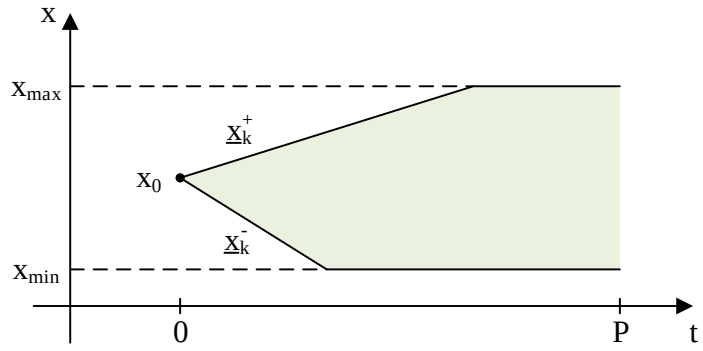

Figure 6.6: Schematic representation of the reachable state space concept for a first order system. Only points within the borders defined by $\underline{X}_k^-$ and $\underline{X}_k^+$ can be reached from X_0.

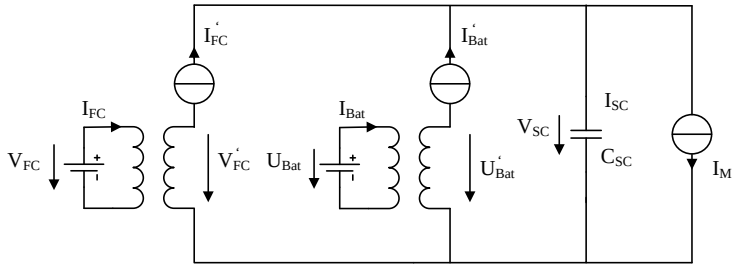

Figure 6.7: Schematic representation of the equivalent circuit used to derive a control oriented system model.

see Section 3.3. Since this system description would result in a highly non linear set of inverse state equations, a simplified approach based on an equivalent circuit, presented in [148], was used. Figure 6.7 depicts a schematic representation of this equivalent circuit.

The underlying assumption used to simplify the modelling process is to neglect the dynamics of the DC-DC converter. In this approach, a converter is represented by a controlled current source and an ideal transformer. The transformer realises the voltage input to output ratio and the current source supplies a current related to the input power divided by the output voltage. A similar simplification was also used by [148] and [286]. Amin et al. state that this assumption is valid as long as the transfer ratio is unchanged and the current reference is sufficiently smooth. Since

the applied approach is a superior control structure and all components are controlled by dedicated controller, this assumption can be considered as valid. The discussed system can be described by two state variables, which are the SC voltage and the SoC of the BAT. The vehicle's velocity, respectively the related power demand of the electric drive, can be considered as the disturbance variable. For simplification an infinite hydrogen storage capacity is assumed. Therefore, the SC and BAT are the only relevant energy storages that determine the system dynamics. Thus two equations that describe the BAT and the SC current, based on the SoC and voltage deviation between two consecutive steps are required. While the focus of the simulation model discussed in Section 3.3 is to derive a virtual test bench capable to simulate the long-term system behaviour, the requirements of the inverse system description are different. Since the inverse system equations have to be solved numerous times at each state node, at each stage of the optimisation process the most important requirement is that the calculation has to be capable to be executed very fast.

The inverse equation that describes the BAT current based on the deviation of the SoC is comparable simple.The SoC is equal to the relative amount of charge stored in BAT. Thus, the current related to the nominal charge of the BAT is equal to the SoC derivative in the sample interval. Equation 6.29 summarises the discrete inverse description of the BAT.

$$I_{\mathrm{BAT}}(k-1) = \frac{SoC(k) - SoC(k-1)}{\Delta t} \cdot \mathrm{Q}_{\mathrm{Bat,nom}} \tag{6.29}$$

The inverse equation of the SC can be derived based on the SC current equilibrium. From Figure 6.7 can be derived that the SC current is equal to the output currents of the FC's and BAT's DC-DC converter minus the current drawn by the motor inverter. Equation 6.30 summarises the current equilibrium of the SC node.

$$I_{\mathrm{SC}}(k) = I_{\mathrm{BAT}}^{'}(k) + I_{\mathrm{FC}}^{'}(k) - I_{\mathrm{M}}(k) \tag{6.30}$$

Since the DC-DC converter dynamics are not considered and they are modelled based on an ideal transformer, the output current of the BAT and of the FC can determined based on the ratio of the specific source voltage and the voltage of the SC. The DC-DC converter efficiency is assumed to

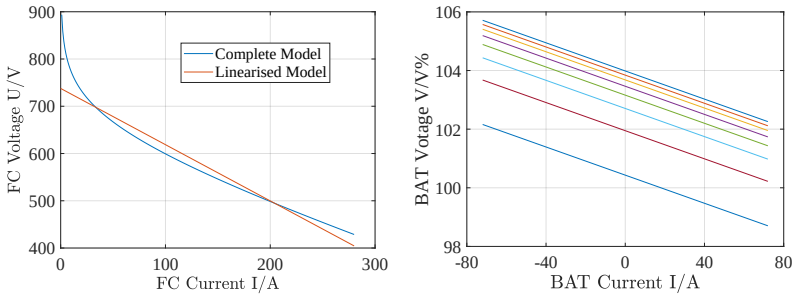

(a) (b)

Figure 6.8: a) Results of a simulated FC current sweep, compared for the non-linear model and the linearised approach. b) Simulation results of a current sweep from the maximum charge to the maximum discharge current for eight different SoC values between 90 % and 20 %.

be constant and expressed with a factor.

$$I'_{\mathrm{BAT}}(k) = I_{BAT}(k) \cdot \frac{\eta_{\mathrm{DC}} \cdot U_{\mathrm{SC}}(k)}{U_{\mathrm{BAT}}} \tag{6.31}$$

$$I'_{\mathrm{FC}}(k) = I_{\mathrm{FC}}(k) \cdot \frac{\eta_{\mathrm{DC}} \cdot U_{\mathrm{SC}}(k)}{U_{\mathrm{FC}}} \tag{6.32}$$

To determine the source voltage is a more difficult task. In accordance to Section 3.3.3, the voltage of the BAT depends non-linear on the SoC. The FC model discussed in Section 3.3.2 also shows that the FC model is not only characterised by the linear ohmic losses but also by the non-linear exponential activation losses. In summary can be stated that the BAT as well as the FC output voltages are determined by non-linear equations. In order to reduce the require calculation time, a simpler linear inverse model is derived.

As long as solely ohmic losses are assumed, the FC voltage can be expressed by a linear equation, see Equation 6.33. Nevertheless, if only the original ohmic losses are assumed, the results for low to medium currents deviate significantly, while the results at high current are accurate. In order to minimise the error over the complete operation range, a linear regression is used to minimises the mean voltage error. The derived equivalent source voltage is 740 V and the equivalent ohmic resistance with 1.2 Ω. Figure 6.8 a) depicts the results of a FC current sweep. The simulation results for both, the complete non-linear model and the linearised

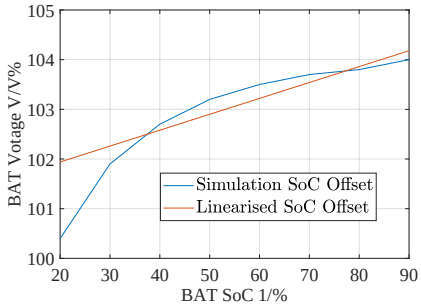

Figure 6.9: Comparison of the BAT voltage, simulated related to the SoC offset and a linearised SoC offset.

approach are compared. It can be seen that over the complete operation range an equally distributed error occurs.

$$U_{\mathrm{FC}}(k) = I_{\mathrm{FC}}(k) \cdot \mathrm{r_{FC}} + U_{\mathrm{FC,Source}} \tag{6.33}$$

Figure 6.8 b) depicts the simulation results of the BAT model, here a current sweep from the maximum charge to the maximum discharge current for eight different SoC values between $90\,\%$ and $20\,\%$ was outlined. The simulation results show that the voltage is proportional to the SoC. In contrast it can be seen that the voltage gradient does not change with the SoC. So, in order to form a linear BAT model, a two stage linearisation was applied. While the voltage gradient can be determined from an arbitrary SoC, the SoC dependency of the offset needed to be linearised. Figure 6.9 depicts the offset related to BAT SoC as well as the linearised offset. Equation 6.34 summarises the linear mathematical expression used to determine the BAT output voltage based on the BAT current and the SoC. The parameters were determined based on a linear interpolation of the SoC and current depended voltage, $\mathrm{m_{Bat}}$ is the voltage gradient, $\mathrm{m_{SoC}}$ and $\mathrm{b_{SoC}}$ describe the SoC related offset.

$$U_{\mathrm{BAT}}(k) = I_{\mathrm{BAT}}(k) \cdot \mathrm{m_{BAT}} + SoC(k) \cdot \mathrm{m_{SoC}} + \mathrm{b_{SoC}} \tag{6.34}$$

Finally with the linear expressions, Equations 6.33 and 6.34, a mathematical term capable to determine the SC voltage solely related to the

inputs, I_{FC} and I_{BAT} and the disturbance I_M, can be derived.

$$\begin{aligned} U_{\mathrm{SC}}(k) = & \frac{\eta_{\mathrm{DC}}}{U_{\mathrm{SC}}} \cdot \left(I_{\mathrm{FC}}^2(k) \cdot \mathrm{r_{FC}} + I_{\mathrm{FC}} \cdot U_{\mathrm{FC,Source}}\right) \\ & \frac{\eta_{\mathrm{DC}}}{U_{\mathrm{SC}}} \cdot (I_{\mathrm{BAT}}^2(k) \cdot \mathrm{m_{BAT}} \\ & + I_{\mathrm{BAT}} \cdot (SoC(k) \cdot \mathrm{m_{SoC}} + b_{\mathrm{SoC}})) - \frac{P_{\mathrm{M}}}{U_{\mathrm{SC}}(k)} \end{aligned} \tag{6.35}$$

Since the BAT current can be determined only based on the deviation of the SoC, the required inverse equation to determine the first input is 6.29. The deviation of the SC voltage in combination with a predefined BAT current and the motor current I_M determines the FC current. When the quadratic Equation 6.35 is solved with regards to the FC current an inverse system description capable to calculate the second input was derived. Equation 6.36 depicts the described inverse state equation used to determine the FC current.

$$\begin{aligned} I_{FC} = & -\frac{U_{\mathrm{FC,source}}}{2 \cdot \mathrm{r_{FC}}} - \left(\frac{U_{\mathrm{FC,source}}^2}{4 \cdot \mathrm{r_{FC}^2}} - (I_{\mathrm{BAT}}^2 \cdot \mathrm{m_{BAT}} \cdot \eta_{\mathrm{DC}} \right. \\ & + I_{BAT} \cdot \eta_{\mathrm{DC}} \cdot (SoC \cdot \mathrm{m_{SoC}} + \mathrm{b_{SoC}}) - P_M - (U_{\mathrm{SC}}(k) \\ & \left. -U_{\mathrm{SC}}(k-1)) \cdot U_{\mathrm{SC}}(k) \cdot \mathrm{C_{SC}}) \cdot \frac{1}{\eta_{\mathrm{DC}} \cdot \mathrm{m_{FC}}} \right)^{\frac{1}{2}} \end{aligned} \tag{6.36}$$

With Equations 6.36 and 6.29 two inverse state equations, which describe the two inputs with regards to a change of the state variable were derived. The BAT current solely depend on the change of the SoC. In contrast the FC current depends on the motor current, the change of the SC voltage, and the BAT current.

6.4. Disturbance Model

In the last section the inverse system model was discussed. The presented state equation conclusively prove the impact of the driver and the vehicle's physical properties which both determine the power demand of the electric drive. Back state that the prediction of the specific characteristics of a driver as well as the driving variation due to the behaviour of other road users is quite difficult. Nevertheless, distinct legal rules and long-term driver characteristics in combination with sufficient future traffic and road data allow to predict the vehicle velocity adequately in order to estimate the future power demand. The driving characteristics or the acceleration are not only related to the driver's preference but severe road conditions

due to bad weather, the road condition or corners and bends also have a significant impact [17]. The prediction of the power demand is an essential requirement in order to determine the optimal FC and BAT current trajectory. The disturbance model derived in this work includes the longitudinal dynamics of the vehicle characterised by the driver, the weather and the road as well as the vehicle and the driving trip characteristics. The overall objective is to derive a power demand prediction based on on-board information. The first part will discuss technical options to predict the vehicle's velocity, subsequently followed by the second part which concentrates on the prediction of the electric drive's power demand.

Today navigational systems are standard features of all medium-sized vehicles. Thus, it can be considered that in all cases a FHEV will contain a navigational system. Back give a brief description of how the vehicle position is adapted to a virtual map based on the internal GPS sensor. A key aspect is the limitation of the vehicle positions to be at defined roads. Based on this assumption, map matching algorithms are typical used to fit the vehicle position to the road system data and estimate the future road section. In order to support the vehicle localisation algorithm data from the internal velocity and the yaw rate sensor are also used. Digital maps help the navigational systems to identify an optimal path to reach a given target. Therefore, roads and road characteristics are described in the Geographic Data Files standard [287]. Freuer emphasise the importance of digital maps to provide predictive trip data. Today digital maps can be used to support the automotive environmental sensors and extend the near-field environment model beyond the standard range of $100\,\mathrm{m}$. This concept is typically called an electronic horizon [287, 288]. An electronic horizon contains information with regards to the road bending, legal speed limits, locations of crossings, signalling installations and pedestrian crossings and specific priority rules. In automotive applications, a standard commercial available system that provide predictive road informations is the Advanced Driver Assistance System Research Platform [289].

Today, the prediction of future road characteristics can be realised based on a navigation system or it can be estimated with a "Most Probable Path" algorithm [290]. Techniques which do not use digital road maps are also discussed, especially self-learning approaches can be considered as promising alternatives. In these approaches vehicle on-board sensor data is used to extract road parameter. Over time, a road information system is successively created [291, 292]. The same technique can also be applied in a swarm approach, here all road users cooperatively contribute to the derivation of a road information system [293, 294].

Table 6.1: Characteristic features of RADAR, LIDAR and camera sensor systems [18, 26].

Criterion	RADAR	LIDAR	Camera
Position	+	+	-
Velocity	+	-	-
Velocity	+	-	-
Object Detection	+	+	+
Object Recognition	+/-	+	+
Lane Detection	-	+/-	+
Traffic Sign Detection	-	-	+
Weather	+	+	-
Light	+	+	-

Not only a digital map can be used to create an electronic horizon, especially in close range environment on-board sensors perform better. Freuer evaluate three close-range environment sensor technologies typically applied in automotive applications. The evaluated sensors concepts are radio detecting and ranging (RADAR), light detecting and ranging (LIDAR) and a camera. Based on the specific fundamental operating principle individual benefits and limitations are discussed, the results of the comparative evaluation are summarised in Table 6.1. RADAR sensors use high frequent electro-magnetic waves and evaluate the reflected response in order to detect objects. Due to the used electro-magnetic waves RADAR sensors are robust against changing light or weather conditions, but suffer from lower resolution. A camera records its environment based on the photoelectric effect. In combination with sophisticated image processing software, objects like other road users or traffic signs can be detected and identified. Since an optical measurement is applied, cameras are vulnerable against non optimal light and weather conditions. Nevertheless, under suitable condition a complete picture of the driving environment can be extracted [295]. The operation principle of LIDAR sensor is similar to the one of a RADAR sensor, but instead of continuous electromagnetic waves, pulsed laser beams are used to determined the distance to recognised objects. LIDAR sensors combine the beneficial feature of RADAR and camera sensors. They are robust against changing light or weather and have a high accuracy and resolution. Drawbacks are the high required volumetric space and the high cost.

In Chapter 3.3 a driver was already technically described as a classic controller. In the virtual test bench a PI controller was tuned in order to realise a predefined maximum acceleration in order to follow a specific velocity profile. In contrast, the electronic horizon based prediction module has to be capable to forecast the vehicle velocity reference trajectory. Different environmental and legal conditions and constraints as well as the driver preference define this velocity reference. The major factors are the legal speed limit, the maximum velocity in bends, the driving environment specific maximum speed and the weather condition related maximum velocity. Back give a comprised list of effects that determine the reference velocity and derive a set of equations which capable to determine the reference velocity. The legal speed limits ($v_{\S}$) are part of the road characteristics and are provided by the electronic horizon. The maximum lateral acceleration determines the maximum velocity when driving through bends and corners. The maximum lateral acceleration depends on the driver's preference as well as on safety requirements. Equation 6.37 defines the maximum velocity (v_b) related to the sharpness of the bend (κ) and the maximum lateral acceleration ($a_{lateral}$).

$$v_{\mathrm{b}} = \sqrt{\frac{a_{\mathrm{lateral}}}{\kappa}} \tag{6.37}$$

The environment also has an impact on the reference velocity. Bad weather or landscape related reduction of the maximum sight distance cause the driver to adapt the velocity to these conditions. If it is assumed that the driver follows legal regulations, the reference velocity is limited so that a full braking is possible within the sight distance. The sight distance related to obstacles or hill tops can be derived from the electronic horizon. The maximum velocity (v_{SD}) at which a full breaking in the sight distance (s_{SD}) is possible, can be determined based on the driver's reaction time (t_{react}) and the maximum deceleration of the vehicle (a_{min}).

$$v_{\mathrm{SD}} = -a_{\min} \cdot t_{\mathrm{react}} \sqrt{a_{\min}^2 \cdot t_{\mathrm{react}}^2 + 2 \cdot a_{\min} \cdot s_{\mathrm{SD}}} \tag{6.38}$$

The limiting influence of the weather, especially the combination of low temperature and rain, induce a significant reduction of the reference velocity. This influence can be determined based on on-board sensors. In commercially available vehicles different sensors are suitable to determine the rain and temperature conditions. Rain-sensing wipers are controlled by a rain sensor, typically an on-board thermometer is available, automated dimmed headlights contain light sensor or the air conditioning system a solar sensor. In [17] an approach to derive a driver specific

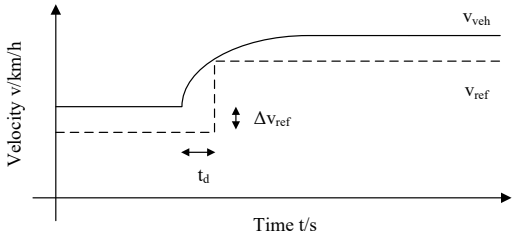

Figure 6.10: Principle concept of reference velocity step and the response of the driver reference velocity.

factor in combination with a fused weather index, a weather condition related reduction factor to adapt the maximum reference velocity v_{SD} was presented.

The maximum velocity reference results from the minimum of the above introduced velocity constraints. Since only location and velocity data of the test scenarios are available, not all of the introduced effects were considered. Instead a reference velocity trajectory based on legal speed limits as well as bends and crossing related velocity profile is determined. Legal speed limits as well as stops related to crossings induce steps in the velocity reference. Since a constraint vehicle acceleration as well as its inertia limit the rate of velocity changes, a modelling of the acceleration and deceleration processes, respectively of the driver characteristic, is required.

If it is assumed that the driver follows a specific reference velocity trajectory, a prediction of the actual vehicle velocity can be realised. Nevertheless a specific driver may not exactly follow the reference. For example, the absolute velocity may be higher or lower than the reference trajectory or the time required to react to a reference step may vary. Both driver and vehicle properties define the maximum acceleration. Figure 6.10 exemplary depicts a step of the reference velocity and the corresponding response of the driver reference. The negative delay time (t_d) points out that the driver starts accelerating prior to a reference velocity. The offset Δv_{ref} indicates that the example driver exceeds the reference velocity, thus the velocity is typically higher than legal or safety requirements demand. In related literature, different approaches to classify and identify driver behaviour are discussed. Murphey et al. introduce a jerk profile and classify driver characteristics based on the measure of how fast a driver is accelerating and decelerating. In [297] drivers are classi-

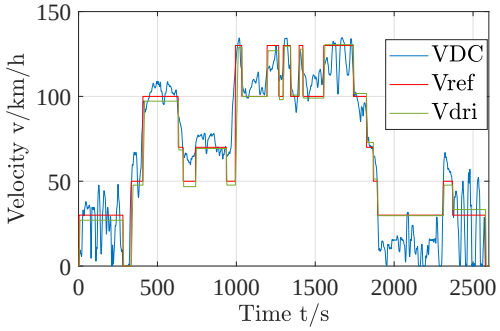

Figure 6.11: Comparison of a recorded DC and the resulting predicted reference and driver velocity.

fied on the basis of fuel consumption, a Fuel Consumption Index (FCI) is introduced and used to compare driver's performance.

In order to predict the trajectory of a vehicle velocity, piecewise constant accelerating and decelerating factors (a_{max}, a_{min}) are assumed. Equation 6.39 summarises the implemented case differentiation. The acceleration is varied between the discrete factors: a_{max}, zero and a_{min}. Whereas ϵ defines the allowable deviation between the vehicle velocity and the reference trajectory. The maximum delay time τ_v is equal to the time span required to reduce the vehicle velocity with the maximum decelerating factor a_{min} after a negative reference velocity step occurs. Thus, in order to guarantee to follow a specific velocity trajectory it is required to find the next negative step and the related maximum time delay τ_v.

$$a(t) = \begin{cases} a_{\max} & v(t) < v_{\text{ref}} - \epsilon \\ 0 & |v(t) - v_{\text{ref}}| \leq \epsilon \\ a_{\max} & v(t) > v_{\text{ref}}(t + \tau_v) \end{cases} \tag{6.39}$$

Because the recorded test cases contains only the vehicle velocity and the road inclination, a method to derive the legal speed limits was developed. The recorded DC is analysed and the actual velocity assigned to a discrete velocity class. In accordance to standard German speed limits these classes are $30\,\mathrm{km\,h^{-1}}$, $50\,\mathrm{km\,h^{-1}}$, $70\,\mathrm{km\,h^{-1}}$ and $100\,\mathrm{km\,h^{-1}}$. In order to also consider stops and not limited motorways, two additional classes, stop and $130\,\mathrm{km\,h^{-1}}$, are formed. Even while German motorways do not have a standard speed limit, the advisory speed is equal to $130\,\mathrm{km\,h^{-1}}$. The transitions between two different consecutive reference speeds are estimated based on the acceleration determined with Equation

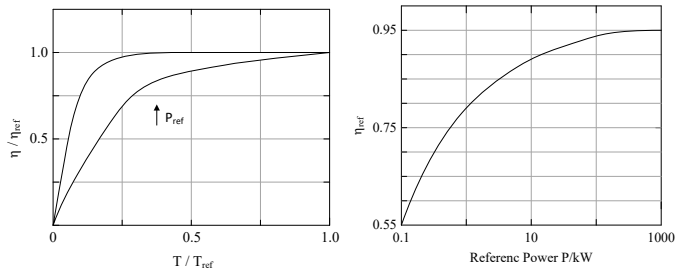

(a) (b)

Figure 6.12: Efficiency characteristics of asynchronous motors. (a) Efficiency characteristic related to the torque demand. (b) Ratio of reference efficiency related to the power reference. [19].

6.39. Figure 6.13 depicts an exemplary DC and the corresponding predicted velocity trajectory.

With the determined future vehicle velocity and road gradient it is possible to predict the power demand of the electric drive. Section 3.3.1 discusses a vehicle model used in the virtual test bench. In that model the longitudinal vehicle dynamics, the electric drive and the tire were modelled with predefined blocks from the MATLAB® Simulink® and Simscape® technical computing and simulation environment. Nevertheless, since the implementation in a MPC algorithm requires a fast calculation time, a simplified model was derived.

Similar to the model discussed in Section 3.3.1, the forces equilibrium is used to derive an equation to determine the torque that acts on the drive shaft. Equation 6.40 determines the torque required from the motor to accelerate the vehicle and to overcome the restive torque which result from the equilibrium of forces. The friction force F_R, the aerodynamic force F_a, the downhill force F_G as well as the inertia have to be overcome in order to propulse the vehicle with the acceleration a.

$$T_{\mathrm{M}} = (F_{\mathrm{R}} + F_{\mathrm{a}} + F_{\mathrm{G}} + m_{\mathrm{Vehicle}} \cdot a) \cdot \frac{r_{\mathrm{W}}}{r_{\mathrm{gear}}} \tag{6.40}$$

The estimation of the losses of an electric drive depends on the type of motor which shall be assessed. Since an asynchronous motor is assumed, the losses are characterised by the hysteresis losses of the stator and the rotor as well as the mechanical friction losses [19]. Key feature of the efficiency characteristics of an asynchronous motor is the positive

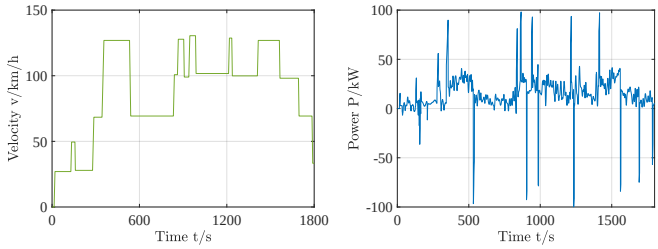

(a) (b)

Figure 6.13: (a) Predicted Velocity Trajectory (b) Predicted Power Demand

correlation between reference power and efficiency as well as the load independent share of the magnetising current. In summary, the efficiency of an asynchronous motor is sensitive against low load condition. Figure 6.12 (a) depicts the ratio of the efficiency to the reference related to the ratio of torque to reference torque. In total, two different characteristics for two different machines with different reference power values are depicted. Figure 6.12 (b) illustrates the reference efficiency related to the reference power. While a significant efficiency reduction for low torques is obvious, also the decreasing dependency of the efficiency with increasing motor reference power can be recognised. In general can be stated that the efficiency reference correlates positive to the power reference. Both figures indicate that an electric drive with an automotive suitable reference power (Toyota Mirai $115\,\mathrm{kW}$) in general has a high reference efficiency and shows a strong efficiency dependency only at low power conditions, under $20\,\%$ of the reference torque. Because an electric motor with comparable high reference power was not available to empirically determine the efficiency characteristic, a constant efficiency of $90\,\%$ was assumed.

Based on a constant motor efficiency and the equilibrium of forces, see Equation 6.40, the power demand of the vehicle can be predicted. Therefore, the predicted driver related velocity is used as a reference, the torque demanded to follow this velocity profile is determined with Equation 6.40, the shaft rotation derived from the requested vehicle speed, finally the power demand is estimated based on a constant motor efficiency. Figure 6.13 (a) exemplary depicts the predicted power demand required to follow the velocity reference shown in Figure 6.13 (a).

6.5. SINGLE STAGE MODEL PREDICTIVE CONTROL

In this section the development of a predictive optimal EMS based on the concepts MPC and DP is discussed. The derived EMS is capable to control the constraint non-linear dynamic system formed by a FHEV. The EMS is designed in order to minimise the hydrogen consumption as well as the degradation of the FC and of the BAT. In the beginning the EMS concept and the developed cost function are going to be discussed. Followed by the derivation of a two dimensional reduced state space, subsequently followed by an introduction of the software implementation. In accordance to Section 6.3 the plant controlled by the EMS can be summarised by the discrete state Equation 6.41. In the depicted equations, the index k represents the stage, respectively the discrete time step the optimisation is executed at. The state values in the subsequent state k+1 are derived based on the state equations F_{SoC} and $F_{V_{SC}}$, which are related to the inputs I_{FC} and I_{BAT} and the disturbance P_M, that corresponds to the power demand of the electric drive. The inputs as well as the states are constrained by the stage dependent minimum and maximum values.

$$\begin{bmatrix} SoC(\mathrm{k}+1) \\ U_{\mathrm{SC}}(\mathrm{k}+1) \end{bmatrix} = \begin{bmatrix} F_{\mathrm{SoC}}\left(SoC(\mathrm{k}), I_{\mathrm{BAT}}\right) \\ F_{\mathrm{V_{SC}}}\left(V_{\mathrm{SC}}(k), I_{\mathrm{BAT}}, I_{\mathrm{FC}}, P_{\mathrm{M}}\right) \end{bmatrix} \tag{6.41}$$

$$\begin{bmatrix} I_{\mathrm{BAT}} \\ I_{\mathrm{FC}} \end{bmatrix} = \begin{bmatrix} I_{\mathrm{BAT,min}}, I_{\mathrm{BAT,max}} \\ 0, I_{\mathrm{FC,max}} \end{bmatrix} \tag{6.42}$$

$$\begin{bmatrix} SoC \\ V_{\mathrm{SC}} \end{bmatrix} = \begin{bmatrix} SoC_{\mathrm{min}}, SoC_{\mathrm{max}} \\ V_{\mathrm{SC,min}}, V_{\mathrm{SC,max}} \end{bmatrix} \tag{6.43}$$

The concept of the presented predictive EMS approach is a MPC which is solved based on DP. A MPC controller and the receding horizon concept was discussed in Section 6.1. DP as a tool to solve a constraint dynamic optimisation problem was introduced in Section 6.2. Figure 6.18 depicts a schematic representation of the implemented MPC based predictive EMS. In each time step the SoC and the SC voltage as well as the vehicle velocity is measured and applied to the prediction module. The disturbance is predicted based on the current vehicle speed and the predictive information of the electronic horizon. This information contain the future vehicle velocity, the acceleration and the road inclination. Based on the measured SoC and SC voltage and the predicted disturbance, the extremal trajectories of the states and inputs are determined. With the predicted load demand and the extremal states, the constraint dynamic optimisation problem can be solved.

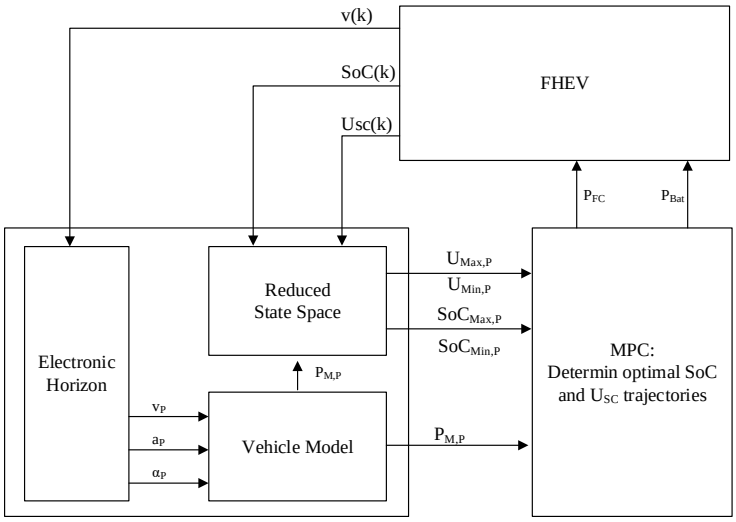

Figure 6.14: Schematic representation of the predictive EMS scheme containing the MPC controller and the states and disturbance prediction.

An essential aspect of the discussed MPC algorithm is the applied cost function. Different objectives have to be followed, the hydrogen consumption has to be minimised, the degradation of the BAT and the FC reduced and the SC voltage and the SoC controlled in a way that those are within the operation boundaries. While the costs which are used to account for the consumed hydrogen can be comparably easy estimated, the costs which are used to evaluate the impact of operation conditions that induce degradation of the FC and of the BAT as well as the costs related to the deviation of the SC voltage are more challenging. The hydrogen costs can be determined based on the FC current and a cost factor C_{H2}. The costs related to the deviation of the SoC and the SC voltage can be evaluated based on two cost factors. The costs which account for the degradation of the BAT can be expressed by the reduction of the SoH. In accordance to Section 2.2.1, the FC degradation is primary caused by high and low load condition. Thus, these costs are related to high and low load condition and can be determined with two factors (C_{LP}, C_{LP}). These two factors are switched between predefined values and zero with regards to the FC current. Equation 6.44 summarises the developed cost function that is used in the predictive EMS approach. Since a combination of state and input related cost is implemented, a parallel optimisation of the state transition and of the energy consumption was realised.

$$\begin{aligned} C_{\text{total}} =& |\Delta SoC| \cdot C_{\text{SoC}} + |\Delta V_{\text{SC}}| \cdot C_{\text{SC}} + \Delta SoH \cdot C_{\text{BAT}} \\ &+ I_{\text{FC}} \cdot (C_{\text{H2}} + C_{\text{HP}} + C_{\text{LP}}) \end{aligned} \tag{6.44}$$

Because the cost for hydrogen and the components are determined by commercial market prices, all other cost factors are estimated related to these fixed costs. In Germany the specific hydrogen cost are set by the H2 Mobility consortium to be $10.70\,\$/\text{kg}$. This consortium is formed by different market-relevant companies. With Equation 3.7, see Section 3.3.2 in Chapter 3.3, the cost related to a specific hydrogen consumption can be estimated with regards to a specific FC. The cost that are caused by a deviation of the BAT SoC can be estimated in analogy to the ECMS scheme discussed in Section 5.5 of the previous chapter. The concept is to assume that every SoC difference has to be balanced by the FC. Thus, when the efficiencies of the two DC-DC converter and a FC energy equivalent related to a specific SoC reduction are considered, the required deviation cost factor can be determined. The factors which account for the component degradation are determined based on the commercial costs of a FC and a BAT. In Section 2.1.3 and 2.1.1 the costs for a commercial available BAT and FC are introduced. With the specific power and specific energy related costs a realistic estimation of the costs for a $100\,\text{kW}$ FC and a $4\,\text{kWh}$ BAT is possible. Since a SoH reduction is directly related to the BAT's cycle life, the factor C_{BAT} is equal to the BAT system cost. The derivation of the SoH based on the operation condition is described in Appendix D. The applied SoH model was derived based on [298] and [27]. The FC degradation cost can be determined based on a lifetime prediction and the FC system cost. Chen et al. present a method to predict the commercial lifetime of a FC. The lifetime can be estimated based on the different voltage degradation factors and the minimum FC voltage. In [24] these degradation factors are empirically determined for the different degradation effects that act on a $10\,\text{kW}$ FC. Based on the presented lifetime prediction model and the commercial FC system cost, two factors (C_{HP}, C_{LP}) which are used to evaluate the cost induced by high and low load condition are derived.

The characteristics of the FHEV energy system, respectively the behaviour of the state variables is defined by the inputs. Due to technical limitations, both inputs are constrained by minimal and maximal currents. A current beyond these extremal parameters would cause either damage the component irreversible or is physical impossible. The minimal FC current is zero, the maximum current of the selected FC is $280\,\text{A}$. Since

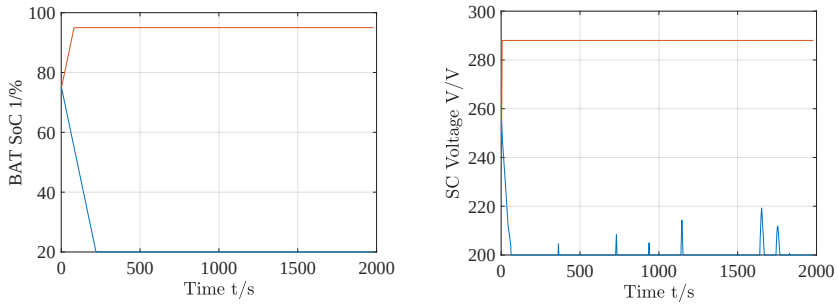

(a) (b)

Figure 6.15: (a) Exemplary trajectory of the reduced state space BAT SoC. (b) Exemplary trajectory of the reduced state space SC voltage.

the BAT can be charged and discharged, the maximum current is defined by the maximum discharge current and the minimal current is equal to the maximal charge current. The state variable itself is also constrained. The BAT's depth of discharge has a significant impact on the BAT life span. The maximum SoC is limited by the fact that in all cases a recuperation reserve is required. The SC voltage is constrained by the voltage demand of the motor inverter. For the assumed system, an operation limit of +/- 25 % is defined.

So far only absolute boundaries were discussed. In order to reduce degradation, inputs transients are also limited. Since current transients significantly reduce the FC health, the maximum allowable FC current transient is set to be equal to 20 % of the reference current per second. Because the BAT is more robust, a maximum current derivative of 40 % of the BAT reference current per second is assumed.

In Section 6.2 the concepts target-aimed, reachable and reduced state space are introduced, since no specific final SoC or SC voltage is required the reachable state space is equal to the reduced state space. The maximum input derivatives in combination with the initial states and inputs can be used to determine extremal trajectories. These are characterised by the stage related minimum and maximum SoC and SC voltage as well as the minimum and maximum BAT and FC current. The extremal trajectories define distinct maximum and minimum states and inputs for all stages. Thus, discritisation and evaluation of state nodes is only required within the extremal trajectory.

The reduced state space is estimated based on an iterative process,

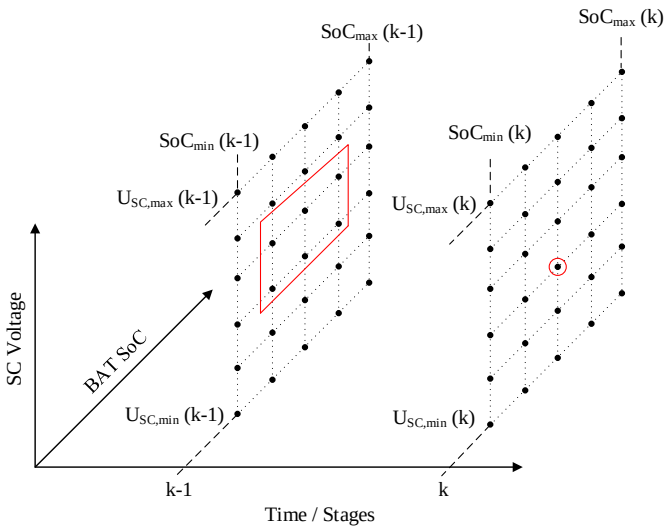

Figure 6.16: Schematic representation of the two dimensional state grid.

which is successively executed for all stages until the end of the prediction horizon. In the first step the maximum and minimum inputs and states are determined. The maximum SoC at a specific state results from the maximum SoC of the previous stage and the maximum BAT current. The determination of the SC voltage based on the FC, the BAT current and the motor power demand was discussed in Section 6.3. Consequently, the minimum SC voltage can be determined with the minimum voltage and the minimum BAT and FC current and the motor power demand. Vice versa the maximum SC voltage based on the maximum BAT and FC current. Figure 6.15 depicts a reduced state and input space for an arbitrary DC. It can be seen that the extremal SoC, see Figure 6.42 (a), is a linear trajectory that starts at the initial SoC and ends at the maximum and minimum SoC. The gradient is defined by the maximum charge and discharge current.

In Section 6.2, DP was introduced as method to solve a constrained dynamic optimisation problem based on a forward recursion. In contrast to the discussed first order system, the solution of a second order system is more resources intensive and requires significantly more processing time. Equation 6.10 gives a simplified estimation of the computational burden. Due to the exponential characteristic, it can be seen that the system order is a crucial factor. The central problem is that with increasing system order, the number of discrete nodes at each stage rises exponentially. Since

the targeted second order system is characterised by two inputs as well as two states the problem is aggravated. Figure 6.18 depicts two exemplary stages of a two dimensional state node grid. At each stage the stage dependent state boundaries, SoC_{min}, SoC_{max} and $V_{SC,min}$ and $V_{SC,max}$ limit the state space. Nevertheless, the discrete state grid consists of n · m discrete nodes, m is the number of discrete SoC nodes and n the number of discrete SC voltage nodes.

The forward oriented DP approach was briefly discussed in Section 6.2. The implemented predictive EMS follows this scheme. In analogy to Figure 6.5 (b), for all stages and for all discrete nodes at each stage, the optimal predecessors and cost to go have to be determined, stored and the corresponding inputs for the previous stage estimated. In contrast to the discussed solution for a one dimensional state space, interdependencies between the two state variables and the inputs may complicate the structured evaluation of all valid predecessor. Nevertheless, since the SoC is independent from the SC voltage, a separated evaluation is possible. In all stages, two nested iterative processes are executed. The superordinated process estimates the cost of a specific SoC transition, the subordinated evaluates all SC voltage transition related to the given SoC transition. In order to limit the evaluation of state transitions, only valid predecessors of a specific discrete state have to be determined. A predecessor is valid if the transition from a specific state in stage k-1 to a given state in stage k can be reached without violating input constraints. Thus, the maximum and minimum inputs define the maximum and minimum predecessor. The concept of valid predecessors is depicted in Figure 6.18, for an arbitrary node at stage k, marked by the red circle, an arbitrary chosen quantity of valid predecessors at stage k-1 is marked by the red rectangle. So only transitions from this quantity of valid predecessors and not for all nodes at stage k-1, have to be evaluated.

The nested iterative evaluation of the state transitions and cost to go for the specific discrete state nodes at stage k starts with the determination of all valid SoC predecessors. The maximum and minimum SoC at stage k-1 depends on the maximum and minimum BAT current and the SoC at the subsequent stage k. With the SoC at stage k-1 and the inverse state equation, which are introduced in Section 6.3, the BAT current that triggers the transition from SoC(k-1) to SoC(k) can be determined. In a next step all valid SC voltage predecessors for a given SoC and a given BAT current are determined. The node dependent maximum and minimum SC voltage can be estimated with the BAT current, the load demand and the maximum and minimum FC current. Finally, all valid SC voltages are

successively varied and the related FC current determined. For all predecessor nodes these are characterised by the specific states SoC(k-1) and V_{SC}(k-1) and the corresponding inputs I_{BAT}(k-1) and I_{FC}(k-1), the cost to go to the discrete node at stage k are determined. Here the beneficial recursive character of the DP approach is utilised. Since the costs related to all nodes in all previous stages are already determined and stored in previous iterations, a recursive determination of the cost to go to the current node can be implemented. Equation 6.45 illustrates the recursive approach to determine the cost to go to the node n - m at stage k based on the cost of the predecessor n1 - m1 at stage k-1 and the corresponding transition cost defined by the related states and inputs.

$$\begin{aligned} J(k,n,m) = J(k-1,n1,m1)+ \\ C_{\mathrm{total}}(SoC(k), V_{\mathrm{SC}}(k), I_{\mathrm{BAT}}(k), I_{\mathrm{FC}}(k)) \end{aligned} \tag{6.45}$$

After all valid predecessors are evaluated, the minimum of all cost to go values is estimated. This minimum corresponds to the optimal cost to go and thus defined the optimal predecessor. In order to enable the recursive cost determination and to be able to reconstruct the optimal path, the predecessor and the related inputs are stored. The results of the forward iteration are matrices which contain the cost to go for each state node in all stages as well as the related inputs that trigger the transition from the optimal predecessor to the current node. In accordance to Section 6.2, the estimation of the optimal path can be realised in a backward oriented approach. This approach follows the minimum cost to go backwards and starts at the final stage. The node with the minimum cost to go defines the start at the final stage. After the optimal final node is identified, the optimal path is defined by the optimal predecessors.

A brief discussion with regards to criteria to determine the sampling interval is given in [17]. The central requirement for an real time application is the computational time. In contrast, when all given constraints shall be considered, the sampling interval has to be as large as possible. Back suggest to choose the maximum sampling interval, which still guarantees that all central system characteristics are time invariant. While standard procedures which are applied to linear system typically define a fixed ratio of sampling interval to system's Eigenvalues [299], comparable methods capable to handle non-linear systems do not exist [17]. For the implemented EMS a fixed sampling interval of $1\,\mathrm{s}$ is assumed. To define the maximum prediction horizon also has a significant impact on the required calculation time. Since an optimal control is the objective of the developed EMS, the optimality of the solution is the key criterion. In

general can be stated that an infinite prediction horizon would generate the best results. Therefore a maximum prediction horizon, which still enables a reasonable processing time should be chosen. Nevertheless, especially the uncertainty in the prediction of the disturbance impend a global optimal solution. The prediction of the road gradients depend on the configuration of the navigational system and the solution of the used map and thus the uncertainty of the road gradient can be considered as time invariant. In contrast, the quality of the prediction of the vehicle's velocity decreases over time. While in close range environment, the impact of other vehicles can be estimated, the prediction of future traffic situations is challenging. An increasing number of reference velocity steps causes a high uncertainty. With each step the real velocity vary stronger. Due to the cumulative characteristic of this error, the difference between actual velocity and reference increase over time. Back state that a reasonable prediction horizon is below one minute, Freuer realise a predictive cruise control based on a MPC with a prediction horizon of $60\,\mathrm{s}$.

In Section 6.2 the reduced discrete state space was introduced. A drawback for the estimation of the number of discrete nodes is the fact that the state boundaries depend on the stage, respectively on the maximal inputs and the disturbance. Thus a high resolution can be realised either in an early stage or in later stages. If a fixed number of grid nodes is defined the distance between the nodes is significantly smaller at early stage. Vice versa, if the distance between the nodes is constant, the number of nodes at early stages is quite small and thus the resolution significantly lower as for a fixed number of nodes. Since the length of the prediction horizon is limited a fixed number of nodes with high resolution in early stages was selected.

In order to analyse the impact of the prediction horizon and of the number of discrete nodes a part of arbitrary selected DC was optimised. The DP algorithm was executed with six different numbers of discrete grid node. The execution starts with ten discrete nodes per state, an increment of ten and a final number 60 discrete nodes was configured. For the prediction horizon three different intervals were selected. Figure 6.17 (a) depicts the required simulation time an a test machine related to the number of discrete nodes and to the length of the prediction horizon. Figure 6.17 (b) depicts the results. In order to guarantee comparability the cost are scaled to represent the final cost after Stage ten. An exponential dependency of the required calculation time can be identified. In contrast the length of the prediction horizon causes a linear offset.

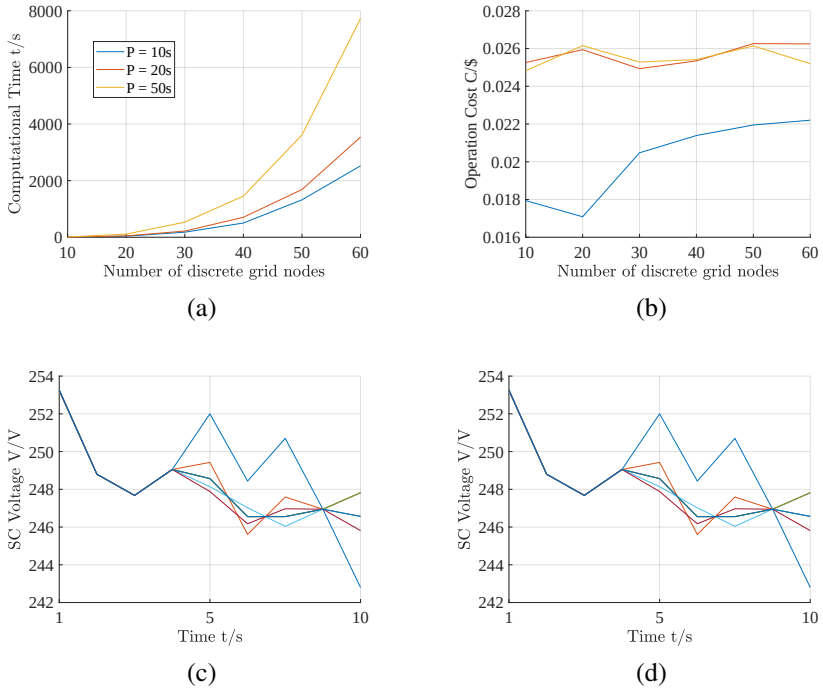

Figure 6.17: (a) Computational burden related to the grid size and prediction horizon P. (b) Estimated cost related to related to the grid size and prediction horizon P. (c) SC voltages for different number of discrete state grid and a prediction horizon P = 10s. (d) SC voltages for different number of discrete state grid and a prediction horizon P = 50s.

Figures 6.17 (c) and (d) depict the optimal SC voltage trajectory with different numbers of state nodes and two different prediction horizons. It can be seen that the results of the long horizon are equal to the one of the short term prediction. Thus, the short prediction horizon of $10\,\mathrm{s}$ can be applied. The cost depicted in Figure 6.17 (b) imply that the minimum cost are achieved with a comparably small number of 20 discrete grid nodes per state variable. Nevertheless, even with the small number of discrete state nodes and the short prediction horizon of $20\,\mathrm{s}$, the required time to solve the DP algorithm is in the range of $40\,\mathrm{s}$. In summary can be stated that due to the high computational burden the two dimensional approach to solve the MPC control problem, can not be implemented in real time. Nevertheless, the discussed concepts and methods are essential in order to derive a novel two level predictive MPC EMS approach.

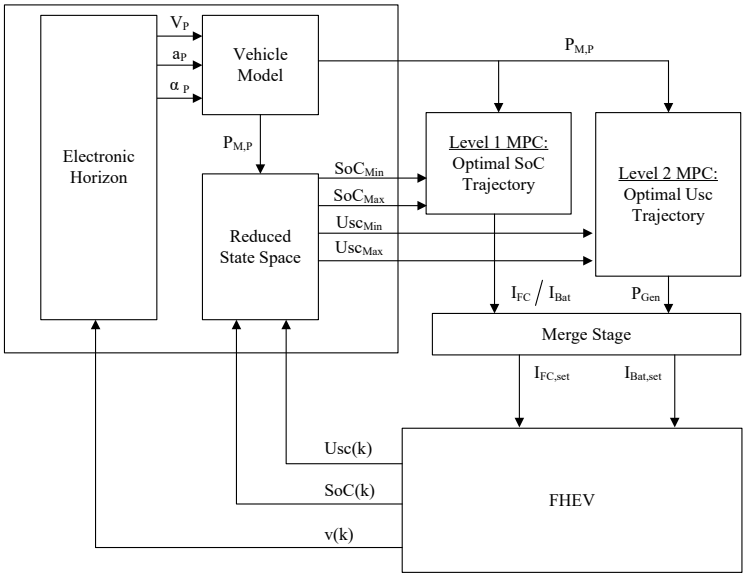

Figure 6.18: Schematic representation of the implemented concept of the predictive EMS scheme using a two level MPC.

6.6. Two Stage Multi-Level Model Predictive Control

In the previous section the high computational burden of the DP algorithm was discussed. However, the calculation time rises with the horizon length and exponentially with the system order and the number of inputs. Thus, for long prediction horizons, frequent updates of the MPC are not possible. A promising solution is to separate the MPC into two or more control levels, by dividing responsibilities between the different control layers, based on horizon length, update frequency, sampling interval or system states. To use a multi-level MPC is an efficient approach to control the powertrain of a HEV, examples are discussed in [31] and [300]. Bi-level approaches which combine an EMS and an optimal velocity control are also presented, [301] or [302]. In [275] a 2-level MPC for the combined energy management and velocity control of a HEV is discussed. The underlying concept of all multi-level DP approaches is to reduce the computational burden by either an independent evaluation of the different state variables or by the adaptation of the required grid resolution related to the given task.

An essential benefit of the given HES is the fact that the BAT SoC solely depends on the BAT current and neither on the FC current nor directly on the disturbance. In contrast, the SC voltage is defined by the BAT and the FC current as well as by the disturbance. Based on the implemented method to successively solve the two state DP, described in the previous section, an independent iterative estimation of the optimal SoC and SC voltage trajectory is possible. The SoC trajectory can be optimised based on the BAT related cost. Since the the BAT current also has an impact on the SC voltage, the disturbance and BAT current related FC current has to be determined and considered when the transition cost are determined. Otherwise, a SC voltage outside the operational borders is possible. The result of this optimisation stage are the optimal SoC path and the corresponding BAT and FC current trajectory, which are combined to create an optimal current ratio trajectory. In a parallel stage the optimisation of the SC voltage can be executed. Since the BAT current has also an impact, the FC current is not directly determined, instead an combined equivalent generator power is optimised. In this stage the cost for SC voltage deviation as well as the hydrogen consumption and the FC degradation are minimised. In a final fusion stage, the FC and the BAT current can be derived based on the generator power and the optimal BAT and FC current ratio.

Figure 6.18 depicts the parallel two level MPC approach. The prediction module works similar like the one described in the single level MPC. Based on the measured states and inputs as well as the information of the electronic horizon and the prediction of the future disturbance, extremal states and the reduced state space are determined. In two parallel executed DP processes the optimal SoC and the SC voltage trajectory are determined. Based on the optimal SoC, the BAT and the FC current ratio can be specified. In the second stage the optimal SC voltage with the related equivalent generator power are estimated. In the final stage both results are combined and the specific BAT and FC current are determined. In this section the implemented two stage MPC is going to be discussed. In the beginning, the determination of the optimal SoC and the corresponding FC and SC trajectory is presented. Therefore, the related SoC cost function as well as the estimation of the required cost factors are introduced. In the next part the optimisation of the SC voltage and the related cost function are discussed. Finally, the fusion stage that determines the FC and the BAT currents is presented.

To estimate the optimal SoC, a forward oriented DP algorithm, similar to the one discussed for the combined MPC, was used. In contrast, since

only one state variable is optimised, a one dimensional state grid has to be evaluated. Nevertheless, the successive evaluation of all discrete state nodes that starts with the second stage and processes forward in time, is outlined. At each node all transitions from all valid predecessors to the current state node have to be analysed. In order to evaluate these transitions, the cost to go from the specific predecessor to the current node, plus the cumulated cost of the predecessor are determined. After all valid predecessor cost are estimated, the one with the minimum cost to go is stored. This node is considered to be the optimal path to the specific node. Additionally to the costs, the optimal predecessor and the corresponding inputs are also stored. In the next stage the stored costs can be recursively used in order to determine the cost to go for that stage.

A predecessor is valid if the SoC value can be reached from without violating the BAT's maximum and minimum current. The SoC transition related BAT current can be determined based on the inverse system model, which was introduced in Section 6.3. In the optimal case, the deviation of the SC voltage is zero. This is guaranteed when the sum of BAT and FC output power is equal to the disturbance. Based on that assumption, a BAT current related FC current can be estimated. Nevertheless, not in all cases this equilibrium can be established. For example the recuperated power can exceed the maximal BAT charging capacity. Thus, a power deviation is also determined and evaluated. With the inputs, the state value and the predecessor cost, the cost to go to the evaluated discrete state node can be determined. If this is executed recursively, a cost to go grid for all state nodes is created. Because all optimal predecessors are also stored, an optimal path can be extracted. The node with minimum cost to go of the final stage determines the end of the optimal state trajectory.

With the stored predecessors, the path can be reconstructed in a backward oriented process, going from each optimal predecessor to the next. The result is the optimal state and input trajectory.

$$\begin{aligned} j_{\mathrm{SoC}} =& \Delta SoH_{\mathrm{Bat}} \cdot C_{\mathrm{Bat}} + C_{\mathrm{H2}} \cdot i_{\mathrm{FC}} + C_{\mathrm{dP}} \cdot dP \\ &+ (SoC \cdot C_{\mathrm{m,Bat}} + C_{\mathrm{b,Bat}}) \cdot i_{\mathrm{Bat}} \end{aligned} \tag{6.46}$$

To determine the cost to go of a specific state node, related to the actual state and the corresponding inputs a cost function is required. Equation 6.46 summarises the SoC related state transition cost. The degradation of the BAT is considered via the reduction of the SoH ($\Delta\mathrm{SoH_{BAT}}$) and the cost of the BAT ($\mathrm{C_{BAT}}$). The hydrogen consumption cost are determined similar to the one discussed for the combined one level DP approach ($\mathrm{C_{H2}}$, $\mathrm{i_{FC}}$). The equivalent BAT energy cost is evaluated based

on a SoC related BAT cost factor and the BAT current. The SoC related factor linearly depend on the SoC, expressed with a factor ($C_{m,BAT}$) and an offset ($C_{b,BAT}$). Both cost factors, C_{BAT}, which used to determine the cost related to the BAT degradation, as well as C_{H2}, that expresses the hydrogen consumption related cost, are determined with regards to the fixed market prices. The FC degradation cost are considered via an C_{H2} offset, which is discretely varied between C_{HP}, C_{LP} and zero related to the FC output current. Similar to Section 6.5, these factors are determined based on [24].

Since the SoC variation as well as the energy taken from the BAT shall both be accounted, the related cost function term depends on both, SoC and the BAT current. The underlying concept can be described as follows, with a decreasing SoC, the cost for discharging increases and the one for charging decreases proportional to the SoC. Vice versa, if the SoC is high the cost for discharging are low and for charging are high. Because for an SoC above the reference SoC an inverse behaviour is required, two different linear functions are determined. For a SoC which is below the reference, the cost factor linearly increases with a decreasing SoC. In that case, a positive discharging current in combination with this cost factor cause positive cost. Consequently, if the BAT is charged, indicated by a negative current, the cost become negative and thus charging is favoured. However, the SoC is above the reference a reverse characteristic is required, if the SoC increases discharging has to be in favour and charging has to cause high positive cost. Therefore, the linear factors are defined in order estimate cost which decrease linearly with an increasing SoC. The linear factors and the offsets of both linear equations are determined with regards to the cost for hydrogen.

In order to determine the required parameter that describes the cost for an SoC above the reference, it was assumed that the operation cost of $95\,\%$ charged BAT, which is charged with the maximum charge current, are equal to the hydrogen cost caused by an FC which generates the similar output power. Vice versa, to determine the required parameter used in the case the SoC is below the reference, it was assumed that the operation cost of $45\,\%$ charged BAT that is discharge with the maximum discharge current shall be equal to the cost caused by a FC which supplies the same power. The linear factor which is used to account for the power deviation (C_{dP}) was determined based on the precondition that the not supplied or not recuperated energy has to be substituted by hydrogen. Based on the mass related hydrogen price, the cost per kWh electrical energy which generated based on hydrogen can be estimated.

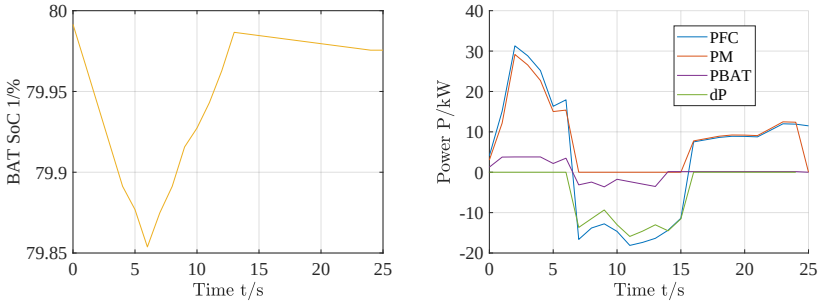

Figure 6.19: (a) Optimal SoC trajectory for an exemplary DC segment. (b) Power trajectory of the disturbance (PM), FC power (PFC), BAT power (PBAT) and power deviation (dP) for an exemplary DC segment.

Figure 6.19 depicts the results of the SoC DP algorithm for an exemplary DC segment. The optimal SoC trajectory is displayed in Figure 6.19 (a). The motor power demand as well as the FC and the BAT power are depicted in Figure 6.19 (b). In the first 10 s, the BAT is discharged, as soon as the power demand gets negative, the BAT power changes to charging. In the end of the trip the BAT is slightly discharged at low power. Over the complete trip the FC supplies the largest share of the demand and follows the motor power. The example shows that for the predicted short horizon the DP ensures that the operation limits are guaranteed.

In a parallel stage, the SC voltage is optimised. The forward oriented optimisation is executed with the target to estimate the optimal SC voltage trajectory and the required generator power under a given disturbance. Since both the BAT and the FC contribute to the power equilibrium that determines the SC voltage deviation, both sources are summarised as one generator. Because in this case only one input has to be considered, the complexity and computational burden of the DP is significantly reduced. The concept of the applied forward DP is similar to the one applied for the SoC optimisation. In this stage the cost to go for all valid predecessor are also successively determined. Again the optimal transition is defined by the predecessor with the minimum cost to go to the specific node under evaluation. With Equation 6.47 an equation that is capable to determine the maximum and the minimum valid predecessor for a specific node is derived. The maximum predecessors can be derived if the maximal BAT charging power and zero FC power is assumed. Consequently,

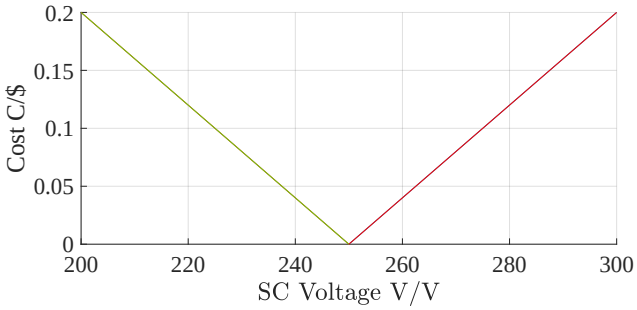

Figure 6.20: Cost factor related to the deviation of the SC voltage.

the minimum predecessor results if the maximum FC and maximum BAT discharging power is applied.

$$V_{\mathrm{SC}}(k+1) = V_{\mathrm{SC}}(k) - \frac{Z - P_{\mathrm{BAT}} - P_{\mathrm{FC}}}{C_{\mathrm{SC}}} \tag{6.47}$$

The input that corresponds to a specific SC voltage transition can in this case be estimated based on the inverse control oriented model, which was also introduced in Section 6.3. The required Equation 6.48 can be derived from Equation 6.47. The SC voltage transition is expressed by the state node (V_{SC}(k+1)) and the predecessor (V_{SC}(k)), the generator power is the sum of FC and the BAT power.

$$P_{\mathrm{Gen}} = C_{\mathrm{SC}} \cdot V_{\mathrm{SC}}(k) \cdot (V_{\mathrm{SC}}(k+1) - V_{\mathrm{SC}}(k)) + Z \tag{6.48}$$

Finally with the predecessors and the related inputs, the cost to go of all valid transitions to a specific state node can be determined. Similar to the SoC optimisation, the state transition with the minimum cost is the optimal one. Again, the stored cost as well as the input and the optimal predecessor are stored and recursively used in the next stage. After the complete grid is evaluated, the optimal SC voltage path can be determined if path of optimal predecessors is followed backward to the first stage of the prediction horizon. Again the node with the minimum cost at the final stage characterises the optimal final state. The optimal predecessors of that optimal final state define the optimal path.

The cost function which is used to evaluate the transition costs is given as Equation 6.49. In order to estimate the cost related to the energy consumption of the generator power, it was assumed that P_{GEN} is completely

supplied by the FC. Thus, the FC degradation costs (C_{HP}, C_{LP}) and the fix hydrogen consumption cost (C_{H2}) define the cost related to the input.

$$j_{SC} = \|P_{GEN}\| \cdot C_{H2} + CV_{SC} \tag{6.49}$$

Because the specific SC voltage has a significant impact on the performance of the complete HES and thus on the performance of the electric drive, not only the input costs, but costs directly related to the state trajectory are also considered. Since both positive and negative deviations of the SC voltage shall cause costs, two linear equations were defined. Figure 6.20 depicts the results of both linear cost factor functions for a SC voltage sweep. The parameters of the functions were determined based on the assumption that a SC voltage deviation of $5\,\mathrm{V}$ shall result in the same cost as the hydrogen cost at maximum FC output power. This narrow band of $10\,\mathrm{V}$ ensures that the SC voltage is within the input voltage range of the motor inverter at all times.

In order to analyse the performance of the DP algorithm used to optimise the SC voltage, two different exemplary DC segments were optimised. The selected example is characterised by an acceleration process with a maximum power demand of $100\,\mathrm{kW}$, the second segment is dominated by regular driving at medium power demand as well as a breaking event that results in a negative power demand which should be recuperated.

The results of both examples are depicted in Figures 6.21 (a)until (d). Figure 6.21 depicts the results of the acceleration example. In (a) the power demand (PM) and the equivalent generator power (PG) is depicted, in (b) the optimal SC voltage are illustrated. It can be seen that the optimal case is characterised by an equilibrium of generation and demand. This equlibrium lead to a constant SC voltage, with no deviation. In the recuperation example, see Figure 6.21 (c) and (d), the optimal case is characterised by maximum recuperation. The depicted results show that in order to maximise the recuperated energy, the SC is used as a buffer to overcome the limited BAT charging capability. Prior to the recuperation phase, that starts at $6\,\mathrm{s}$, the SC voltage is reduced and the BAT charged. As soon as the power demand gets negative, the BAT is charged and the SC voltage increases. This allows to maximise the recuperation. The overcharging of the SC to $255\,\mathrm{V}$ enables to supply the next acceleration process, which occurs at $18\,\mathrm{s}$, to be supplied by SC energy. After $20\,\mathrm{s}$ the power equilibrium is restored and the generator supplies the load.

After both parallel DP stages are executed, the final FC and BAT currents can be estimated. In order to determine the final optimal input tra-

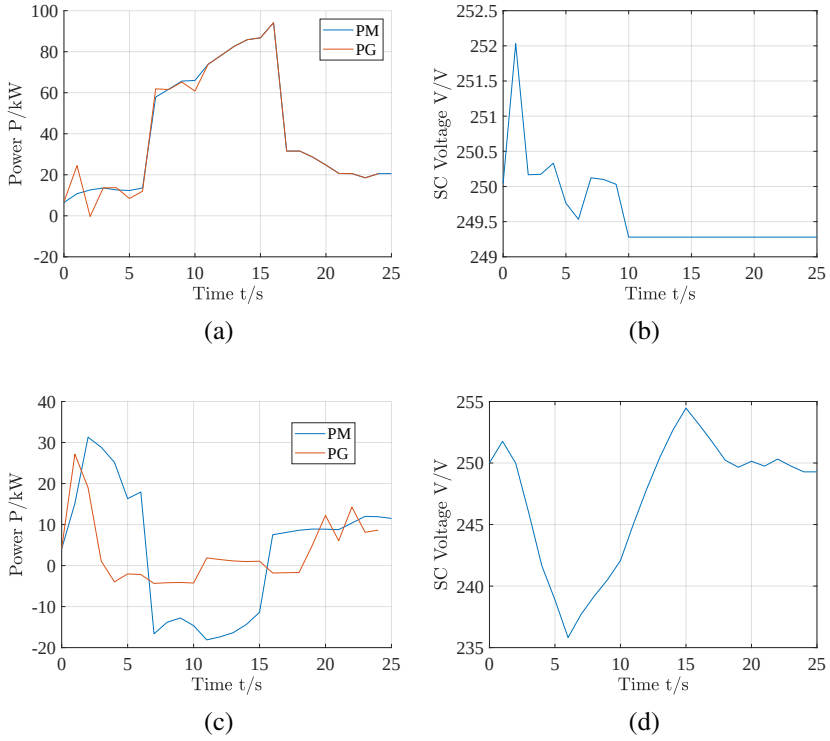

Figure 6.21: (a) Generator and motor power acceleration example. (b) Optimal SC voltage trajectory acceleration example. (c) Generator and motor power recuperation example. (d) Optimal SC voltage trajectory recuperation example.

jectory the results of both stages have to be combined. Because the SC voltage has the most significant impact, the results of the SC voltage optimisation has to be emphasised over the one of the SoC optimisation. This was realised in the final merge stage. To guarantee the optimal SC voltage trajectory, the sum of the combined power is equal to the estimated generator power. The power share between FC and BAT is oriented at the results of the SoC optimisation. As long as the estimated generator power is positive, respectively power has to be supplied, the sum of the BAT and the FC output power has to be equal to the generator power. The ratio of the FC to the BAT output power, which are estimated during the SoC optimisation, defines the distribution of the reference power. The related FC output power can be determined based on the difference

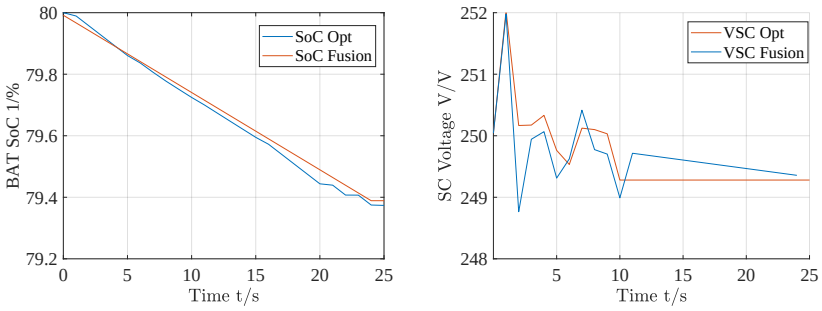

(a) (b)

Figure 6.22: (a) Optimal SoC and resulting SoC after the merge stage. (b) Optimal SC voltage and resulting SC voltage after the merge stage.

of the generator and the BAT power. Equations 6.51 and 6.52 summarises the power references for a positive power demand. In the case that the BAT power is zero, the final BAT reference power is also zero and the FC supplies the complete generator power. If the generator power is negative, which means that energy has to be recuperated, the BAT output power reference is set to the negative generator power and the FC output reference to zero.

$$P_{\mathrm{BAT,ref}} = P_{\mathrm{G}} \cdot \frac{P_{\mathrm{BAT}}}{P_{\mathrm{FC}}} \tag{6.50}$$

$$P_{\mathrm{FC,ref}} = P_{\mathrm{G}} - P_{\mathrm{BAT,ref}} \tag{6.51}$$

$$\tag{6.52}$$

Figure 6.22 depicts the optimal state trajectories and the results of the merge stage. It can be seen that the reference SoC is close to the optimal one. While in the optimal case the BAT is in general discharged faster, the merged results show a smaller overall discharge rate. Only in the first $4\,\mathrm{s}$ the reference SoC decreases stronger than the optimal one. The reference SC voltage is close to the optimal trajectory, only between $t_1 = 4\,\mathrm{s}$ and $t_2 = 4\,\mathrm{s}$ a deviation of $1\,\mathrm{V}$ occur. Because a MPC applies only the first input values to the actuators, this deviation can be neglected.

In order to test and evaluate the performance of the developed predictive optimal EMS scheme, the scheme was implemented based on the Matlab® technical computation environment and simulated on the Matlab® Simulink® based virtual test bench introduced in Chapter 3.

Table 6.2: Simulation results for DP based EMS

Criterion	MF	MD	RF	RD	UF	UD
η_{system} [%]	53.7	53.8	51.6	53.0	53.8	62
SoC_{max} [%]	80.0	80.0	80.0	80.0	80.0	80.0
SoC_{min} [%]	55.9	58.8	65.9	58.7	70.0	58.0
$\text{U}_{\text{SC, max}}$ [V]	305.0	293.8	304.6	302.0	294.4	310
$\text{U}_{\text{SC, min}}$ [V]	193.8	207.2	200.6	201.0	216.2	221.2
$\text{P}_{\text{FC,mean}}$ [kW]	37.5	25.2	26.5	20.3	18.9	15.7
$\text{E}_{\text{Bat,mean}}$ [kWh]	1.24	1.62	1.27	0.96	0.63	1.12
n_{H2} [$\text{kg}\,100\,\text{km}^{-1}$]	1.30	1.21	0.82	0.67	0.80	0.74
FC_{max} [s]	40	41	26	10	11	11
FC_{min} [s]	120	332	278	203	231	298

All functional modules were implemented as Matlab® functions. The single functions were than combined in order to form the control scheme depicted in Figure 6.18. To guarantee a sampling interval of 1 s, the complete EMS scheme was executed in a simulation time controlled subsystem. In order to test the DP algorithm under the same condition as the standard EMS schemes, the test cases described in Section 3.1 were used as test DCs.

Table 6.2 depicts the results of the evaluation of the two stage DP EMS scheme. Since the applied test procedure is similar to the one outlined in Chapter 5, which was used to evaluate the state of the art EMS approaches, the same evaluation criteria were used in order to assess the performance of the novel DP EMS. In contrast to the standard EMS schemes, in most test cases the DP control is capable to use the BAT more efficiently. Clear indicators are the lower average SoC and the low overall BAT energy equilibrium deviation ($\text{E}_{\text{Bat,mean}}$). The low minimum SoC indicates that during one test scenario the BAT highly contributes to the overall energy supply. Even while the BAT is significantly discharged, the low overall BAT energy reduction ($\text{E}_{\text{Bat,mean}}$) proves that the BAT is also regularly charged. The higher BAT usage leads to two beneficial effects, one is the higher overall efficiency and the second is that high FC power fluctuations are also reduced.

The average maximum and minimum SC voltage indicates that the SC usage is also significantly higher than for the standard schemes. This high SC utilisation enables to operate the FC and the BAT more often in optimal operation regions, which minimises both hydrogen consumption

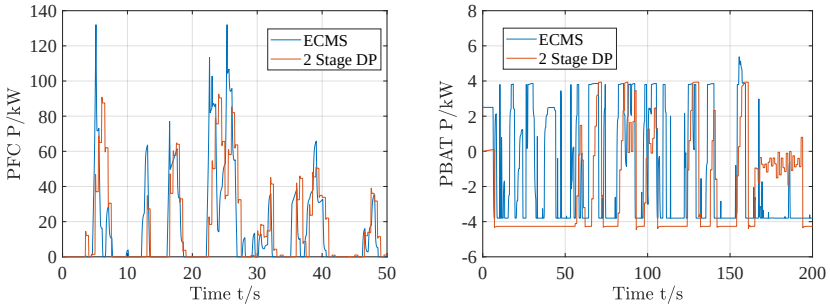

(a) (b)

Figure 6.23: (a) FC power for ECMS and DP EMS approaches in an exemplary interval of the Artemis 130MW DC. (b) BAT power for ECMS and DP EMS approaches in an exemplary interval of the Artemis 130MW DC.

and the degradation of the components. The essential advantage is that not the current power demand, but the energy required to ensure that the state variables are within the operation limits, is provided. The improvements of the presented EMS scheme can clearly be seen when it comes to the hydrogen consumption. Only in motorway driving scenarios the ECMS approach achieves a lower consumption rate, in all other driving scenarios the DP approach has the lowest consumption rates. Furthermore, the operation intervals when the FC provides non optimal low and high power are significantly reduced. This proves that the new two stage DP control approach also induce the lowest FC degradation, only the ECMS approach operates the FC under comparable optimal conditions.

Figure 6.23 (a) depicts the FC power trajectory of the ECMS and the one of the DP approach for an exemplary interval of the Artemis MW130 DC. Since the ECMS showed best performance in the evaluation outlined in Chapter 3, it was selected as performance measure to evaluate the DP approach. The depicted interval was selected because it contains both high acceleration rates as well as medium velocity and thus high power peaks as well as medium power demand. In the depicted trajectories, two significant differences can be derived. Both, the maximum as well as the derivative of the DP generated FC power are lower than the one determined by the ECMS scheme. While the ECMS controlled FC has to follow steep power transitions, the FC output power defined by the DP approach is characterised by stepwise transitions. These steps ensure

smooth power transients and limit the maximum FC power transients, this guarantees a minimum FC degradation.

Figure 6.23 (b) depicts the BAT power generated by both control schemes in the same DC interval. While in the ECMS controlled system the BAT power changes frequently direction and amplitude, these changes occur in the DP controlled system scheme less frequently. Additionally these changes are executed as stepwise transitions. Both power trajectories, FC and BAT, indicate that high frequent changes as well as the maximum derivatives are limited and thus component degradation is also limited. In summary can be stated that the presented two stage optimal DP based MPC control approach is capable to both minimise the energy consumption as well as the degradation of the FC and of the BAT. Due to the two stage parallel approach the computation time required to solve both DP procedures was reduced from $40\,\mathrm{s}$ to under $250\,\mathrm{ms}$.

The time required to solve the optimisation of the SoC is $147\,\mathrm{ms}$, the one required to solve the optimisation of the SC voltage $70\,\mathrm{ms}$. The calculation times were determined for a prediction horizon of $25\,\mathrm{s}$ and a SoC grid with 25 nodes per time step and 50 discrete nodes per stage for the SC voltage grid. The algorithm was executed based on Matlab® working on an Intel® Core™ i7-4770 and 16 GB main memory. Thus, a real time execution with a sampling interval of $1\,\mathrm{s}$ is possible. Further improvements are expected if the discussed approach is implemented on an embedded micro-controller system.

6.7. SUMMARY

In this chapter the predictive optimal control of a FHEV was discussed. Based on the analysis and evaluation of the standard EMS schemes outlined in Chapter 5, the need for a predictive optimal approach was derived. The related literature emphasises that a MPC oriented approach is the most suitable one [17, 31, 149, 272, 274]. The central objective to minimise the hydrogen consumption and the degradation of the BAT and the FC is characterised by a constrained non-linear optimisation problem, which was solved based on DP. A key drawback of the DP algorithm is its exponential dependency of the computational burden on the number of states and inputs. In order to overcome this challenge, a novel two stage DP approach which optimises the SoC and the SC voltage in parallel was developed and implemented. The underlying concept of the developed approach is to separately optimise the BAT SoC and the SC voltage. When both state variables are optimised in two separate DP algorithms, the specific system order is reduced to one and the computational burden of the

single DP procedure is significantly be reduced. In this chapter a comprehensive overview of the required background regarding MPC and DP concepts are given. Additionally, a control oriented inverse system model as well as a disturbance model are introduced.

In a first step the development of a combined DP approach capable to optimise both state variables is discussed, based on this single stage approach the two stage concept is derived and the implementation of the novel approach presented. Because the underlying control scheme of the predictive EMS was implemented as a MPC controller, the chapter starts with introducing the concept and basics of a MPC control scheme. After the receding horizon concept and the optimisation problem that arises from the MPC concept were introduced, DP as powerful mathematical tool capable to find the global optimal of a constraint non-linear optimisation problems was discussed. The analysis of standard backward oriented DP approaches proves that a forward oriented DP algorithm offers significant advantage. An essential benefit is that neither interpolation of inputs nor of states between different nodes of the discrete state and input space is required. Based on the theoretical discussion of the forward oriented DP it is derived that both a load demand and driving prediction as well as, a control oriented inverse system model is required. The prediction of the future load and velocity trajectory was realised with an electronic horizon. Because in a forward oriented approach the inputs are determined based on specified deviations of the states, an inverse model was also required.

Based on this inverse system description corresponding inputs which are related to defined states deviation can be estimated. In Section 6.3 and 6.4 both concepts are discussed. In the next Section 6.5 the development, implementation and test of a combined DP based MPC is presented. Because of the high computational burden and the long processing time, the test proves that this single stage approach can not be applied to real systems. Finally, in the last section the development and evaluation of a two stage approach is discussed. A schematic representation of the novel two stage DP can be found in Figure 6.18. The evaluation was done based on the virtual test bench presented in Chapter 3. The results prove that both energy consumption as well as degradation enhancing operation condition are minimised. Additionally the execution time was also reduced, so that a implementation in a real time system can be outlined.

The developed two stage approach is executed in different consecutive steps. Each sampling interval starts with the measurement of the states, inputs and the disturbance. Based on the current states and inputs, in combination with a driving condition prediction based on an electronic

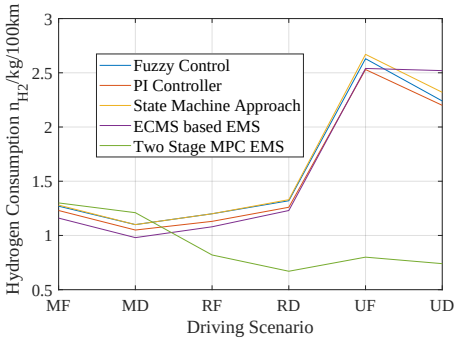

Figure 6.24: Overall hydrogen consumption rates for the different EMS approaches and simulated DCs.

horizon, the future load demand and the maximum and minimum future states and inputs are estimated. These extremal states and inputs allow to determine two reduced discrete state grids. These grids correspond to discrete representations of the SoC and the SC voltage. In two parallel forward DP procedures the optimal paths through the discrete state grids are determined. Therefore, in each stage for all discrete state nodes the cost to go are estimated. The cost to go results from the sum of cost to go of the predecessor and the cost related to the state transition. Based on the inverse system model described as in Section 6.3, the inputs to a specific state variation are determined. In combination with the cost function the related cost can estimated. After all discrete nodes are evaluated for all stages, the optimal trajectory can be extracted with a backward oriented recursion which follows the path with minimum cost to go. Finally, in a last step, the two different sets of optimal inputs which result from the two independently determined optimal state trajectories are merged and the optimal actuator reference is determined.

The key measures to evaluate the performance of the presented EMS strategy are the hydrogen consumption, the BAT degradation and the operation induced degradation of the FC. A comparison with the results of the standard EMS evaluation discussed in Chapter 5, points out the significant improvements and contribution offered by the two stage multi-level MPC in relation to state of the art EMS strategies. Figure 6.24 shows the hydrogen consumption rates for the evaluated driving scenarios and the EMS strategies under test. The depicted results illustrate the reduction of the hydrogen consumption especially for rural as well as urban driving which can be achieved in the case the discussed two level MPC is applied.

Table 6.3: Performance indicators for all EMS strategies under test.

Criterion	Fuzzy Control	PI Control	State Machine	ECMS	Two Stage MPC
η_{system} [%]	50.7	52.8	49.9	52.9	54.7
$\Delta\text{SoC}_{\text{max}}$ [%]	3	4	3	13	18
$\text{E}_{\text{Bat,mean}}$ [kWh]	1.2	1.3	2.2	2.9	1.1
Deg_{FC} [$\text{s}\,\text{kW}^{-1}$]	3.3	35.5	8.3	83	11
n_{H2} [$\text{kg}\,100\,\text{km}^{-1}$]	1.63	1.57	1.65	1.59	0.93

In contrast to the consumption rate, there is no clear measure to rate the reduced degradation of the components. Table 6.3 summarises performance criteria as mean values over all simulated driving scenarios. A measure for the static degradation cost of the FC can be derived based on the time in low and high load condition related to the mean FC power (Deg_{FC}). The index expresses the ratio of the FC in harmful operation condition to optimal operation points. The FC degradation caused by dynamic load changes for standard EMS was evaluated in Figure 5.13. The depicted results indicate that both the state machine as well as the Fuzzy controller cause high dynamic load changes and power transients and thus high FC dynamic FC degradation. Hence, combining both measures (static operation points and dynamic load changes), the presented two stage DP EMS cause the lowest overall FC degradation. The BAT usage can be summarised based on the SoC deviation and the energy transferred. Even while the two level MPC shows a high SoC deviation, the energy transferred is lowest. Which means that in total less SoC cycles are passed and thus less BAT degradation encountered.

In terms of computational burden, the processing time of the DP program for a specific stage is the key measure. Figure 6.17 depicts the required computation time for the discussed standard one stage DP approach related to the number of discrete nodes and the prediction horizon. For a prediction horizon of $25\,\text{s}$ and 25 nodes per time step the single stage approach can be solved in $1800\,\text{s}$. In contrast, the two stage approach which split the DP program into two parallel first order systems can be solved in $200\,\text{ms}$. Thus, the presented two level approach enables the implementation of a DP based MPC as EMS in a real FHEV.

7

CONCLUSION AND OUTLOOK

In general FC (Fuel Cell) based vehicles show significant advantages compared to a BEV (Battery Electric Vehicle) or ICV (Internal Combustion Engine Vehicle): they do not depend on depleting fossil fuels, do not produce harmful emission, can be refuelled fast, the energy density of a FC based storage is high and the waste heat generated by the FC can be used to support the heating of the vehicle's passenger compartment. In total, these advantages enables a FHEV (Fuel Cell Hybrid Electric Vehicle) to drive longer distances and cause that the operation of a FHEV is closer to the costumer mobility patterns so far dominated by ICVs. Nevertheless, FCs have to face some drawbacks. The limited power dynamics of the FC and the lack to store recuperated energy while breaking have to be named. FHEV powered by a combination of a FC, a BAT (Battery), and a SC (Super Capacitor) are capable to overcome these limitations. The underlying concept of a FHEV is to make best use of the specific benefits of the different energy sources in order to overcome the drawbacks of the single technologies. Unfortunately, a FHEV also has some drawbacks, especially these are the cost, the uncertain durability and the spare refuel infrastructure, which yet have prevented FHEVs from being competitive with ICEs. Nevertheless, economics of scale and technological advances will lead to reduced costs. [3] proved that for a large scale deployment of FHEV, the costs required to implement a sufficient infrastructure are below the infrastructure costs for a comparable high BEV market share. One essential aspect that can have a significant

effect on the performance and contributes to increase the durability of the FC of the vehicle as a whole, is the EMS.

The key objective of the presented work was to develop an optimal operation concept of a FHEV, which is capable to both minimise the hydrogen consumption as well as the degradation of the BAT and of the FC. Since the operation characteristic, the operation temperature as well as the specific operation scenario have a significant impact on the performance and degradation of the system, all three aspects have to be considered. The solutions discussed in this work approach both. These are an EMS which controls the power distribution and operation states of the individual sources as well as a TMS (Thermal Management System) which is capable to guarantee the optimal operation temperatures of the components and to support the heating of the passenger compartment by reuse of the FC's waste heat.

Evaluation and test always requires test cases. Because the driving scenario has an important impact on the performance of a FHEV, representative test cases which were generated based on real world driving data were used as test scenarios. The required driving data was gathered with a smartphone application which record data from the smartphone's internal GPS sensor. In total over 500 different trips were recorded and used to generate the required test cases. In order to identify three basic drive scenarios (motorway driving, rural and urban), a feature set was configured. The identification of the specific driving scenario was realised based on FCM (Fuzzc c-means Clustering). A second FCM was used to subdivide the three sets, each in two different clusters representing dense traffic and free flow. In order to be able to test the developed EMS approach, a test bench based on a forward oriented physical model which includes the vehicle's forward dynamic as well as the components of the HES (hybrid Energy System), was implemented. The required power capacities of the motor and the individual power sources were determined based on literature as well as drivability constraints. The parameters which describe the configuration of the modelled power train were solely determined based on data sheets. A laboratory scaled version of the hybrid power system was configured and used to validate the developed models.

In the second part a TMS was developed. The first step was the development of a suitable cooling loop topology as well as a control strategy. After the system configuration was completed, a detailed physical mathematical model that integrates the fluid mechanics, the heat transfer, and all relevant component was designed. Additionally, a hierarchical control strategy to operate the thermal system was developed and implemented.

The control approach contains sub controllers for each component which were optimised for the specific operation state. A state machine governs the overall operation of the system. The performance of the TMS was validated based on the simulation model. The presented TMS is capable to ensure optimal operation temperature for all components in all relevant operation condition.

Prior to the development of the novel EMS (Energy Management System) scheme, standard EMS approaches were analysed. Therefore, the most discussed control approaches (PI Control, State Machine, Fuzzy, and ECMS) were implemented and tested. The evaluation was outlined based on the virtual test bench introduced in Chapter 3. In summary can be stated that both the high efficiency and the low hydrogen consumption confirm that the ECMS ($\eta_{\text{System}} = 52.8\,\%$, $n_{H2} = 1.57\,\text{kg}\,100\,\text{km}^{-1}$) and the PI ($\eta_{\text{System}} = 52.8\,\%$, $n_{H2} = 1.57\,\text{kg}\,100\,\text{km}^{-1}$) approach are the most promising EMS schemes. Even if the evaluation shows that some of the approaches, here especially the PI approach and the ECMS, show with regards to the hydrogen consumption satisfying results, non approach is capable to completely take the component degradation into account.

The evaluation of the standard EMS schemes clearly indicates the potential for optimisation. In order to fill this gap, a MPC (Model Predictive Control) in combination with a DP (Dynamic Programming) approach was developed. The prediction of the future load and velocity trajectory was realised with an electronic horizon. Since the recorded test cases contain only the vehicle velocity and the road inclination, the prediction of the electronic horizon was emulated based on the apriori known DC. Due to its significant advantages, especially the fact that interpolation between discrete point is not necessary, a discrete forward oriented DP approach was implemented. The required inverse system model, that is capable to determine the inputs based on state variations was derived with regards to the models used to implement the virtual test bench. Since the standard DP algorithm suffers from a high computational burden which increases exponentially with the system order and with the number of inputs, a novel two stage approach based on DP was developed. Because the BAT SoC (State of Charge) is an independent state variable and solely depends on the BAT current, an independent DP based optimisation is possible. Since the BAT current influences the SC voltage and the FC current, this also has to be considered for the optimisation of the SoC. The related cost functions include costs which account for the SoC deviation, the BAT as well as the FC current and the degradation of both BAT and FC. The BAT related degradation costs are determined based

on the reduction of the SoH (State of Health), whereas the costs with regards to the FC degradation were directly derived from the FC current. In a second parallel executed stage, the SC voltage is optimised. The results of this optimisation are the optimal voltage trajectory as well as an optimal trajectory of a virtual generator power. In order to estimate the costs caused by the generator power, it was assumed that this power is solely generated based on the FC, respectively on hydrogen. Finally both optimal trajectories are combined and the optimal input for the specific time step is determined. In summary, a predictive optimal EMS based on a MPC control scheme and a two stage DP approach that is capable to minimise the hydrogen consumption and the components degradation was presented and the implementation discussed.

It can be stated that the major objectives of this thesis were achieved. In the detailed analysis of all relevant aspects of FHEV, outlined in Chapter 2, the specific operation characteristics of the components of a FHEV were discussed. The operation conditions which induce and catalyse degradation mechanism are identified and analysed in detail. Finally the most suitable system topology and a conventional system design, both electrical and thermal were outlined. In Chapter 2 a comprehensive survey of the technological challenges and opportunities offered by FHEV was given. After an analysis of existing TMS was given, requirements for efficient control of a FHEV were derived. Based on this analysis the design of a suitable TMS system which guarantees optimal operation temperatures and enables the reuse of waste heat for heating the passenger compartment was presented. The model based implementation shows that the TMS controlled by a hierarchical control system is capable to control the operation temperatures of all components included in a FHEV. The reuse of waste is also realised. The presented virtual test bench was used to outline a detailed performance analysis of the most important state of the art EMS schemes. Real world driving data was transferred to a set of representative test cycles which enables to test the EMS schemes under all driving scenarios. Finally the development of an energy optimal predictive EMS which minimises both, the hydrogen consumption and the component degradation was presented. The reduction of the applied DP's computational burden and processing time, was achieved by the development of a two stage parallel optimisation approach. The presented approach enables the application of DP for a two input second order system and the optimisation in a reasonable processing time. Each of the applied cost factors have been weighted based on a real component data and commercial hydrogen costs. Since the total operation costs which

include the costs caused by component degradation, are considered. The real operation costs of the FHEV are minimised.

The analysis outlined in the beginning of this work shows that in the wide field of operation condition which induce the degradation of a BAT, overcharging, deep-discharge, excessive cycling as well as high and low temperatures have the strongest impact. The analysis of FC degradation mechanism proves that high cell potentials, frequent start-up and shut-down, fuel starvation caused by high currents and current transients as well as a high operation temperature and current cycling have a strong negative effect. Thus, the EMS has to consider that these negative operations are avoided. The components operation temperatures are controlled by the developed and implemented TMS. The presented simulation results indicates that the designed system is capable to solve the given task. Exemplary, the warm up of the BAT as well as BAT radiator cooling were analysed. Also the warm up of the FC through the waste heat of the power electronic components and the cooling of the vehicle interior at an environmental temperature of $30\,^{\circ}\mathrm{C}$ are evaluated. In order to access the performance of the standard EMS schemes, specific criteria were defined. The simulation with the representative real world test DC (Drive Cycle) shows that the ECMS as well as the PI control scheme are capable to operate the FHEV under the lowest hydrogen consumption. The PI scheme achieves an average hydrogen consumption rate of $1.57\,\mathrm{kg}\,100\,\mathrm{km}^{-1}$, the ECMS approach $1.58\,\mathrm{kg}\,100\,\mathrm{km}^{-1}$. The novel optimal predictive EMS control scheme was tested based on the same virtual test bench and with the same test DC. The simulation results prove the superior performance of the MPC control scheme. In the outlined tests, the predictive EMS was capable to operate the FHEV with an average hydrogen consumption rate of $0.8\,\mathrm{kg}\,100\,\mathrm{km}^{-1}$. Whereas optimisation was achieved evenly over all examined DC categories. Thus, related to the hydrogen consumption a significant increase of the performance is proved. Especially in urban and rural drive scenarios the novel approach shows significant advantages. A clear indicator of the operation induced degradation of the FC is the time the FC is operating under high or low power. In the group of standard EMS schemes, the PI control shows the best results. The FC operates in total $8\,\mathrm{s}$ at high power and $3099\,\mathrm{s}$ at low power. The DP approach also shows a superior performance in this criteria, the FC controlled by the DP approach in total $133\,\mathrm{s}$ at high power and $1462\,\mathrm{s}$ with low output power. The power transients which result from the EMS scheme are analysed based on the Artemis 130MW DC and compared to the results of the ECMS approach. In comparison, the change of the BAT power,

in both directions as well as power amplitude, occur less frequent for the DP based EMS. A similar reduction of the FC power transients can be noticed. In summary can be stated that the MPC control scheme limits both high frequent changes as well as the maximum current derivatives and thus also the degradation effects.

In conclusion, the work outlined in this thesis demonstrates that a predictive optimal EMS implemented as a DP based MPC is suitable to minimise in parallel the hydrogen consumption and the degradation of the FC and BAT of a FHEV. Additionally, it was proven that a TMS based on four different cooling loops is capable to guarantee optimal operation temperatures of the component and that an integration of the FC waste heat in the PCs heating is possible. Considering the achieved performance with regards to the reduction of the hydrogen consumption rate as well as operation condition that cause the reduction of the FC and the BATs durability, the presented concept shows great potential to contribute to the goal that FHEV become more competitive with current ICE and BEV vehicles.

There are a number of recommendations for further research and actions on the matter. These can be separated into two major tasks. One task is to integrate and implement the presented predictive optimal MPC based on the two stage parallel DP as well as the presented TMS at real hardware. The second central task is to utilise synergy effects which arise if the TMS is integrated in the overall EMS control scheme. Even while the simulation results show that the processing time was significantly reduced after the two stage DP approach was implemented. Nevertheless, the application of the presented approach on a real hardware system is the next step to further validate the concepts and the results discussed in this thesis. In order to realise this implementation, the scaled hardware system which was used to validate the component models is going to be extended. So far, a multi-input DC-DC converter was developed and implemented on a PCB. The developed DC-DC converter is capable to control the output current of the FC and of the BAT. Thus, this converter is the optimal actuator that is capable to realise the FC and BAT currents which are determined by the EMS.

The control of the hardware test bench was realised as a model-based control approach based on the National Instrument's technical computation environment LabVIEW^{TM}. With the model of the vehicle and the electric drive, the power demand of the drive-train that follows a specific DC is estimated. This power demand is scaled to the power reference of the hardware. Finally, a DC load controlled by LabVIEW^{TM} applies the

determined power demand to the hardware system. In a further project the developed MPC EMS is evaluated on this scaled hardware system. This test and evaluation will prove that the presented approach is capable to be implemented on a real time system and can be executed within a required sampling interval of $1\,\mathrm{s}$. After the validation based on the scaled hardware test bench is successfully completed, the EMS has to be implemented on an embedded system and integrated in real HES or vehicle power train.

To make best use of the developed TMS, it has to be included into the EMS scheme. Different concepts are possible. So far the most promising approach is to add an additional DP stage. Because the discussed TMS control system is used to follow predefined reference currents, the proposed system can easily be integrated into a superior control structure. The DP based MPC determines the optimal component temperatures and the TMS follows the references. In this stage the operation temperatures of the components are optimised. Therefore, an inverse simplified model of the TMS has to be developed. The model has to be capable to determine the power demand of the TMS related to the change of the components temperatures. A cost function which considers the component degradation related to a deviation of the specific component's temperature from the optimal temperature and the power demand caused by a desired temperature change has to be developed. The costs which arise from the energy demand of the TMS, can be assessed similarly to the assumption used to optimise the SC voltage. If it is assumed that the demanded power is solely supplied by the FC, the specific power demand related costs, can be determined only based on a linear hydrogen consumption related cost factor. Since so far the developed TMS was validated only based on a model, the design and implementation of a hardware system is also required. The system shall be oriented at the proposed system topology with four cooling loops. Since most of the required components are not standard commercially available systems, the implementation of the TMS is challenging. Thus it is planned to realise the hardware system as well as a MPC based superior control in an additional research project.

REFERENCES

[1] U. Eberle, B. Müller, and R. von Helmolt, "Fuel cell electric vehicles and hydrogen infrastructure: status 2012," vol. 5, p. 8780.

[2] A. Mahmoudzadeh Andwari, A. Pesiridis, S. Rajoo, R. Martinez-Botas, and V. Esfahanian, "A review of battery electric vehicle technology and readiness levels," *Renewable and Sustainable Energy Reviews*, vol. 78, pp. 414–430, 2017.

[3] "Comparative analysis of infrastructures: Hydrogen fueling and electric charging of vehicles," Jülich, Germany.

[4] "Fuel cell technologies office: Multi-year research, development, and demonstration plan." [Online]. Available: https://www.energy.gov/eere/fuelcells/downloads/fuel-cell-technologies-office-multi-year-research-development-and-22

[5] Q. Xun, Y. Liu, and E. Holmberg, "A comparative study of fuel cell electric vehicles hybridization with battery or supercapacitor," in *2018 International Symposium on Power Electronics, Electrical Drives, Automation and Motion (SPEEDAM)*. Piscataway, NJ: IEEE, 2018, pp. 389–394.

[6] R. Schmuch, R. Wagner, G. Hörpel, T. Placke, and M. Winter, "Performance and cost of materials for lithium-based rechargeable automotive batteries," *Nature Energy*, vol. 3, no. 4, pp. 267–278, 2018.

[7] F. Herb, "Alterungsmechanismen in lithium-ionen-batterien und pem-brennstoffzellen und deren einfluss auf die eigenschaften von daraus bestehenden hybrid-systemen," Disseration, Universität Ulm, Ulm, 2010.

[8] E. V. Thomas, H. L. Case, D. H. Doughty, R. G. Jungst, G. Nagasubramanian, and E. P. Roth, "Accelerated power degradation of li-ion cells," *Journal of Power Sources*, vol. 124, no. 1, pp. 254–260, 2003.

[9] P. Zhou, "Electric vehicle thermal management system," Patent.

[10] T. Mahlia, S. Tohno, and T. Tezuka, "A review on fuel economy test procedure for automobiles: Implementation possibilities in malaysia and lessons for other countries," *Renewable and Sustainable Energy Reviews*, vol. 16, no. 6, pp. 4029–4046, 2012.

[11] S. M. Njoya, O. Tremblay, and L.-A. Dessaint, "A generic fuel cell model for the simulation of fuel cell vehicles," in *IEEE Vehicle Power and Propulsion Conference, 2009*. Piscataway, NJ: IEEE, 2009, pp. 1722–1729.

[12] S. N. Motapon, O. Tremblay, and L. A. Dessaint, "Development of a generic fuel cell model: application to a fuel cell vehicle simulation," *International Journal of Power Electronics*, vol. 4, no. 6, p. 505, 2012.

[13] O. Tremblay and L.-A. Dessaint, "Experimental validation of a battery dynamic model for ev applications," *World Electric Vehicle Journal*, vol. 3, no. 2, pp. 289–298, 2009.

[14] H. Großmann, "Heizung, lüftung, klimatisierung von pkw," in *VDI-Buch, Aerodynamik des Automobils: Eine Brücke von der Strömungsmechanik zur Fahrzeugtechnik*, pp. 757–805.

[15] D. Wen, "Analysis of buck converter efficiency."

[16] I. Staffell, "Results from the microcab fuel cell vehicle demonstration at the university of birmingham," vol. 3, p. 62.

[17] M. Back, "Prädiktive antriebsregelung zum energieoptimalen betrieb von hybridfahrzeugen," Ph.D. dissertation, Universität Fridericiana Karlsruhe.

[18] A. Freuer, *Ein Assistenzsystem für die energetisch optimierte Längsführung eines Elektrofahrzeugs*. Wiesbaden: Springer Fachmedien Wiesbaden, 2016.

[19] G. Müller, B. Ponick, and (Keine Angabe), *Grundlagen elektrischer Maschinen*, ser. Elektrische Maschine. Hoboken: John Wiley & Sons, 2012.

[20] X. Hu, C. Zou, C. Zhang, and Y. Li, "Technological developments in batteries: A survey of principal roles, types, and management needs," *IEEE Power and Energy Magazine*, vol. 15, no. 5, pp. 20–31, 2017.

[21] A. Berrueta, A. Ursua, I. S. Martin, A. Eftekhari, and P. Sanchis, "Supercapacitors: Electrical characteristics, modeling, applications, and future trends," vol. 7, pp. 50 869–50 896.

[22] A. Hintz, U. R. Prasanna, and K. Rajashekara, "Novel modular multiple-input bidirectional dc–dc power converter (mipc) for hev/fcv application," vol. 62, pp. 3163–3172.

[23] F. A. de Bruijn, V. A. T. Dam, and G. J. M. Janssen, "Review: Durability and degradation issues of pem fuel cell components," *Fuel Cells*, vol. 8, no. 1, pp. 3–22, 2008.

[24] H. Chen, P. Pei, and M. Song, "Lifetime prediction and the economic lifetime of proton exchange membrane fuel cells," *Applied Energy*, vol. 142, pp. 154–163, 2015.

[25] B. Vural, S. Dusmez, M. Uzunoglu, E. Ugur, and B. Akin, "Fuel consumption comparison of different battery/ultracapacitor hybridization topologies for fuel-cell vehicles on a test bench," *IEEE Journal of Emerging and Selected Topics in Power Electronics*, vol. 2, no. 3, pp. 552–561, 2014.

[26] H. Winner, S. Hakuli, and G. Wolf, *Handbuch Fahrerassistenzsysteme: Grundlagen, Komponenten und Systeme für aktive Sicherheit und Komfort*, 2nd ed., ser. ATZ/MTZ-Fachbuch. Wiesbaden: Vieweg + Teubner, 2012.

[27] S. Ebbesen, P. Elbert, and L. Guzzella, "Battery state-of-health perceptive energy management for hybrid electric vehicles," *IEEE Transactions on Vehicular Technology*, vol. 61, no. 7, pp. 2893–2900, 2012.

[28] C. C. Chan, "The state of the art of electric, hybrid, and fuel cell vehicles," vol. 95, pp. 704–718.

[29] B. G. Pollet, I. Staffell, and J. L. Shang, "Current status of hybrid, battery and fuel cell electric vehicles: From electrochemistry to market prospects," vol. 84, pp. 235–249.

[30] J. Kurz, S. Sprik, C. Ainscough, and G. Saur, "Fuel cell electric vehicle evaluation."

[31] H.-G. Wahl, "Optimale regelung eines prädiktiven energiemanagements von hybridfahrzeugen," Ph.D. dissertation.

[32] F.-Y. Wang, H. Zhang, and D. Liu, "Adaptive dynamic programming: An introduction," *IEEE Computational Intelligence Magazine*, vol. 4, no. 2, pp. 39–47, 2009.

[33] R. Hussain and S. Zeadally, "Autonomous cars: Research results, issues, and future challenges," vol. 21, pp. 1275–1313.

[34] S. Roeglinger and C. Facchi, "How can car2x-communication improve road safety: A statistical based selection and discussion of feasible scenarios," Working Papers, Hochschule Ingolstadt, 2009.

[35] A. Emadi, K. Rajashekara, S. S. Williamson, and S. M. Lukic, "Topological overview of hybrid electric and fuel cell vehicular power system architectures and configurations," vol. 54, pp. 763–770.

[36] U. R. Prasanna, P. Xuewei, A. K. Rathore, and K. Rajashekara, "Propulsion system architecture and power conditioning topologies for fuel cell vehicles," vol. 51, pp. 640–650.

[37] S. Williamson, M. Lukic, and A. Emadi, "Comprehensive drive train efficiency analysis of hybrid electric and fuel cell vehicles based on motor-controller efficiency modeling," vol. 21, pp. 730–740.

[38] A. Khaligh and Z. Li, "Battery, ultracapacitor, fuel cell, and hybrid energy storage systems for electric, hybrid electric, fuel cell, and plug-in hybrid electric vehicles: State of the art," vol. 59, pp. 2806–2814.

[39] C. Marks, E. A. Rishavy, and F. A. Wyczalek, "Electrovan-a fuel cell powered vehicle," in *Transactions-V76-A*.

[40] N. Qin, P. Brooker, and Raissi, "Evtc project 10 – fuel cell vehicle technologies, infrastructure and requirements."

[41] U. Eberle and R. von Helmolt, "Fuel cell electric vehicles, battery electric vehicles, and their impact on energy storage technologies," pp. 227–245.

[42] J. Larminie and A. Dicks, *Fuel cell systems explained*, 2nd ed. Chichester, West Sussex: J. Wiley, 2011.

[43] Brian D James, Jennie M Huya-Kouadio, Cassidy Houchins, and Daniel A Desantis, "Mass production cost estimation of direct h2

pem fuel cell systems for transportation applications: 2017 update."

[44] A. Wilson, G. Kleen, and D. Papageorgopoulos, "Doe fuel cell technologies office record 17007: Fuel cell system cost – 2017."

[45] M. Klell, H. Eichlseder, and A. Trattner, *Wasserstoff in der Fahrzeugtechnik: Erzeugung, Speicherung, Anwendung*, 4th ed., ser. ATZ/MTZ-Fachbuch. Wiesbaden: Springer Vieweg, 2018.

[46] J. Axsen, A. Burke, and K. Kurani, "Batteries for plug-inhybrid electric vehicles: Goals and the state of technology," Davis, CA.

[47] W. Su, H. Eichi, W. Zeng, and M.-Y. Chow, "A survey on the electrification of transportation in a smart grid environment," *IEEE Transactions on Industrial Informatics*, vol. 8, no. 1, pp. 1–10, 2012.

[48] M. Catenacci, E. Verdolini, V. Bosetti, and G. Fiorese, "Going electric: Expert survey on the future of battery technologies for electric vehicles," *Energy Policy*, vol. 61, pp. 403–413, 2013.

[49] D. Ansean, M. Gonzalez, V. M. Garcia, J. C. Viera, J. C. Anton, and C. Blanco, "Evaluation of lifepo4 batteries for electric vehicle applications," *IEEE Transactions on Industry Applications*, vol. 51, no. 2, pp. 1855–1863, 2015.

[50] S. B. Chikkannanavar, D. M. Bernardi, and L. Liu, "A review of blended cathode materials for use in li-ion batteries," *Journal of Power Sources*, vol. 248, pp. 91–100, 2014.

[51] B. Scrosati and J. Garche, "Lithium batteries: Status, prospects and future," *Journal of Power Sources*, vol. 195, no. 9, pp. 2419–2430, 2010.

[52] L. Guzzella and A. Sciarretta, *Vehicle Propulsion Systems*. Berlin, Heidelberg: Springer Berlin Heidelberg, 2013.

[53] Hydrogenics, "Hypm-hd power modules," Gladbeck, 2019.

[54] Honda, "Honda clarity vehicle specifications," 2019.

[55] GS Yuasa Corporation, "Blue energy ehw5," Kyoto, 2016.

[56] S. Cuk, "A new zero-ripple switching dc-to-dc converter and integrated magnetics," vol. 19, pp. 57–75.

[57] M. Kabalo, B. Blunier, D. Bouquain, and A. Miraoui, "State-of-the-art of dc-dc converters for fuel cell vehicles," in *IEEE Vehicle Power and Propulsion Conference (VPPC), 2010*. Piscataway, NJ: IEEE, 2010, pp. 1–6.

[58] G. Fontes, C. Turpin, S. Astier, and T. A. Meynard, "Interactions between fuel cells and power converters: Influence of current harmonics on a fuel cell stack," *IEEE Transactions on Power Electronics*, vol. 22, no. 2, pp. 670–678, 2007.

[59] M. I. Marei, S. Lambert, R. Pick, and M. Salama, "Dc/dc converters for fuel cell powered hybrid electric vehicle," in *IEEE Conference Vehicle Power and Propulsion, 2005*. Piscataway, NJ: IEEE Operations Center, 2005, pp. 556–559.

[60] M. Kabalo, D. Paire, B. Blunier, D. Bouquain, M. G. Simoes, and A. Miraoui, "Experimental validation of high-voltage-ratio low-input-current-ripple converters for hybrid fuel cell supercapacitor systems," vol. 61, pp. 3430–3440.

[61] Y. Zhang, J. Shi, L. Zhou, J. Li, M. Sumner, P. Wang, and C. Xia, "Wide input-voltage range boost three-level dc–dc converter with quasi-z source for fuel cell vehicles," *IEEE Transactions on Power Electronics*, vol. 32, no. 9, pp. 6728–6738, 2017.

[62] G. Dotelli, R. Ferrero, P. G. Stampino, S. Latorrata, and S. Toscani, "Pem fuel cell drying and flooding diagnosis with signals injected by a power converter," *IEEE Transactions on Instrumentation and Measurement*, vol. 64, no. 8, pp. 2064–2071, 2015.

[63] M. Mohr, W. T. Franke, B. Wittig, and F. W. Fuchs, "Converter systems for fuel cells in the medium power range—a comparative study," *IEEE Transactions on Industrial Electronics*, vol. 57, no. 6, pp. 2024–2032, 2010.

[64] S. Dusmez, A. Hasanzadeh, and A. Khaligh, "Comparative analysis of bidirectional three-level dc–dc converter for automotive applications," *IEEE Transactions on Industrial Electronics*, vol. 62, no. 5, pp. 3305–3315, 2015.

[65] F. Akar, Y. Tavlasoglu, E. Ugur, B. Vural, and I. Aksoy, "A bidirectional nonisolated multi-input dc–dc converter for hybrid energy storage systems in electric vehicles," *IEEE Transactions on Vehicular Technology*, vol. 65, no. 10, pp. 7944–7955, 2016.

[66] C. Zhao, S. d. Round, and J. W. Kolar, "An isolated three-port bidirectional dc-dc converter with decoupled power flow management," *IEEE Transactions on Power Electronics*, vol. 23, no. 5, pp. 2443–2453, 2008.

[67] H. Tao, J. L. Duarte, and M. Hendrix, "Three-port triple-half-bridge bidirectional converter with zero-voltage switching," *IEEE Transactions on Power Electronics*, vol. 23, no. 2, pp. 782–792, 2008.

[68] A. Khaligh, J. Cao, and Y.-J. Lee, "A multiple-input dc–dc converter topology," *IEEE Transactions on Power Electronics*, vol. 24, no. 3, pp. 862–868, 2009.

[69] W. Jiang and B. Fahimi, "Multiport power electronic interface—concept, modeling, and design," *IEEE Transactions on Power Electronics*, vol. 26, no. 7, pp. 1890–1900, 2011.

[70] S. Vengatesan, M. W. Fowler, X.-Z. Yuan, and H. Wang, "Diagnosis of mea degradation under accelerated relative humidity cycling," *Journal of Power Sources*, vol. 196, no. 11, pp. 5045–5052, 2011.

[71] J. Wu, X.-Z. Yuan, J. J. Martin, H. Wang, D. Yang, J. Qiao, and J. Ma, "Proton exchange membrane fuel cell degradation under close to open-circuit conditions," *Journal of Power Sources*, vol. 195, no. 4, pp. 1171–1176, 2010.

[72] W. Schmittinger and A. Vahidi, "A review of the main parameters influencing long-term performance and durability of pem fuel cells," *Journal of Power Sources*, vol. 180, no. 1, pp. 1–14, 2008.

[73] L. Placca and R. Kouta, "Fault tree analysis for pem fuel cell degradation process modelling," *International Journal of Hydrogen Energy*, vol. 36, no. 19, pp. 12 393–12 405, 2011.

[74] D. Zhou, Y. Wu, F. Gao, E. Breaz, A. Ravey, and A. Miraoui, "Degradation prediction of pem fuel cell stack based on multiphysical

aging model with particle filter approach," *IEEE Transactions on Industry Applications*, vol. 53, no. 4, pp. 4041–4052, 2017.

[75] Y. Wu, E. Breaz, F. Gao, and A. Miraoui, "A modified relevance vector machine for pem fuel-cell stack aging prediction," *IEEE Transactions on Industry Applications*, vol. 52, no. 3, pp. 2573–2581, 2016.

[76] Y. Wu, E. Breaz, F. Gao, D. Paire, and A. Miraoui, "Nonlinear performance degradation prediction of proton exchange membrane fuel cells using relevance vector machine," *IEEE Transactions on Energy Conversion*, vol. 31, no. 4, pp. 1570–1582, 2016.

[77] S. J. Bae, S.-J. Kim, J. I. Park, C. W. Park, J.-H. Lee, I. Song, N. Lee, K.-B. Kim, and J.-Y. Park, "Lifetime prediction of a polymer electrolyte membrane fuel cell via an accelerated startup–shutdown cycle test," *International Journal of Hydrogen Energy*, vol. 37, no. 12, pp. 9775–9781, 2012.

[78] V. B. Avakov, V. A. Bogdanovskaya, A. V. Kapustin, O. V. Korchagin, A. V. Kuzov, I. K. Landgraf, M. M. Stankevich, and M. R. Tarasevich, "Lifetime prediction for the hydrogen–air fuel cells," *Russian Journal of Electrochemistry*, vol. 51, no. 6, pp. 570–586, 2015.

[79] T. Fletcher, R. Thring, and M. Watkinson, "An energy management strategy to concurrently optimise fuel consumption & pem fuel cell lifetime in a hybrid vehicle," *International Journal of Hydrogen Energy*, vol. 41, no. 46, pp. 21 503–21 515, 2016.

[80] S. ZHANG, X. YUAN, H. WANG, W. MERIDA, H. ZHU, J. SHEN, S. WU, and J. ZHANG, "A review of accelerated stress tests of mea durability in pem fuel cells," *International Journal of Hydrogen Energy*, vol. 34, no. 1, pp. 388–404, 2009.

[81] X.-Z. Yuan, H. Li, S. Zhang, J. Martin, and H. Wang, "A review of polymer electrolyte membrane fuel cell durability test protocols," *Journal of Power Sources*, vol. 196, no. 22, pp. 9107–9116, 2011.

[82] T. Fletcher, R. H. Thring, M. Watkinson, and I. Staffell, "Comparison of fuel consumption and fuel cell degradation using an optimised controller," *ECS Transactions*, vol. 71, no. 1, pp. 85–97, 2016.

[83] K. Smith, Y. Shi, and S. Santhanagopalan, "Degradation mechanisms and lifetime prediction for lithium-ion batteries — a control perspective," in *American Control Conference (ACC), 2015*. Piscataway, NJ: IEEE, 2015, pp. 728–730.

[84] J. Vetter, P. Novák, M. R. Wagner, C. Veit, K.-C. Möller, J. O. Besenhard, M. Winter, M. Wohlfahrt-Mehrens, C. Vogler, and A. Hammouche, "Ageing mechanisms in lithium-ion batteries," *Journal of Power Sources*, vol. 147, no. 1-2, pp. 269–281, 2005.

[85] S. Käbitz, "Untersuchung der alterung von lithium-ionen-batterien mittels elektroanalytik und elektrochemischer impedanzspektroskopie," Dissertation, RWTH Aachen, 2016.

[86] J. Jaguemont, L. Boulon, P. Venet, Y. Dube, and A. Sari, "Lithium-ion battery aging experiments at subzero temperatures and model development for capacity fade estimation," *IEEE Transactions on Vehicular Technology*, vol. 65, no. 6, pp. 4328–4343, 2016.

[87] D.-I. Stroe, M. Swierczynski, S. K. Kar, and R. Teodorescu, "Degradation behavior of lithium-ion batteries during calendar ageing—the case of the internal resistance increase," *IEEE Transactions on Industry Applications*, vol. 54, no. 1, pp. 517–525, 2018.

[88] M. J. Brand, M. H. Hofmann, S. S. Schuster, P. Keil, and A. Jossen, "The influence of current ripples on the lifetime of lithium-ion batteries," *IEEE Transactions on Vehicular Technology*, vol. 67, no. 11, pp. 10 438–10 445, 2018.

[89] M. Safari, M. Morcrette, A. Teyssot, and C. Delacourt, "Multimodal physics-based aging model for life prediction of li-ion batteries," *Journal of The Electrochemical Society*, vol. 156, no. 3, p. A145, 2009.

[90] G. Ning and B. N. Popov, "Cycle life modeling of lithium-ion batteries," *Journal of Power Sources*, vol. 151, no. 10, p. A1584, 2004.

[91] Q. Zhang and R. E. White, "Capacity fade analysis of a lithium ion cell," *Journal of Power Sources*, vol. 179, no. 2, pp. 793–798, 2008.

[92] M. Koller, T. Borsche, A. Ulbig, and G. Andersson, "Defining a degradation cost function for optimal control of a battery energy

storage system," in *2013 IEEE Grenoble Conference*. IEEE, 16.06.2013 - 20.06.2013, pp. 1–6.

[93] M. A. Ortega-Vazquez, "Optimal scheduling of electric vehicle charging and vehicle-to-grid services at household level including battery degradation and price uncertainty," *IET Generation, Transmission & Distribution*, vol. 8, no. 6, pp. 1007–1016, 2014.

[94] S. B. Peterson, J. Apt, and J. F. Whitacre, "Lithium-ion battery cell degradation resulting from realistic vehicle and vehicle-to-grid utilization," *Journal of Power Sources*, vol. 195, no. 8, pp. 2385–2392, 2010.

[95] B. Xu, A. Oudalov, A. Ulbig, G. Andersson, and D. S. Kirschen, "Modeling of lithium-ion battery degradation for cell life assessment," *IEEE Transactions on Smart Grid*, vol. 9, no. 2, pp. 1131–1140, 2018.

[96] J. Bauman and M. Kazerani, "A comparative study of fuel-cell–battery, fuel-cell–ultracapacitor, and fuel-cell–battery–ultracapacitor vehicles," *IEEE Transactions on Vehicular Technology*, vol. 57, no. 2, pp. 760–769, 2008.

[97] P. Thounthong, V. Chunkag, P. Sethakul, B. Davat, and M. Hinaje, "Comparative study of fuel-cell vehicle hybridization with battery or supercapacitor storage device," *IEEE Transactions on Vehicular Technology*, vol. 58, no. 8, pp. 3892–3904, 2009.

[98] M. Zandi, A. Payman, J.-P. Martin, S. Pierfederici, B. Davat, and F. Meibody-Tabar, "Energy management of a fuel cell/supercapacitor/battery power source for electric vehicular applications," *IEEE Transactions on Vehicular Technology*, vol. 60, no. 2, pp. 433–443, 2011.

[99] G. Dawei, J. Zhenhua, and L. Qingchun, "Performance comparison of different fuel cell vehicle power trains," in *2008 IEEE Vehicle Power and Propulsion Conference*, pp. 1–5.

[100] D. Gao, J. Zhenhua, and L. Qingchun, "Performance comparison of different fuel cell vehicle power trains," in *IEEE Vehicle Power and Propulsion Conference, 2008*. Piscataway, NJ: IEEE, 2008, pp. 1–5.

[101] G. D. Mathur, *Vehicle thermal management: heat exchangers & climate control*, ser. PT. Warrendale, Pa.: Society of Automotive Engineers, 2004, vol. 97.

[102] P. Sabhapathy and L. Zheng, "Hybrid vehicle powertrain thermal management system and method for cabin heating and engine warm up," Patent.

[103] G. A. Dage and L. W. Smith, "Method of thermal management for hybid vehicle," Patent.

[104] G. W. Skala, "14984158073958387 81-06360835," Patent.

[105] J. Nolan and J. Kolodziej, "Modeling of an automotive fuel cell thermal system," vol. 195, pp. 4743–4752.

[106] M. Nasri and D. Dickinson, "Thermal management of fuel cell-driven vehicles using ht-pem and hydrogen storage," pp. 1–6.

[107] P. T. Tennessen, J. C. Weintraub, and W. A. Hermann, "Over-molded thermal inter-face for use with a battery cooling system," Patent US8 541 127 B2,.

[108] G. s. Bower, "Who has the best battery thermal managment system - tesla or gm?" [Online]. Available: https://www.hybridcars.com/who-has-the-best-battery-thermal-management-system-tesla-or-gm/

[109] Porsche, "Thermal management in vehicles with electric drive system," in *Porsche Engineering Magazine*, vol. 1.

[110] S. Ketkar, P. Laurain, and R. McCormick, "Battery system and method for cooling the battery system," Patent US20 140 322 563A1, 2014.

[111] J. Smith, M. Hinterberger, C. Schneider, and J. Koehler, "Energy savings and increased electric vehicle range through improved battery thermal management," vol. 101, pp. 647–656.

[112] G. Zhang and S. G. Kandlikar, "A critical review of cooling techniques in proton exchange membrane fuel cell stacks," vol. 37, pp. 2412–2429.

[113] G. Fontaras, V. Franco, P. Dilara, G. Martini, and U. Manfredi, "Development and review of euro 5 passenger car emission factors

based on experimental results over various driving cycles," *The Science of the total environment*, vol. 468-469, pp. 1034–1042, 2014.

[114] P. De Hann and M. Keller, "Modelling fuel consumption and pollutant emissions based on real-world driving patterns: the hbefa approach," *Int. J. Environment and Pollution*, no. 22, pp. 250–258, 2004.

[115] T.-K. Lee, B. Adornato, and Z. S. Filipi, "Synthesis of real-world driving cycles and their use for estimating phev energy consumption and charging opportunities: Case study for midwest/u.s," *IEEE Transactions on Vehicular Technology*, vol. 60, no. 9, pp. 4153–4163, 2011.

[116] M. André, "Driving cycles development: Characterization of the methods," in *SAE Technical Paper Series*, ser. SAE Technical Paper Series. SAE International400 Commonwealth Drive, Warrendale, PA, United States, 1996.

[117] A. Froberg and L. Nielsen, "Efficient drive cycle simulation," *IEEE Transactions on Vehicular Technology*, vol. 57, no. 3, pp. 1442–1453, 2008.

[118] V. Schwarzer and R. Ghorbani, "Drive cycle generation for design optimization of electric vehicles," *IEEE Transactions on Vehicular Technology*, vol. 62, no. 1, pp. 89–97, 2013.

[119] V. Boscaino and R. Miceli, "Analysis of driving cycles effects on power supply requirements of a fuel cell powered light-weight electric vehicle," in *IEEE International Electric Machines and Drives Conference (IEMDC)*. Piscataway, NJ: IEEE, 2015, pp. 853–859.

[120] M. Jafari, A. Gauchia, K. Zhang, and L. Gauchia, "Simulation and analysis of the effect of real-world driving styles in an ev battery performance and aging," *IEEE Transactions on Transportation Electrification*, vol. 1, no. 4, pp. 391–401, 2015.

[121] M. André, R. Joumard, R. Vidon, P. Tassel, and P. Perret, "Real-world european driving cycles, for measuring pollutant emissions from high- and low-powered cars," *Atmospheric Environment*, vol. 40, no. 31, pp. 5944–5953, 2006.

[122] M. André, "The artemis european driving cycles for measuring car pollutant emissions," *The Science of the total environment*, vol. 334-335, pp. 73–84, 2004.

[123] P. Nyberg, E. Frisk, and L. Nielsen, "Using real-world driving databases to generate driving cycles with equivalence properties," *IEEE Transactions on Vehicular Technology*, vol. 65, no. 6, pp. 4095–4105, 2016.

[124] W. Zimmermann and R. Schmidgall, *Bussysteme in der Fahrzeugtechnik: Protokolle, Standards und Softwarearchitektur*, 5th ed., ser. ATZ / MTZ-Fachbuch. Wiesbaden: Springer Vieweg, 2014.

[125] B. A. Renfro, M. Stein, N. Boecker, and A. Terry, "An analysis of global positioning system (gps) standard positioning service (sps) performance for 2017."

[126] D. M. Bevly, J. C. Gerdes, C. Wilson, and G. Zhang, "The use of gps based velocity measurements for improved vehicle state estimation," in *Proceedings of the American Control Conference*, pp. 2538–2542 vol.4.

[127] T. G. Farr, P. A. Rosen, E. Caro, R. Crippen, R. Duren, S. Hensley, M. Kobrick, M. Paller, E. Rodriguez, L. Roth, D. Seal, S. Shaffer, J. Shimada, J. Umland, M. Werner, M. Oskin, D. Burbank, and D. Alsdorf, "The shuttle radar topography mission," vol. 45, p. 1485.

[128] B. Y. Liaw and M. Dubarry, "From driving cycle analysis to understanding battery performance in real-life electric hybrid vehicle operation," *Journal of Power Sources*, vol. 174, no. 1, pp. 76–88, 2007.

[129] Q. Gong, Y. Li, and Z.-R. Peng, "Trip-based optimal power management of plug-in hybrid electric vehicles," *IEEE Transactions on Vehicular Technology*, vol. 57, no. 6, pp. 3393–3401, 2008.

[130] S. Shahidinejad, E. Bibeau, and S. Filizadeh, "Statistical development of a duty cycle for plug-in vehicles in a north american urban setting using fleet information," *IEEE Transactions on Vehicular Technology*, vol. 59, no. 8, pp. 3710–3719, 2010.

[131] A. Ashtari, E. Bibeau, and S. Shahidinejad, "Using large driving record samples and a stochastic approach for real-world driving

cycle construction: Winnipeg driving cycle," *Transportation Science*, vol. 48, no. 2, pp. 170–183, 2014.

[132] T. K. Lee and Z. S. Filipi, "Synthesis of real-world driving cycles using stochastic process and statistical methodology," vol. 57, p. 17.

[133] E. Silvas, K. Hereijgers, H. Peng, T. Hofman, and M. Steinbuch, "Synthesis of realistic driving cycles with high accuracy and computational speed, including slope information," *IEEE Transactions on Vehicular Technology*, vol. 65, no. 6, pp. 4118–4128, 2016.

[134] P. Nyberg, E. Frisk, and L. Nielsen, "Driving cycle equivalence and transformation," *IEEE Transactions on Vehicular Technology*, vol. 66, no. 3, pp. 1963–1974, 2017.

[135] M. D. Petersheim and S. N. Brennan, "Scaling of hybrid electric vehicle powertrain components for hardware-in-the-loop simulation," in *2008 IEEE International Conference on Control Applications*. Piscataway, NJ: IEEE Service Center, 2008, pp. 720–726.

[136] L. Guzzella and A. Sciarretta, *Vehicle Propulsion Systems*. Berlin, Heidelberg: Springer Berlin Heidelberg, 2013.

[137] A. Isidori, *Nonlinear Control Systems*, third edition ed., ser. Communications and Control Engineering. London: Springer, 1995.

[138] V. H. Johnson, "Battery performance models in advisor," vol. 110, pp. 321–329.

[139] L. Guzzella and C. H. Onder, *Introduction to Modeling and Control of Internal Combustion Engine Systems*. Berlin, Heidelberg: Springer Berlin Heidelberg, 2010.

[140] U. Kiencke and L. Nielsen, *Automotive Control Systems: For Engine, Driveline, and Vehicle*, second edition ed. Berlin, Heidelberg: Springer-Verlag Berlin Heidelberg, 2005.

[141] X. Hu, J. Jiang, B. Egardt, and D. Cao, "Advanced power-source integration in hybrid electric vehicles: Multicriteria optimization approach," *IEEE Transactions on Industrial Electronics*, vol. 62, no. 12, pp. 7847–7858, 2015.

[142] Z. Hu, J. Li, L. Xu, Z. Song, C. Fang, M. Ouyang, G. Dou, and G. Kou, "Multi-objective energy management optimization and parameter sizing for proton exchange membrane hybrid fuel cell vehicles," *Energy Conversion and Management*, vol. 129, pp. 108–121, 2016.

[143] L. Xu, C. D. Mueller, J. Li, M. Ouyang, and Z. Hu, "Multi-objective component sizing based on optimal energy management strategy of fuel cell electric vehicles," *Applied Energy*, vol. 157, pp. 664–674, 2015.

[144] A. Tani, M. B. Camara, B. Dakyo, and Y. Azzouz, "Dc/dc and dc/ac converters control for hybrid electric vehicles energy management-ultracapacitors and fuel cell," vol. 9, pp. 686–696.

[145] D. Zhou, A. Al-Durra, I. Matraji, A. Ravey, and F. Gao, "Online energy management strategy of fuel cell hybrid electric vehicles: A fractional-order extremum seeking method," *IEEE Transactions on Industrial Electronics*, vol. 65, no. 8, pp. 6787–6799, 2018.

[146] X. Zhang, C. C. Mi, A. Masrur, and D. Daniszewski, "Wavelet-transform-based power management of hybrid vehicles with multiple on-board energy sources including fuel cell, battery and ultracapacitor," *Journal of Power Sources*, vol. 185, no. 2, pp. 1533–1543, 2008.

[147] R. Beck, F. Richert, A. Bollig, D. Abel, S. Saenger, K. Neil, T. Scholt, and K.-E. Noreikat, "Model predictive control of a parallel hybrid vehicle drivetrain," in *2005 44th IEEE Conference on Decision and Control & European Control Conference*. Piscataway, N.J: Institute of Electrical and Electronics Engineers, 2005, pp. 2670–2675.

[148] Amin, B. R. Trilaksono, A. Sasongko, A. S. Rohman, C. J. Dronkers, and R. Ortega, "Model predictive control of hybrid fuel cell/battery/supercapacitor power sources," in *2012 International Conference on System Engineering and Technology (ICSET)*. Piscataway, NJ: IEEE, 2012, pp. 1–6.

[149] Amin, R. T. Bambang, A. S. Rohman, C. J. Dronkers, R. Ortega, and A. Sasongko, "Energy management of fuel

cell/battery/supercapacitor hybrid power sources using model predictive control," *IEEE Transactions on Industrial Informatics*, vol. 10, no. 4, pp. 1992–2002, 2014.

[150] B. Geng, J. K. Mills, and D. Sun, "Two-stage energy management control of fuel cell plug-in hybrid electric vehicles considering fuel cell longevity," *IEEE Transactions on Vehicular Technology*, vol. 61, no. 2, pp. 498–508, 2012.

[151] T. Miro-Padovani, G. Colin, A. Ketfi-Cherif, and Y. Chamaillard, "Implementation of an energy management strategy for hybrid electric vehicles including drivability constraints," in *IEEE Trans. Veh. Technol. (IEEE Transactions on Vehicular Technology)*, vol. 65, pp. 5918–5929.

[152] S. Njoya Motapon, L.-A. Dessaint, and K. Al-Haddad, "A comparative study of energy management schemes for a fuel-cell hybrid emergency power system of more-electric aircraft," *IEEE Transactions on Industrial Electronics*, vol. 61, no. 3, pp. 1320–1334, 2014.

[153] X. Hu, N. Murgovski, L. M. Johannesson, and B. Egardt, "Optimal dimensioning and power management of a fuel cell/battery hybrid bus via convex programming," vol. 20, pp. 457–468.

[154] Toyota, "Outline of the mirai," 2017.

[155] Y. Feng and C. Zhang, "Core loss analysis of interior permanent magnet synchronous machines under svpwm excitation with considering saturation," vol. 10, p. 1716.

[156] H. B. Pacejka and I. Besselink, *Tire and vehicle dynamics*, 3rd ed. Amsterdam and Boston: Elsevier/BH, 2012.

[157] J. Larminie and A. Dicks, *Fuel cell systems explained*, 2nd ed. Chichester, West Sussex: J. Wiley, 2011.

[158] Q. Yu, A. K. Srivastava, S.-Y. Choe, and W. Gao, "Improved modeling and control of a pem fuel cell power system for vehicles," pp. 331–336.

[159] P. Acharya, P. Enjeti, and I. J. Pitel, "An advanced fuel cell simulator," pp. 1554–1558.

[160] M. J. Kim, H. Peng, C.-C. Lin, E. Stamos, and D. Tran, "Testing, modeling, and control of a fuel cell hybrid vehicle," pp. 3859–3864.

[161] K. J. Runtz and M. D. Lyster, "Fuel cell equivalent circuit models for passive mode testing and dynamic mode design," pp. 794–797.

[162] D. W. Dees, V. S. Battaglia, and A. Bélanger, "Electrochemical modeling of lithium polymer batteries," vol. 110, pp. 310–320.

[163] J. Newman, K. E. Thomas, H. Hafezi, and D. R. Wheeler, "Modeling of lithium-ion batteries," vol. 119-121, pp. 838–843.

[164] M. Chen and G. A. Rincon-Mora, "Accurate electrical battery model capable of predicting runtime and i–v performance," vol. 21, pp. 504–511.

[165] P. Rong and M. Pedram, "An analytical model for predicting the remaining battery capacity of lithium-ion batteries," *IEEE Transactions on Very Large Scale Integration (VLSI) Systems*, vol. 14, no. 5, pp. 441–451, 2006.

[166] Y. Cao, R. C. Kroeze, and P. T. Krein, "Batterie // multi-timescale parametric electrical battery model for use in dynamic electric vehicle simulations," *IEEE Transactions on Transportation Electrification*, vol. 2, no. 4, pp. 432–442, 2016.

[167] B. Y. Liaw, G. Nagasubramanian, R. G. Jungst, and D. H. Doughty, "Modeling of lithium ion cells?a simple equivalent-circuit model approach," vol. 175, pp. 835–839.

[168] S. Buller, M. Thele, R. DeDoncker, and E. Karden, "Impedance-based simulation models of supercapacitors and li-ion batteries for power electronic applications," vol. 41, pp. 742–747.

[169] C. M. Shepherd, "Design of primary and secondary ceils: An equation describing battery discharge," in *Journal of the Electrochemical Society Vol. 112*, vol. 7, p. 657.

[170] O. Tremblay, L.-A. Dessaint, and A.-I. Dekkiche, "A generic battery model for the dynamic simulation of hybrid electric vehicles," in *IEEE Vehicle Power and Propulsion Conference, 2007*. Piscataway, NJ: IEEE, 2007, pp. 284–289.

[171] L. Zubieta and R. Bonert, "Characterization of double-layer capacitors (dlcs) for power electronics applications," in *IAS '98*. Piscataway, N.J: IEEE, 1998, pp. 1149–1154.

[172] R. Bonert and L. Zubieta, "Measurement techniques for the evaluation of double-layer power capacitors," in *IAS '97*. New York, N.Y. and Piscataway, N.J: Institute of Electrical and Electronics Engineers, 1997, pp. 1097–1100.

[173] A. S. Weddell, G. v. Merrett, T. J. Kazmierski, and B. M. Al-Hashimi, "Accurate supercapacitor modeling for energy harvesting wireless sensor nodes," *IEEE Transactions on Circuits and Systems II: Express Briefs*, vol. 58, no. 12, pp. 911–915, 2011.

[174] N. Xu and J. Riley, "Nonlinear analysis of a classical system: The double–layer capacitor," *Electrochemistry Communications*, vol. 13, no. 10, pp. 1077–1081, 2011.

[175] K. B. Oldham, "A gouy–chapman–stern model of the double layer at a (metal)/(ionic liquid) interface," *Journal of Electroanalytical Chemistry*, vol. 613, no. 2, pp. 131–138, 2008.

[176] V. F. Pires and J. Silva, "Teaching nonlinear modeling, simulation, and control of electronic power converters using matlab/simulink," *IEEE Transactions on Education*, vol. 45, no. 3, pp. 253–261, 2002.

[177] J. Chen, C. Xu, C. Wu, and W. Xu, "Adaptive fuzzy logic control of fuel-cell-battery hybrid systems for electric vehicles," *IEEE Transactions on Industrial Informatics*, vol. 14, no. 1, pp. 292–300, 2018.

[178] V. Valdivia, A. Barrado, A. Lazaro, M. Sanz, D. L. del Moral, and C. Raga, "System-level black-box modeling of dc-dc converters with input current control for fuel cell power conditioning," in *Twenty-Seventh Annual IEEE Applied Power Electronics Conference and Exposition (APEC), 2012*. Piscataway, NJ: IEEE, 2012, pp. 443–450.

[179] T. Yuksel and J. J. Michalek, "Effects of regional temperature on electric vehicle efficiency, range, and emissions in the united states," vol. 49, pp. 3974–3980.

[180] A. Abdollahi, N. Raghunathan, X. Han, B. Pattipati, B. Balasingam, K. R. Pattipati, Y. Bar-Shalom, and B. Card, "Battery health degradation and optimal life management," pp. 146–151.

[181] T. M. Bandhauer, S. Garimella, and T. F. Fuller, "A critical review of thermal issues in lithium-ion batteries," vol. 158, p. R1.

[182] M. Ouyang, X. Feng, X. Han, L. Lu, Z. Li, and X. He, "A dynamic capacity degradation model and its applications considering varying load for a large format li-ion battery," vol. 165, pp. 48–59.

[183] "Bu-502: Discharging at high and low temperatures," 23.04.2019. [Online]. Available: https://batteryuniversity.com/learn/article/discharging_at_high_and_low_temperatures

[184] J. Lopez-Sanz, C. Ocampo-Martinez, J. Alvarez-Florez, M. Moreno Eguilaz, R. Ruiz-Mansilla, J. Kalmus, M. Graber, and G. Lux, "Nonlinear model predictive control for thermal management in plug-in hybrid electric vehicles," p. 1.

[185] F. Martel, Y. Dube, S. Kelouwani, and K. Agbossou, "Active battery thermal management integrated to cold weather optimal phev autonomy extension," pp. 1–6.

[186] E. Kim, K. G. Shin, and J. Lee, "Real-time battery thermal management for electric vehicles," pp. 72–83.

[187] F. Barbir, J. Neutzler, and B. Balasubramanian, "Optimal operating temprature and pressure of pem fuel cell systemsin automotive application," *Proceedings 218 ACS National Meeting, no. 44*, pp. 977–981, 1999.

[188] M. V. Moreira and G. E. da Silva, "A practical model for evaluating the performance of proton exchange membrane fuel cells," vol. 34, pp. 1734–1741.

[189] Schunk Bahn- und Industrietechnik GmbH, "Handbuch für schunk brennstoffzellen-stacks: Fc-42 fc-08," vol. 4th ed.

[190] D. Wenger, "Metallhydridspeicher zur wasserstoffversorgung und kühlung von brennstoffzellenfahrzeugen," Dissertation, Technische Universität München, 2009.

[191] Brusa Elektronik AG, “Gic-bidirectional 750v dc/dc-converter: New state of the art galvanically isolated high-power converter.” Sennwald.

[192] ——, “Hybrid synchronous motor 50 kw: Powerfull drive for small vehicles.” Sennwald.

[193] H. Großmann, *Pkw-Klimatisierung: Physikalische Grundlagen und technische Umsetzung*, 2nd ed., ser. VDI-Buch. Berlin, Heidelberg and s.l.: Springer Berlin Heidelberg, 2013.

[194] X. Tao, “Design, modeling and control of a thermal management system for hybrid electric vehicles,” Dissertation, Clemson University, Clemson, 2016.

[195] J. Zang, X. Yan, S. Huang, X. Zeng, Y. Li, Y. Huang, and J. Yu, “A general method for developing friction factor formulas under supercritical conditions and in different geometries,” vol. 65, pp. 262–271.

[196] F. M. White, *Fluid mechanics*, 7th ed. Singapore: McGraw-Hill, 2011.

[197] S. Genic, I. Arandjelovic, P. Kolendic, M. S. Jaric, N. J. Budimir, and V. Genic, “A review of explicit approximations of colebrook’s equation,” *FME Transactions*, no. 39, pp. 67–71, 2011.

[198] S. E. Haaland, “Simple and explicit formulas for the friction factor in turbulent pipe flow,” vol. 105, p. 89.

[199] International Organization for Standardization, “Measurement of fluid flow by means of pressure differential devices inserted in circular cross-section conduits running full: Iso 5167-1:2003.”

[200] Mathworks, “Variable area orifice (tl): Orifice with variable cross-sec-tional area specified through physical signal input.” [Online]. Available: https://de.mathworks.com/help/physmod/hydro/ref/variableareaorificetl.html

[201] J. Nolan and J. Kolodziej, “Modeling of an automotive fuel cell thermal system,” vol. 195, pp. 4743–4752.

[202] J. F. Gülich, *Centrifugal Pumps*, 2nd ed. s.l.: Springer-Verlag, 2010.

[203] A. Akers, M. Gassman, and R. J. Smith, *Hydraulic power system analysis*, ser. Fluid Power and Control. Boca Raton, FL: CRC/Taylor & Francis, 2006.

[204] M.-H. Charlap, *Comprehensive thermal management system model for hybrid electric vehicles*. [Place of publication not identified]: Proquest, Umi Dissertatio, 2011.

[205] A. M. Fsadni, J. P. Whitty, M. A. Stables, and A. A. Adeniyi, "Numerical study on turbulent heat transfer and pressure drop characteristics of a helically coiled hybrid rectangular-circular tube heat exchanger with al 2 o 3 -water nanofluids," vol. 114, pp. 466–483.

[206] B. S. Petukhov, "Heat transfer and friction in turbulent pipe flow with variable physical properties," vol. 6, pp. 503–564.

[207] C. Kleinstreuer, Ed., *Engineering fluid dynamics: An interdisciplinary systems approach*. Cambridge: Cambridge University Press, 1997.

[208] Y. A. Çengel and A. J. Ghajar, *Heat and mass transfer: Fundamentals & applications*, 5th ed. New York, NY: McGraw-Hill Education, 2015.

[209] C. Forgez, D. Vinh Do, G. Friedrich, M. Morcrette, and C. Delacourt, "Thermal modeling of a cylindrical lifepo4/graphite lithium-ion battery," vol. 195, pp. 2961–2968.

[210] S. Rogg, M. Höglinger, E. Zwittig, C. Pfender, W. Kaiser, and T. Heckenberger, "Cooling modules for vehicles with a fuel cell drive," vol. 3, pp. 153–158.

[211] K. Lahmer, R. Bessaïh, A. Scipioni, and M. El Ganaoui, "Thermal modeling of hydrogen storage by absorption in a magnesium hydrides tank," vol. 5, p. A21.

[212] A. Ravey, S. Faivre, C. Higel, F. Harel, and A. Djerdir, "Energy management of fuel cell electric vehicle with hydrid tanks," pp. 3962–3967.

[213] M. S. Rajagopal, K. N. Seetharamu, and P. A. Ashwathnarayana, "Transient thermal analysis of induction motors," vol. 13, pp. 62–69.

[214] A. M. EL-Refaie, N. C. Harris, T. M. Jahns, and K. M. Rahman, "Thermal analysis of multibarrier interior pm synchronous machine using lumped parameter model," vol. 19, pp. 303–309.

[215] H. D. Baehr and K. Stephan, *Wärme- und Stoffübertragung*, 8th ed. Berlin, Heidelberg: Springer Berlin Heidelberg, 2013.

[216] C. Shao, X. Sun, G. Wang, Y. Yue, X. Li, and L. Yang, "Numerical modeling and simulation analysis of vehicle thermal management system for a power-split hybrid electric vehicle," in *2015 International Conference on Electrical Systems for Aircraft, Railway, Ship Propulsion and Road Vehicles (ESARS)*. Piscataway, NJ: IEEE, 2015, pp. 1–6.

[217] S. Park and L. Thompson, "A comprehensive thermal management system model for hybrid electric vehicles."

[218] Y.-J. Chang and C.-C. Wang, "A generalized heat transfer correlation for iouver fin geometry," vol. 40, pp. 533–544.

[219] H.-J. Steemann, A. Janssens, and M. D. Paepe, "About the use of the heat and mass analogy in building simulation," in *Proc. 12th Symposium for Building 2007*.

[220] N. Vorayos and T. Kiatsiriroat, "Thermal characteristics of louvered fins with a low-reynolds number flow," vol. 24, pp. 845–850.

[221] X. Wang and H. T. Chua, "Two bed silica gel–water adsorption chillers: An effectual lumped parameter model," vol. 30, pp. 1417–1426.

[222] Z. Lei and M. Zaheeruddin, "Dynamic simulation and analysis of a water chiller refrigeration system," vol. 25, pp. 2258–2271.

[223] H. Yang, Y. Wang, and T. He, "The analysis on the effect of passenger car air conditioning and distribution with different inlet parameters," *International Journal of Vehicle Design*, no. 4, pp. 292–311, 1983.

[224] S. R. Ahmed, B. Bayer, N. Deußen, H.-J. Emmelmann, H. Flegl, A. Gilhaus, H. Götz, H. Großmann, R. Hoffmann, W.-H. Hucho, D. Hummel, G. A. Necati, R. Piatek, M. Rauser, D. Schlenz, W. Sebbeße, and P. Steinberg, *Aerodynamik des Automobils: Eine*

Brücke von der Strömungsmechanik zur Fahrzeugtechnik, ser. VDI-Buch. Berlin and Heidelberg: Springer, 1999.

[225] J. Nitz and W. H. Hucho, "The heat transfer coefficient of a passenger car's body."

[226] Fabian Schueppel, "Heizung und klimatisierung von fahrzeugen mit geringer antriebsstrangabwärme."

[227] H.-G. Wagemann and H. Eschrich, *Grundlagen der photovoltaischen Energiewandlung: Solarstrahlung, Halbleitereigenschaften und Solarzellenkonzepte*, ser. Teubner Studienbücher Angewandte Physik. Wiesbaden: Vieweg+Teubner Verlag, 1994.

[228] J. Lopez-Sanz, C. Ocampo-Martinez, J. Alvarez-Florez, M. Moreno-Eguilaz, R. Ruiz-Mansilla, J. Kalmus, M. Graeber, and G. Lux, "Thermal management in plug-in hybrid electric vehicles: A real-time nonlinear model predictive control implementation," *IEEE Transactions on Vehicular Technology*, vol. 66, no. 9, pp. 7751–7760, 2017.

[229] H. Esen, T. Tashiro, D. Bernardini, and A. Bemporad, "Cabin heat thermal management in hybrid vehicles using model predictive control," in *22nd Mediterranean Conference of [i.e. on] Control and Automation (MED), 2014*. Piscataway, NJ: IEEE, 2014, pp. 49–54.

[230] Y. Masoudi and N. L. Azad, "Mpc-based battery thermal management controller for plug-in hybrid electric vehicles," in *2017 American Control Conference*. Piscataway, NJ: IEEE, 2017, pp. 4365–4370.

[231] Y. Masoudi, A. Mozaffari, and N. L. Azad, "Battery thermal management of electric vehicles: An optimal control approach," p. V001T13A003.

[232] J. Han, S. Yu, and S. Yi, "Advanced thermal management of automotive fuel cells using a model reference adaptive control algorithm," *International Journal of Hydrogen Energy*, vol. 42, no. 7, pp. 4328–4341, 2017.

[233] E. Breaz, F. Gao, A. Miraoui, and R. Tirnovan, "A short review of aging mechanism modeling of proton exchange membrane fuel cell in transportation applications," pp. 3941–3947.

[234] F. Tianheng, Y. Lin, G. Qing, H. Yanqing, Y. Ting, and Y. Bin, "A supervisory control strategy for plug-in hybrid electric vehicles based on energy demand prediction and route preview," vol. 64, pp. 1691–1700.

[235] F. R. Salmasi, "Control strategies for hybrid electric vehicles: Evolution, classification, comparison, and future trends," vol. 56, pp. 2393–2404.

[236] Z. Amjadi and S. S. Williamson, "Power-electronics-based solutions for plug-in hybrid electric vehicle energy storage and management systems," *IEEE Transactions on Industrial Electronics*, vol. 57, no. 2, pp. 608–616, 2010.

[237] P. Garcia, L. M. Fernandez, C. A. Garcia, and F. Jurado, "Energy management system of fuel-cell-battery hybrid tramway," *IEEE Transactions on Industrial Electronics*, vol. 57, no. 12, pp. 4013–4023, 2010.

[238] B. Vural, A. R. Boynuegri, I. Nakir, O. Erdinc, A. Balikci, M. Uzunoglu, H. Gorgun, and S. Dusmez, "Fuel cell and ultracapacitor hybridization: A prototype test bench based analysis of different energy management strategies for vehicular applications," *International Journal of Hydrogen Energy*, vol. 35, no. 20, pp. 11 161–11 171, 2010.

[239] R. Sangili Vadamalu and C. Beidl, *Online optimization based energy management of hybrid electric vehicles using direct optimal control*.

[240] M. Vajedi, A. Taghavipour, N. L. Azad, and J. McPhee, "A comparative analysis of route-based power management strategies for real-time application in plug-in hybrid electric vehicles," pp. 2612–2617.

[241] J. Han, D. Kum, and Y. Park, "Synthesis of predictive equivalent consumption minimization strategy for hybrid electric vehicles based on closed-form solution of optimal equivalence factor," *IEEE Transactions on Vehicular Technology*, vol. 66, no. 7, pp. 5604–5616, 2017.

[242] F. Zhang, J. Xi, and R. Langari, "Real-time energy management strategy based on velocity forecasts using v2v and v2i communications," vol. 18, pp. 416–430.

[243] V. T. Minh and A. A. Rashid, "Modeling and model predictive control for hybrid electric vehicles," vol. 13, pp. 477–485.

[244] Y. Hu, L. Yang, B. Yan, T. Yan, and P. Ma, "An online rolling optimal control strategy for commuter hybrid electric vehicles based on driving condition learning and prediction," vol. 65, pp. 4312–4327.

[245] P. Thounthong and S. Rael, "The benefits of hybridization," *IEEE Industrial Electronics Magazine*, vol. 3, no. 3, pp. 25–37, 2009.

[246] P. Thounthong, S. Rael, and B. Davat, "Control strategy of fuel cell and supercapacitors association for a distributed generation system," *IEEE Transactions on Industrial Electronics*, vol. 54, no. 6, pp. 3225–3233, 2007.

[247] K. Jin, X. Ruan, M. Yang, and M. Xu, "A hybrid fuel cell power system," *IEEE Transactions on Industrial Electronics*, vol. 56, no. 4, pp. 1212–1222, 2009.

[248] E. Vinot, J. Scordia, R. Trigui, B. Jeanneret, and F. Badin, "Model simulation, validation and case study of the 2004 ths of toyota prius," *International Journal of Vehicle Systems Modelling and Testing*, vol. 2008, no. 3, p. 139.

[249] P. Fragiacomo and P. Francesco, "Energy performance of a fuel cell hybrid system for rail vehicle propulsion," *Energy Procedia*, vol. 126, pp. 1051–1058, 2017.

[250] P. García, J. P. Torreglosa, L. M. Fernández, and F. Jurado, "Viability study of a fc-battery-sc tramway controlled by equivalent consumption minimization strategy," *International Journal of Hydrogen Energy*, vol. 37, no. 11, pp. 9368–9382, 2012.

[251] O. Föllinger, U. Konigorski, B. Lohmann, G. Roppenecker, and A. Trächtler, *Regelungstechnik: Einführung in die Methoden und ihre Anwendung ; [aktualisierter Lehrbuch-Klassiker*, 11th ed. Berlin: VDE-Verl., 2013.

[252] K. J. Åström and R. M. Murray, *Feedback systems: An introduction for scientists and engineers*. Princeton, NJ: Princeton Univ. Press, 2008.

[253] J. Schiffer, O. Bohlen, R. W. de Doncker, D. U. Sauer, and K. Y. Ahn, "Optimized energy management for fuelcell-supercap hybrid electric vehicles vpp track 4: Energy storage components/systems," in *IEEE Conference Vehicle Power and Propulsion, 2005*. Piscataway, NJ: IEEE Operations Center, 2005, pp. 716–723.

[254] W.-w. Xiong, Y. Zhang, and C.-l. Yin, "Configuration design, energy management and experimental validation of a novel series-parallel hybrid electric transit bus," vol. 10, pp. 1269–1276.

[255] Q. Zeng and J. Huang, "The design and simulation of fuzzy logic controller for parallel hybrid electric vehicles," pp. 908–912.

[256] S. Caux, W. Hankache, M. Fadel, and D. Hissel, "On-line fuzzy energy management for hybrid fuel cell systems," *International Journal of Hydrogen Energy*, vol. 35, no. 5, pp. 2134–2143, 2010.

[257] N.-s. Lee, G.-m. Jeong, and H.-s. Ahn, "Improvement of fuel economy using fuzzy logic-based power distribution control strategy for a fchev," in *International Conference on Computational Intelligence and Security, 2006*, Y.-m. Cheung, Ed. Piscataway, NJ: IEEE Operations Center, 2006, pp. 891–894.

[258] H. Hemi, J. Ghouili, and A. Cheriti, "A real time fuzzy logic power management strategy for a fuel cell vehicle," vol. 80, pp. 63–70.

[259] D. Gao, Z. Jin, and Q. Lu, "Energy management strategy based on fuzzy logic for a fuel cell hybrid bus," vol. 185, pp. 311–317.

[260] S. Onori, L. Serrao, and G. Rizzoni, "Adaptive equivalent consumption minimization strategy for hybrid electric vehicles," in *Proceedings of the ASME 2010 Dynamic Systems and Control Conference*, pp. 499–505.

[261] L. Serrao, S. Onori, and G. Rizzoni, "A comparative analysis of energy management strategies for hybrid electric vehicles," vol. 133, p. 031012.

[262] B. Gu and G. Rizzoni, "An adaptive algorithm for hybrid electric vehicle energy management based on driving pattern recognition," pp. 249–258.

[263] S.-i. Jeon, S.-T. Jo, Y.-i. Park, and J.-M. Lee, "Multi-mode driving control of a parallel hybrid electric vehicle using driving pattern recognition," vol. 124, p. 141.

[264] B. Jeanneret and T. Markel, “Adaptive energy management strategy for fuel cell hybrid vehicles.”

[265] C. Musardo, G. Rizzoni, Y. Guezennec, and B. Staccia, “A-ecms: An adaptive algorithm for hybrid electric vehicle energy management,” vol. 11, pp. 509–524.

[266] A. Sciarretta, L. Guzzella, and M. Back, “A real-time optimal control strategy for parallel hybrid vehicles with on-board estimation of the control parameters,” vol. 37, pp. 489–494.

[267] B. De Jager, M. Steinbuch, and T. van Keulen, “An adaptive sub-optimal energy management strategy for hybrid drive-trains,” vol. 41, pp. 102–107.

[268] D. Ambuhl and L. Guzzella, “Predictive reference signal generator for hybrid electric vehicles,” vol. 58, pp. 4730–4740.

[269] C. Manzie, P. Dewangan, G. Corde, O. Grondin, and A. Sciarretta, “State of charge management for plug in hybrid electric vehicles with uncertain distance to recharge,” pp. 1–6.

[270] J. P. Torreglosa, F. Jurado, P. García, and L. M. Fernández, “Hybrid fuel cell and battery tramway control based on an equivalent consumption minimization strategy,” *Control Engineering Practice*, vol. 19, no. 10, pp. 1182–1194, 2011.

[271] O. Föllinger and G. Roppenecker, *Optimale Regelung und Steuerung*, 3rd ed., ser. Methoden der Regelungs- und Automatisierungstechnik. München: De Gruyter, 1994.

[272] V. Puig, R. Costa-Castello, and J. L. Sampietro, “Economic mpc for the energy management of hybrid vehicles including fuel cells and supercapacitors,” in *The 2016 UKACC International Conference on Control (UKACC Control 2016)*. Piscataway, NJ: IEEE, 2016, pp. 1–6.

[273] W. Greenwell and A. Vahidi, “Predictive control of voltage and current in a fuel cell–ultracapacitor hybrid,” in *IEEE Transactions on Industrial Electronics*, vol. 57, pp. 1954–1963.

[274] X. Hu, C. Zou, X. Tang, T. Liu, and L. Hu, “Cost-optimal energy management of hybrid electric vehicles using fuel cell/battery

health-aware predictive control," *IEEE Transactions on Power Electronics*, p. 1, 2019.

[275] S. Uebel, N. Murgovski, B. Baker, and J. Sjoberg, "A 2-level mpc for energy management including velocity control of hybrid electric vehicles," *IEEE Transactions on Vehicular Technology*, no. (Early Access), 2019.

[276] S. Uebel, N. Murgovski, C. Tempelhahn, and B. Baker, "Optimal energy management and velocity control of hybrid electric vehicles," *IEEE Transactions on Vehicular Technology*, vol. 67, no. 1, pp. 327–337, 2018.

[277] T. Binder, L. Blank, H. G. Bock, R. Bulirsch, W. Dahmen, M. Diehl, T. Kronseder, W. Marquardt, J. P. Schlöder, and O. von Stryk, *Introduction to Model Based Optimization of Chemical Processes on Moving Horizons*, vol. 33.

[278] E. F. Camacho and C. Bordons, *Model Predictive control*, second edition ed., ser. Advanced Textbooks in Control and Signal Processing. London: Springer, 2007.

[279] J. M. Maciejowski, *Predictive control: With constraints*. Harlow: Prentice Hall, 2002.

[280] L. Grüne and J. Pannek, *Nonlinear model predictive control: Theory and algorithms*, ser. Communications and Control Engineering. London and Dordrecht and Heidelberg and New York: Springer, 2011.

[281] R. Dittmar and B.-M. Pfeiffer, *Modellbasierte prädiktive Regelung: Eine Einführung für Ingenieure*. München and Wien: Oldenbourg, 2009.

[282] D. P. Bertsekas, *Dynamic programming and optimal control*, [teilw. nachdr. der ausg.] 1987, dynamic programming : deterministic and stochastic models, prentice-hall ed. Belmont, Mass.: Athena Scientific, 1995.

[283] M. Papageorgiou, M. Leibold, and M. Buss, *Optimierung: Statische, dynamische, stochastische Verfahren für die Anwendung*, 4th ed. Berlin and Heidelberg: Springer Vieweg, 2015.

[284] R. Bellman, *Dynamic programming*. New Jersey, USA: Princeton University Press, 1957.

[285] R. Bellmann, *Dynamische Programmierung und selbstanpassende Regelprozesse*. New Jersey, USA: Oldenbourg, 1967.

[286] M. Y. Ayad, M. Becherif, and A. Henni, "Vehicle hybridization with fuel cell, supercapacitors and batteries by sliding mode control," vol. 36, pp. 2627–2634.

[287] International Organization for Standardization, "Intelligent transport systems - geographic data files (gdf) - gdf5.0 (iso 14825:2011)," 2011.

[288] J. Ludwig, *Elektronischer Horizont –Vorausschauende Systeme und deren Anbindung an Navigationseinheiten*.

[289] S. Durekovic, "Development on the electronic horizon: An integrated development environment for map-based driver assistance systems," in *sSpace Magazin*, vol. 2, pp. 50–57.

[290] P. Engel, J. Wietse Balkerna, and A. Varchmin, "Method for determining most probable path of car by software modules, involves providing personal and impersonal driving probability data for correcting original path, where data is derived from previous driving behavior of vehicle," Patent DE102 011 078 946A1.

[291] A. Carlsson, H.-C. Reuss, and G. Baumann, "Implementation of a self-learning route memory for forward-looking driving," vol. 1, pp. 62–70.

[292] P. Sahlholm and K. Henrik Johansson, "Road grade estimation for look-ahead vehicle control using multiple measurement runs," vol. 18, pp. 1328–1341.

[293] R.-P. Schäfer, K.-U. Thiessenhusen, and P. Wagner, "A traffic information system by means of real-time floating-car data," in *9th World Congress on Intelligent Transportation Systems*.

[294] S. Lorkowski, E. Brockfeld, P. Mieth, B. Passfeld, K.-U. Thiessenhusen, and R.-P. Schäfer, "Erste mobilitätsdienste auf basis von "floating car data"," in *4. Aachener Kollouium Mobilität und Stadt*, pp. 93–100.

[295] M. Maurer and C. Stiller, *Fahrerassistenzsysteme mit maschineller Wahrnehmung: Basiert auf ausgewählten Vorträgen eines Workshops in Walting (Altmühltal)*. Berlin: Springer, 2005.

[296] Y. L. Murphey, R. Milton, and L. Kiliaris, "Driver's style classification using jerk analysis," in *2009 IEEE Workshop on Computational Intelligence in Vehicles and Vehicular Systems (CIVVS)*, pp. 23–28.

[297] K. K. Sibi, P. Pathiyil, and R. Sunitha, "Driver classification for hybrid electric vehicles based on fuel consumption index," in *2016 International Conference on Computation of Power, Energy Information and Commuincation (ICCPEIC)*, pp. 321–325.

[298] J. Wang, P. Liu, J. Hicks-Garner, E. Sherman, S. Soukiazian, M. Verbrugge, H. Tataria, J. Musser, and P. Finamore, "Cycle-life model for graphite-lifepo4 cells," *Journal of Power Sources*, vol. 196, no. 8, pp. 3942–3948, 2011.

[299] J. Ackermann, *Abtastregelung*. Berlin and Heidelberg: Springer, 1972.

[300] N. Stroe, S. Olaru, G. Colin, K. Ben-Cherif, and Y. Chamaillard, "A two-layer predictive control for hybrid electric vehicles energy management," vol. 50, pp. 10 058–10 064.

[301] A. Hamednia, N. Murgovski, and J. Fredriksson, "Predictive velocity control in a hilly terrain over a long look-ahead horizon," vol. 51, pp. 485–492.

[302] L. Guo, B. Gao, Y. Gao, and H. Chen, "Optimal energy management for hevs in eco-driving applications using bi-level mpc," *IEEE Transactions on Intelligent Transportation Systems*, vol. 18, no. 8, pp. 2153–2162, 2017.

[303] A. Züttel, A. Borgschulte, and L. Schlapbach, *Hydrogen as a Future Energy Carrier*. Weinheim: Wiley, 2011.

[304] Hydrogenics, "Celerityplus 60kw fuel cell power system: Installation, 3rd ed." Mississauga.

[305] Brusa Elektronik AG, "Evb1-hv-battery (16kwh/400v or 14kwh/350v)." Sennwald.

[306] ——, “Dmc5-high power inverter: The solid, powerful basis for electric motors,” Sennwald.

[307] ——, “Hsm1-hybrid synchronous motor: Optimum perfor-mance from zero speed.”

[308] H. E. Perez, X. Hu, S. Dey, and S. J. Moura, “Optimal charging of li-ion batteries with coupled electro-thermal-aging dynamics,” *IEEE Transactions on Vehicular Technology*, vol. 66, no. 9, pp. 7761–7770, 2017.

A

THERMAL SYSTEM DESIGN

The assessment of the losses are the basis in order to derive the technical requirements of the cooling loops and TMS of a FHEV. The components are specified in Chapter 2.2. For a full-size car the required components as well as the corresponding power losses and efficiency are summarised in table A.2. The component efficiency were assumed based on standard literature. Since the TMS has to be capable to guarantee the optimal operation temperatures at maximum power operation, for the system configuration these worst power losses at maximum power are assumed.

Table A.2 summarises the required power losses which have to be dissipated by the TMS. The metal hydride storage acts as an additional heat sink, which can dissipate a heat of $10\,\mathrm{MJ\,kg^{-1}}$ [190, 303]. With an energy density of $39.4\,\mathrm{kW\,h\,kg^{-1}}$, the energy dissipation of the metal hydride storage is equal to $70.3\,\mathrm{W\,kW^{-1}}$. In accordance to the introduced system topology, see 4.2, the FC radiator has to dissipate the heat of both,

Table A.1: Heat Sources

Component	Efficiency [%]	Rated Power [kW]	Power Loss [kW]
Electric Motor	95	100	5
Inverter	98	100	3
DC-DC Converter	95	100	5
BAT	90	4	0.4
FC	55	100	80

Table A.2: Heat Sinks

Component	Power Loss [kW]
Metal hydride storage	22
BAT radiator	70
FC radiator	0.5
Chiller	8

the FC and the power electronics and the electric motor minus the heat dissipated by the metal hydride storage. Equation A.1 summarises the heat equilibrium.

$$\dot{Q}_{FC,rad} = \dot{Q}_{FC} + \dot{Q}_{EM+Inv} + \dot{Q}_{DC-DC} - \dot{Q}_{MHS} \tag{A.1}$$

The air flow rate into the passenger compartment is specified by [193] as 4 - 12 $\mathrm{kg\,min^{-1}}$, while it is specified that the outflow temperature has to 5 - 10 °C below the ambient temperature. For a maximum ambient temperature of $50\,^{\circ}\mathrm{C}$, the temperature, therefore, is to be cooled down to $45\,^{\circ}\mathrm{C}$. The required chiller power can be determined based on equation A.2.

$$P_{chill} = c_{p,a} \cdot \dot{m}_a \cdot \Delta T \tag{A.2}$$

With the determined maximum power losses, the required mass flow rates and maximum temperature increase can be estimated. With an average heat capacity of $3.5\,\mathrm{kJ\,kg^{-1}\,K}$ and a maximum temperature rise of $5\,^{\circ}\mathrm{C}$ the mass flow rates of the FC and BAT cooling loop can be determined with equation A.16.

$$\dot{m}_{BAT} = \frac{\dot{Q}_{BAT}}{c_{c,p} \cdot \Delta T} \tag{A.3}$$

The FC heat exchanger can be determined by the temperature differences across the heat exchanger. For the operation in summer at maximum ambient temperature of $50\,^{\circ}\mathrm{C}$, it is considered that the inlet temperature to the FC is $60\,^{\circ}\mathrm{C}$ [188, 304]. The inlet temperature of the heat exchanger can be determined backwards through the fluid flow rate and the power losses of the components, see equation **??**. For the outlet temperature of the hot fluid, the maximum temperature is assumed which ensures that the inlet temperature of the motor is at its maximum of $65\,^{\circ}\mathrm{C}$. The

Table A.3: Recommended flow rate and inlet temperature of the high-temperature components

Component	Rated Flow Rates [$\mathrm{L\,min^{-1}}$]	Maximum Inlet Temperature [°C]
Electric Motor	6 - 8	65
Inverter	6 - 8	65
DC-DC Converter	>15	65

Table A.4: Flow rates, pressure loss and temperature increase in the high-temperature circuit19

Component	Flow rate [$\mathrm{kg\,min^{-1}}$]	Pressure loss [mbar]	Temperature rise [K]
Electric Motor	0.1362	260.4	7.72
Inverter	0.1463	260.4	2.77
DC-DC Converter	0.2825	<800	3.72

corresponding outlet temperature can be determined similar to equation A.16.

$$T_2^{'} = T_2^{''} - \frac{\dot{Q}_{PE}}{\dot{m}_{FC} \cdot c_{c,p}} \tag{A.4}$$

Considering an inlet temperature of $60\,^{\circ}\mathrm{C}$ into and $65\,^{\circ}\mathrm{C}$, resulting from a maximum temperature deviation of $5\,^{\circ}\mathrm{C}$, out of the FC, the temperature of the metal hydride storage can be determined as equation A.5.

$$T_{FC,out} + \Delta T = T_{FC,out} + \frac{\dot{Q}_{MHS}}{c_{c,p} \cdot \dot{m}_{FC}} \tag{A.5}$$

The FC radiator is to dissipate $80\,\mathrm{kW}$ by enforcing a temperature deviation of $5\,^{\circ}\mathrm{C}$. The recommended flow rates of the electric motor and the converters are specified in the datasheet and summarized in table A.3. Considering a maximum flow rate of $0.2825\,\mathrm{kg\,min^{-1}}$, the pressure losses and the temperature increases can be calculated. The results are summarised in table A.4

For the specification of the BAT's heat exchanger, the inlet temperature of the passenger compartment's heat exchanger has to be specified first. The passenger compartment's heat exchanger is a counter-flow heat exchanger. Due to the about three times higher heat capacity of the coolant,

the inlet temperature of this heat exchanger's coolant is assumed to be $5\,^{\circ}\mathrm{C}$ – the minimum air temperature. For an optimal operation, the temperature increase over this heat exchanger is determined to be $5\,^{\circ}\mathrm{C}$. The mass-flow rate is then determined as:

$$\dot{m}_c = \frac{\dot{Q}_{PC}}{\Delta \cdot c_{p,c}} \tag{A.6}$$

For the definition of the fluid flow of the air conditioning pump, a maximum temperature deviation over the chiller of $5\,^{\circ}\mathrm{C}$ was assumed. For a dissipation capability of $8\,\mathrm{kW}$, the coolant flow rate was determined to be $0.46\,\mathrm{kg\,s^{-1}}$.

The hot temperature as well as the BAT heat exchanger can be specified based on the inlet and outlet temperature as well as related to the mass flow rate. Table A.6 summarises these parameter for both heat exchanger. In accordance to Section 4.3.3, the non-dimensional temperature differences can be calculated as follows:

$$\epsilon_1 = \frac{T_1' - T_1''}{T_1' - T_2'} \tag{A.7}$$

$$\epsilon_2 = \frac{T_2'' - T_2'}{T_1' - T_2'} \tag{A.8}$$

$$C_1 = \frac{\epsilon_2}{\epsilon_1} \tag{A.9}$$

$$C_1 = \frac{1}{C_1} \tag{A.10}$$

$$\tag{A.11}$$

The calculation of the counter-flow heat exchanger can be calculated based on [215].

$$N_1 = \frac{1}{1 - C_1} \ln\left(\frac{1 - C_1 \cdot \epsilon_1}{1 - \epsilon_1}\right) \tag{A.12}$$

$$N_2 = \frac{1}{1 - C_2} \ln\left(\frac{1 - C_2 \cdot \epsilon_2}{1 - \epsilon_2}\right) \tag{A.13}$$

$$\tag{A.14}$$

With the values depicted in equation A.13 and A.14, the thermal transmittance can be specified with equation A.15.

$$k_1 \cdot A_1 = k_2 \cdot A_2 = \dot{W}_1 \cdot N_1 = \dot{W}_2 \cdot N_2 \tag{A.15}$$

Table A.5: Summary of inlet and outlet temperature and mass flow rate of the heat exchanger

Fluid	Inlet Temperature [$\mathrm{L\,min^{-1}}$]	Outlet Temperature [°C]	Mass flow rate [$\mathrm{kg\,s^{-1}}$]
Hot fluid BAT	20	15	0.03
Cold fluid BAT	5	7.03	0.383
Hot fluid FC	70.16	61.28	0.2825
Cold fluid FC	59.4	60	4.5

Table A.6: Components' pressure loss at measured and nominal flow rate

Component	Pressure Loss (measured) [mbar]	Pressure Loss (nominal flow rate) [mbar]
BAT [305]	124	170.3
FC [304]	120	208
Inverter [306]	150	208
Motor [307]	<400	<400
DC-DC [191]	<200	<128
Metal Hydride	<200	<182

For the specification of the BAT's heat exchanger, the mass flows have to be determined. The mass flow of the BAT's coolant is specified to be $0.03\,\mathrm{kg\,s^{-1}}$. For an optimal temperature of $26\,^{\circ}\mathrm{C}$, the required inlet temperature is assumed to be $15\,^{\circ}\mathrm{C}$ [305]. The temperature rise was specified to be $5\,^{\circ}\mathrm{C}$. The mass flow rate of the low temperature side was calculated as $0.383\,\mathrm{kg\,s^{-1}}$. The inlet temperature of the low-temperature side is $5\,^{\circ}\mathrm{C}$, the outlet temperature is calculated as follows:

$$T_{cold,out} = T_{cold,in} + \frac{Q_{BAT}}{c_{p,c} \cdot \dot{m}_{cold}} \tag{A.16}$$

The pumps have to be configured in order to guarantee the specified fluid flow rates. In order to determine the coolant pumps, the maximum pressure loss of the components need to be calculated. Rough turbulent flow is considered. Baehr and Stephan state that most liquid cooling concepts are designed to be turbulent due the better heat transfer. No heat exchangers have been designed or chosen so far. Thus values for the heat exchangers and the radiator as assumed. The values have been chosen similarly to the components where it was assumed that the pressure loss

Table A.7: Pressure drop, mass flow rate and rated power of the pumps.

Pump	Pressure Loss [mbar]	Mass flow rate [mbar]	Power W
FC	914	4.5	350
Air condition	150	0.46	6.3
BAT	340	0.03	3
Power Electronics	1208	0.02825	31

is generally smaller. Fixed displacement pumps are chosen for the pumps. The required power of each pump can be estimated based on the corresponding mass flow rate and pressure drop. The required performance parameter of each coolant loop pump are summarised on table A.7.

B

SINGLE STAGE DP ALGORITHM

Algorithm 1 Backward Oriented DP

```
1:  procedure CALCBACK
2:      j ← Y.j                                   ▷ Initialise optimal predecessors
3:      X ← Y.x                                   ▷ Initialise optimal states
4:      position ← min(Y.j(P))                    ▷ Set predecessor at prediction horizon
5:      for k = P : −1 : 2 do                     ▷ For all stages
6:          [I_Bat(k-1)] ← Y.u(k,position,1)       ▷ Set optimal BAT current at stage k
7:          [I_FC(k-1)] ← Y.u(k,position,2)        ▷ Set optimal FC current at stage k
8:          position ← X(k,position)              ▷ Set next optimal states
9:      end for
10:     return [I_Bat(1), I_FC(1)]                ▷ Return input trajectory
11: end procedure
```

Algorithm 2 Forward Oriented DP

procedure OPTPATH
  for $n = 1 : +1 : grid_1$ **do** ▷ For all points in BAT state grid
    $I_B \leftarrow$ InvBat(SoC(1,1,1),SoC(2,n,1)) ▷ Determine BAT current from SOC deviation
    for $m = 1 : +1 : grid_2$ **do** ▷ For all points in SC state grid
      $I_{FC} \leftarrow$ InvSC(I_B, SoC(1,1,1), V_{SC}(1,1,1),V_{SC}(2,n,m),Z(2))
▷ Determine FC current based on deviation of states and given I_B
      J(2,n,m) $\leftarrow$ CalcJ(SoC(2,n,m), V_{SC}(2,n,m),I_B,I_{FC})
▷ Determine cost for specific states and inputs
      Y(2,n,m).u $\leftarrow$ [I_B,I_{FC}] ▷ Store inputs
      Y(2,n,m).x $\leftarrow$ [n,m] ▷ Store predecessors
    end for
  end for

  for $k = 3 : +1 : P$ **do** ▷ For all stages till prediction horizon
    for $n = 1 : +1 : grid_1$ **do** ▷ For all points in BAT state grid
      $SoC_{min} \leftarrow$ detSoC(SoC(k,n,m),$I_{Bat,min}$(k)) ▷ Determine minimum SoC
      $SoC_{max} \leftarrow$ detSoC(SoC(k,n,m),$I_{Bat,max}$(k)) ▷ Determine maximum SoC
      for $l = 1 : +1 : grid_1$ **do** ▷ For all points in BAT state grid
        if $SoC(k-1,l,1) \geq SoC_{\min}$ **then** ▷ Check if predecessor is valid
          if $SoC_{\max} \geq SoC(k-1,l,1)$ **then**
            $I_B(l) \leftarrow$ InvBat(SoC(k-1,l,1),SoC(k,n,1)) ▷ Determine I_B based on SoC deviation
          end if
        end if
      end for
      for $m = 1 : +1 : grid_2$ **do** ▷ For all points in SC state grid
        for $p = 1 : +1 : grid_1$ **do** ▷ For all points in BAT state grid
          $V_{SC,min} \leftarrow$ detV($I_{FC,max}$, I_B(p), ...
            SoC(k-1,n,m),V_{SC}(k,n,m),Z(k-1) ▷ Determine minimum SC voltage
          $V_{SC,max} \leftarrow$ detV($I_{FC,min}$, I_B(p), ...
            SoC(k-1,n,m),V_{SC}(k,n,m), Z(k-1) ▷ Determine maximum SC voltage
          for $o = 1 : +1 : grid_1$ **do** For all points in BAT state grid
            $I_{FC}(o) \leftarrow$ InvSC(I_B(p), SoC(k-1,p,1),...
              V_{SC}(k-1,p,o), V_{SC}(k,m,n), Z(k-1)) ▷ Determine I_{FC}
            j(o,p) $\leftarrow$ CalcJ(SoC(k,n,m), V_{SC}(k,n,m),I_B(p),I_{FC}(p,o))
▷ Determine corresponding transition cost
          end for
        end for
        $X \leftarrow$ min(j) ▷ Store position of cost minimum
        Y(k,n,m).x $\leftarrow$ [SoC(X), V_{SC}(X)] ▷ Store corresponding states
        Y(k,n,m).u $\leftarrow$ [I_{Bat}(X), I_{FC}(X)] ▷ Store corresponding inputs
        Y(k,n,m).j $\leftarrow$ j(X) ▷ Store corresponding predecessor
      end for
    end for
  end for

  return Y ▷ Return result structure

end procedure

C

TWO STAGE DP ALGORITHM

Algorithm 3 Optimal Bat SoC

procedure OPTBAT
  for $n = 1:1:grid$ **do** ▷ For all points in BAT state grid at stage 2
    $I_B(n)$ ← InvBat(SoC(1,1),SoC(2,n)) ▷ Determine I_{BAT} from SoC deviation
    $[I_{FC}(n), dP(n)]$ ← CalcIfc(I_B(n),SoC(1,1),Z(1)) ▷ Determine corresponding I_{FC} and power deviation
    $J(2,n)$ ← calcJB(SoC(2,1), I_B(n), I_{FC}(n), dP(n)) ▷ Determine corresponding transition cost
  end for

  for $k = 3:1:P$ **do** ▷ For stages till prediction horizon
    for $n = 1:1:grid$ **do** ▷ For point in SoC grid
      SoC_{max} ← detSoC(SoC(k,n),$I_{Bat,min}$(k)) ▷ Determine maximum SoC
      SoC_{min} ← detSoC(SoC(k,n),$I_{Bat,max}$(k)) ▷ Determine minimum SoC
      for $nk1 = 1:1:grid$ **do** ▷ For point in SoC grid at predecessor stage
        $I_B(nk1)$ ← InvBat(SoC(k-1,nk1),SoC(k,n)) ▷ Determine I_{Bat} based on SoC transition
        $[I_{FC}(nk1), dP(nk1)]$ ← CalcIfc(I_B(nk1), SoC(k-1,nk1),Z(k-1)) ▷ Determine I_{Bat} and dP based on SoC transition, I_{BAT} and load
        $j(k,nk1)$ ← J(k-1,nk1) + calcJB(SoC(k,1), I_B(nk1), I_{FC}(nk1), dP(nk1)) ▷ Determine corresponding transition cost
      end for
      X ← min(j) ▷ Determine minimum transition cost
      $J(k,n)$ ← j(k,X) ▷ Store optimal cost at specific state
      $Y(k,n).x$ ← SoC(X) ▷ Store optimal SoC
      $Y(k,n).u$ ← [I_{Bat}(X),I_{FC}(X) ▷ Store corresponding inputs
      $Y(k,n).j$ ← j(X) ▷ Store predecessor
    end for
  end for

  return$Y$ ▷ Return result structure

end procedure

Algorithm 4 Backward SoC Path

procedure BACKSOC
  j ← Y.j ▷ Initialise optimal predecessors
  X ← Y.x ▷ Initialise optimal states

  $position$ ← min(Y.j(P)) ▷ Set predecessor at prediction horizon
  for $k = P:-1:2$ **do**
    $[I_{Bat}(k-1)]$ ← Y.u(k,position,1) ▷ Set optimal BAT current at stage k
    $[I_{FC}(k-1)]$ ← Y.u(k,position,2) ▷ Set optimal FC current at stage k
    $position$ ← X(k,position) ▷ Set next optimal states
  end for

  return$[I_{\text{Bat}}, I_{\text{FC}}]$ ▷ Return input trajectory

end procedure

Algorithm 5 Optimal Vsc

procedure OPTVSC
  for $m = 1:1:grid$ **do** ▷ For all points in SC state grid at stage 2
    P_{Gen}*(2,n)* ← V_{SC}(1,1), V_{SC}(2,n)) ▷ Determine equivalent generator power
    J(2,n) ← calcJV(V_{SC}(2,n), P_{Gen}(n)) ▷ Determine corresponding transition cost
  end for

  for $k = 3:1:P$ **do** ▷ For stages till prediction horizon
    for $n = 1:1:grid$ **do** ▷ For points in SC grid
      $V_{SC,max}$ ← detVsc(V_{SC}(k,m), $I_{Bat,min}$, 0, Z(k-1))
    ▷ Determine maximum SC voltage
      $V_{SC,min}$ ← detVsc(V_{SC}(k,m), $I_{Bat,max}$, $I_{FC,max}$, Z(k-1))
    ▷ Determine minimum SC voltage
      for $mk1 = 1:1:grid$ **do** ▷ For points in SC grid at predecessor stage
        P_{Gen}*(k,mk1)* ← V_{SC}(k-1,mk1), V_{SC}(k,m)) ▷ Determine dP_{Gen} based on V_{SC} deviation
        j(mk1) ← J(k-1,mk1) + calcJV(V_{SC}(k,m), P_{Gen}(mk1))
    ▷ Determine corresponding transition cost
      end for
      X ← min(j) ▷ Determine minimum transition cost
      J(k,m) ← j(k,X) ▷ Store optimal cost at specific state
      Y(k,m).u ← P_{Gen}(X) ▷ Store dP_{Gen}
      Y(k,m).j ← j(X) ▷ Store predecessor
    end for
  end for

  return$Y$ ▷ Return result structure

end procedure

Algorithm 6 Backward Vsc Path

procedure BACKSOC
  j ← Y.j ▷ Initialise optimal predecessors
  X ← Y.x ▷ Initialise optimal states

  position ← min(Y.j(P)) ▷ Set predecessor at prediction horizon
  for $k = P:-1:2$ **do**
    [P_{Gen}(k-1)] ← Y.u(k,position,2) ▷ Set optimal generator power at stage k
    position ← X(k,position) ▷ Set next optimal states
  end for

  return P_{Gen} ▷ Return input trajectory

end procedure

D

STATE OF HEALTH

The BAT SoH model was derived based on [274] and [27]. Ebbesen et al. describe the capacity loss of a lithium BAT with equation D.1. Thus, the reduction of the cell capacity, ΔQ is the capacity reduction in percent, is determined by c-rate, respectively by the cell current. The pre-exponential factor M has also a significant impact, nevertheless M also depends on the C-rate.

$$\Delta Q = M(C)e^{A(C)^z \cdot \frac{-E_a(C)}{RT_{cell}}} \tag{D.1}$$

T_{cell} is the lumped BAT temperature and A is the discharged ampere-hour throughput, E_a is the activation energy and z the power-law-factor. [27] used an empirical approximation in order to determine E_a:

$$E_a = 31700 - 370.3 \cdot c. \tag{D.2}$$

M was determined by [27] based on an empirical measurement, table D.1 summarises the results related to the C-rate. In accordance to [274], the end of life of an automotive BAT is defined by a capacity loss of $20\,\%$. With equation D.1 and D.2, the total discharge throughput A_{tot} can be

Table D.1: Pre-exponential factor as a function of the C-rate [27].

C-rate	0.5	2	6	10
M	31630	21681	12934	15512

determined and acquired by:

$$A_{tot} = \left[\frac{20}{M(c) e^{\frac{-E_{\alpha}(c)}{R_c T_c}}} \right]^{\frac{1}{z}}. \tag{D.3}$$

The number of cycles (N) until the end of life of the BAT is reached, is defined by [308], see equation D.5.

$$N(C, T_c) = \frac{3600 \cdot A_{tot}(C, T_c)}{Q} \tag{D.4}$$

Combining equation D.2 and D.5, result in an equation describing the change of the BAT's state of health, related to the BAT current.

$$\Delta SoH_{BAT} = \frac{i_{BAT}(k) \cdot \Delta t}{2 \cdot N(c, T_C) \cdot Q} \tag{D.5}$$